Yield Modeling of Agrivoltaic Concepts

Ertragsmodellierung von Agrivoltaik Konzepten

Von der Fakultät für Maschinenwesen der Rheinisch-Westfälischen Technischen Hochschule Aachen zur Erlangung des akademischen Grades einer Doktorin der Naturwissenschaften genehmigte Dissertation

vorgelegt von

Anna Clara Pauline Kujawa

Berichter/in: Univ.-Prof. Dr.-Ing. Robert Pitz-Paal
Prof. Cristina Cornaro, PhD

Tag der mündlichen Prüfung: 19.06.2026

„Diese Dissertation ist auf den Internetseiten der Universitätsbibliothek online verfügbar.“

Abstract

To mitigate the ongoing climate change, carbon-neutral sources of energy are required. Large scale photovoltaic (PV) systems are considered one of the most promising technologies in this regard, as they have proven to be a green, cheap and reliable energy source. With the exponential growth of installed PV capacities worldwide, direct land-use changes have been triggered as ground-mounted PV systems have been installed on arable land formerly used for food production. However, renewable energy does not threaten agricultural production; indeed, they can coexist in the concept of agrivoltaics (APV). Describing the combination of agriculture and PV energy production on the same plot of land, APV is a promising solution when it comes to meeting the growing demand for both food and energy while also addressing land use conflicts.

This thesis presents the development and validation of a simulation tool for APV greenhouses (GHs). The model enables the simulation of irradiance levels under APV conditions within GHs and gives an estimation of crop yield. The ray-tracing-based irradiance model focuses on mapping light transmission through GH cover materials and PV modules. The crop model includes two different approaches. One approach is based on daily light integral (DLI) requirements of different crops. The second approach focuses particularly on tomatoes and uses a functional-structural plant model (FSPM).

The irradiance model was validated using both data from literature and experimentally measured data from an APV GH experiment performed from September 2023 to March 2024. The experiment was conducted in a "raspa y amagado" GH in Almería, Spain, and two roof cover ratios of 30% and 50% shading were compared against an unshaded control zone. The nRMSE of the global horizontal irradiance was determined to be 0.09 for the control zone, 0.18 for 30% shading and 0.27 for 50% shading using the irradiance data from the experiment. For the literature-based validation, a "Venlo"-type APV GH experiment from 2014–2015 was reproduced, resulting in a deviation of 2.88 percentage points in the simulated reduction in radiation over the entire crop cycle. The crop model was validated exclusively with data from the 2023–2024 APV GH experiment. The nRMSE of yield of the DLI analysis for the simulated crop cycle was 0.10 for the control zone, 0.07 for 30% shading and 0.06 for 50% shading. The validation of the FSPM approach yielded an nRMSE of dry weight of 0.04 for the unshaded control zone and 0.07 for the 30% shading zone, while the data from the 50% shading zone was used to calibrate the model.

The economic assessment of the experimental APV GH showed a potential profit increase of +15% under the case of 30% of the GH roof covered with PV. For the 50% cover scenario, the economic profitability increased to 22% for one tomato crop cycle. The developed simulation tool provides a solid foundation for modeling the irradiance distribution within APV GHs and assessing its effects on expected crop yield. It can serve in the future as a basis for deriving optimal APV GH designs tailored to specific locations, climate conditions and crop types.

Kurzfassung

Um den Klimawandel abzuschwächen, sind CO_2-neutrale Energiequellen erforderlich. Großflächige Photovoltaikanlagen (PV-Anlagen) gelten als eine vielversprechende Technologie, da sie sich als umweltfreundliche, kostengünstige und zuverlässige Energiequelle bewährt haben. Mit dem exponentiellen Wachstum der weltweit installierten PV-Kapazitäten kam es zu direkten Landnutzungsänderungen, da PV-Anlagen auf Landflächen installiert wurden, die zuvor für die Nahrungsmittelproduktion genutzt wurden. Erneuerbare Energien stellen jedoch keine Bedrohung für die landwirtschaftliche Produktion dar, sondern können im Rahmen des Konzepts der Agriphotovoltaik (AgriPV) koexistieren.

Diese Arbeit präsentiert die Entwicklung und Validierung einer Simulationsumgebung für AgriPV-Gewächshäuser. Das Modell ermöglicht die Simulation der Einstrahlung unter AgriPV-Bedingungen in Gewächshäusern und liefert eine Ertragsabschätzung. Das auf Raytracing basierende Strahlungsmodell konzentriert sich auf die Transmittanz durch Gewächshausabdeckungsmaterialien und PV-Module. Das Pflanzenmodell umfasst zwei verschiedene Ansätze. Der erste Ansatz basiert auf den täglichen Lichtintegralanforderungen (DLI) verschiedener Pflanzen. Der zweite Ansatz fokussiert sich auf Tomaten und verwendet ein funktional-strukturelles Pflanzenmodell (FSPM).

Das Strahlungsmodell wurde sowohl anhand von Daten aus der Literatur als auch anhand von experimentell gemessenen Daten aus einem AgriPV-Gewächshausversuch validiert, der von September 2023 bis März 2024 durchgeführt wurde. Das Experiment wurde in einem "raspa y amagado"-Gewächshaus in Almería, Spanien, durchgeführt, wobei Abschattungen von 30% und 50% mit einer unbeschatteten Kontrollzone verglichen wurden. Der nRMSE der globalen Horizontalstrahlung beträgt 0,09 für die Kontrollzone, 0,18 für 30% Beschattung und 0,27 für 50% Beschattung. Für die literaturbasierte Validierung wurde ein AgriPV-Gewächshaus-Experiment vom Typ "Venlo" aus den Jahren 2014–2015 reproduziert, was zu einer Abweichung von 2,88 Prozentpunkten bei der simulierten Strahlungsreduktion über den gesamten Erntezyklus führte. Das Pflanzenmodell wurde ausschließlich mit Daten aus dem AgriPV-Gewächshaus-Experiment 2023–2024 validiert. Der nRMSE des Ertrages der DLI-Analyse für den simulierten Anbauzyklus betrug 0,10 für die Kontrollzone, 0,07 für 30% Beschattung und 0,06 für 50% Beschattung. Die Validierung des FSPM-Ansatzes ergab einen nRMSE des Ertrages von 0,04 für die unbeschattete Kontrollzone und 0,07 für 30% Beschattung, während die Daten der 50% Zone zur Kalibrierung des Modells verwendet wurden.

Die wirtschaftliche Bewertung des AgriPV-Gewächshauses ergab eine Gewinnsteigerung von +15% bei einer 30-prozentigen Dachabdeckung mit PV. Bei 50% Abdeckung stieg die Gewinnsteigerung auf 22%. Die entwickelte Simulationsumgebung bietet eine solide Grundlage für die Modellierung der Strahlungsverteilung in AgriPV-Gewächshäusern und die Bewertung ihrer Auswirkungen auf den erwarteten Ernteertrag. Das Modell kann in Zukunft als Grundlage für die Herleitung optimaler AgriPV-Gewächshausdesigns dienen, die an bestimmte Standorte, Klimabedingungen und Pflanzenarten angepasst sind.

Abbreviations

General abbreviations and variables

α	scale factor in yield estimation for maximum yield under optimal temperature and RH conditions
$\alpha_{\odot}$	angular radius of the solar disc
$a(month)$	linear regression coefficients for the PAR to GHI estimation
a_6	total transmissivity parameter of a `Radiance trans` material
a_7	transmitted specularity fraction of a `Radiance trans` material
APV	agrivoltaic
$b(month)$	linear regression coefficients for the PAR to GHI estimation
BSDF	bidirectional-scattering distribution function
$\mathbf{C}$	diffuse reflectance colour vector $(red, green, blue)$
CAMS	Copernicus Atmosphere Monitoring Service
CIE	International Commission on Illumination
CIEMAT	Centro de Investigaciones Energéticas, Medioambientales y Tecnológicas
$conv.$	conversion factor to change PAR unit from $\mathrm{W\,m^{-2}}$ to $\mu\mathrm{mol\,m^{-2}\,s^{-1}}$, with a constant value of $4.6\,\mu\mathrm{mol\,J^{-1}}$
D_0	cumulative DLI threshold before yield onset
DHI	diffuse horizontal irradiance
DLI	daily light integral
$\mathrm{DLI_{APV}}(t)$	DLI of day t under APV (shaded) conditions
$\mathrm{DLI_{cum}}(t)$	sum of DLI values up to day t
$\mathrm{DLI_{min}}$	minimum DLI required to maintain full yield
$\mathrm{DLI_{opt}}$	optimal DLI requirements
DNI	direct normal irradiance
eFAST	extended Fourier Amplitude Sensitivity Test
$E_0(d)$	extraterrestrial normal irradiance as a function of the day of year d
E_{sc}	solar constant ($\approx 1367\,\mathrm{W\,m^{-2}}$)
EU	European Union
$E(x)$	irradiance at a surface point x
$\varepsilon_{\mathrm{RH}}$	yield sensitivity parameter to changes in RH
ε	sky clearness parameter (Perez model)
FSPM	functional structural plant model
GH	greenhouse
GHI	global horizontal irradiance
I_0	incident irradiance
I_{diff}	diffusely transmitted irradiance
I_{dir}	direct transmitted irradiance
$I_{trans,total}$	total transmitted irradiance
IR	infrared

k_{DLI}	sensitivity parameter to express changes in yield due to DLI reductions
L_e	emitted radiance
L_i	incident radiance
L_r	reflected (outgoing) radiance
$L_{\text{sky}}(\theta, \gamma)$	sky radiance distribution function
$L_\odot$	solar radiance
L_z	zenith sky radiance
LCOE	levelized cost of electricity
LDPE	low-density polyethylene
MAE	mean absolute error
MBE	mean bias error
m	relative optical air mass
n	number of measurements/observations
$\mathbf{n}$	outward surface normal at point x
NIR	near-infrared
nMAE	normalized mean absolute error
nMBE	normalized mean bias error
nRMSE	normalized root mean square error
$\boldsymbol{\omega}$	direction vector
$\Omega_\odot$	solid angle of the solar disc
Ω^+	(sky) hemisphere above the surface
PAR	photosynthetically active radiation
P_{max}	maximum photosynthetic rate due to saturation
p.p.	percentage points
PPFD	photosynthetic photon flux density
PPFD_{sat}	PAR saturation levels
PSA	Plataforma Solar de Almería
PSO	Particle Swarm Optimization
PV	photovoltaic
R^2	coefficient of determination
RGB	red, green, blue colour channels used internally by `Radiance`
RH	relative humidity
$RH_{\text{mean}}(t)$	mean daytime RH of day t inside the GH
RH_{opt}	optimal daytime RH inside the GH
RMSE	root mean square error
r_s	specularity parameter of a `Radiance trans` material
ρ_{bd}	bidirectional reflectance–transmittance distribution function
$\rho_{r,\text{diff}}$	diffuse reflection component
$\rho_{r,\text{spec}}$	specular reflection component
$\rho_{t,\text{diff}}$	diffuse transmission component
$\rho_{t,\text{spec}}$	specular transmission component
σ	standard deviation
τ	overall transmittance
t	time
Δt	time interval

Δ	sky brightness parameter (Perez model)
θ_{rot}	rotation angle
θ_s	solar zenith angle
ϕ_s	solar azimuth angle
T_{diff}	diffuse transmission in the definition of a `Radiance` `trans` material
T_{spec}	specular transmission in the definition of a `Radiance` `trans` material
$T_{\text{mean}}(t)$	mean daytime temperature of day t inside the GH
T_{opt}	optimal daytime temperature inside the GH
TOMGRO	Tomato Growth Model
UV	ultraviolet
γ_{T}	yield sensitivity to changes in temperature
γ	angular distance between sun and sky element
y_i	observed value
$\hat{y}_i$	predicted (or simulated) value
$\overline{y}$	mean of the observed values
$Y(t)$	relative yield under APV conditions, expressed as a percentage of the control (no shading) yield

TOMGRO variables

α_F	maximum partitioning of new growth to fruit
β	coefficient in expolinear LAI–N equation
D	maximum leaf conductance to water vapor
$D_F(T_d)$	function describing the rate of fruit development
δ	maximum leaf area expansion per node
E	growth efficiency
$f_F(T_d)$	function to modify partitioning to fruit for mean daily temperature
$f_N(T)$	function reducing node development under non-optimal temperature
$g(T_d)$	function reducing growth at high temperature
GR_{net}	net above-ground growth rate
k_F	development time from first fruit to first ripe fruit
K	light extinction coefficient
$\lambda(T_d)$	temperature-reduction function for leaf expansion
LAI	leaf area index
LAI_{max}	maximum leaf area index
m	leaf light transmission coefficient
N	node number for the main stem
N_b	projection of linear segment of LAI vs. N to horizontal axis
N_{FF}	node position where the first fruit appears
N_m	node appearance rate per day
p_1	loss of leaf dry weight per node after LAI_{max} is reached
Q_{10}	coefficient in maintenance respiration equation
Q_e	quantum efficiency of photosynthesis
ρ_{plant}	plant density
r_m	maintenance respiration coefficient
T_{CRIT}	critical temperature for photosynthesis decline
τ_{CO_2}	Carbon dioxide use efficiency
$\nu(\vartheta)$	transition coefficient between vegetative and full fruit growth
V_{max}	maximum increase in vegetative tissue dry weight growth per node
W	total plant dry weight
W_f	total fruit dry weight
W_m	mature fruit dry weight

Contents

ABSTRACT iii

KURZFASSUNG v

ABBREVIATIONS vii

CONTENTS xiii

1 INTRODUCTION AND OBJECTIVES 1

2 STATE-OF-THE-ART AND THEORY OF AGRIVOLTAICS 5
2.1 From concept to application – the development of agrivoltaic systems 5
2.2 Greenhouse agriculture in Almería, Spain 8
2.2.1 Radiation and plant growth in greenhouses 9
2.2.1.1 Broadband radiation parameters 9
2.2.1.2 Photosynthetically active radiation (PAR) 9
2.2.1.3 Daily light integral (DLI) 12
2.2.2 Greenhouse types in Almería, Spain 12
2.2.2.1 "Raspa y amagado" greenhouses 13
2.2.2.2 "Venlo" greenhouses 15
2.2.3 Greenhouse roof cover transmittance control practices 16
2.3 State-of-the-art in agrivoltaic greenhouse applications 17
2.3.1 Technical approaches for integrating photovoltaics into greenhouses 18
2.3.2 Experimental studies on agrivoltaic greenhouses 20
2.3.3 Modeling approaches for agrivoltaic greenhouses 23
2.3.3.1 Irradiance modeling for agrivoltaic greenhouses 23
2.3.3.2 Estimating crop yield in agrivoltaic systems 25
2.4 Statistical error metrics 28
2.4.1 Root Mean Square Error and Normalized Root Mean Square Error . 28
2.4.2 Mean Bias Error and Normalized Mean Bias Error 28
2.4.3 Mean Absolute Error and Normalized Mean Absolute Error 29
2.4.4 Coefficient of Determination (R^2) 29
2.4.5 Irradiation error 29

3 METHODOLOGY OF THE AGRIVOLTAIC SIMULATION FRAMEWORK 31
3.1 Irradiance model 31
3.1.1 Theory of radiative transfer modeling and irradiance calculation in Radiance 32
3.1.1.1 Kajiya's rendering equation 33
3.1.1.2 Sky and sun as radiative boundary conditions 34

3.1.1.3 Irradiance calculation . . . 36
3.1.2 Geometrical details . . . 37
3.1.2.1 Virtual greenhouse library . . . 37
3.1.2.2 Virtual PV module library . . . 38
3.1.2.3 Rotating the virtual greenhouse . . . 39
3.1.3 Material properties . . . 39
3.1.3.1 Scattering model of the `trans` material . . . 40
3.1.3.2 Parameterization of the `trans` material . . . 40
3.1.3.3 Sensitivity analysis on overall transmittance . . . 42
3.1.3.4 Sensitivity analysis on haze . . . 44
3.1.4 Satellite-derived irradiance data . . . 46
3.1.5 Ray-tracing analysis . . . 47
3.2 Crop models . . . 49
3.2.1 PAR estimation from GHI . . . 49
3.2.2 Daily light integral-based models . . . 50
3.2.2.1 Yield estimation based on daily light integral . . . 50
3.2.2.2 Yield estimation based on daily light integral, temperature and relative humidity . . . 53
3.2.3 Functional structural plant models - tomato growth model (TOMGRO) . . . 54

4 AGRIVOLTAIC GREENHOUSE EXPERIMENT 59
4.1 Materials and methods of the experimental setup . . . 59
4.1.1 Greenhouse characteristics . . . 59
4.1.2 Microclimate monitoring system . . . 64
4.1.3 Plant physiology and fruit quality parameters . . . 65
4.2 Experimental results of the agrivoltaic greenhouse . . . 67
4.2.1 Shading effect on microclimate . . . 67
4.2.1.1 Irradiance . . . 67
4.2.1.2 Temperature and relative humidity . . . 69
4.2.2 Crop yield . . . 72
4.2.3 Plant physiology and fruit quality . . . 74
4.3 Discussion of the agrivoltaic greenhouse experiment . . . 76
4.4 Economic assessment . . . 78
4.4.1 Electricity self-consumption and grid feed-in during the winter tomato growing cycle . . . 78
4.4.2 Electricity self-consumption and grid feed-in during the full year . . . 81
4.4.3 Potential application of agrivoltaic-generated electricity for desalination plants . . . 82

5 VALIDATION IRRADIANCE MODEL 85
5.1 Case study 1: "Venlo" greenhouse . . . 85
5.1.1 Definition greenhouse plastic . . . 87
5.1.2 Definition sensor position . . . 87
5.1.3 Validation based on single-day irradiance measurements . . . 89

5.1.4 Radiation reduction for one crop cycle . . . 92
5.1.5 Discussion of case study 1: "Venlo" greenhouse . . . 93
5.2 Case study 2: "raspa y amagado" greenhouse . . . 96
5.2.1 Definition sensor position . . . 97
5.2.2 Validation based on single-day irradiance measurements . . . 98
5.2.3 Validation based on irradiance measurements of two complete crop cycles . . . 100
5.2.4 Uncertainty analysis based on irradiance measurements of two complete crop cycles . . . 104
5.2.4.1 Angular dependence of transmittance . . . 104
5.2.4.2 Discrepancy between outside GHI and measured GHI inside the greenhouse . . . 106
5.3 Discussion of the irradiance model . . . 108
5.3.1 Analysis of computational resources . . . 110

6 VALIDATION CROP MODEL 113
6.1 Daily light integral-based models . . . 113
6.1.1 Yield estimation based on daily light integral . . . 114
6.1.2 Yield estimation based on daily light integral, temperature and relative humidity . . . 116
6.1.3 Discussion of daily light integral-based crop modeling and comparison to state of the art . . . 118
6.2 TOMGRO . . . 120
6.2.1 Calibration TOMGRO . . . 121
6.2.2 Validation TOMGRO with experimental data . . . 123
6.2.3 Discussion of simulation with the TOMGRO model . . . 124
6.3 Comparison and evaluation of crop models . . . 125
6.3.1 General comparison of the three methods . . . 125
6.3.2 Error sources of the three methods . . . 126

7 CONCLUSION AND OUTLOOK 129
7.1 Conclusion . . . 129
7.2 Outlook . . . 132

BIBLIOGRAPHY 135

APPENDIX 155
A Fertilizer and phytosanitary treatments . . . 155
B Plant physiological and fruit quality measurements . . . 156
B.1 Additional figures plant physiology . . . 156
B.2 Additional figures fruit quality . . . 161

ACKNOWLEDGEMENTS 163

1

Introduction and objectives

"The science is abundantly clear, compellingly clear about the urgency that we're facing."

—Christiana Figueres,
Executive Secretary of the U.N. Framework Convention on Climate Change

The year 2024 was the warmest year worldwide since records began in 1850 with a global temperature about 1.47 °C higher than in the late 19th century [1, 2]. The ten most recent years have been the warmest on record [1]. Multiple studies show that climate-warming trends over the past century are extremely likely due to human activities [3, 4, 5, 6, 7, 8, 9]. Climate models predict that if greenhouse gas emissions continue at current rates, Earth's global average temperature could rise by an additional 4 °C until the year 2100 [10]. Even a one-degree increase has significant effects on the planet, including more frequent and severe droughts, heavy rainfall, and heatwaves worldwide [10]. Given the impacts of climate change, the United Nations declared in the Paris Agreement in 2015 global warming should be limited to below 1.5 °C, preferably 2 °C, compared to pre-industrial levels [11].

By launching the European Green Deal in 2019, the European Commission aims to make Europe the first carbon-neutral continent by 2050 [12]. This includes the 2030 Climate Target Plan, which seeks to reduce the emission of greenhouse gases by 55% and to increase the share of renewable energies in total energy production to at least 32% by 2030 [12]. In 2023, the European Union (EU) updated this renewable energy target for 2030 to a binding minimum of 42.5%, with an aspiration to reach 45% [13].

The expansion of renewable energies requires large portions of land and might also affect food security. Since the early 1960s the world population has doubled [14]. The United Nations estimates the human population will reach 8.5 billion in 2030 and 9.7 billion in 2050 [14]. In order to meet the global food demand, overall food production has to be increased by about 70% until 2050 [15]. Although direct coherences between energy production and food security are more complex and still being discussed [16], concerns about the land-use conflict between food and energy production are reasonable given a present and prospective land scarcity.

In many countries, the targets of the Paris Agreement to increase the share of renewable energies for combating climate change have triggered direct land use changes in order to meet the objectives of different EU programs. Ground-mounted photovoltaic (PV) systems have been installed on arable land formerly used for food production, and high-quality soils have been taken out of agricultural production [17].

However, renewable energy does not threaten agricultural production; indeed, they can coexist in harmony. Agrivoltaics (APV), a form of solar sharing or dual land use, is a concept that combines agriculture and PV systems, allowing for the simultaneous use of land for crop cultivation and solar energy production. The Joint Research Center estimates that 5.2% of the land in the EU is ideally suited for accelerated renewable deployment, excluding natural protected areas and high-value agricultural land [18]. Yet, the European Environmental Bureau's latest report finds that only 2.2% of the EU's land area would be needed to accommodate sufficient renewable energy sources to entirely replace fossil fuel and nuclear generation [19]. The deployment of APV alone could surpass the EU's 20230 targets for PV expansion [18].

APV offers especially high potential in semi-arid and arid regions, where various positive side effects can be expected such as protection of crops from extreme weather events, dual incomes for growers, and the supply of energy to industry [20, 21]. The province of Almería, Spain, one of the driest regions in Europe, is known for its extensive horticultural practice with over 30,000 ha of land occupied by greenhouses (GHs) [22]. Due to its climatic conditions and already established infrastructure, the region is particularly suited for the application of APV, where PV panels are installed on the roof or inside the already existing GH structures [23, 24]. Here, crop cultivation can suffer from the adverse effects of high solar radiation and farmers are often required to reduce light transmission of the GH covers, mostly achieved by applying white chalk paint to the GH roofs [25]. APV concepts can actively support or even replace the whitening practice by the growers, and sunlight could additionally be used to produce energy. Hence, the energy efficiency in agriculture could be improved, which directly translates into a higher profitability for farmers [26]. Furthermore, several studies showed that water use efficiency is improved underneath PV panels in APV systems [20, 27, 28]. These findings are becoming even more relevant, as water demand for irrigation is expected to increase in prospective future climatic conditions [28, 29]. In addition to improved water use efficiency, crops cultivated in arid climates may also directly benefit from the reduction in solar radiation through the PV panels [30, 31]. The study of [32] estimated that shading of up to 44% of GH roofs in Almería would still secure sufficient irradiance levels for crops without reducing crop yields [32]. Therefore, APV can be an important component of future renewable energy production systems, while simultaneously ensuring food production and the economic viability of agriculture [31].

Designing and optimizing APV GHs involves several challenges. First of all, all APV installations must comply with legal requirements of the perspective country or region. The main priority of APV systems remains continuous agricultural production [33]. However, electrical yield and economic profit are higher with a higher density of PV modules, which will then directly reduce crop available radiation [34] and hence, can negatively affect crop yield.

The impact of APV related shading on crop development and yield in Mediterranean GHs has so far been investigated only by a limited amount of experimental studies [35, 36, 37, 38, 39, 40]. Since their experimental results are diverse and dependent on the individual experimental setups, it remains unclear to what extent GH crops can tolerate shading without yield reduction. Further experimental studies across Europe also indicate that developing simulation tools will be an important step toward the design and optimization of APV GHs [41]. This specific research gap is tackled within this thesis.

The central task of this thesis is the development of a simulation framework for APV GHs that enables the simulation of light distribution under different PV systems and the subsequent estimation of crop yield. The research questions addressed are:

1. How can the irradiance distribution in APV GHs be modeled for different GH designs and PV module patterns?
2. How can crop yield be estimated for APV GHs dependent on modeled irradiance levels?
3. How is the microclimate inside the GH affected by shading of the PV modules?
4. Is there an economic benefit in integrating PV modules on the roof of GHs?

In this thesis, APV concepts and horticultural practices in the Almería region are presented alongside with experimental APV GH studies from literature as well as current state-of-the-art modeling approaches (Chapter 2). Chapter 3 presents the methodology of the developed APV GH simulation framework, divided into irradiance modeling and crop yield modeling. Chapter 4 describes the experimental setup and results from an APV GH experiment, conducted in an Almería-type greenhouse during the 2023–2024 tomato growing season. In Chapter 5, the ray-tracing-based irradiance model is validated using both literature data and the irradiance measurements from the APV GH experiment. Chapter 6 addresses the validation of the crop modeling approaches using microclimate and crop measurements of the APV GH experiment. Finally, chapter 7 summarizes the main findings of this work and provides an outlook on future research directions and potential developments of the presented model.

2

State-of-the-art and theory of agrivoltaics

"Science and everyday life cannot and should not be separated."

—Rosalind Franklin

This chapter summarizes the state-of-the-art in the field of APV for GHs which is relevant for this thesis. The content of this chapter has been partially published in [42] and [43].

2.1 From concept to application – the development of agrivoltaic systems

Already in 1982, the concept of integrating solar collectors into agricultural production to increase land benefit was proposed by [33] (see Figure 2.1). Based on their theoretical calculations, a collector height of 2 m with a row spacing of 3 m would allow crops underneath to receive two-thirds of the available solar radiation, while only one-third of the arable land would be used for energy production [33].

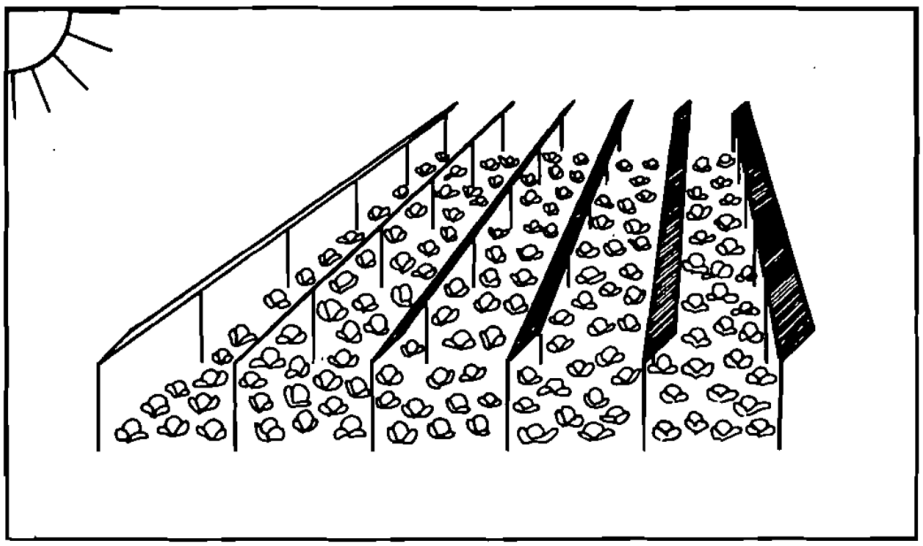


Figure 2.1: First draft of an APV system from the year 1982. Figure taken from [33].

The authors were clearly ahead of their time, especially since PV technology was still new when the study came out and the first commercial projects had just started operating. From 1982 it took more than two decades until scientists in Japan picked up the topic in 2004 and combined farmland with PV modules in a first pilot project (referred to as "solar sharing") [44]. They found that sufficient crop yields can be maintained for shading rates of up to 32% [44]. In the following, such dual-use systems, combining agricultural production with PV, will be denoted as agrivoltaic (APV) systems, which is up to now the most established term in scientific literature [45]. Depending on the region or country, further terms like "solar sharing" (Japan), "Agrophotovoltaik" or "Agriphotovoltaik" (AgriPV) (Germany) as well as "Agrivoltaico" (Italy) are commonly used [45]. Even though different pilot projects for APV appeared in the following years, it is only since 2020 that research about APV (experimental studies and modeling approaches) gained attention and research publications increased [46]. Following a search in the Web of Science database using the keyword "agrivoltaic", the publication frequency by year is observed, as shown in Figure 2.2.

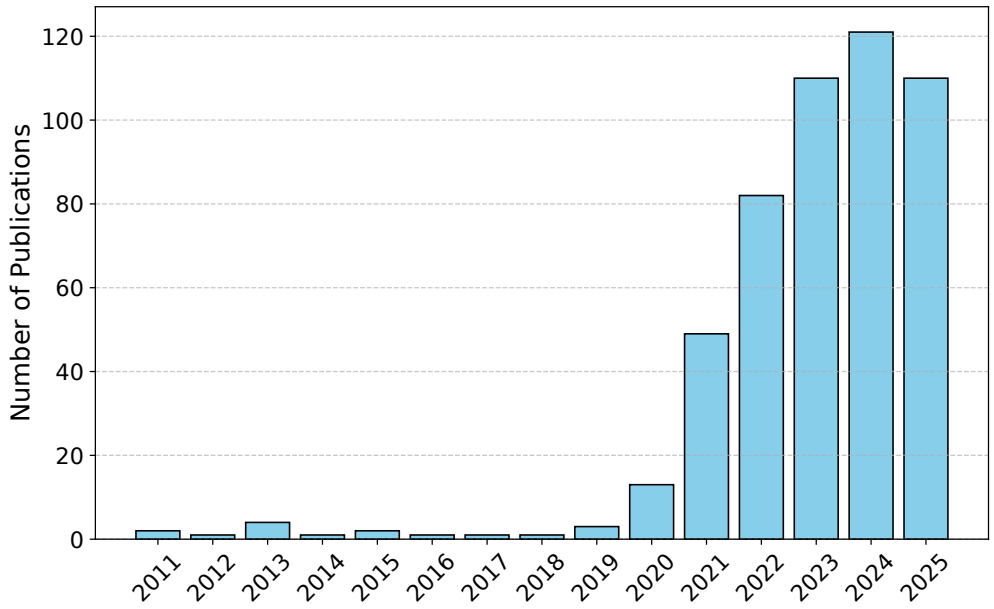


Figure 2.2: "Agrivoltaic" keyword search result, number of publications per year (state 25 September 2025).

According to [31], the application of APV can increase farmers' incomes by over 30% if yield losses through shading effects are minimized by the selection of suitable crops. The study of [34] applied the land equivalent ratio, a method of evaluating the productivity of an intercropping system in comparison to a single-crop cultivation system [47], to determine the advantages of a dual-use APV system over a single-crop system and PV production. According to their simulations, the productivity of APV systems can increase up to 73 % for crops benefiting from low-light conditions. The modeling study of [48] showed that renewable-energy land productivity can be even doubled by APV for biogas maize production in comparison to the separate production of maize and energy with ground-mounted PV modules.

Going along with increased research activities and APV deployment, throughout the years multiple technical solutions to combine agriculture and energy production on the same land have been developed. A classification to distinguish different APV technologies has been proposed by [49], as seen in Figure 2.3. This thesis focuses on APV for GHs (marked in orange).

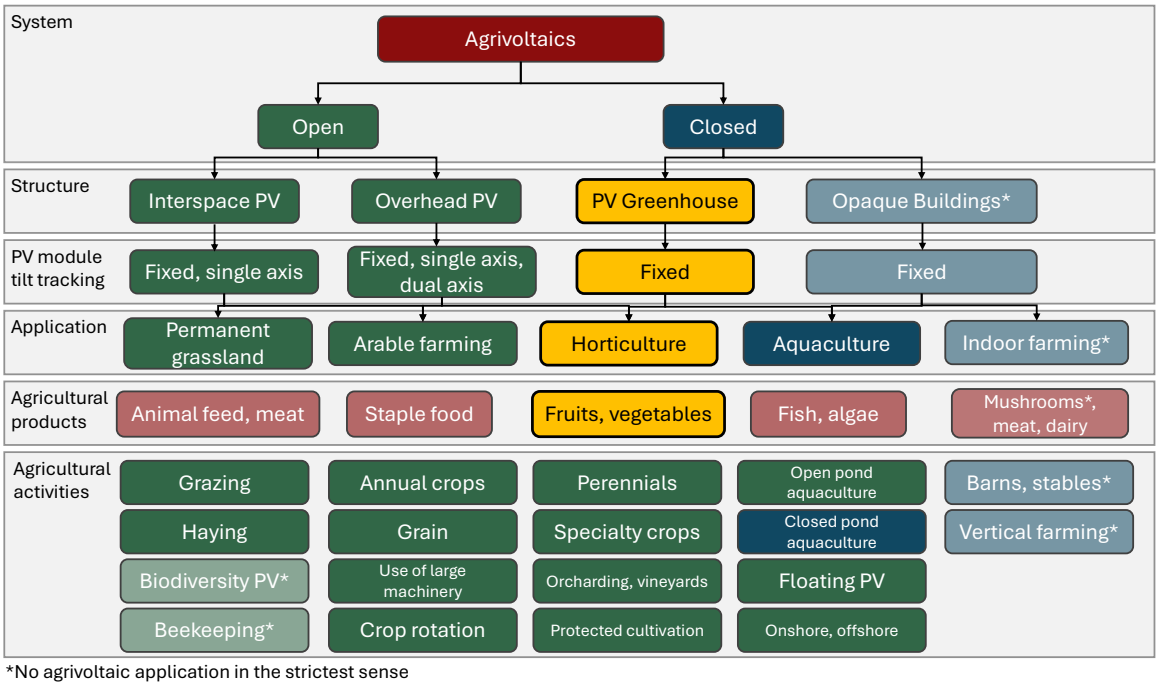


Figure 2.3: Classification of APV systems adapted from [49].

APV systems can be classified into two main categories, namely open and closed systems. Open APV systems include interspaced PV systems and overhead PV systems. Interspaced systems allow agricultural activities to take place between PV rows while overhead systems are typically elevated 2–6 m above ground level to ensure that farming operations beneath the PV panels can continue unobstructed. Commonly cultivated crops in open APV systems include orchards, vineyards, hay and fodder species, and various vegetables. Several review papers have summarized the state-of-the-art in open-field APV research, covering both experimental studies and modeling approaches [46, 50, 51, 52, 53, 54, 55, 56, 57]. Closed APV systems primarily include PV GHs, which are typically applied in horticulture and aquaculture. Commonly cultivated crops in PV GHs include mostly fruits and vegetables. In general, the global APV market grew from 14 GW in 2024 to an estimated 18.4 GW by mid-2025 [58]. While much of this growth stems from pilot expansions, more countries are beginning to approve commercial-scale APV installations, especially in Southern Europe and East Asia [58]. In this thesis, we are focusing on APV concepts for GHs. In Section 2.2, GH agriculture in Almería, Spain, is presented, including typical GHs of the region and important radiation parameters for crop growth in GHs. Then, in Section 2.3, the state-of-the-art in APV GH applications is presented.

2.2 GREENHOUSE AGRICULTURE IN ALMERÍA, SPAIN

In southern Spain, especially in the region of Almería, approximately 32,000–33,500 ha of land are covered with plastic GHs [22]. It remains the largest continuous GH concentration in Europe, see Figure 2.4, and the second largest worldwide, following the Weifang region in Shandong, China, where the protected-cropping area exceeds 80,000 ha [59]. The region of southern Spain has some of the driest conditions in Europe, yet with access to groundwater and an abundance of sun, it offers optimal conditions for year-round crop production. According to the European Commission's PVGIS database, typical values of annual global horizontal irradiation in the Almería region range between 1900 $\mathrm{kW\,h\,m^{-2}}$ and 2100 $\mathrm{kW\,h\,m^{-2}}$ [60, 61].



Figure 2.4: The sea of greenhouses surrounding El Ejido, a town in the south east of Almería, Spain. Image credit: European Union, Copernicus Sentinel-2 imagery [62].

Almería's fruit and vegetable exports in the 2024/2025 season reached 2.5 million tons and 3,716 million euros, accounting for the growth of an associated complex industrial and service sector [63]. The most produced crops in terms of value were pepper (€1.432 billion), tomatoes (€908 million), cucumbers (€677 million), watermelons (€478 million), and zucchini (€373 million) [63]. The fruits exported from the region reach a total of 87 different countries, but 99% of international sales go to other European countries, with Germany as the main destination (€1.598 billion) [63].

2.2.1 RADIATION AND PLANT GROWTH IN GREENHOUSES

GHs provide a controlled microclimate that can be optimized for efficient crop production. Among all inputs to GH cultivation, sunlight is the most fundamental, as it supplies the energy required for plant growth. Light is the primary driver of photosynthesis, the biochemical process through which plants convert light energy into chemical energy. During photosynthesis, photons absorbed by chlorophyll and other plant pigments initiate reactions that transform CO_2 and water into carbohydrates, releasing oxygen as a by-product. In the following subsections, the relevant radiation parameters for GH cultivation are summarized in more detail.

2.2.1.1 BROADBAND RADIATION PARAMETERS

Solar radiation is the electromagnetic radiation that is emitted by the sun. The fraction of the solar radiation that reaches the Earth's surface is usually described by three quantities: direct normal irradiance (DNI), diffuse horizontal irradiance (DHI) and global horizontal irradiance (GHI). GHI is the total amount of shortwave solar radiation received on a horizontal surface and is confined to wavelengths between 290 nm and 3000 nm. It consists of two parts: direct irradiance that comes straight from the sun, and diffuse irradiance that has been scattered by clouds, aerosols, or other atmospheric components. DHI refers only to the scattered portion of irradiance that reaches a horizontal surface. It excludes the direct beam from the sun's disk and therefore represents the diffuse sky contribution. DNI describes the beam radiation that comes directly from the sun without being scattered or reflected. It is measured on a surface that is kept perpendicular to the sun's rays. The unit of GHI, DHI and DNI is $\mathrm{W\,m^{-2}}$.

2.2.1.2 PHOTOSYNTHETICALLY ACTIVE RADIATION (PAR)

For plant growth, the most relevant fraction of solar radiation is the photosynthetically active radiation (PAR). PAR designates the spectral range of solar radiation from 400 nm to 700 nm that photosynthetic organisms are able to use in the process of photosynthesis [64]. This spectral region corresponds more or less with the range of light visible to the human eye (380 nm to 750 nm). PAR can be expressed as a photosynthetic photon flux density (PPFD), with units of $\mu\mathrm{mol\,m^{-2}\,s^{-1}}$ because photosynthesis is a quantum process, or in terms of photosynthetic radiant flux density (PAR irradiance, $\mathrm{W\,m^{-2}}$), which is more suitable for energy balance studies [65]. Figure 2.5 shows the AM1.5 solar spectrum (direct + circumsolar component) based on the ASTM G173-03 reference spectrum (ASTM International, 2008) obtained via NREL [66], overlaid with the absorption spectra of chlorophyll a, chlorophyll b, and β-carotene, as well as the photosynthetic action spectrum.

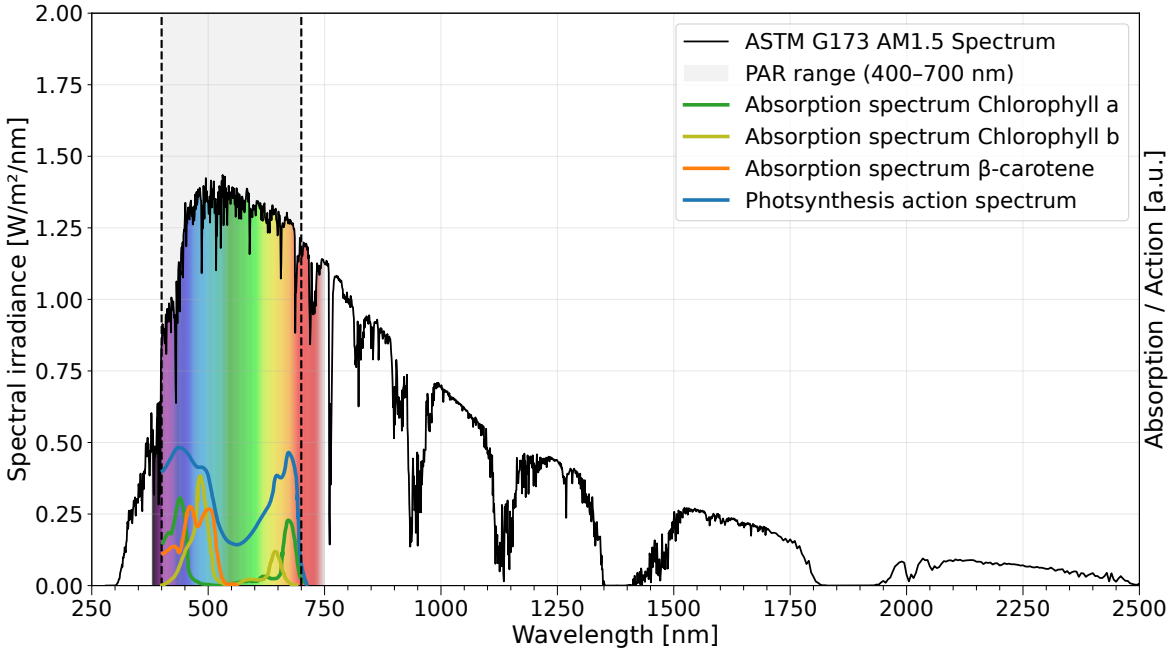


Figure 2.5: Spectral distribution of the ASTM G173 AM1.5 direct+circumsolar irradiance [66], overlaid with the absorption spectra of chlorophyll a, chlorophyll b, and β-carotene, as well as the photosynthetic action spectrum. The visible range between 380 and 750 nm is highlighted with a color gradient corresponding to wavelength. The PAR range between 400 nm and 700 nm is marked in grey with black, dashed lines.

The solar spectrum that reaches the Earth's surface, see Figure 2.5, consists of approximately 5% ultraviolet (UV) radiation (250 nm to 400 nm), 45% PAR (400 nm to 700 nm), and about 50% near-infrared (NIR) radiation (700 nm to 2500 nm) [67]. Although these proportions can shift depending on location and cloud cover, each spectral component plays a distinct role in GH crop production. UV radiation primarily affects plant growth and development [67]. Moderate UV exposure can be beneficial, stimulating the synthesis of secondary metabolites such as flavonoids, phenolics, carotenoids, and ascorbic acid, which can improve leaf, flower, and fruit coloration, enhance flavor, and increase resistance to pests and diseases [67, 68, 69]. Excessive UV radiation, however, may cause DNA damage, inhibit photosynthesis, reduce growth, and promote compact plant forms [70]. NIR radiation mainly influences the GH microclimate through its heating effect. Most of the incoming NIR radiation is absorbed by the GH surfaces, while leaves reflect roughly 40% of it [71]. PAR contributes both to the GH energy balance and, critically, to plant growth and development. It drives photosynthesis and influences photomorphogenic responses, making maximized PAR transmission one of the most crucial considerations in GH design for most crops.

Within the PAR region, not all wavelengths contribute equally to photosynthesis, as indicated by the absorption spectra in Figure 2.5. The primary photosynthetic pigments exhibit distinct absorption maxima in the blue and red parts of the spectrum: chlorophyl a absorbs most strongly near 430 nm and 662 nm, while chlorophyll b absorbs mostly around 453 nm and 642 nm [64]. These regions are therefore most efficiently used for the photochemical reactions of photosynthesis. At the canopy scale, however, plants make use of a broad range of photons across roughly 400 nm to 700 nm to drive photosynthetic carbon

gain [67]. Beyond chlorophyll a and chlorophyll b, several accessory pigments, such as carotenoids and non-photosynthetic photoreceptor pigments, including phytochromes, cryptochromes, and phototropins, also absorb in specific spectral bands [67]. Even at relatively low light intensities, these receptors regulate numerous developmental and metabolic processes, which influence seed germination, plant architecture, flavor formation, and nutritional quality [67]. Most of the activating wavelengths fall within the blue (400 nm to 500 nm), red (600 nm to 700 nm), and far-red (700 nm to 800 nm) regions of the spectrum. Green light (500 nm to 600 nm) is absorbed less strongly by these pigments but it plays a meaningful physiological role due to its deeper penetration into plant canopies [67]. By reaching shaded lower leaves more effectively than blue or red wavelengths, green light can support photosynthesis in inner canopy layers [72].

Similarly to the incoming GHI, PAR reaching the ground surface has two primary incoming streams, i.e. "diffuse" and "direct". Their share is essentially affected by the quantity of clouds and aerosols in the atmosphere, and for GHs by the composition of the GH covering material. Photosynthesis in a canopy can be calculated from the amount of light absorbed by the canopy and the light response of the leaves. Besides light intensity, the directional light distribution in the GH throughout the canopy also plays an important role [73]. Several studies showed that plants use diffuse PAR, which leads to a more homogeneous light profile in the plant canopy, more efficiently than direct PAR [74, 75, 76]. Furthermore, the photosynthetic rate of leaves shows a nonlinear response to the PPFD, as depicted in Figure 2.6, converging towards a saturation point in which a further increase in PAR radiation does not translate into a higher value of photosynthetic rate [77].

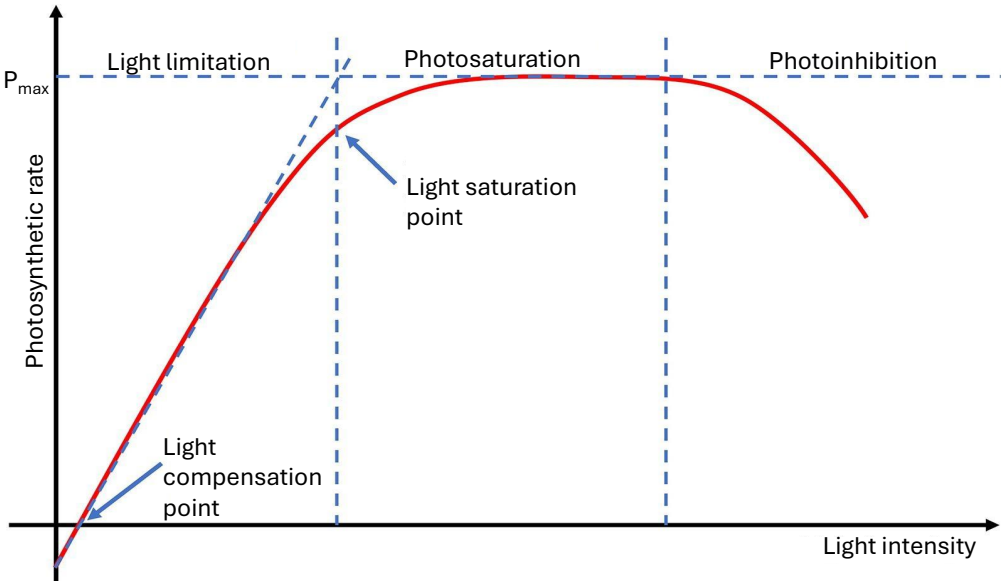


Figure 2.6: Generalized photosynthetic light response curve. Figure adapted from [78].

A positive photosynthetic rate can lead to a positive growth rate. As shown in Figure 2.6, the photosynthetic rate is negative at intensities below the light compensation point. At intensities above the light compensation point, the initial slope of the photosynthetic rate is limited to a maximum (P_{max}) due to light saturation. Per definition, light saturation

sets in at an intensity at which a linear growth would reach P_{max}. At high light intensities, photoinhibition sets in [78]. For example, tomatoes typically require 400 µmol m^{-2} s^{-1} to 700 µmol m^{-2} s^{-1} of PAR for efficient photosynthesis depending on the development stage of the plant [79]. The light saturation point for tomato photosynthesis is around 700 µmol m^{-2} s^{-1} to 1000 µmol m^{-2} s^{-1}, above which photosynthesis plateaus or decreases due to stress or photoinhibition [79]. In addition, the exposure of tomatoes to intense light for long periods affects the accumulation of antioxidants in the fruits, like lycopene and Vitamin C, especially during the ripening stage, as these elements are sensitive to oxidation. It has been shown that excessive light may lead to oxidative degradation, while moderate shading can enhance or preserve these compounds in tomato fruit by reducing stress and photoinhibition [80, 81].

2.2.1.3 DAILY LIGHT INTEGRAL (DLI)

The daily light integral (DLI), expressed in mol m^{-2} day^{-1}, describes the total amount of photons in the PAR spectrum received per m^2 per day. Equation 2.1 describes the DLI calculation from PPFD.

$$\mathrm{DLI} = \int_0^{24} PPFD(t)\,dt \approx \sum_{i=1}^{n} PPFD_i \cdot \Delta t \tag{2.1}$$

with $PPFD(t)$ being the Photosynthetic Photon Flux Density at time t, in µmol m^{-2} s^{-1}. For discrete measurements, $PPFD_i$ describes PPFD at time step i and Δt describes the time interval between measurements in seconds. The variable describes n the number of measurements per day.

2.2.2 GREENHOUSE TYPES IN ALMERÍA, SPAIN

There are different types of GHs in the region of Almería. The traditional GHs were developed from wire supporting structures for growing table grapes, a traditional crop in the area of Almería [22]. Also nowadays, the GHs in the Almería region are mainly simple structures covered with polyethylene plastic sheets.

As indicated in Figure 2.7, so-called "raspa y amagado" GHs represent the majority of GHs, followed by the flat top GHs and asymmetric GHs. Only 5.7% of the area is covered by different types of GHs, such as the more modern "Venlo" GHs.

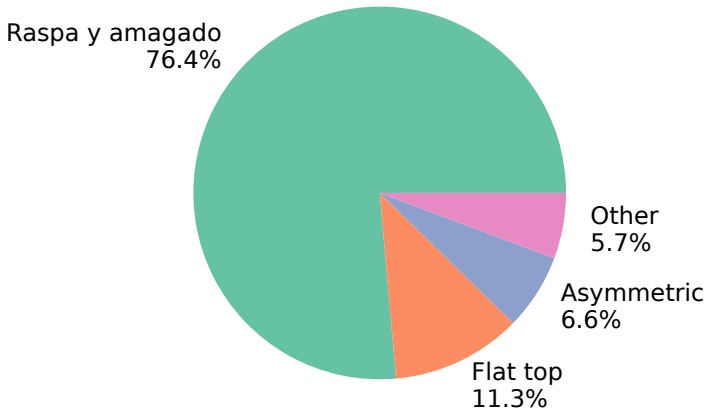


Figure 2.7: Percentages of different types of GHs in the agricultural region of Almería [22].

"Raspa y amagado", flat top and asymmetric GHs are all three classified as Almería-type GHs. The Almería-type GHs are characterized by the fexibility of the structural elements,which are composed of individual wires or braids that are subject to initial tension during the process of construction [22]. The three subtypes can be differentiated by the shape of their roof. The flat top GHs evolved first and have a cover of plastic that is perforated to allow entry of rainwater. The "raspa y amagado" GH evolved from the flat top GH and consists of symmetrical gabled parcels. In contrast, the asymmetric GHs consists of gabled parcels with different slopes. In addition, during the last years GHs from other European countries are also gaining ground in the Almería region, such as the multi-span type used in France and "Venlo" GHs used in the Netherlands. In the next two subsections, detailed descriptions of the "raspa y amagado" and "Venlo" GH types are presented as they will be central to the analyses conducted later in this thesis.

2.2.2.1 "RASPA Y AMAGADO" GREENHOUSES

The "raspa y amagado" GHs are a special type of GH design common in Almería. They are characterized by the shape of the roof, which is angled from 6° to 20°. The primary goal of the design development was to improve rainwater drainage and reduce the risk of structural damage compared with flat-roof GHs. Increasing the roof slope also enhances solar radiation interception, although it requires greater structural strength due to wind loads [22].

The roof consists of two main elements: the "raspa" and the "amagado". The "raspa" is the upper junction where the two roof slopes meet at the highest point of each parcel [22]. It is supported by a framework of galvanized steel tubes, laminated profiles, and wires or wire strands that ensure roof stability. The "amagado" refers to the lower junction between adjacent parcels, where the rainwater gutters are installed [22]. It connects the upper "raspa" to the ground through cables and iron forks, which provide anchoring and allow proper positioning of the gutter system [22].



a)



b)



c)

Figure 2.8: a) Side of a "raspa y amagado" GH. Most GHs have lateral openings for temperature and microclimate control. **b)** Inside of a "raspa y amagado" GH before cultivation. The GH ground is covered with plastic foil to maintain moisture levels in preparation for the crop cycle. **c)** Tomato plants in a "raspa y amagado" GH two weeks after transplantation. Image credit: Anna Kujawa (DLR).

The maximum height of the "raspa y amagado" GH is located at the ridge and typically ranges from 3 m to 4.2 m. The height of the "amagado" section varies between 2 m and 2.8 m, while the sidebands range from 2 m to 2.5 m. The standard spacing between pillars and the tension braces of the threads is usually 2×4 m, although other configurations such as 2.5×4 m, 2×6 m, and 2×8 m are also common [22]. The widespread adoption of the "raspa y amagado" structure in the Almería region is largely due to its adaptability to local climatic conditions and its suitability for different types of crops [22]. Additional factors contributing to its expansion include its relatively low construction cost (4.5–15 €/m^2) and its higher thermal inertia, which help increase nighttime temperatures and create a more hermetic environment compared with flat-roof GHs [22]. In this thesis, a virtual representation of an Almería typical "raspa y amagado" GH is presented and simulated.

2.2.2.2 "VENLO" GREENHOUSES

"Venlo" GHs are industrial, multispan structures originally developed in northern Europe, where low winter temperatures and the need for precise climate control require rigid metal frames and glass covers [22]. The limited adoption of the "Venlo" GH in Almería is mainly due to high construction costs and their design being optimized for cold, low-radiation climates rather than the arid, high-radiation conditions of southeastern Spain [22].

Traditionally, "Venlo" GHs are glass-covered, symmetrical structures with narrow spans, roof slopes of approximately 22°, and robust metallic frames capable of supporting considerable loads, as depicted in Figure 2.9. In the Netherlands, "Venlo"-type GHs are often being managed with two floors and a height greater than 8 m [22]. In these GHs, crops are grown at two different heights in order to achieve twice the usual planting density. On the lower floor, continuous artificial lighting is used, whereas on the upper floor, solar radiation is used. In addition, the temperature is controlled by heating and recirculating hot air from the top to bottom floors [22]. Due to the materials required for a "Venlo" GH, these types of GHs have comparably high construction costs of approximately 30-40 €/m^2, which is substantially higher than that of Almería-type GHs, ranging from 4.5–15 €/m^2.



a) **b)**

Figure 2.9: a) A glass "Venlo" GH in the Netherlands. Image credit: [82].
b) The SOLNOVA "Venlo"-type GH in Almería. Image credit: [83].

Despite this conventional definition of the "Venlo" GH having glass walls and roofs, some research and development initiatives in Almería have adopted "Venlo"-type geometries without using glass. An example is the SOLNOVA GH, developed at the Centro Tecnológico TECNOVA [83]. The SOLNOVA structure, shown in Figure 2.9, is a GH that resembles the "Venlo" design but is covered with Almería-typical plastic films, rather than glass. It was engineered and calculated specifically for Almería's climatic conditions, including the additional structural load of PV modules, which has been already investigated in several studies [83, 40]. The SOLNOVA case illustrates that, within the local research context, the term "Venlo-type" may refer to the geometry and structural concept rather than strictly the material of the cover. In this thesis, a virtual representation of the SOLNOVA "Venlo" GH is presented and simulated.

2.2.3 Greenhouse roof cover transmittance control practices

Mediterranean GHs are typically covered with transmissive plastic materials [22]. To increase the diffuse light distribution inside the GH, these materials have high haze values, i.e. the fraction of transmitted light, which deviates from the incident direction [84]. Overall light transmission in the PAR range is typically between 80 % and 89 %. According to various manufacturers, the fraction of diffuse PAR transmission is typically between 55 % and 60 % [85].

In the Mediterranean region, low-density polyethylene (LDPE) films are widely used as GH covering materials, primarily due to their affordability, mechanical attributes, and resistance to chemicals [86]. These plastic films are often multi-layered with an UV-protection film toward the outside and agrochemical-resistant films toward the inside of the GH [40]. The materials have been developed to maximize the fraction of diffuse light inside GHs, with a transmission dependent on the angle of the incident light [84, 87].

As high light levels can lead to photosynthetic saturation and a decrease in light use efficiency of the plants (see Section 2.2.1.2), farmers actively manage light and heat inside GHs by reducing the transmission of GH plastics throughout the crop cycles, e.g. by applying white chalk paint, the so-called "whitewash" [25]. The majority of farmers in Almería (99%) whitewash the GH cover several times throughout the growing cycles to increase its reflection coefficient to solar radiation, which reduces the contribution of energy that heats the GH during the central hours of the day. They mostly use micronised calcium carbonate to whitewash the GH covering, whereas some farmers also add adhesives to improve its permanence on the GH covering. In addition, there are other techniques to reduce light transmission and manage the GH microclimate, such as the use of shading nets (applied internally or externally) [88], thermal screens [89], or even wavelength-selective plastic films, that block out a fraction of the infrared (IR) spectrum [90, 91] (both applied internally).

APV concepts offer another option to actively support this microclimate management of the growers. Shading techniques, both traditional shading nets or APV structures, can modify light intensity, spectrum and duration, affecting both yield and quality of the GH crops. To maintain successful GH cultivation, the balance between sufficient light for photosynthesis and avoiding stress-induced degradation is crucial. Traditional shading methods, such as shading nets or whitening agents, primarily reduce light intensity and slightly alter the spectrum by scattering more UV and blue light and blocking out a fraction of IR light. In contrast, conventional silicon PV modules absorb a portion of PAR, especially in the blue and red regions, to generate electricity. As this may negatively affect the availability of PAR to the crops, more recent approaches for GH-implemented APV solutions focus on semi-transparent or spectrally selective PV technologies in order to allow more PAR transmission while still producing energy.

2.3 STATE-OF-THE-ART IN AGRIVOLTAIC GREENHOUSE APPLICATIONS

GH cultivation is expanding rapidly worldwide to help meet the rising food demand associated with a growing global population [92]. Recent global estimates report 1.3 million hectares of GHs worldwide, distributed across 119 countries [92]. China alone accounts for 60.4% of global GH coverage, while Mediterranean countries, i.e. Spain, Italy, France, Turkey, and Morocco, collectively contribute about 16% [92]. Within the Mediterranean basin, Spain is the leading country, representing 5.6% of global GH area, with 32,000–33,500 ha concentrated in the province of Almería, southern Spain [22]. Beyond these, large GH clusters have also been identified in Mexico, and GH cultivation is increasingly present across 22 African countries, mainly for vegetable and cut-flower production [92]. High-tech GHs, such as the "Venlo" GHs in The Netherlands as described in Section 2.2.2.2, that use advanced climate control and vertical production systems require less land and deliver higher yields, however, their construction and operation are expensive, which limits their adoption in many regions [22]. Plastic-covered, low-tech GHs, such as the "raspa y amagado" GHs in Spain as described in Section 2.2.2.1, remain essential for small-scale farming worldwide, yet represent one of the main sources of agricultural plastic pollution when not recycled properly [93, 94, 95]. Globally, GH cultivation continues to grow at an estimated 6% per year [67].

Given the global scale of GH agriculture, the application of APV systems to GHs has gained attention as a promising approach to simultaneously address energy demand, plastic reduction, and sustainable food production. APV is particularly suitable for regions with a high density of already existing GH infrastructures [96], where PV modules could (partially) replace plastic films or shading elements. In recent years, research on APV GHs has developed as a distinct field of study and is the focus of several review articles [97, 98, 99, 100]. Figure 2.10 combines the work of [92] who used satellite image mapping to identify major clusters of GHs worldwide, and [97] whose work includes a review of 122 studies on APV GHs worldwide from 2010 to 2025.

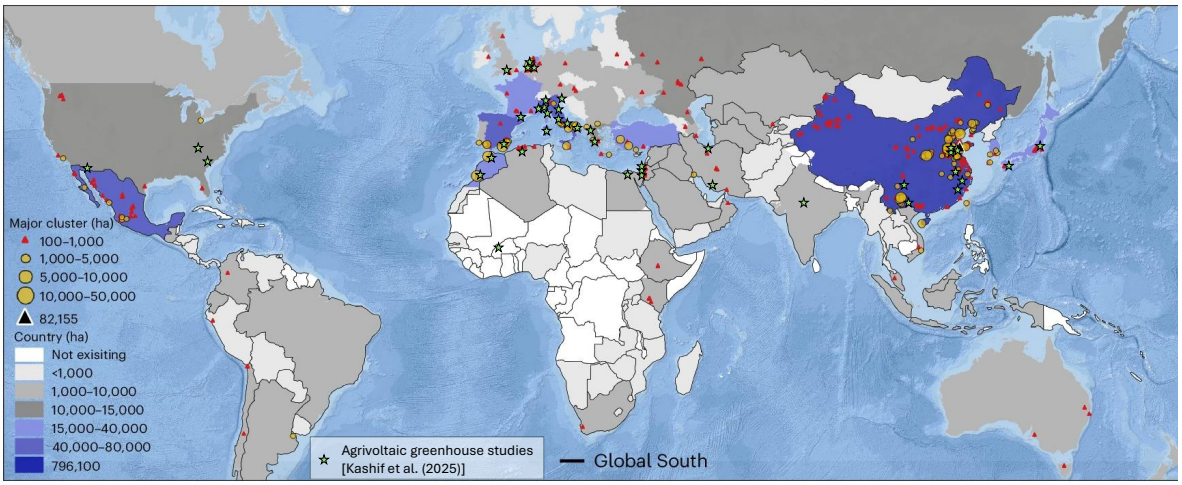


Figure 2.10: Global distribution of GH production clusters and locations of published APV GH studies. The basemap and data on GH clusters is taken from [92]. Green stars indicate the locations of APV GH studies summarized by [97].

Numerous studies emphasize that well-designed APV systems can maintain or even improve crop performance while contributing to farm-level energy self-sufficiency [99, 101]. However, several studies also pointed out that the integration of PV panels into the GH roof can create a significant reduction in solar radiation inside the GH with possible effects on microclimate and subsequently crop production [102, 103, 104]. It is therefore crucial to study the effect of shading caused by PV panels in APV GHs and the availability and distribution of PAR inside APV GHs. In recent years, both experimental and numerical studies on APV GHs have been conducted under various climatic conditions, which reported differing results depending on GH type, shading configuration, and crop species. In the following subsection, an overview of different technical approaches to integrate PV into GHs is presented. Then, the relevant state-of-the-art publications for the classification of the presented results in this thesis are described in detail.

2.3.1 TECHNICAL APPROACHES FOR INTEGRATING PHOTOVOLTAICS INTO GREENHOUSES

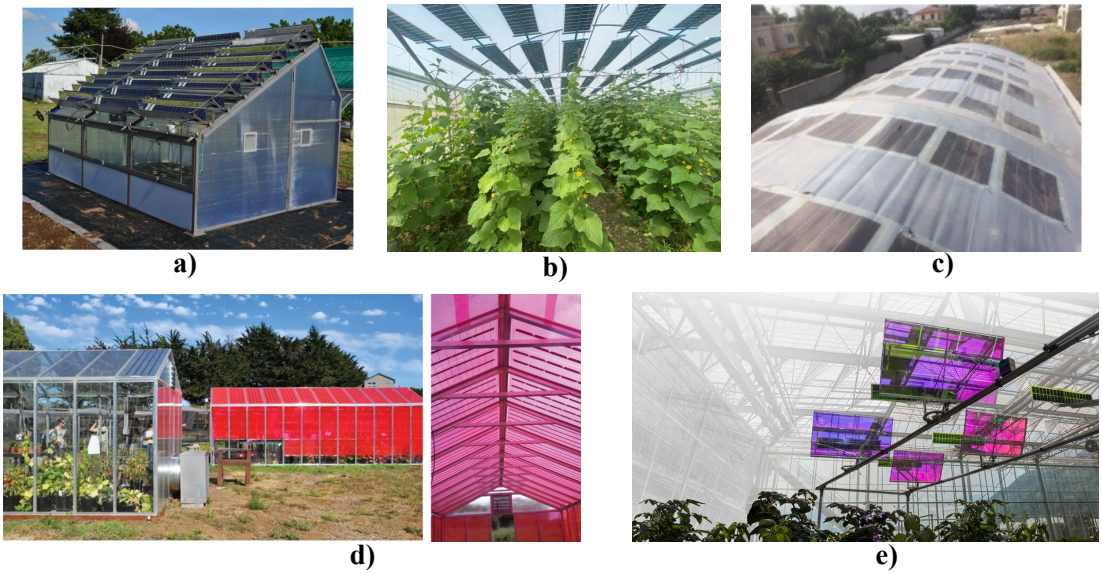


Figure 2.11: Different technical solutions to integrate PV modules in GHs. **a)** Roof-integrated PV [105]. **b)** GH-integrated PV system of the REGACE project [106]. **c)** Flexible, semi-transparent PV modules on the roof of a tunnel GH [107]. **d)** Wavelength-selective PV system combining a luminescent solar concentrator with conventional crystalline silicon solar cells [108]. **e)** Voltiris system inside a glass GH: a spectral filtering PV solution consisting of dichroic filters that reflect a part of the spectrum of the incident irradiance towards a PV module [109].

The integration of conventional PV modules into GHs has been described for both traditional and thin-film crystalline silicon modules [110, 111, 39, 35, 112, 113]. The review paper of [97] summarized 24 studies (experimental and modeling studies) about integrating conventional, opaque PV modules into the roofs of APV GHs. Figure 2.11 **a)** shows the prototype GH of [105] where the shading provided by roof-mounted PV panels could be adjusted dynamically depending on external climate. Similarly, the study of [114] and [115] examined the effects of semi-transparent PV modules installed on a GH

with cultivated lettuce and tomatoes inside. Although the measurements indicated that modules block 35–40% more irradiance than the polyethylene cover and decrease the air temperature, no significant variations in the growth trends of the lettuce or tomatoes were observed. In another study [116], the growth of lettuce was investigated experimentally under a small-scale pilot GH with semi-transparent PV modules and with a light diffusion film underneath the PV modules. The results indicated that the growth trend of the lettuce plant is comparable to the case without PV and that the diffuse film improves agricultural yield. Comparably, the study conducted by [117] also focused on cultivating lettuce in a prototype GH. Their findings showed that the PV system resulted in a 20% shading effect within the GH. More recently, the experimental study of [118] also reported crop yield responses under an opaque, bifacial PV roof configuration of a Venlo APV GH in Türkiye. The authors observed a yield reduction of approximately 26–32% in the first growing season compared to a reference GH. In the following growing season, the reduction in crop yield was reduced to about 15–18% after improvements in shading management and system operation.

PV modules can also be integrated inside the GH beneath the roof, as illustrated in Figure 2.11 **b)**. The TriSolar tracking system uses semi-transparent bifacial PV modules to optimize light distribution within the APV GH while maximizing electrical output. This system is currently being tested within the REGACE project at six sites across Europe, including four universities in Germany, Austria, Greece, and Israel, as well as two operational farms in Germany and Italy. The core technology consists of a responsive tracking system mounted inside the GH that adjusts its angle according to crop needs. The collaboration is also investigating CO_2 enrichment as a strategy to increase electricity generation under low-light conditions by modifying the angle of incidence for the bifacial modules. In addition, REGACE aims to develop a comprehensive digital twin for PV-integrated GHs and has recently presented an application of Spatio-Temporal Graph Neural Networks for GH microclimate modeling [119]. Further research within the consortium focuses on outdoor performance monitoring for perovskite module degradation studies [120] and on developing models to estimate the rear-side energy production of bifacial modules [121].

Figure 2.11 **c)** shows the integration of flexible, semi-transparent PV modules on the roof of a tunnel GH by [107]. They used semi-transparent dye-sensitized solar cells as an alternative GH cover material for agrivoltaic applications. While dye-sensitized solar cells incorporate organic dye molecules, they are not strictly classified as organic PV. According to [107], their spectral transmission can be tuned to avoid major chlorophyll absorption bands while preserving high transmittance in the red wavelength region required for photosynthesis. Outdoor characterization reported efficiencies of up to approximately 2% under low irradiance and similar performance under both direct and diffuse illumination. The semi-transparent modules were validated in a 100 m^2 GH prototype in Greece with tomato cultivation [107]. In the GH with PV modules, the tomatoes grew better than in the control GH, while at the same time the electricity produced by the dye-sensitized solar cells could be used to power the measurement sensors [107].

Wavelength-selective PV systems, as shown in Figure 2.11 **d)** were tested at the University of California, where scientists developed a semi-transparent system combining a luminescent solar concentrator with conventional crystalline silicon solar cells [122, 108, 123]. The

wavelength-selective PV system can directly substitute the plastic and glass coverings of GHs, which offers the opportunity for electricity production and light control for the plants at the same time. The luminescent material used in the wavelength-selective PV system can increase the panel's efficiency and adapt the light to the needs of plants. In addition, the authors stated a relatively cheap price of 10 USD/m^2 [108].

The Voltiris system, shown in Figure 2.11 **e)**, is a wavelength-selective, low-concentration PV technology designed for high-tech glass GHs. It uses dichroic filters and dual-axis tracking to transmit most PAR to the crop canopy while concentrating non-PAR wavelengths onto PV cells [124]. In an eight-month trial at Agroscope in Switzerland, tomatoes, peppers, and basil grown under Voltiris modules showed no significant yield reduction compared with unshaded controls, while PV yields were comparable to those of conventional PV installations [124]. However, the system requires substantial mounting height to accommodate the dual-axis trackers which makes it suitable only for tall, stable structures.

2.3.2 EXPERIMENTAL STUDIES ON AGRIVOLTAIC GREENHOUSES

This subsection presents in detail the experimental APV GH studies relevant to the classification of the results in this thesis. The findings of this work will later be compared with those reported in these studies.

The study of [35] analyzed the effect of flexible PV modules on tomato cultivation in a "raspa y amagado" GH in Almería, Spain, during the 2009–2010 growing season. The GH was divided into three zones: one unshaded control and two PV treatment zones, where flexible amorphous silicon panels were arranged in a checkerboard pattern covering 9.8% of the roof area. The authors found no significant differences in total or marketable yield among treatments, though fruits grown under PV shading showed slightly smaller size and lower color intensity.

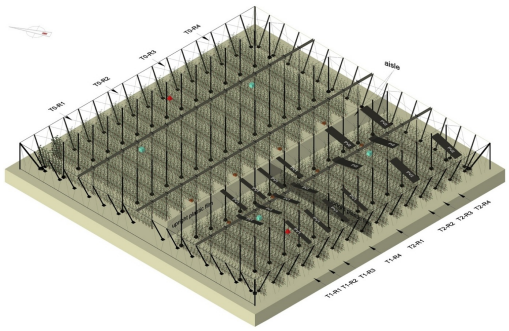
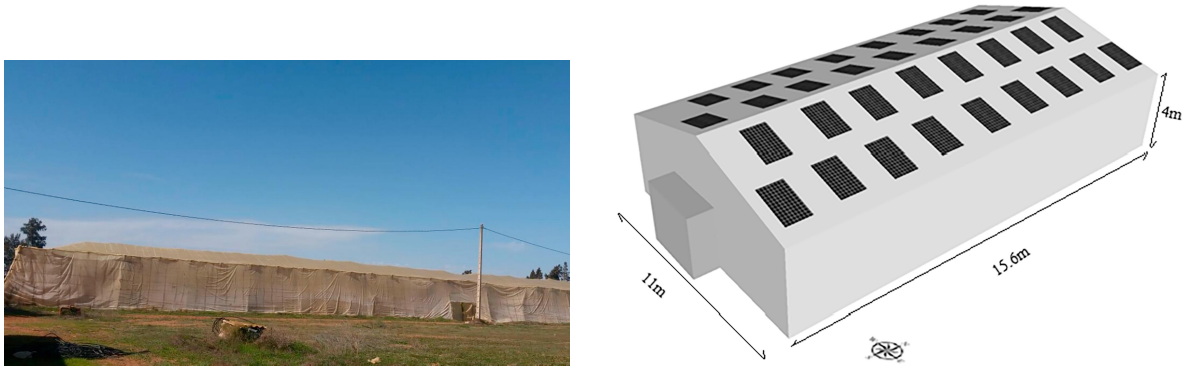


Figure 2.12: Experimental "raspa y amagado" GH used in Almería, Spain, divided into one control and two PV-shaded zones with flexible amorphous silicon modules covering 9.8% of the roof area in both zones. Figure taken from [35].

In a subsequent publication on the same trial by [36], the authors analyzed in depth the effects of the shading treatment (9.8%) on the morphology, yield, and quality of tomato fruits. Inside the GH, there was greater PAR radiation absorption in the control area than in the shaded areas. This had no effect on total production, commercial production, plant morphology, number of flowers, color, firmness, or pH of the fruit. Although shading

reduced fruit size, it did not affect overall yield because there were more fruits in the shaded treatments, albeit smaller ones. Likewise, a slight increase in soluble solids content in the fruit was observed in the shaded treatments.

The study of [37] performed an APV GH experiment with tomato crop and 10% roof cover ratio in two 172 m^2 Canarian GHs located in Agadir, Morocco. They arranged the flexible PV panels in East-West oriented strips, as depicted in Figure 2.13. The experiment was conducted during the 2017 tomato growing cycle to assess the impact of partial shading on the GH microclimate and tomato yield. The results showed that this low level of PV coverage did not significantly affect air temperature, humidity, or tomato yield. On the contrary, a slightly higher yield was recorded in the PV-shaded treatment, which the authors attributed to a lower incidence of the pest Tuta absoluta observed in the shaded GH.



a) b)

Figure 2.13: a) Experimental APV Canarian-type GH located in Agadir, Morocco. **b)** Geometric model showing the 10% roof coverage with flexible PV panels arranged in east–west-oriented strips, as described by [37]. Image credit: [37].

A subsequent study by the same authors [38] compared the effect of 40% PV cover ratio in checkerboard pattern on GH microclimate and tomato production during summer and winter season of the 2018–2019 growing campaign. They found that 40% PV shading with flexible panels on a Canary-type GH did not have a significant effect on tomato production, although it did have a negative effect on fruit ripeness.

The study of [39] investigated the performance of a commercial PV GH located in Decimomannu, Sardinia (Italy), where 50% of the roof area was covered with multi-crystalline silicon PV panels providing a rated power of 68 kWp over a total GH area of 960 m^2 (see Figure 2.14). Two cherry tomato cultivation cycles were carried out between August 2011 and July 2012 to evaluate the effects of shading on crop productivity. Measurements over a full year showed that the PV system reduced internal global radiation by 64% compared to an uncovered GH, with reductions of 82% under PV-covered roofs and 46% under plastic-covered roofs. Solar radiation followed a marked north–south gradient, leading to uneven light distribution and yield variation among rows, with plants grown under the plastic roof achieving the highest yields. The average total yield amounted to 7.5 $kg\,m^{-2}\,year^{-1}$, with marketable production representing 76% of this value, which was lower than typical cherry tomato yields in southern Europe. Supplementary high-pressure sodium lighting powered by the PV system was tested during winter but did not significantly improve

yields, while its energy cost exceeded the revenue from crop sales. In contrast, the PV installation generated approximately 108,000 kWh annually, resulting in energy revenues substantially higher than agricultural revenues. The study concluded that, while such PV GHs can be highly profitable in terms of energy generation, their agronomic sustainability is compromised, and design adaptations, e.g. semi-transparent panels or alternative PV layouts, are needed to achieve a balance between energy and crop production.

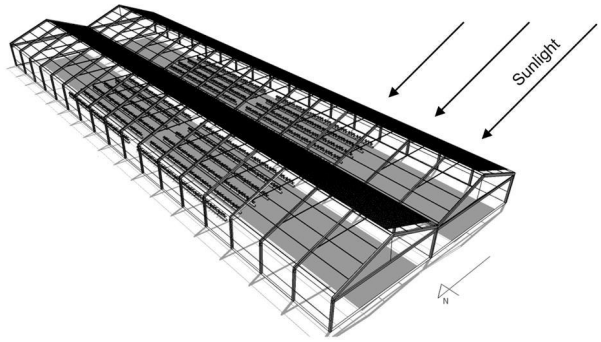


Figure 2.14: Schematic representation of the PV GH studied by [39] in Decimomannu, Sardinia (Italy). Figure taken from [39].

The study of [125] evaluated the effect of shading produced by PV panels installed on the roof of a tunnel-type GH. Conducted in Viterbo, Central Italy, the experiment investigated a prototype structure covered with flexible semi-transparent mono-crystalline silicon PV modules (18% efficiency) arranged in a checkerboard pattern, as depicted in Figure 2.15. The authors analyzed the temporal and spatial variation of shading within the GH and reported that, from mid-March 2017 to mid-September 2017, shading remained almost entirely inside the structure throughout the day, while during the remaining months it was partly inside and partly outside. The annual shading percentage never exceeded 40% under the adopted configuration. The study focused primarily on the geometric analysis of light interception in curved tunnel GHs and did not include an evaluation of crop yield or microclimatic effects.



Figure 2.15: Prototype PV tunnel GH located at Tuscia University (Viterbo, Italy) as described by [125]. The structure is covered with flexible semi-transparent mono-crystalline silicon PV modules arranged in a checkerboard pattern to limit shading, achieving a maximum annual shading of about 40%. Image credit: [125].

The study of [40] experimentally analyzed the effect of different roof-top shading levels (15%, 30%, and 50%) on tomato crop cultivated during the 2014–2015 growing season in a Mediterranean "Venlo"-type GH, mentioned in Section 5.1, located in Almería, Spain. The authors simulated the shading effect of PV panels using opaque black polyethylene sheets arranged in linear strips along the north–south-oriented roof (Figure 2.16). Their results indicated that moderate shading (up to 30%) did not significantly affect total or marketable tomato yield, whereas higher shading levels (50%) led to notable reductions in both yield and fruit quality. Increasing shading delayed fruit maturation and reduced total soluble solids, while fruit firmness increased under stronger shading conditions.



a) b)

Figure 2.16: a) Roof-top installation of opaque polyethylene sheets simulating the shading effect of PV panels in a "Venlo" GH located in Almería, Spain [40]. **b)** Tomato crop grown inside the "Venlo"-type APV GH. Image credit: [40].

2.3.3 Modeling approaches for agrivoltaic greenhouses

The results of previous experimental APV GH studies show that it is difficult to predict crop responses to artificial shading as they are complex and depend on many different factors. In order to improve the understanding of APV systems and their influence on crop yield, modeling approaches are increasingly being employed in APV. This subsection summarizes the most relevant state-of-the-art modeling approaches for irradiance modeling and yield predictions in APV systems, which will be compared with the results of this thesis.

2.3.3.1 Irradiance modeling for agrivoltaic greenhouses

The study of [126] summarized results of numerical simulations as well as experimental results of GHs in Europe with PV cover ratios of 25% to 100%. For their study, four APV GH types were simulated and compared to real commercial large-scale APV GHs in Sardinia, Italy. The types differ mainly for the roof design, thus the amount and the installation pattern of the PV panels, as presented in Figure 2.17.

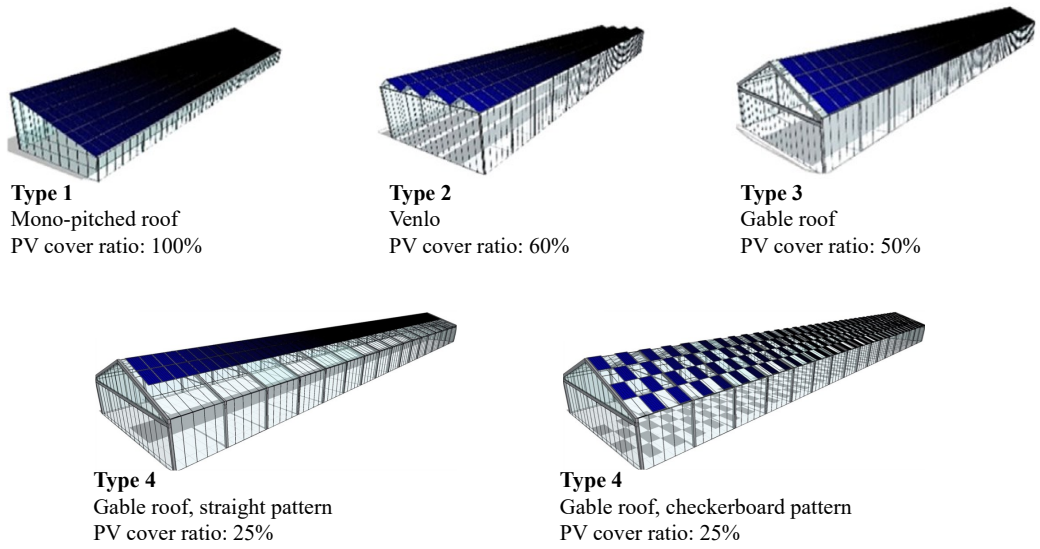


Figure 2.17: GH types and shading levels studied by [126]. Figures adapted from [126].

To calculate solar radiation, the authors used a geometric approach. Their algorithm computed the solar path throughout the year and compared the sun's position with the roof geometry in order to determine whether an observation point inside the GH was shaded or illuminated. If an observation point was not shaded, it received the sum of direct and diffuse radiation multiplied by the average transmissivity of the GH cover, whereas shaded points only received diffuse radiation through the cover. The simulations were performed under clear-sky conditions with an assumed transmissivity coefficient of 0.65. For each GH type, radiation was calculated at 100 observation points arranged in a 10×10 grid across the GH floor and aggregated into light distribution maps. The results were expressed as cumulated global radiation relative to a conventional GH, which made the indices independent of the cladding material, and the uniformity of radiation was evaluated using the coefficient of variation across all observation points. Their simulations summarized a decrease in yearly global radiation by 0.8% for east–west-oriented and 0.6% for north–south-oriented GHs for each additional 1% PV cover ratio. Additionally, GH height was shown to increase available radiation by an additional 3.8% for each additional meter of GH gutter height.

[127] developed a simulation tool to calculate the irradiance uniformity inside a "Venlo" GH by applying a decomposition model, based on the method developed by [128]. The method was originally used to simulate the global horizontal radiation distribution in open-field APV systems. The approach of [127] provides a vector-based geometric representation of the GH and PV panels, as depicted in Figure 2.18. To determine the solar radiation entering a GH, any given point inside the GH is assessed if it is shaded by PV panels or exposed to direct sunlight, depending on the solar position. Irradiance maps for the GH ground are then estimated based on solar irradiance for representative days in each month taken from a typical meteorological year. By integrating these values over time, the model estimates both monthly and annual radiation levels for different points inside a GH and provides averaged irradiation maps for the ground of the GH.

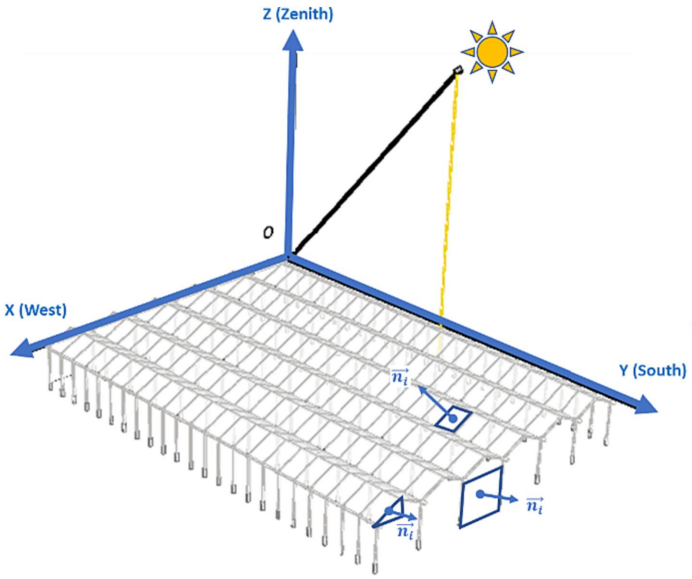


Figure 2.18: Schematic representation of the GH irradiance model developed by [127]. The model computes direct and diffuse irradiance at each point inside a "Venlo"-type GH by assessing shading from PV panels based on solar geometry. Figure taken from [127].

2.3.3.2 ESTIMATING CROP YIELD IN AGRIVOLTAIC SYSTEMS

A direct approach for crop yield estimation is the application of crop growth and functional–structural plant models for specific crop types. The review of [57] summarized various studies validating crop models in APV systems, detailing the crops studied, the models used, and their calibration methods. Crop growth models can simulate biomass accumulation, fruit yield, and other physiological processes over time, however, accurate yield predictions require thorough calibration to local environmental conditions. For GH applications, one of the most established models is the Tomato Growth model (TOMGRO) [129], which has recently been extended to APV contexts [130, 131]. As highlighted by [57], while these models effectively capture plant responses to varying light and shade conditions, significant challenges remain in representing the dynamic composition of diffuse and direct radiation under PV structures. Consequently, local validation with data remains essential to ensure model reliability in APV environments.

Given these challenges in modeling the complex light environment of APV systems, empirical approaches have become equally important for understanding crop yield responses. The yield of crops in APV systems is particularly difficult to predict because the shade patterns created by PV panels differ substantially from the irradiance distributions in conventional agriculture without PV. In general, there is a strong debate about the shading ratio that is acceptable in APV systems. However, the shading ratio itself is challenging to quantify, as it fluctuates hourly and daily depending on factors such as latitude, system design, and spatial position. To address this uncertainty, the study of [132] conducted a meta-analysis to quantify how different crop types respond to shading in order to assess

their suitability for APV. They summarized 58 field studies from temperate and subtropical regions that reported both yield and the corresponding reduction in solar radiation. Data were standardized as relative yield under shading (unshaded = 100%) and categorized into nine crop groups. The authors related relative yield to the reduction in solar radiation and derived crop-type-specific response curves, as depicted in Figure 2.19.

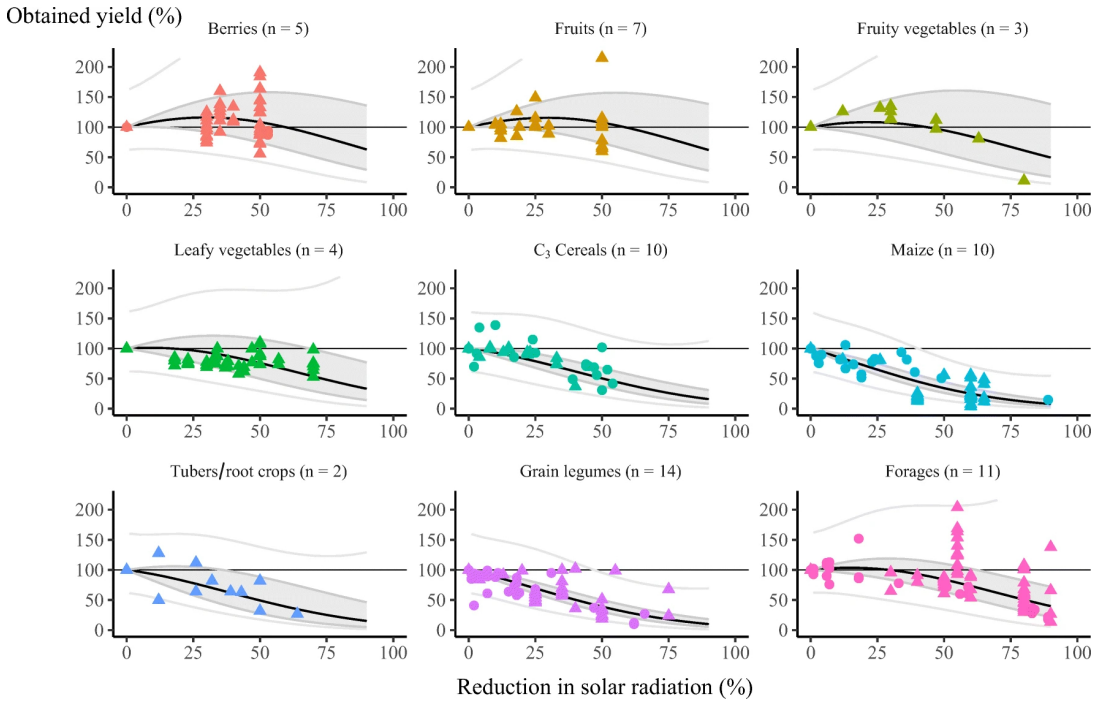


Figure 2.19: Impact of shading on the relative yield of various types of crops according to [132]. Figure taken from [132].

The work of [132] is widely used in the APV research community to estimate crop yield responses under varying shading levels, as several studies included in their meta-analysis reported high relative yields (>100%) for crops such as berries, fruit trees, and forages. Their results generally indicate yield increases for many crop types under moderate shading. However, it is important to note that most experiments included in their analysis used shade nets instead of PV panels and studies about GHs were generally excluded. Shading nets provide homogeneous shading patterns, which differ substantially from the shade patterns created by APV systems. Of the 58 studies analyzed, only two originated from APV experiments. In contrast to shade nets, which provide uniform shade throughout the day, APV systems expose plants to frequent transitions between full sunlight and complete shade. Since stomatal reopening following a transition from shade to sun may take 10–60 minutes [133], crop performance under APV systems may be lower than under shade nets at the same average shading level. This means that one should be careful from directly extrapolating such results to APV systems and their results should be confirmed in APV studies [134].

In comparison to [132], the study of [134] proposed using the ground coverage ratio, the ratio of PV panel area to cultivated land area, as a measure for estimating crop yield potential in APV systems. Based on the results of 21 studies, including APV GH studies, they established a relationship between crop yield and ground coverage ratio, as depicted in Figure 2.20. According to their calculations, yields generally remain around 80% at 25% ground coverage ratio but drop to about 60% at 50% ground coverage ratio.

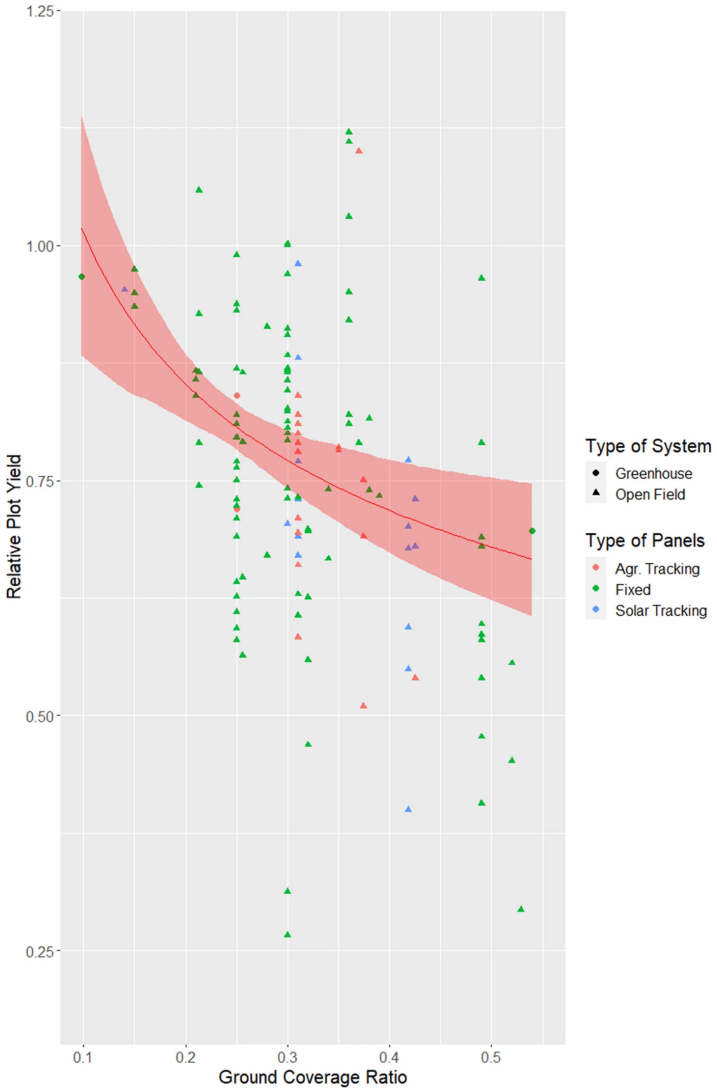


Figure 2.20: Relationship between ground coverage ratio and relative plot yield in APV and GH systems [134]. Figure taken from [134].

Based on the previously reviewed studies, it is evident that APV research for GH applications is expanding. However, APV installations in Almería-typical "raspa y amagado" GHs have so far been investigated only for low shading ratios that did not affect marketable crop yield. Consequently, it remains unclear whether a threshold shading level exists above 10% at which crops in this GH type can no longer tolerate additional light reduction. In this thesis, this research gap is approached and an experimental study conducted in a "raspa y amagado" GH with two higher shading ratios (30% and 50% roof coverage) is

presented and analyzed. Furthermore, to date, no simulation model for APV greenhouses is available that accurately represents the irradiance perceived by plants as a function of PV layout and light transmission through the surrounding cover materials. This thesis addresses these research gaps by developing a holistic APV greenhouse model that enables layout optimization. The experimental measurements are used to validate the developed model, a step that is still largely missing in the current state-of-the-art.

2.4 Statistical error metrics

Throughout this thesis, several statistical error metrics are used to evaluate model performance. The following subsections introduce each metric using general terminology, where:

- n is the number of observations,
- y_i is the observed value,
- $\hat{y}_i$ is the simulated value,
- $\overline{y}$ is the mean of the observed values, calculated as $\overline{y} = \frac{1}{n}\sum_{i=1}^{n} y_i$.

2.4.1 Root Mean Square Error and Normalized Root Mean Square Error

The Root Mean Square Error (RMSE) quantifies the average magnitude of the simulation error and is defined in Equation 2.2.

$$\mathrm{RMSE} = \sqrt{\frac{1}{n}\sum_{i=1}^{n}(\hat{y}_i - y_i)^2} \tag{2.2}$$

The normalized RMSE (nRMSE) expresses the RMSE relative to the mean of the observed values and is calculated as in Equation 2.3.

$$\mathrm{nRMSE} = \frac{\mathrm{RMSE}}{\overline{y}} \tag{2.3}$$

2.4.2 Mean Bias Error and Normalized Mean Bias Error

The Mean Bias Error (MBE) indicates the average bias in the simulations and is defined in Equation 2.4.

$$\mathrm{MBE} = \frac{1}{n}\sum_{i=1}^{n}(\hat{y}_i - y_i) \tag{2.4}$$

The normalized MBE (nMBE) expresses this bias as a fraction of the mean observed value and is calculated as in Equation 2.5.

$$\mathrm{nMBE} = \frac{\mathrm{MBE}}{\overline{y}} \tag{2.5}$$

2.4.3 Mean Absolute Error and Normalized Mean Absolute Error

The Mean Absolute Error (MAE) reflects the average magnitude of the errors in a set of simulations, without considering their direction, and is defined in Equation 2.6.

$$\text{MAE} = \frac{1}{n}\sum_{i=1}^{n}|\hat{y}_i - y_i| \tag{2.6}$$

The normalized Mean Absolute Error (nMAE) expresses the MAE relative to the mean of the observed values and is typically reported as a fraction, as given in Equation 2.7.

$$\text{nMAE} = \frac{\text{MAE}}{\overline{y}} \tag{2.7}$$

This normalization facilitates the comparison of prediction accuracy across different scales or datasets.

2.4.4 Coefficient of Determination (R^2)

The Coefficient of Determination (R^2) measures the proportion of the variance in the observed data that is predictable from the model and is calculated according to Equation 2.8.

$$R^2 = 1 - \frac{\sum_{i=1}^{n}(y_i - \hat{y}_i)^2}{\sum_{i=1}^{n}(y_i - \overline{y})^2} \tag{2.8}$$

2.4.5 Irradiation error

The irradiation error quantifies the relative deviation between simulated and observed cumulative irradiation over a given period, e.g. per day. The irradiation error evaluates the total bias in the simulated sum compared to the observed sum. It is expressed as a percentage and calculated as in Equation 2.9.

$$\text{Irradiation Error (\%)} = \frac{\sum_{i=1}^{n}(\hat{y}_i - y_i)}{\sum_{i=1}^{n} y_i} \times 100 \tag{2.9}$$

A positive value indicates overestimation of cumulative irradiation by the model, whereas a negative value indicates underestimation.

3

Methodology of the agrivoltaic simulation framework

"One never notices what has been done; one can only see what remains to be done."

—Marie Curie

The model developed and validated in this thesis is divided into two main components, i.e. the irradiance model and the crop model. The two components are coupled to estimate the yield in APV GHs dependent on different sites, GH types, crops and PV modules and independent of designated experimental studies. The following chapter explains the workflow of the two sub-models in detail and is hence split into two separate sections.

Section 3.1 explains the procedure of the irradiance model. The objective of the irradiance model is to assess how PV modules on GHs affect the irradiance distribution inside the GH with high spatial and temporal resolution. Therefore, a ray-tracing-based approach was chosen, utilizing the `Radiance` software, version 5.4 [135].

Section 3.2 focuses on the crop modeling part. The objective of the crop model is to evaluate how different types of crop develop under APV conditions and to estimate the expected crop yield. Here, two approaches are presented, one flexible and more general approach based on the light requirements of different types of crops and one detailed approach using a functional-structural plant model specific for tomato crop. Both approaches are implemented into the simulation framework and validated in Chapter 6.

3.1 Irradiance model

The irradiance model focuses on correctly mapping light transmission through GH cover materials, the adaptability of PV arrangement patterns, and the simulation of GHI distributions inside APV GHs. The model is implemented using the `C++`-based `Radiance` ray-tracing software, version 5.4 [135]. `Radiance` employs backward ray-tracing algorithms, meaning that the light 'rays' are traced back from the point of measurement or view to the light source.

Radiance is a flexible and optimised lighting simulation tool that has been continuously improved and validated over the last three decades [135]. The software was developed to run on UNIX machines with its source code being freely available.

Radiance is a modular software, as most UNIX-based software programs, which offers flexibility and freedom in the development of own functions and applications for the user. The here presented irradiance model is based on the common Radiance workflow, depicted in Figure 3.1, which is extended to simulate APV GHs.

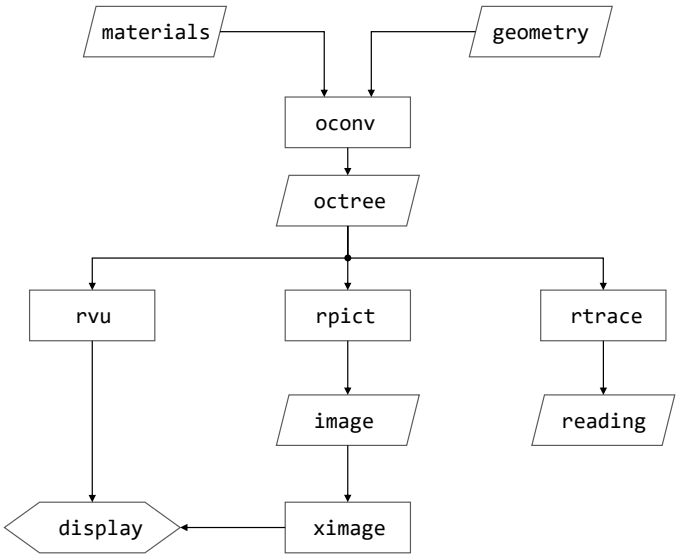


Figure 3.1: The main components of the Radiance rendering system. Figure taken from [135].

The diagram in Figure 3.1 shows the flow between programs (boxes) and data (parallelograms). Geometrical objects (geometry) get assigned a material and are combined into an octree using the oconv command. The rvu and rpict commands can be used to render images. The command rvu directly displays the image in an interactive viewer, while rpict writes its output into a readable image file. The file can then be displayed using the ximage command. Ray-tracing calculations to simulate irradiance in the scene are started using the rtrace command. Results are stored in a readable file (reading).

3.1.1 Theory of radiative transfer modeling and irradiance calculation in Radiance

Radiance was developed as a research tool for predicting the distribution of visible radiation in illuminated spaces [136]. It takes as input a three-dimensional geometric model of the physical environment, and produces a map of spectral radiance values in a color image [136]. Because it can produce realistic images from a simple description, Radiance has a wide range of applications in graphic arts, lighting design, computer-aided engineering and architecture [136]. Furthermore, Radiance is the most widely adopted backward ray-tracing software in the field of PV [137, 138, 139, 140, 141].

3.1.1.1 KAJIYA'S RENDERING EQUATION

`Radiance` is a physically-based rendering system tailored to the demands of lighting design and architecture [142]. Herewith, the term "physically-based rendering" refers to rendering techniques based on physical principles of light behavior for local and global illumination.

The theoretical foundation underlying such physically-based systems is the rendering equation, an integral equation introduced by James Kajiya in 1986 that describes the amount of light leaving a point on a surface as the sum of emitted light and incoming light that is subsequently scattered or reflected [143]. The rendering equation formalizes the relationship between radiometric quantities and the bidirectional reflectance distribution function used in rendering.

Equation 3.1 shows Kajiya's rendering equation [143] with the notion of energy transfer between two points replaced by energy passing through a point in a specific direction [142]. `Radiance` uses ray-tracing in a recursive evaluation of Equation 3.1 at each surface point x [142].

$$L_r(x, \boldsymbol{\omega}_r) = L_e(x, \boldsymbol{\omega}_r) + \int_{\Omega^+} L_i(x, \boldsymbol{\omega}_i)\, \rho_{bd}(x; \boldsymbol{\omega}_i, \boldsymbol{\omega}_r)\, (\boldsymbol{\omega}_i \cdot \mathbf{n})\, \mathrm{d}\boldsymbol{\omega}_i \tag{3.1}$$

where x denotes a surface point, $\boldsymbol{\omega}_i$ and $\boldsymbol{\omega}_r$ are unit direction vectors for incoming and outgoing directions, respectively, and $\mathbf{n}$ is the outward unit surface normal at x. The variable Ω^+ describes the hemisphere above the surface, defined by $\boldsymbol{\omega}_i \cdot \mathbf{n} > 0$, and $\mathrm{d}\boldsymbol{\omega}_i$ is the differential solid angle element (in units of sr). The term $L_r(x, \boldsymbol{\omega}_r)$ describes the outgoing radiance from point x in direction $\boldsymbol{\omega}_r$, $L_e(x, \boldsymbol{\omega}_r)$ describes the emitted radiance of point x in direction $\boldsymbol{\omega}_r$, and $L_i(x, \boldsymbol{\omega}_i)$ describes incident radiance at point x from direction $\boldsymbol{\omega}_i$ (all in units of $\mathrm{W\,sr^{-1}\,m^{-2}}$). The function $\rho_{bd}(x; \boldsymbol{\omega}_i, \boldsymbol{\omega}_r)$ describes the bidirectional reflectance–transmittance distribution function of the material at surface point x (in units of sr^{-1}).

The formulation of the rendering problem in the form of Kajiya's rendering equation in 3.1 is natural for ray-tracing because it calculates outgoing radiance in terms of incoming radiance over the projected sphere, without any explicit mention of the model geometry [142]. In this formulation, radiative transfer is evaluated locally at each surface interaction point by computing the hemispherical integral of incident radiance based on recursively spawned rays [142]. As a consequence, the method imposes no restrictions on the number, topology, or shape of surface elements, and no spatial discretization of the scene geometry is required [142].

Solving the rendering equation for any given scene is the primary challenge in realistic rendering. `Radiance` uses a hybrid approach combining deterministic and stochastic ray-tracing. Contributions from explicit light sources, such as the sun, are treated deterministically. Instead of relying solely on random hemisphere sampling, `Radiance` sends dedicated rays towards known light sources. If such a ray reaches the source without obstruction, the full contribution of the source is evaluated analytically based on its angular extent and radiance. Similarly, specular reflection and transmission are handled deterministically. For materials exhibiting directional scattering, such as glass or highly reflective

surfaces, `Radiance` traces deterministic rays in the mirror and refracted directions. These rays account for the dominant transport paths associated with specular interactions, while stochastic sampling is used only for the remaining diffuse component. Diffuse interreflection is evaluated using Monte Carlo hemisphere sampling. Incoming radiance is sampled over the projected hemisphere above the surface point, and recursive ray tracing is used to account for multiple reflections and transmissions. To improve efficiency, `Radiance` caches indirect irradiance values and interpolates them spatially [142].

3.1.1.2 SKY AND SUN AS RADIATIVE BOUNDARY CONDITIONS

Radiative transfer in `Radiance` is formulated as a boundary value problem in which the sky and sun define the radiative boundary conditions [142]. These boundary conditions specify the angular distribution and magnitude of radiance entering the scene.

The sky is modeled as a hemispherical light source emitting radiance into the scene according to the Perez All-Weather sky model [144]. The Perez model describes the spatial distribution of diffuse sky radiance as a function of atmospheric clearness, brightness, and solar position, accounting for circumsolar brightening and horizon enhancement [144]. The sky radiance distribution $L_{\text{sky}}(\theta, \gamma)$ is defined as shown in Equation 3.2 below.

$$L_{\text{sky}}(\theta, \gamma) = L_z \, F(\theta, \gamma) \tag{3.2}$$

where L_z describes the zenith sky radiance, the variable θ is the zenith angle of the sky element, the variable γ is the angular distance between the sky element and the sun, and $F(\theta, \gamma)$ describes the relative sky luminance distribution function.

Perez relative luminance distribution

The Perez relative luminance distribution $F(\theta, \gamma)$ is given in Equation 3.3 [144].

$$F(\theta, \gamma) = \left(1 + A \exp\left(\frac{B}{\cos\theta}\right)\right)\left(1 + C \, \exp(D\gamma) + E \cos^2\gamma\right) \tag{3.3}$$

where the variables A, B, C, D, and E describe empirical coefficients that depend on atmospheric clearness and brightness.

The angular distance between a sky element and the sun is computed according to [144] with Equation 3.4.

$$\cos\gamma = \cos\theta \cos\theta_s + \sin\theta \sin\theta_s \cos(\phi - \phi_s) \tag{3.4}$$

where the variables θ_s and ϕ_s describe the solar zenith and azimuth angles.

The zenith radiance L_z is determined from the DHI by normalization of the sky radiance distribution [144] according to Equation 3.5.

$$L_z = \frac{\text{DHI}}{\int_{\Omega^+} F(\theta, \gamma) \cos\theta \, \mathrm{d}\boldsymbol{\omega}} \tag{3.5}$$

where Ω^+ describes the sky hemisphere and $\mathrm{d}\boldsymbol{\omega}$ denotes the differential solid angle element, defined in spherical coordinates as $\mathrm{d}\boldsymbol{\omega} = \sin\theta \, \mathrm{d}\theta \, \mathrm{d}\phi$.

Atmospheric parameters

The Perez coefficients A, B, C, D, and E depend on two atmospheric parameters: sky clearness ε and sky brightness Δ [144], defined in Equations 3.6 and 3.7.

$$\varepsilon = \frac{\mathrm{DNI} + \mathrm{DHI}}{\mathrm{DHI}} + 1.041\,\theta_s^3 \tag{3.6}$$

$$\Delta = \frac{\mathrm{DHI}\,m}{E_0} \tag{3.7}$$

where the variable E_0 describes the extraterrestrial normal irradiance, and m is the relative optical air mass. The sky clearness ε describes the relative dominance of direct versus diffuse radiation, while the sky brightness Δ characterizes the overall sky luminance.

The extraterrestrial normal irradiance $E_0(d)$ is computed as a function of the day of year d using a correction for the varying Earth–Sun distance [144, 145] according to Equation 3.8.

$$E_0(d) = E_{sc}\left(1 + 0.033\cos\left(\frac{2\pi d}{365}\right)\right) \tag{3.8}$$

where E_{sc} describes the solar constant ($\approx 1367\,\mathrm{W\,m^{-2}}$) and d is the day of year.

The relative optical air mass m is computed using the empirical formulation of Kasten and Young [146] according to Equation 3.9.

$$m = \frac{1}{\cos\theta_s + 0.50572(96.07995 - \theta_s)^{-1.6364}} \tag{3.9}$$

with the variable θ_s expressed in degrees.

Direct solar radiation

Direct solar radiation is represented in `Radiance` by an explicit directional source corresponding to the solar disc [142, 135]. The sun is modeled as a finite angular source with angular radius $\alpha_\odot \approx 0.2665°$ and solid angle $\Omega_\odot$ given by Equation 3.10 [142, 135].

$$\Omega_\odot = 2\pi\,(1 - \cos\alpha_\odot)\,. \tag{3.10}$$

The solar radiance $L_\odot$ is computed from the DNI as described in Equation 3.11.

$$L_\odot = \frac{\mathrm{DNI}}{\Omega_\odot}. \tag{3.11}$$

The resulting solar source emits directional beam radiation and produces sharp shadows. Together with the diffuse Perez sky dome, the incoming directional radiance field is defined which provides the emitted radiance term $L_e(x, \boldsymbol{\omega}_r)$ in Kajiya's rendering equation 3.1 [143].

3.1.1.3 IRRADIANCE CALCULATION

Once the directional radiance field inside the scene has been computed by solving the rendering equation [143, 142], irradiance is obtained by hemispherical integration of incoming radiance. The physical definition of irradiance at a surface point x is defined in Equation 3.12 according to [147].

$$E(x) = \int_{\Omega^+} L(x, \boldsymbol{\omega})(\boldsymbol{\omega} \cdot \mathbf{n}) \, \mathrm{d}\boldsymbol{\omega} \tag{3.12}$$

where $L(x, \boldsymbol{\omega})$ denotes the spectral radiance arriving at point x from direction $\boldsymbol{\omega}$. The vector $\mathbf{n}$ describes the outward surface normal at point x, and Ω^+ denotes the hemisphere above the surface, defined by $\boldsymbol{\omega} \cdot \mathbf{n} > 0$.

In `Radiance`, this integral is evaluated numerically using the `rtrace -I` command [142, 135]. `Radiance` computes a Monte Carlo approximation of the hemispherical integral by tracing rays from the evaluation point into the surrounding hemisphere, sampling incoming radiance from the diffuse Perez sky dome, the solar source, and surrounding surfaces, and accumulating their cosine-weighted contributions. By default, `rtrace -I` returns three color channel values, R, G, and B, which are linearly related to the color matching functions defined by the International Commission on Illumination (CIE) [148, 149]. The CIE 1931 tristimulus response functions describe the spectral sensitivity of the standard human observer and form the basis for computing luminance and colorimetric quantities from spectral radiance [150]. In `Radiance`, the R, G, and B channels approximate the broadband shortwave irradiance field [148, 149]. Subsequently, the R, G, and B values are averaged to obtain a single broadband irradiance value, which is interpreted as GHI at the evaluation point according to Equation 3.13 [138].

$$\mathrm{GHI} = \frac{1}{3}(\mathrm{R} + \mathrm{G} + \mathrm{B}) \tag{3.13}$$

In the following sections, the previously presented theoretical background of `Radiance` internal radiative transfer calculations is going to be related to the application of the developed irradiance model. In order to build virtual APV GHs with `Radiance` and simulate irradiance with the presented model, the design and orientation of the GH, the location coordinates, and the arrangement of the PV modules are defined first (Section 3.1.2 and 3.1.3). This geometrical scene is then combined with input solar radiation data (Section 3.1.4). Ray-tracing simulations are performed with a temporal and spatial resolution defined by the user (Section 3.1.5). The final output of the simulations is then GHI in units of $\mathrm{W\,m^{-2}}$, according to Equation 3.13, which can be fed into the crop model (Section 3.2).

3.1.2 GEOMETRICAL DETAILS

Radiance uses a Cartesian coordinate system. A Radiance scene is aligned so that the x-axis points East, the y-axis points North, and the z-axis points upwards to the zenith, as shown in Figure 3.2.

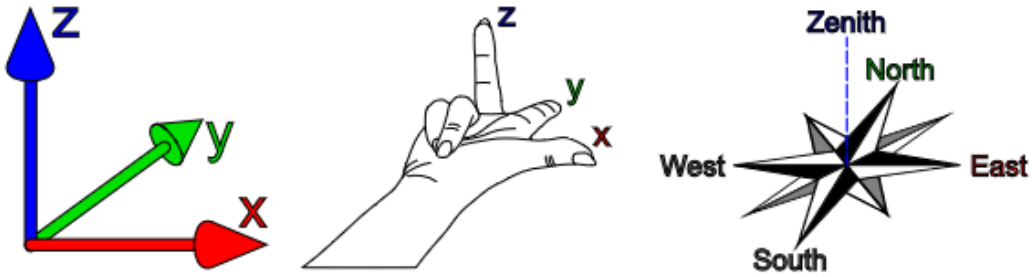


Figure 3.2: The Radiance convention on alignment of the coordiante system follows the right-hand rule. Figure taken from [135].

All information on the scene, such as dimensions and coordinates, is stored in ASCII text format, so it can be edited with any text editor. In general, in Radiance objects (i.e. PV modules, buildings, etc.) are represented by geometrical figures with specific dimension and materials. These objects can be moved (shifted along an axis, rotated, etc.) to user specified positions and therefore be combined into forming complex sceneries, such as a GH with a PV installation integrated into the roof.

3.1.2.1 VIRTUAL GREENHOUSE LIBRARY

The geometrical details of the GH structure and its materials have to be defined, so that a 3D representation of the GH can be generated. Within this PhD thesis, a virtual GH library was developed which contains different GH geometries that can be further customized by the user of the model. All 3D GH representations presented in this thesis were generated by the author. In its current state, the library contains GHs that can be commonly found in the Mediterranean region [22]: "Venlo", "multitunel" and "raspa y amagado" GHs. In the future, the library can be further expanded with other GH types, such as glass GHs which are typically found in northern Europe [151].

In order to build a virtual GH in Radiance, the primitives genrev, genbox and genprism are used. All Radiance primitives describe surface objects with their surface normal vector pointing outwards. Detailed information on Radiance object definition can be found in [135]. The structural base of GHs are the support pillars and beams made from metal. In the model, beams and pillars are implemented using the genrev or genbox primitives. The general expression for a cylinder-like pillar used for the APV GHs in the model can examplary be seen below.

$$
\begin{aligned}
&! \; genrev \; Metal_Aluminum_Anodized \; pillar \; t*z(t) \; r(t) \; n_{seg} \; | \\
&xform \; -rx \; \alpha_x \; -ry \; \alpha_y \; -rz \; \alpha_z \; | \\
&xform \; -t \; \Delta x \; \Delta y \; \Delta z
\end{aligned}
$$

Metal_Aluminum_Anodized is a predefined `Radiance` material, resembling the optical properties of reflecting, not transmissive anodized aluminum, which is often used in the construction of GHs. The first three numbers $z(t), r(t)$ and n_{seg} refer to the height, the radius and the segmentation of the object. Height and radius are variables of t, which is defined as $t = \frac{1}{n_{seg}}$ and takes values between 0 and 1. The second line describes the rotation in space in x-, y- and z-direction. The third line refers to a lateral movement in x-, y- and/or z-direction in the overall Cartesian coordinate system of the scene. All values are defined in meters for lateral movement and dimension and degree for the rotation angles. By defining the basic geometrical shapes, the GH will then be composed by duplicating the single objects to complete the structure of the virtual GH. Figure 3.3 presents an exemplary "raspa y amagado" type GH generated with the model.

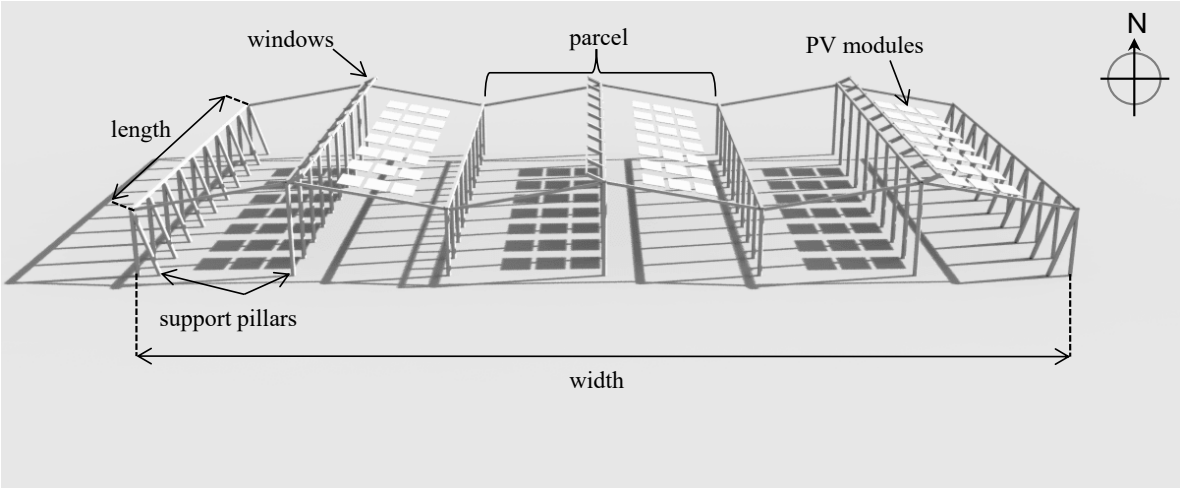


Figure 3.3: Rendered image of an exemplary "raspa y amagado" APV GH generated with the model consisting of three individual parcels stacked together.

To modify the GH, the user has to define the GH type and define case-specific dimensions, i.e. total length in meter, total width in meter, height in meter, orientation in the coordinate system, number of parcels, number and dimension of support pillars per row, size and location of windows in meter (indicated in Figure 3.3). As the last step in the GH building process, windows, roof and side walls will be added to the geometry, which are implemented using the `genprism` primitive to create 3-dimensional polygons to fit to the user-defined dimensions. The implementation of the material that gets assigned to the side walls and roof is described in Section 3.1.3. A custom `load_greenhouse()` function loads the GH type and modifies it according to the user defined parameter values.

3.1.2.2 VIRTUAL PV MODULE LIBRARY

Depending on the available roof area and the desired roof cover ratio, the model allows the user to distribute PV modules on the GH roof. Individual PV modules are defined as rectangles with user-defined dimensions. In the current form of the irradiance model, PV modules are modeled with a fully opaque material, but semi-transparent modules can also be implemented in the future. The user can specify the PV module arrangement pattern (checkerboard or linear placement) and the cover ratio. The model automatically

computes the number of PV modules and the gaps considering both the roof and PV module dimensions.

A custom `make_module_coverratio()` function has been implemented for this purpose. The user may specify values between 0% and 100% for the roof cover ratio. The function calculates the number of panels that can fit next to each other on the available area along the length of the GH roof and the gap between the panels. Since it might not be possible to exactly reach the specified roof cover ratio, the function also calculates the true cover ratio achievable with the given configuration and the deviation from the input cover ratio. Moreover, the user can specify the arrangement pattern of the panels on the GH roof. Therefore, virtually all combinations and arrangements are possible, such as a checkerboard pattern or line placement.

3.1.2.3 ROTATING THE VIRTUAL GREENHOUSE

All virtual GHs in the library are by default facing south. In order to realistically model GHs, which are often rotated in the x-y-plane, a rotation matrix, given in Equation 3.14, is introduced.

$$\begin{bmatrix} x_{\text{rotated}} \\ y_{\text{rotated}} \end{bmatrix} = \begin{bmatrix} \cos(\theta_{\text{rot}}) & -\sin(\theta_{\text{rot}}) \\ \sin(\theta_{\text{rot}}) & \cos(\theta_{\text{rot}}) \end{bmatrix} \begin{bmatrix} x_{\text{unrotated}} \\ y_{\text{unrotated}} \end{bmatrix} \tag{3.14}$$

The orientation is described with the θ_{rot} parameter. By default $\theta_{\text{rot}} = 180°$ describes a south facing orientation of the GH and the PV modules. The user may specify values in the range of $[0°, 360°]$ to rotate the virtual APV GH system to match the desired rotation.

3.1.3 MATERIAL PROPERTIES

In the current version of `Radiance`, implementing realistic GH plastic materials is a challenging task. As introduced in Section 2.2.3, GH cover materials are often multi-layered with high haze values to increase diffusely transmitted light inside the GH.

According to Kajiya's rendering equation (Eq. 3.1), the outgoing radiance in direction $\boldsymbol{\omega}_r$ is given by the sum of the emitted radiance and the integral of the incoming radiance over the hemisphere, weighted by the surface's bidirectional reflectance–transmittance distribution function $\rho_{bd}(x; \boldsymbol{\omega}_i, \boldsymbol{\omega}_r)$. Consequently, all information describing a material's scattering behavior, including reflection, transmission, diffusion, and specular effects, is contained in $\rho_{bd}(x; \boldsymbol{\omega}_i, \boldsymbol{\omega}_r)$. In order to solve the rendering equation, `Radiance` does not require a continuous function for each material model. Instead, `Radiance` provides a set of physically-based material models, such as `dielectric`, `plastic`, `glass`, and `trans`, which represent parameterized approximations of the bidirectional reflectance–transmittance distribution function [148]. GH cover materials as a transmissive material are represented by the material category `trans`.

3.1.3.1 SCATTERING MODEL OF THE `trans` MATERIAL

The scattering behavior of a transmissive `trans` material is approximated by a decomposition into four components, i.e. $\rho_{r,\text{diff}}$, $\rho_{r,\text{spec}}$, $\rho_{t,\text{diff}}$ and $\rho_{t,\text{spec}}$, as in Equation 3.15.

$$\rho_{bd} = \rho_{r,\text{diff}} + \rho_{r,\text{spec}} + \rho_{t,\text{diff}} + \rho_{t,\text{spec}} \tag{3.15}$$

where $\rho_{r,\text{diff}}$ describes the diffuse reflection component, $\rho_{r,\text{spec}}$ describes the specular reflection component, $\rho_{t,\text{diff}}$ describes the diffuse transmission component, and $\rho_{t,\text{spec}}$ describes the specular transmission component.

Therefore, at each interaction point x of a ray with a `trans` material, `Radiance` evaluates the integral in Equation 3.16 to obtain the outgoing radiance $L_r(x, \boldsymbol{\omega}_r)$ in direction ω_r.

$$L_r(x, \boldsymbol{\omega}_r) = \int_\Omega L_i(x, \boldsymbol{\omega}_i) \left[\rho_{r,\text{diff}} + \rho_{r,\text{spec}} + \rho_{t,\text{diff}} + \rho_{t,\text{spec}}\right] (\boldsymbol{\omega}_i \cdot \mathbf{n}) \, \mathrm{d}\boldsymbol{\omega}_i \tag{3.16}$$

As described in Section 3.1.1, `Radiance` then uses the hybrid approach of deterministic and stochastic ray-tracing, in which deterministic rays are distributed for specular reflection and transmission and Monte Carlo sampling is used for diffuse reflection and transmission.

3.1.3.2 PARAMETERIZATION OF THE `trans` MATERIAL

In order to define a `trans` material as a user of `Radiance`, seven parameters have to be specified, i.e. red, $green$, $blue$, $specularity$, $roughness$, T_{diff}, and T_{spec}, as below.

```
0
0
7  red   green   blue
   specularity   roughness
   T_diff   T_spec
```

The seven parameters of the `trans` material control the relative weights of the four scattering components $\rho_{r,\text{diff}}$, $\rho_{r,\text{spec}}$, $\rho_{t,\text{diff}}$, and $\rho_{t,\text{spec}}$ (Equation 3.15). The diffuse reflectance term $\rho_{r,\text{diff}}$ is scaled by the three color parameters ($red, green, blue$), which define the overall color of the material and relate to the diffuse reflectance in the three color channels RGB. They can each take values from 0.00 to 1.00: all three parameters equal 0.00 refers to a black color while all three parameters equal to 1.00 refers to a white color [135]. The specular reflection term $\rho_{r,\text{spec}}$ is controlled by the `specularity` parameter, which refers to the gloss of the material. Values can range from 0.00 (matte) to a suggested maximum of 0.07 (satin) [135]. The reflected specularity of common uncoated glass is around 0.06 [135]. The angular spread of the specular scattering lobe is controlled by the `roughness` parameter, which describes the surface roughness and can take values from 0.00 to a suggested maximum of 0.02. A value of 0.00 means polished, and a value of 0.02 refers to a low gloss [135].

The last two parameters T_{diff} and T_{spec} describe the transmissive behavior of the material and refer to the diffuse and specular transmission of the material, respectively. The diffuse transmittance coefficient T_{diff} scales the diffuse transmission term $\rho_{t,\text{diff}}$, representing the fraction of incident radiance that is transmitted through the material and scattered diffusely. The specular transmittance coefficient T_{spec} scales the specular transmission term $\rho_{t,\text{spec}}$, representing the fraction of incident radiance that is transmitted specularly. Both parameters can take values between 0.00 and 1.00. $T_{diff} = 0.00$ refers to a completely opaque material while $T_{diff} = 1.00$ describes a completely transparent material. $T_{spec} = 0.00$ means solely diffuse transmission and $T_{spec} = 1.00$ means a completely clear material without diffuse transmission.

Internally, the `trans` material follows the Radiance scattering model described by [152]. Let $\mathbf{C} = (red, green, blue)$ denote the diffuse reflectance colour vector and let r_s denote the reflected specularity parameter. The total transmissivity a_6 is defined in Equation 3.17.

$$a_6 = T_{\text{diff}} + T_{\text{spec}}, \tag{3.17}$$

The transmitted specularity fraction a_7 is defined in Equation 3.18.

$$a_7 = \frac{T_{\text{spec}}}{T_{\text{diff}} + T_{\text{spec}}}. \tag{3.18}$$

Using this parameterization, the diffuse reflection and transmission coefficients $\rho_{r,\text{diff}}$ and $\rho_{t,\text{diff}}$ are given by [152] in Equations 3.19 and 3.20.

$$\rho_{r,\text{diff}} = \pi\,\mathbf{C}(1-r_s)(1-a_6) \tag{3.19}$$

$$\rho_{t,\text{diff}} = \pi\,\mathbf{C}\,a_6(1-r_s)(1-a_7) \tag{3.20}$$

The purely specular components $\rho_{r,\text{spec}}$ and $\rho_{t,\text{spec}}$ are given in Equations 3.21 and 3.22.

$$\rho_{r,\text{spec}} = r_s \tag{3.21}$$

$$\rho_{t,\text{spec}} = a_6\,a_7\,(1-r_s) \tag{3.22}$$

3.1.3.3 SENSITIVITY ANALYSIS ON OVERALL TRANSMITTANCE

Setting the values of the seven parameters of the `trans` material to realistically describe transmissive polymers is a complex process. Experimentally measured values for diffuse and specular reflectance or transmittance do not directly equal the values set in the definition of the referring `Radiance trans` material but have to follow the equations given in Section 3.1.3.2. Usually, the only available information of commercially available plastic sheets for GHs is the transmittance value, without separation into direct and diffuse fractions. In order to be able to relate the overall transmittance of a material to a combination of T_{diff} and T_{spec} in `Radiance`, a sensitivity analysis on the correlation of T_{diff} and T_{spec} with the 1.) overall transmittance and 2.) diffuse light transmission in the simulation was performed.

A test environment for `trans` materials was set up with a rectangular surface of the GH plastic material at a specific height, see Figure 3.4.

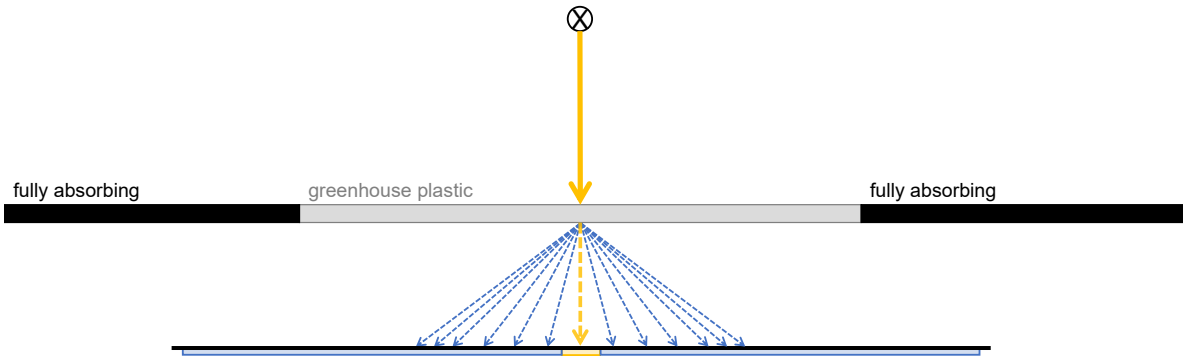


Figure 3.4: Test environment for `trans` materials to investigate transmittance behaviour under defined simulation conditions.

A point-like light source was placed directly above the test material and emitted one direct ray with constant intensity I_0 vertically onto the test material's surface. The transmitted irradiance was analyzed along the projected area straight underneath the test material, dependent on the choice of T_{diff} and T_{spec}.

For the analysis, the first five parameters of the test material definition were kept constant whilst iterating through combinations of T_{diff} and T_{spec}, since the transmission behavior of the material is only dependent on these two parameters. T_{diff} and T_{spec} were both varied in range $[0, 1]$ in steps of 0.01 with a total of $101^2 = 102021$ combinations. The overall transmittance τ, i.e. the ratio of total transmitted irradiance $I_{trans,total}$ to incident irradiance I_0, was then determined for all the tested combinations, as in Equation 3.23.

$$\tau = \frac{I_{trans,total}}{I_0} \tag{3.23}$$

Figure 3.5 depicts the results of the sensitivity analysis for the overall transmittance τ.

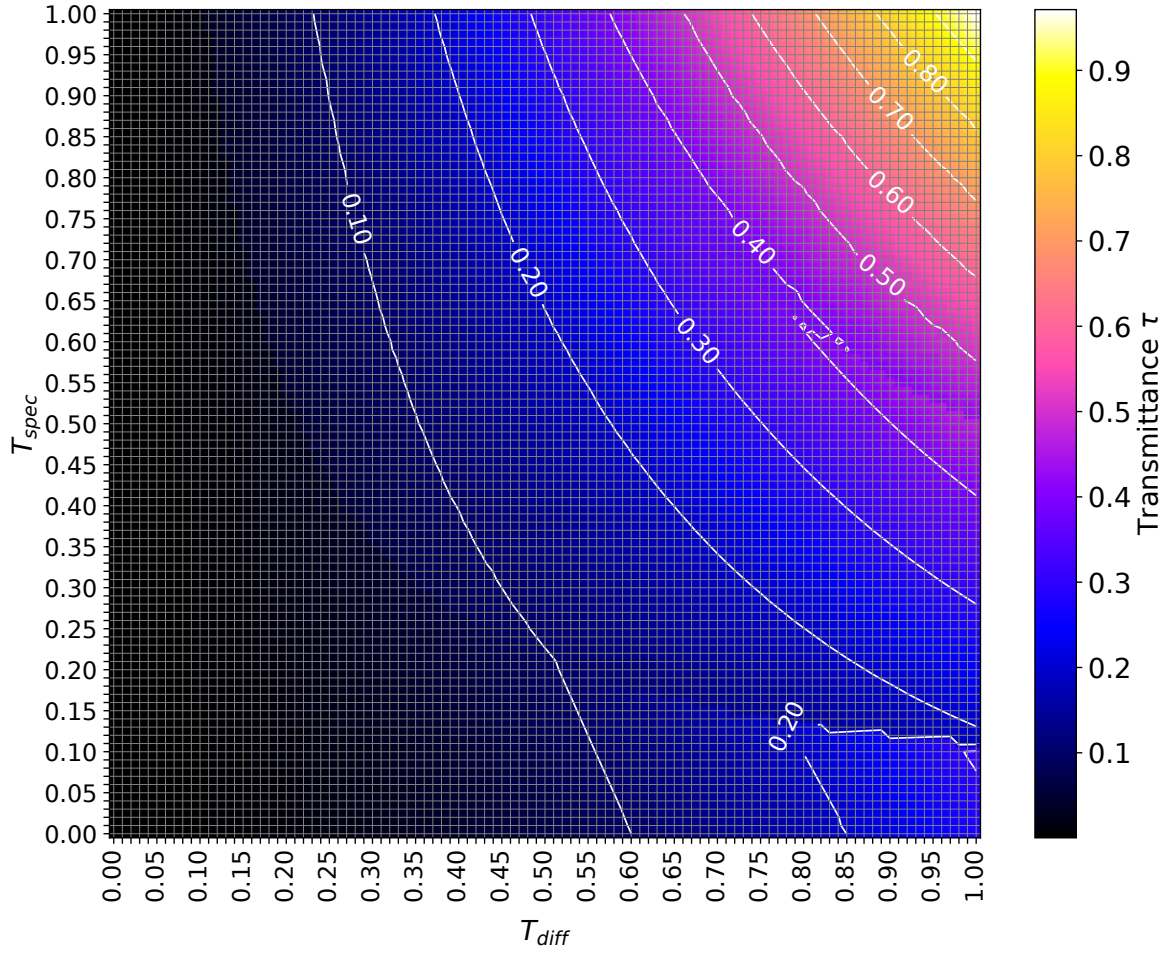


Figure 3.5: Overall transmittance of `Radiance trans` materials depending on T_{diff} and T_{spec}. The color scheme relates to the overall transmittance τ of the tested material, i.e. the ratio of transmitted irradiance to incident irradiance.

Figure 3.5 shows distinct structures and color patterns for different combinations of T_{spec} and T_{diff}. For T_{diff} values below 0.30, transmittance τ resulted in values below 0.10 independent of T_{spec}. The transmittance increased with the simultaneous increase in T_{diff} and T_{spec}. Transmittance values of approximately 80% to 89% (as typical values for GH plastics) are described by the yellow area in the upper right corner in Figure 3.5. For T_{diff} as well as for T_{spec}, values between 0.80 and 1.00 are suitable, depending on the choice of T_{diff} or T_{spec} accordingly. For a given transmittance of a GH cover material, the possible combinations of values for T_{diff} and T_{spec} move along a curve, similar to the depicted isolines, in Figure 3.5.

Intriguingly, the isolines included in Figure 3.5 have step-wise edges, in particular for $\tau = 0.20$ and $\tau = 0.40$. These edges are not the result of a physical optical effect but are caused by numerical sampling artifacts due to the stochastic ray sampling in `Radiance`. For materials with zero roughness, `Radiance` probabilistically classifies each incident ray as absorbed, reflected, or transmitted based on the specified material coefficients. With a finite number of traced rays, small incremental changes in T_{diff} and T_{spec} shift the probability at which an additional ray is transmitted instead of reflected, which then results in the edges of the isolines visible in Figure 3.5.

3.1.3.4 SENSITIVITY ANALYSIS ON HAZE

The test environment of Figure 3.4 was used to separate the direct light transmission from the diffuse component. The position of the direct beam was determined by simulating only the vertical light beam without test material, as as indicated by the red rectangle in the left plot in Figure 3.6. Then the 101^2 combinations of T_{diff} and T_{spec} were tested again while separating the diffusely transmitted rays from the direct components of the beam inside and outside the red rectangle. Figure 3.6 on the right visualizes the separation of direct and diffuse components in the simulation for one exemplary tested parameter combination.

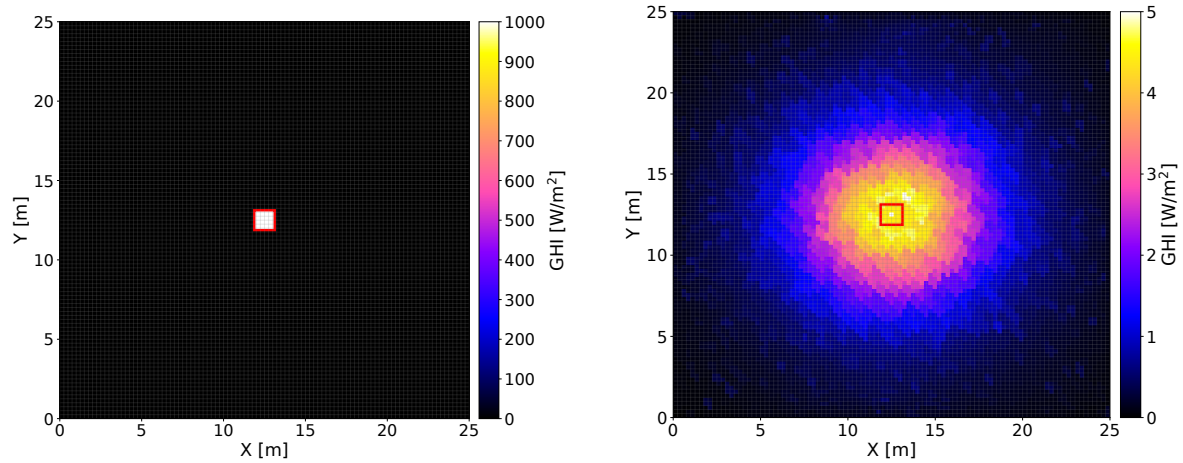


Figure 3.6: a) Without test material: extraction of position of direct beam, i.e. white spot inside the red rectangle. **b)** With test material: separation of direct (inside red rectangle) and diffuse (outside of red rectangle) components of light transmission. The color scheme depicts the transmitted irradiance under the test material.

The total transmitted irradiance $I_{trans,total}$ under the test material was evaluated for each of the tested combinations. The direct and diffuse transmission were determined by distinguishing between direct transmitted irradiance (I_{dir}) and diffusely transmitted irradiance (I_{diff}). Then, haze Φ was determined according to Equation 3.24.

$$\Phi = \frac{I_{diff}}{I_{trans,total}} \tag{3.24}$$

Figure 3.7 depicts the results of the sensitivity analysis for the haze effect.

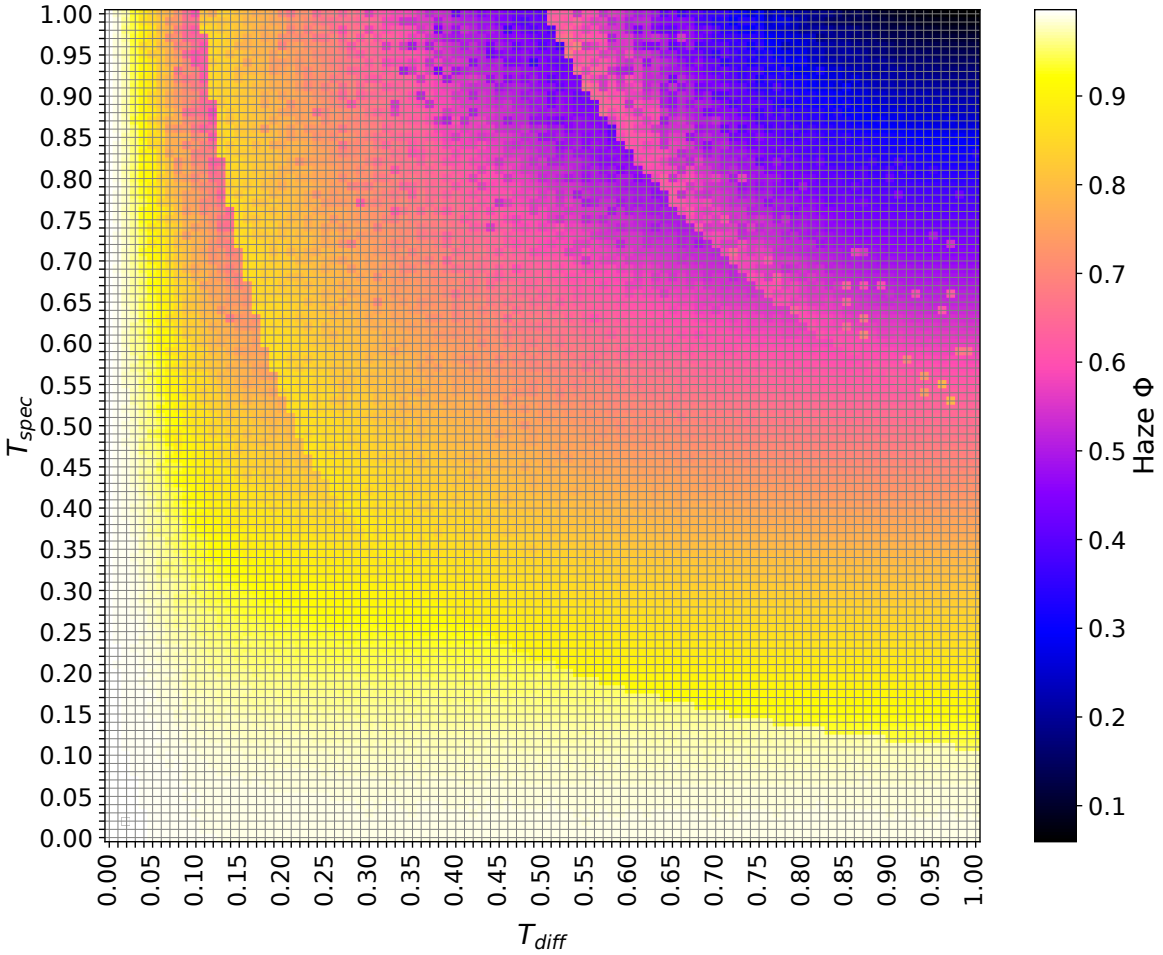


Figure 3.7: Haze analysis of `Radiance` `trans` materials depending on T_{diff} and T_{spec}. The color scheme relates to the haze Φ of the tested material, i.e. the ratio of diffusely transmitted irradiance to total transmittance.

Figure 3.7 reveals clear structures for the dependency of haze on the choice of T_{diff} and T_{spec}. For $T_{diff} = T_{spec} \to 1$, the direct transmission is dominant leading to haze equal to zero. Haze increases gradually while decreasing T_{diff} and T_{spec}. For low T_{spec}, diffuse transmission is overall dominant independent on the actual choice of T_{diff}, resulting in high haze values. Notably, for $T_{spec} \to 1$ and $T_{diff} = 0$, a high haze value is still maintained, contrary to the assumption that specular transmission would dominate after a certain threshold, resulting in a decrease of haze. However, in `Radiance's` way of sampling direct rays, purely specular transmission with zero diffuse contribution leads to both numerator and denominator in Equation 3.24 equal to zero, so $\Phi = 1$ is modeled.

Intriguingly, diagonal contour lines can be identified throughout the plot where haze decreases instead of increasing. These curvatures are sampling artifacts which are mostly caused by the roughness value of 0, which was kept constant for the simulations. In case of zero roughness materials, `Radiance` classifies each ray as transmitted inside (specular) or outside (diffuse) of a 3°-wide cone, as given by default internal `Radiance` settings [135]. Decreasing T_{diff} or T_{spec} stepwise from 1.00 to 0.00 means that those discrete rays may be accounted inside or outside of the cone, producing the contour lines rather than a completely smooth gradient.

3.1.4 SATELLITE-DERIVED IRRADIANCE DATA

As described in Section 3.1.1.2, radiative transfer in `Radiance` is formulated as a boundary value problem in which the sky and ground define the radiative boundary conditions. The sky and ground are represented as two hemispheres which enclose the scene. These hemispheres are not physical objects but abstract boundary surfaces that emit radiance into the simulation domain. The ground hemisphere represents the ground contribution to the scene and accounts for ground-reflected radiation through a diffuse emitting surface. The sky hemisphere represents the sky dome and provides the directional sky radiance distribution using an analytical sky model generated with the `gendaylit` function. Together, these hemispheres define the incoming radiative field that drives the radiative transfer problem, as introduced in Section 3.1.1.

The `gendaylit` function generates a sky description based on the Perez All-Weather model [144], as described in Section 3.1.1.2. Based on this model, Radiance determines the sky conditions (e.g., overcast, intermediate, clear) from the input parameters provided by the user. In order to generate a description of the light sources in the simulation, irradiance conditions, i.e. GHI, DHI, DNI and the solar position are specified for each timestamp. In the presented model, satellite-based irradiance data, provided by the Copernicus Atmosphere Monitoring Service (CAMS) [153], are used to generate irradiance conditions outside of the GH and simulate the inside irradiance for each investigated timestamp. CAMS products are quarterly benchmarked against a variety of ground stations to monitor their consistency. One of the regular benchmarking sites is CIEMAT's Plataforma Solar de Almería, located approximately 30 km from the location of the two experimental GHs used for validation, as presented in Chapter 5. A standard uncertainty of 2% for GHI measurements was estimated based on the RMSE, as described by [154].

The use of satellite-based irradiance data makes the model flexible in simulating different locations and time periods. With the latest CAMS product (version 4.0 of the CAMS radiation service), time series of GHI, DHI, and DNI are available from 2004 to the day before yesterday [155, 156]. Additionally, the temporal resolution of the simulations can be adjusted based on the user's needs. For localized, detailed simulations, a high temporal resolution of 15 minutes can be used. For a more general analysis of the irradiance distribution, a lower temporal resolution with 1 hour intervals may be sufficient. The choice of temporal resolution correlates with the estimated computation time of the simulations. The influence of temporal and spatial resolution on computational efficiency is further discussed in Section 5.3.1.

By default, CAMS data is right-labeled, i.e. for example, for a 15-min temporal resolution the timestamp of 08:15:00 represents the mean irradiance between 8:00 and 8:15. For each 15-min interval, the sun position is modeled at the middle of this interval. For example, for the period from 08:00:00 to 08:15:00, the sun's position is modeled at 08:07:30. In the model, the sun position is calculated using a `PVlib` (V0.9.4) Python routine [157, 158] and combined with the CAMS irradiance data in the `Radiance` sky file.

3.1.5 RAY-TRACING ANALYSIS

The developed irradiance model simulates GHI inside the virtual GH at specific points defined by the user using the `rtrace` function, according to the description in Section 3.1.1.3. In the presented model, virtual irradiance sensors are placed inside the virtual GH at positions defined by the user. These sets of coordinates, along with an orientation vector, are saved in a `line.pts` file.

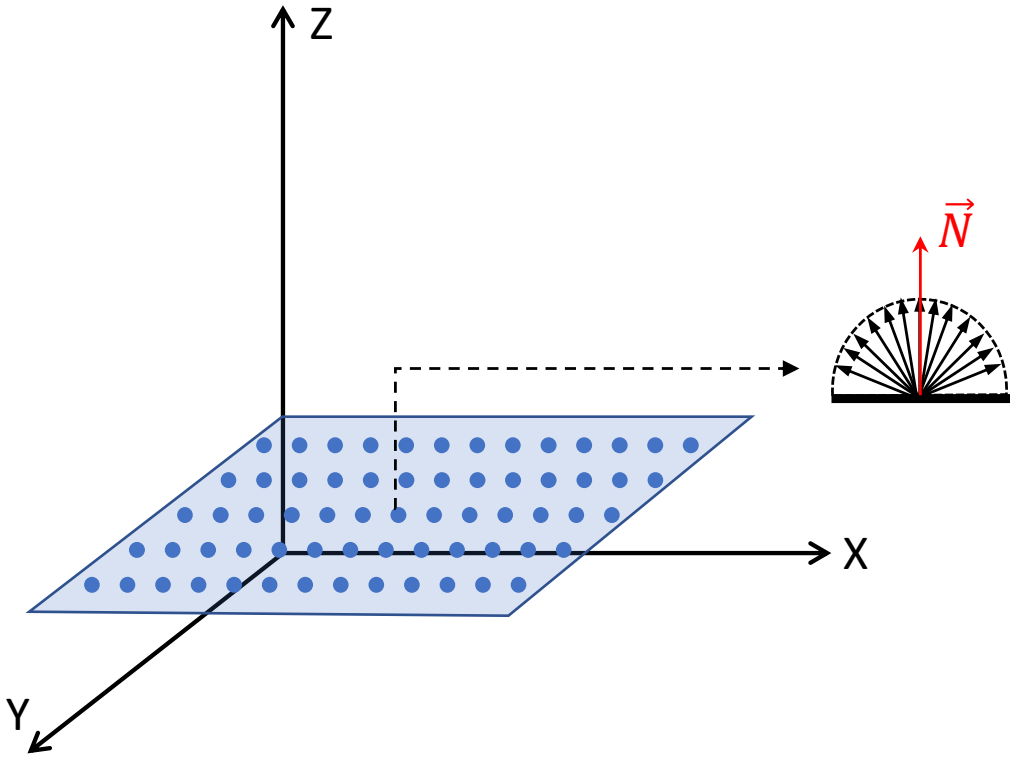


Figure 3.8: Schematic picture of an examplary ray-tracing grid with virtual sensor positions (blue dots). Each virtual sensor is defined with an x-, y- and z-coordinate and an orientation vector (red vector). Primary rays are distributed hemispherically for each grid point.

Each virtual sensor is a starting point of a set of primary rays. Primary rays are distributed hemispherically aligned with the plane perpendicular to the orientation vector of the grid point. If the ray does not reach the virtual light source, i.e. the sky dome, or is absorbed at some point within a certain number of bounces (ambient bounces), it is discarded. Direct and diffuse light sources are sampled separately in the simulation [135].

Figure 3.9 illustrates the ray-tracing procedure for the presented model. When hitting a surface, a ray may get reflected, absorbed and/or transmitted depending on the optical properties of the surface material.

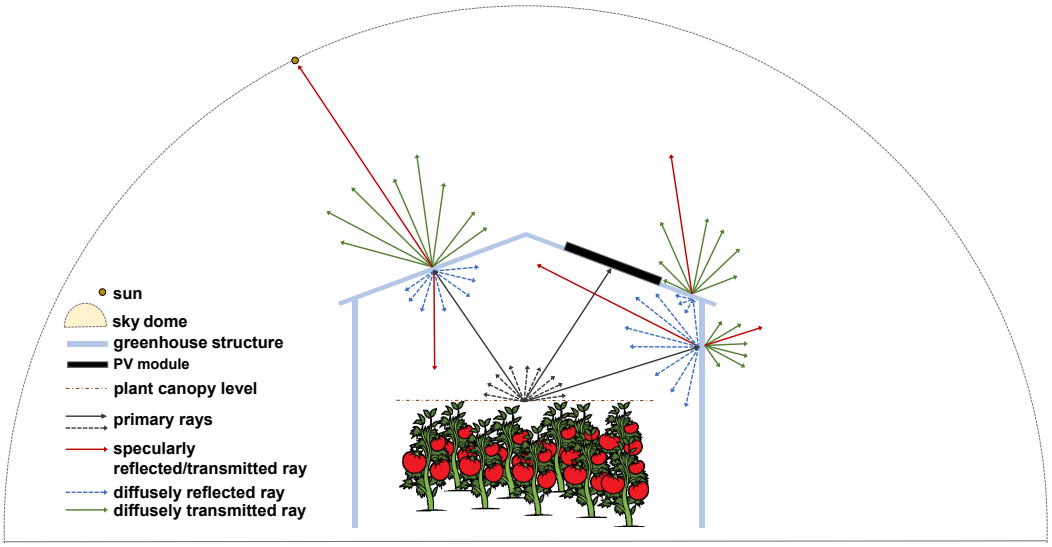


Figure 3.9: Schematic picture of the ray-tracing procedure for an agrivoltaic (APV) GH. Specular reflection (red), diffuse reflection (blue), specular transmission (red), and diffuse transmission (green) are shown. The sky dome is indicated with the dotted semicircle, and the sun is indicated with a yellow circle.

When a ray strikes a PV module, it is absorbed. Rays are reflected both specularly and diffusely when they hit parts of the GH support structure, with diffuse reflections generating new primary rays. When interacting with the transmissive GH cover material, rays can also be transmitted both specularly and diffusely.

The presented model evaluates GHI at the x-, y-, and z-coordinates provided by the user, according to the method presented in Section 3.1.1.3. The user decides if the virtual sensors are placed symmetrically along a grid over the total area of the GH, only a partial area of particular interest or at only discrete, single coordinates. The number of coordinates defines the spatial resolution of the irradiance scan and correlates with the computation time, which will be discussed in Section 5.3.1.

In the simulation, all objects, materials and sky files are combined in an `octree`. Raytracing per timestamp is then performed with the following settings in the `rtrace` function.

```
rtrace -I -ab 2 -aa 0.1 -ar 256 -ad 2048 -as 256
```

Table 3.1 summarizes the parameter settings and their explanation.

Table 3.1: Explanation of `rtrace` parameters.

Parameter	Explanation	Additional Note
`-I`	Request irradiance values rather than directional radiance.	Integrates over the hemisphere; reports irradiance in Wm^{-2}.
`-ab 2`	Sets number of ambient bounces to 2	0 = direct only; 1 = one diffuse bounce; 2 = two diffuse bounces.
`-aa 0.1`	Ambient accuracy tolerance (relative error) of 0.1.	Lower values reduce noise but increase computation time.
`-ar 256`	Ambient resolution of 256 samples.	Hemisphere sampling grid is $\sqrt{256} \times \sqrt{256} = 16 \times 16$.
`-ad 2048`	Number of primary rays.	Higher values yield smoother indirect lighting.
`-as 256`	Maximum additional ambient super-samples per point.	Fires extra rays in noisy regions, up to this cap.

The setting of these values is crucial to ensure accuracy while maintaining reasonable computation time of the simulation. Changing these values to reduce noise in the simulations is possible under the cost of additional computation time. If noise was observed in the resulting simulated irradiance, options to reduce noise are to increase `-ad` (more rays), lower `-aa` (stricter accuracy), or raise `-ar` (finer ambient grid). Conversely, these settings can be ruled down to reduce computation time.

3.2 CROP MODELS

The development of the crop models focused on linking the simulation results of the irradiance model to an estimation of crop development and crop yield obtained under APV conditions. In this chapter, two approaches for crop modeling are presented, which have been implemented and tested.

For both modeling approaches, the GHI simulation results of the irradiance model have to be converted into PPFD first, as photosynthetic processes for crop growth are mainly dependent on the incoming PAR spectrum. In this thesis, we make use of the linear regression model of Vindel et al. [159] to convert GHI into PPFD. While there are more complex approaches, such as radiative transfer and spectral decomposition models, which provide more accurate PAR estimations, these methods often require detailed spectral data, which is out of the scope of this thesis. The method is presented and discussed in Section 3.2.1.

The first crop modeling approach is based on the DLI, i.e. the amount of radiation perceived by the plants per day per unit of area, as introduced in Section 2.2.1.3. This method offers a flexible and computationally fast way to evaluate if the plants inside the APV GH perceive sufficient amounts of radiation to develop normally. This approach is described in Section 3.2.2 and validated in Section 6.1.

The second presented approach for crop modeling is the application of a functional-structural plant model to estimate yield of tomatoes grown under APV conditions. The approach offers a detailed analysis of crop response to altered microclimate conditions in the APV GH and gives insights into deeper structural behavior of the plant physiology. This method was developed and applied within the Master thesis of J. Kornas [160], which was supervised within the scope of this PhD thesis. The method is presented in Section 3.2.3 and its performance is validated in Section 6.2.

3.2.1 PAR ESTIMATION FROM GHI

The method of Vindel et al. [159] was developed using satellite-derived broadband GHI and PAR estimations for mainland Spain and has been validated against ground measurements at different sites. For the validation of the linear regression model, the site of PSA was chosen, as for the CAMS data. For this location, a correlation coefficient higher than 0.99, a mean bias error of −2.36% and an RMSE of 2.8 $\mathrm{W\,m^{-2}}$ were found. Equation 3.25 describes how the model derives PAR [$\mu\mathrm{mol\,m^{-2}\,s^{-1}}$] from GHI [$\mathrm{W\,m^{-2}}$].

$$PAR(t) = [a(month) \cdot GHI(t) + b(month)] \cdot conv. \tag{3.25}$$

The conversion factor $conv.$ has a constant value of $4.6\,\mu mol\,J^{-1}$ [64]. For the region of southern Spain, the coefficients a and b of [159], shown in Table 3.2, are applied.

Table 3.2: Coefficients a and b for the region of southern Spain taken from [159].

	Jan	Feb	Mar	Apr	May	Jun	Jul	Aug	Sep	Oct	Nov	Dec
a [-]	0.42	0.42	0.41	0.41	0.38	0.39	0.36	0.39	0.39	0.41	0.41	0.41
b [$W\,m^{-2}$]	0.35	0.49	1.37	2.15	10.94	9.37	18.05	8.63	7.12	2.25	1.45	1.25

3.2.2 DAILY LIGHT INTEGRAL-BASED MODELS

Depending on the investigated PV technology or distribution of PV modules on the GH roof, the PPFD transmitted to the plants will vary. As crops respond to altered PPFD with a change in their photosynthetic productivity, the DLI can be used as a metric to estimate yield.

Two approaches for yield estimation using DLI are presented in the following subsections. In Subsection 3.2.2.1, simulated DLI values are compared to threshold values from the literature. Yield is then estimated and accumulated on a daily basis until end of the harvest using this method. In Section 6.1.1, the results are compared to experimentally measured yield values for tomato crops, measured in the APV GH experiment described in Chapter 4.

The second method, described in 3.2.2.2, builds upon the DLI-based approach by incorporating temperature and relative humidity (RH) measurements to simulate microclimate conditions and evaluate their influence on yield. This hybrid approach combines simulated irradiance data with experimentally measured microclimate parameters from the APV GH experiment. Yield is estimated using a combined exponential-factorization function of DLI, temperature, and RH, and the results are compared to the experimental yield data in Section 6.1.2.

3.2.2.1 YIELD ESTIMATION BASED ON DAILY LIGHT INTEGRAL

Different types of crops have different DLI requirements. The here proposed methodology compares the simulated PAR inside the virtual APV GH to the PAR required by the plants and has been adapted from [161]. The estimated DLI requirements of 14 common horticultural and floricultural crops, taken from [161], recommended for optimal crop growth and production are given in Table 3.3.

Table 3.3: DLI crop requirements and photosynthetic light saturation points ($PPFD_{sat}$).

Species	DLI_{opt} [mol m^{-2} d^{-1}]	DLI_{min} [mol m^{-2} d^{-1}]	$PPFD_{sat}$ [µmol m^{-2} s^{-1}]	References
High light demanding: DLI_{opt} > 30 mol m^{-2} d^{-1}				
Tomato (*Solanum lycopersicum*)	30.0	15.0	700–1000	[162, 163, 164, 165, 166, 167, 79]
Cucumber (*Cucumis sativus*)	30.0	12.0	800–1000	[163, 164, 168, 167, 169]
Sweet pepper (*Capsicum annuum*)	30.0	12.0	800–1000	[163, 164, 170, 167, 171]
Medium light demanding: DLI_{opt} = 10–20 mol m^{-2} d^{-1}				
Lettuce (*Lactuca sativa*)	20.0	12.0	200–400	[172, 173, 174, 164, 167, 175]
Chrysanthemum (*C. morifolium*)	20.0	10.0	300–600	[176, 177]
Rose (*Rosa chinensis*)	20.0	10.0	400–700	[176, 168, 178]
Strawberry (*Fragaria ananassa*)	19.0	12.0	400–600	[164, 166, 179]
Basil (*Ocimum basilicum*)	17.3	5.3	200–400	[180, 166, 181]
Spinach (*Spinacia oleracea*)	17.0	8.0	300–500	[172, 173, 174, 182]
Asparagus (*Asparagus officinalis*)	16.7	6.5	400–500	[166, 167, 183]
Ficus (*Ficus benjamina*)	16.0	8.0	150–300	[176, 166, 184]
Low light demanding: DLI_{opt} = 5–10 mol m^{-2} d^{-1}				
Poinsettia (*Euphorbia pulcherrima*)	10.0	6.0	–	[176, 166]
Dracaena (*Dracaena fragrans*)	8.0	4.0	–	[176, 166]
Kalanchoe (*K. blossfeldiana*)	8.0	4.0	–	[176, 166]

The collected species are classified according to their optimal DLI (DLI_{opt}) in high (DLI_{opt} > 30 mol m^{-2} d^{-1}), medium (DLI_{opt} of 10 to 20 mol m^{-2} d^{-1}) and low (DLI_{opt} of 5 to 10 mol m^{-2} d^{-1}) light demanding crops [167]. The minimum amount of radiation required for sufficient crop growth is denoted as DLI_{min}. Good and healthy crop development is achievable with DLI levels between DLI_{min} and DLI_{opt}. As a time-integrated quantity, DLI varies only gradually as radiation accumulates throughout the day and is primarily determined by day length and seasonal solar elevation. PAR saturation, on the other hand, is an instantaneous response of photosynthetic rate and is dependent on environmental and physiological conditions. The reported saturation levels $PPFD_{sat}$ in Table 3.3 vary with CO_2 concentration, air temperature, plant developmental stage, leaf position, cultivar, and light acclimation history.

High light demanding crops (DLI_{opt} > 30 mol m^{-2} d^{-1}) such as tomato, cucumber, and sweet pepper are the most common GH crops worldwide [185]. They are particularly important in regions such as the Netherlands, Spain, Canada, and Mexico, where controlled environments or climatic conditions allow year-round production [185]. In northern latitudes commercial growers often employ supplemental lighting during winter months to reach sufficient DLI levels for optimal yield and fruit quality [186]. In Mediterranean GHs shading is often required to prevent excessive light and heat stress during summer [22].

Medium light demanding crops (DLI_{opt} = 10–20 mol m^{-2} d^{-1}) include leafy vegetables such as lettuce and spinach, herbs like basil, and soft fruits such as strawberry. Many of these crops are widely produced in both high- and low-tech GHs across Europe, North America, and Asia [185]. In temperate regions, they can often be grown without supplemental lighting except in winter, while again in Mediterranean GHs shading is sometimes required to prevent excessive light and heat stress during summer [22].

Low light demanding crops (DLI_{opt} = 5–10 mol m^{-2} d^{-1}) are typically ornamental plants, such as poinsettia, kalanchoe, and dracaena. These are often cultivated in commercial GHs

for the potted plant market, particularly in Europe and North America [185]. Because of their low light requirements, they are well suited for production in shaded environments or in seasons with limited natural light, and excessive irradiance may even reduce quality by causing compactness issues or leaf damage [185].

To estimate daily yield Y based on daily DLI values compared to the minimum DLI values (DLI_{min}) we propose a piece wise approach following Equation 3.26.

$$Y(t) = \begin{cases} 100\%, & \text{if } DLI_{APV} \geq DLI_{min} \\ \left(\frac{DLI_{APV}(t)}{DLI_{min}}\right)^{k_{DLI}} \cdot 100\%, & \text{if } DLI_{APV} < DLI_{min} \end{cases} \tag{3.26}$$

where $Y(t)$ describes relative yield under APV conditions, expressed as a percentage of the control (no shading) yield. $DLI_{APV}(t)$ describes the DLI of day t under APV (shaded) conditions in mol m^{-2} d^{-1}. DLI_{min} describes the minimum DLI required to maintain full yield. Parameter k_{DLI} regulates the sensitivity of changes in yield due to DLI reductions.

For the presented method we assume that DLI requirements are constant during the crop cycle and no reduction in yield and fruit quality is observed at the end of the crop cycle if radiation levels inside the APV GH succeed the minimum DLI values (DLI_{min}) everyday during the crop cycle. The presented approach assumes full yield above the minimum light threshold (DLI_{min}), and a nonlinear decline below it, as schematically depicted in figure 3.10.

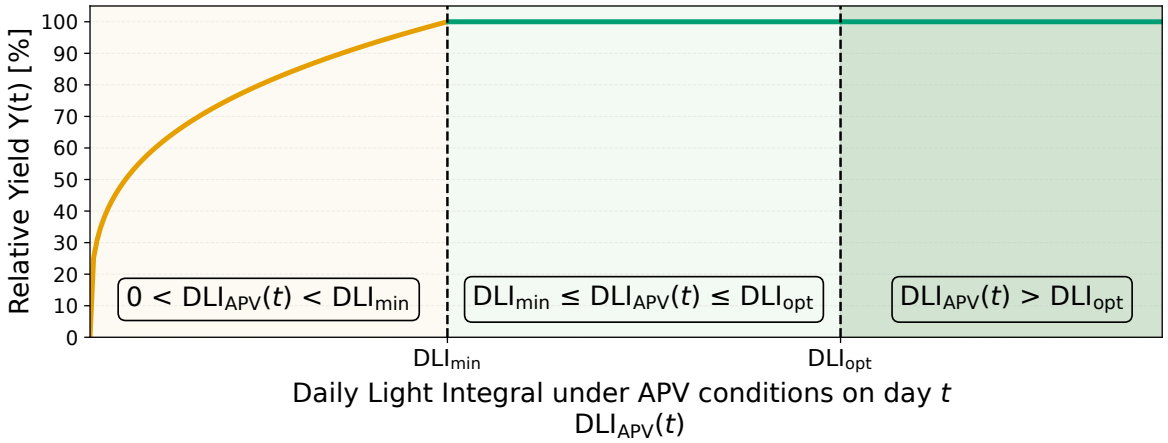


Figure 3.10: Schematic representation of the piecewise yield response function, Equation 3.26, relating DLI values under APV conditions, $DLI_{APV}(t)$, to relative crop yield $Y(t)$. For light-limited conditions ($0 < DLI_{APV}(t) < DLI_{min}$), relative daily yield increases with increasing DLI following Equation 3.26 (orange curve, orange region). Full yield (100%) is obtained for each day with $DLI_{min} \leq DLI_{APV}(t) \leq DLI_{opt}$ (green curve, light green region). For light-saturated conditions ($DLI_{APV}(t) > DLI_{opt}$), no further increase in relative yield is assumed and yield remains constant at 100%.

In order to estimate total accumulated yield at the end of the crop cycle, daily yield values are calculated based on the nonlinear DLI response model in Equation 3.26 and subsequently summed over the entire cultivation period. The final cumulative yield is then normalized relative to the unshaded control zone to express APV yield as a fraction of yield in the conventional, no APV scenario.

3.2.2.2 YIELD ESTIMATION BASED ON DAILY LIGHT INTEGRAL, TEMPERATURE AND RELATIVE HUMIDITY

While DLI is one of the primary drivers of photosynthesis and biomass accumulation [64], there are also other important factors contributing to plant development, such as GH microclimate. We would like to extend the previously presented approach based solely on DLI values by adding in variables for temperature and RH and estimate yield based on a factorized function using these three variables. In this thesis, the approach is adapted to GH tomatoes, as experimentally measured microclimate data obtained during the APV GH experiment from Chapter 4 is used for the simulations. In principle, any other horticultural crop could also be treated with the model if microclimate data would be available.

In general, a GH tomato production cycle can be divided into three main phases: a lag phase with no yield at the beginning of the cycle, followed by a phase of rapid growth and yield accumulation, and finally a plateau phase during which yields stabilize towards the end. The duration of these phases depends strongly on the tomato variety as well as the climatic conditions. For a crop cultivated over seven months in the GH and terminated after pruning, the lag phase can last about 100 days from transplanting to first flowering, the rapid growth and yield accumulation phase extends for roughly 90 days until peak harvest, and the final plateau phase covers around 20 days due to the pruning of the plants [187].

To describe this behavior and estimate yield, we use a modified Mitscherlich function [188], i.e. a combined exponential-saturation curve. The function is a mathematical model to describe plant development dependent on different growth factors and is given in Equation 3.27.

$$\begin{aligned} Y(t) &= Y_{\max}(t)\big[\,1-\exp\big(-k_{\mathrm{DLI}}\,[\mathrm{DLI}_{\mathrm{cum}}(t)-D_0]\big)\big], \\ Y_{\max}(t) &= \alpha\left(\frac{T_{\mathrm{mean}}(t)}{T_{\mathrm{opt}}}\right)^{\gamma_{\mathrm{T}}}\left(\frac{RH_{\mathrm{mean}}(t)}{RH_{\mathrm{opt}}}\right)^{\varepsilon_{\mathrm{RH}}} \end{aligned} \tag{3.27}$$

where $Y(t)$ describes relative yield under APV conditions, expressed as a percentage of the control (no shading) yield. α describes a scale factor for maximum yield under optimal temperature and RH conditions. $T_{\mathrm{mean}}(t)$ describes the mean daytime temperature of day t inside the GH, T_{opt} describes the optimal daytime temperature inside the GH, and parameter γ_{T} describes the yield sensitivity to changes in temperature. $RH_{\mathrm{mean}}(t)$ describes the mean daytime RH of day t inside the GH, RH_{opt} describes the optimal daytime RH inside the GH, and parameter $\varepsilon_{\mathrm{RH}}$ describes the yield sensitivity to changes in RH. Parameter k_{DLI} regulates the sensitivity of changes in yield due to DLI reductions. $\mathrm{DLI}_{\mathrm{cum}}(t)$ describes the sum of DLI values up to day t in $\mathrm{mol\,m^{-2}}$. D_0 is the cumulative DLI threshold before yield onset.

The approach captures the three phases of GH tomato yield accumulation taking into account three input variables describing the microclimate inside the GH. In addition to radiation, temperature affects enzyme kinetics and respiration rates of the tomato plants. Outside the optimal ranges of 21 °C to 27 °C for tomato GH cultivation, fruit-set failures and reduced lycopene synthesis may occur [81, 80]. RH influences stomatal conductance,

transpiration cooling, and pollination success. Too low RH (< 40%) can lead to excessive transpiration and flower drop, while too high RH (> 85%) favors fungal disease. For GH cultivation, an intermediate optimum around 60% to 70% RH is generally recommended [81, 80].

3.2.3 Functional structural plant models - tomato growth model (TOMGRO)

This section focuses on the integration of a functional-structural plant model (FSPM), i.e. a biophysical modeling approach to estimate the entire plant behavior and yield under dynamic conditions [189]. FSPMs simulate crop growth dynamically based on physiological processes, organ-level development, and environmental interactions and therefore deliver more comprehensive insights into crop growth and yield development. We present a modeling approach for horticultural tomatoes, using the reduced TOMGRO model by [190]. This work is part of the Master thesis of J. Kornas [160], which was supervised within the scope of this PhD thesis. The first version of TOMGRO, developed by [129], is a model used to simulate growth and development of GH tomatoes based on environmental parameters measured inside the GH, i.e. air temperature, solar radiation and CO_2 concentration. In its initial version, TOMGRO comprised 574 state variables, which is why it was ultimately reduced to five main state variables in the reduced TOMGRO model [190]:

1. Node number for the main stem, N (node);
2. Leaf Area Index, LAI ($\mathrm{m}^2_{\mathrm{leaf}}\,\mathrm{m}^{-2}_{\mathrm{ground}}$);
3. Total plant dry weight, W ($\mathrm{g}_{\mathrm{dry}}\,\mathrm{m}^{-2}_{\mathrm{ground}}$);
4. Total fruit dry weight, W_f ($\mathrm{g}_{\mathrm{dry}}\,\mathrm{m}^{-2}_{\mathrm{ground}}$);
5. Mature fruit dry weight, W_m ($\mathrm{g}_{\mathrm{dry}}\,\mathrm{m}^{-2}_{\mathrm{ground}}$).

The state variables are based on a set of first-order time-dependent differential equations, as in Equation 3.28.

$$\frac{d\mathbf{u}}{dt} = f(\mathbf{u}, \mathbf{p}) \tag{3.28}$$

where the **u** vector contains the input GH microclimate data (temperature, PPFD and CO_2) and the vector **p** the parameters and biological constants.

In order to model the development of tomatoes grown under APV conditions, the state variables' differential equations have to be solved $\left(\frac{dN}{dt}, \frac{d\,\mathrm{LAI}}{dt}, \frac{dW_f}{dt}, \frac{dW}{dt}, \frac{dW_m}{dt}\right)$, being related to photosynthesis,transpiration, nutrient transport and other physiological processes to quantify changes in stems, leaves and fruits, and generally the growth of the whole plant.

The rate of node development, $\frac{dN}{dt}$, is modeled as in Equation 3.29.

$$\frac{dN}{dt} = N_m f_N(T) \tag{3.29}$$

where N_m is the node appearance rate per day and $f_T(T)$ is a function that reduces vegetative development under non-optimal temperatures.

The equation for the time changes in LAI is given in Equation 3.30.

$$\frac{d\text{LAI}}{dt} = \begin{cases} \rho_{\text{plant}}\ \delta\ \lambda(T_d)\ \dfrac{\exp\left[\beta\,(N-N_b)\right]}{1+\exp\left[\beta\,(N-N_b)\right]}\ \dfrac{dN}{dt}, & \text{LAI} \leq \text{LAI}_{\text{max}}, \\ 0, & \text{LAI} > \text{LAI}_{\text{max}} \end{cases} \tag{3.30}$$

where ρ_{plant} is plant density (plants m^{-2}), δ is maximum leaf-area expansion per node ($\text{m}^2_{\text{leaf}}\,\text{node}^{-1}$), $\lambda(T_d)$ is a temperature-reduction function, β is a expo-linear coefficient, N_b is a projection of linear segment of LAI vs. N to horizontal axis and LAI_{max} is the maximum possible LAI.

The above-ground biomass accumulation is computed according to Equation 3.31.

$$\frac{dW}{dt} = \min\left(\frac{dW_f}{dt} + (V_{\text{max}} - p_1)\,\rho_{\text{plant}}\,\frac{dN}{dt}\ ,\ GR_{\text{net}} - p_1\,\rho_{\text{plant}}\,\frac{dN}{dt}\right) \tag{3.31}$$

where GR_{net} is the net above-ground growth rate, p_1 is the loss of leaf dry weight per node after LAI_{max} is reached, and V_{max} is the maximum increase in vegetative tissue dry weight growth per node.

Partitioning of above-ground growth to fruit each day begins at node position N_{FF} and increases asymptotically to a maximum partitioning according to Equation 3.32.

$$\frac{dW_f}{dt} = GR_{\text{net}}\ \alpha_F\ f_F(T_d)\left[1-\exp\left(-\nu(\vartheta)\,(N-N_{FF})\right)\right] g(T_d) \quad \text{if } N > N_{FF} + k_F \tag{3.32}$$

where α_F is the maximum partitioning to fruit, $f_F(T_d)$ is a function to modify partitioning to fruit for mean daily temperature, $\nu(\vartheta)$ is the transition coefficient between vegetative and full fruit growth, $g(T_d)$ reduces growth at high temperatures, and k_F is the development time from first fruit to first ripe fruit.

The transfer of fruit from green to mature stages is given in Equation 3.33.

$$\frac{dW_m}{dt} = D_F(T_d)\,(W_f - W_m) \quad \text{if } N > N_{FF} + k_F \tag{3.33}$$

where $D_F(T_d)$ is the function to describe the rate of fruit development.

Node development N and LAI are solved hourly. Their values are then used at the end of each day to calculate the weights W, W_f and W_m.

In order to apply the model to local APV conditions of the APV GH experiment (presented in Chapter 4), a calibration of the model parameters is necessary. First, all model parameters and their value ranges are summarized from literature. Table 3.4 presents all model parameters and their initial values. The original values are taken from [129]. The parameter ranges were defined based on the literature sources given in the table.

Table 3.4: Reduced TOMGRO model parameters, their original values taken from [129] and [190], and range of variation during the sensitivity analysis.

	Description	Original Value	Range of Variation	Unit
N_m	Node appearance rate per day	0.5 [129]	[0.1–0.9] [191]	node d^{-1}
δ	Maximum leaf area expansion per node	0.038 [190]	[0.010–0.100] [191]	m^2node^{-1}
β	Coefficient in expolinear equation	0.169 [190]	[0.060–0.500] [191]	node^{-1}
N_b	Projection of linear segment of LAI vs. N to horizontal axis	16.0 [190]	[8.0–25.0] [191]	node
LAI_{max}	Maximum leaf area index	4.0 [190]	[±10% of 4.0] [129]	unitless
p_1	Loss of leaf dry weight per node after LAI_{max} is reached	2.0 [190]	[±10% of 2.0] [129]	g node^{-1}
V_{max}	Maximum increase in vegetative tissue dry weight growth per node	8.0 [190]	[2.0–12.0] [191]	g node^{-1}
NFF	Nodes per plant when first fruit appears	22.0 [190]	[4.0 [192]–22.0 [190]]	node
k_F	Development time from first fruit to first ripe fruit	5.0 [190]	[0.5 [193]–5.0 [129]]	node
τ_{CO_2}	Carbon dioxide use efficiency	0.0693 [129]	[0.0100–0.5000] [191]	µmol$m^{-2}s^{-1}$
D	Maximum leaf conductance to water vapor	2.593 [129]	[0.100 [193]–2.600 [190]]	g $m^{-2}h^{-1}$
K	Light extinction coefficient	0.58 [129]	[0.3–0.9] [191]	unitless
m	Leaf light transmission coefficient	0.1 [129]	[±10% of 0.1] [129]	unitless
Qe	Quantum efficiency of photosynthesis	0.0645 [129]	[0.0100–0.5000] [191]	unitless
Q10	Coefficient in maintenance respiration equation	1.4 [129]	[1.4 [190]–1.6 [193]]	unitless
rm	Maintenance respiration coefficient	0.016 [190]	[0.005 [193]–0.016 [129]]	g[CH_2O] g^{-1}[d.w.] d^{-1}
E	Growth efficiency	0.7 [190]	[0.5–0.9] [191]	g[d.w.] g^{-1}[CH_2O]
T_{CRIT}	Critical temperature for photosynthesis decline	24.4 [129]	[17.0–29.0] [191]	°C
α_F	Maximum partitioning of new growth to fruit	0.8 [129]	[0.1–0.8] [191]	d^{-1}
$\nu(\vartheta)$	Transition coefficient between vegetative and full fruit growth	0.135 [129]	[0.050–0.900] [191]	node^{-1}
f_F	Fraction of dry matter allocated to fruits	not specified	[0–1] [190]	unitless

In general, the model is first calibrated and subsequently validated using an independent dataset. In this thesis, the model is calibrated and validated using data obtained during the APV GH experiment presented in Chapter 4. Although the experiment comprised only a single crop cycle, the GH was spatially divided into three shading treatments. Model calibration was therefore performed using data from one shading zone, while the remaining two datasets were reserved for model validation.

A sensitivity analysis of these parameters, using the Extended Fourier Amplitude Sensitivity Test (eFAST) [194], is performed to identify the parameters most sensitive to calibration. The corresponding value ranges for all parameters are also provided in Table 3.4. Following the sensitivity analysis, the Particle Swarm Optimization (PSO) algorithm [195] is then employed to find the set of calibrated model parameters by minimizing the RMSE, as defined in Equation 2.2, between simulated and observed mature fruit dry weights, as this quantity relates to the final yield obtained in the GH. Following the calibration process, the model is validated and compared to the experimentally measured fruit dry weight of the presented APV GH experiment.

Concluding, two approaches for crop yield modeling were presented for the methodology of the model: DLI-based models and FSPMs. The DLI-based modeling approach is divided into two methods; one relying only on radiation data and the other one is an extension that additionally takes into account temperature and RH in the GH. For the FSPM, the application of the reduced TOMGRO model is proposed.

In the two DLI-based methods yield is aggregated over time and described as a relative fraction of the conventional, no APV scenario. The method using solely radiation data is tested and compared against tomato yield data from the APV GH experiment in Section 6.1.1. The DLI-based method extended with temperature and RH data is an approach to additionally take into account GH microclimate and its effect on crop growth and yield. In Section 6.1.2, the resulting yield from the model is compared against the experimentally measured yield from the APV GH experiment.

For the coupling of a FSPM to the irradiance model, the application of the reduced TOMGRO model is proposed. In this thesis, the reduced TOMGRO model is presented using the experimentally measured irradiance and temperature data from the APV GH experiment. In Section 6.2, the simulated dry weight of the tomatoes is compared against experimentally measured dry weight.

4

Agrivoltaic greenhouse experiment

"Experiment is the sole judge of scientific truth."

—Ada Lovelace

This section presents the setup and results of the agrivoltaic greenhouse experiment performed within the scope of this thesis. The objective of the experiment was to monitor crop response to high shading levels and collect microclimate and irradiance data to validate the APV GH simulation framework. The results from this chapter have been published in [43].

Section 4.1 presents the materials and methods of the experimental setup. Section 4.2 describes the experimental results of the shading effects on GH microclimate, plant physiology and crop yield and quality. Section 4.3 presents the discussion of the experimental results in the context of agrivoltaic greenhouse experiments. Section 4.4 includes an economic assessment of the APV greenhouse in terms of expected PV yield and economic profitability.

4.1 Materials and methods of the experimental setup

4.1.1 Greenhouse characteristics

The experiment was conducted during the 2023–2024 tomato growing season in a "raspa y amagado" GH in Almería at Fundación Finca Experimental UAL-Anecoop (36.864° N, −2.282° E, 180 m above sea level), covering a total area of 1765 m^2. Due to their low construction and maintenance costs, "raspa y amagado" GHs are the most common GH type in the Almería region [22]. Figure 4.1 shows the location of the experimental test GH within the Almería region in southern Spain.

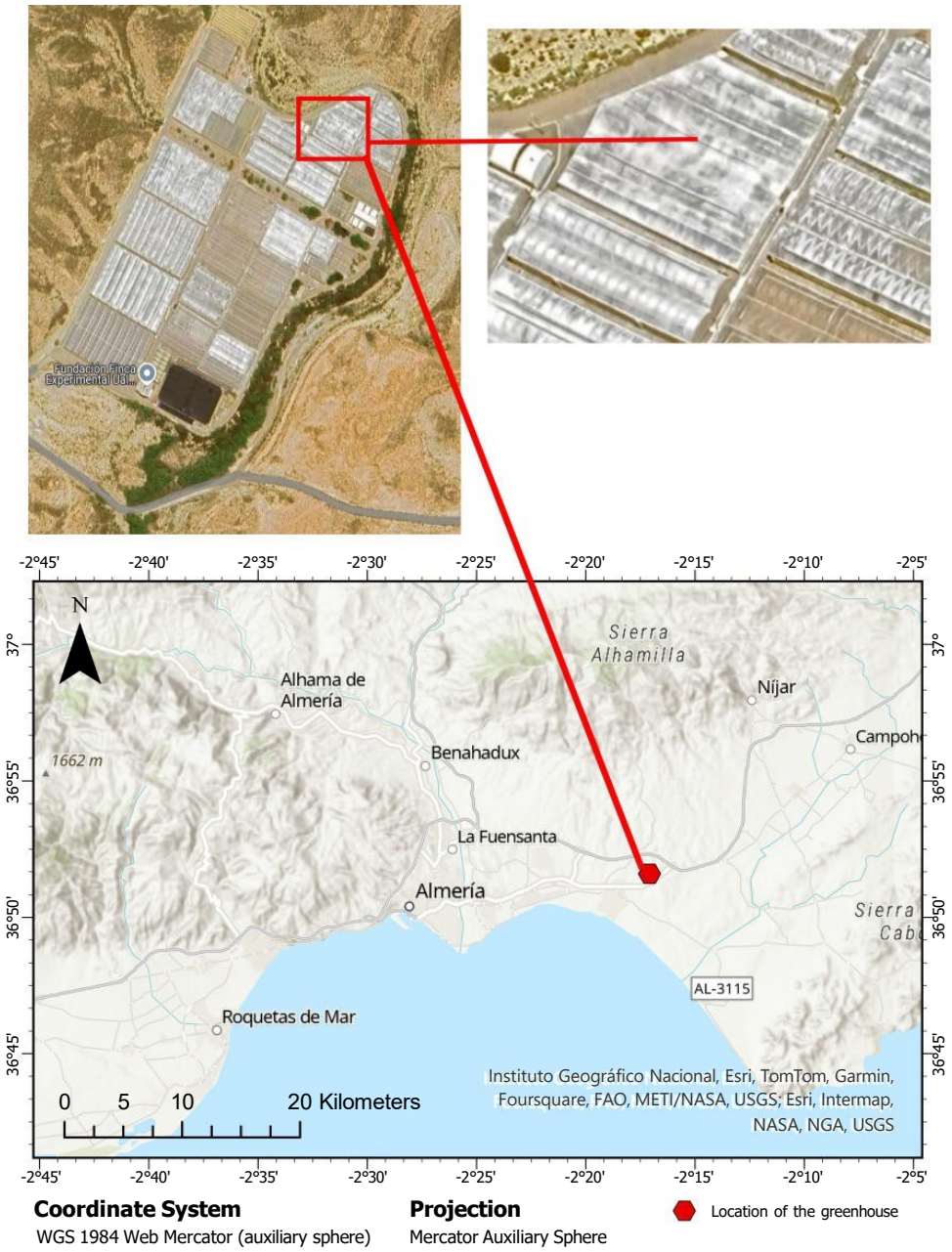


Figure 4.1: Top left: Aerial view of the ANECOOP facilities. Inside the red rectangle: the experimental GH. **Top right**: Closer aerial view of the analyzed GH. (source for both: Google Maps, accessed 14 January 2025). **Bottom**: Overview map of the study area.

The GH structure consists of galvanized steel tubes, featuring a central corridor and two parcels 8 m in width expanding towards each side of the corridor. The roof's lowest points (the corridor) are at a height of 3.4 m, while the highest points at the gables reach 4.5 m. The roof and walls are covered with a multilayered polyethylene film of 200 µm thickness with an 89% light transmission in the 400 nm to 700 nm range. Figure 4.2 shows the experimental GH at the facilities of Fundación Finca Experimental UAL-Anecoop.



Figure 4.2: View over the experimental test GH and the facilities of Fundacion UAL-Anecoop. Image credit: Anna Kujawa (DLR).

The overall GH and crop maintenance, i.e., ventilation, irrigation, fertilization and pest control, was carried out by Fundación UAL-Anecoop (Appendices A.1 and A.2). Passive ventilation was provided by three zenithal windows, each 0.8 m wide and protected with insect-proof nets. These windows were opened when the indoor to outdoor temperature difference exceeded 10 °C according to the common horticultural practices of Fundación UAL-Anecoop. A central irrigation system served the entire GH without separation of the test zones.

The cultivation cycle started with the transplantation of 'Lygalan' tomatoes, a novel variety developed by ANECOOP S.COOP [196], on 14 September 2023. Before transplantation, the tomato seedlings were raised outside the GH in a nursery. Pruning was carried out on 9 January 2024 (115 days after transplantation). The last harvest took place on 15 March 2024 (181 days after transplantation). Figure 4.3 shows two pictures from the day of transplantation of the tomato plants.



Figure 4.3: Top and bottom: Tomato plants on 14 September 2023 after transplantation into the GH. Image credit: Anna Kujawa (DLR).

To mimic the shading effect of PV modules, opaque plastic panels (1.0 m × 1.7 m) were mounted on the roof. Two shaded test zones with 30% and 50% roof cover ratios were compared against a control zone without any shading, as shown in Figures 4.2 and 4.4.

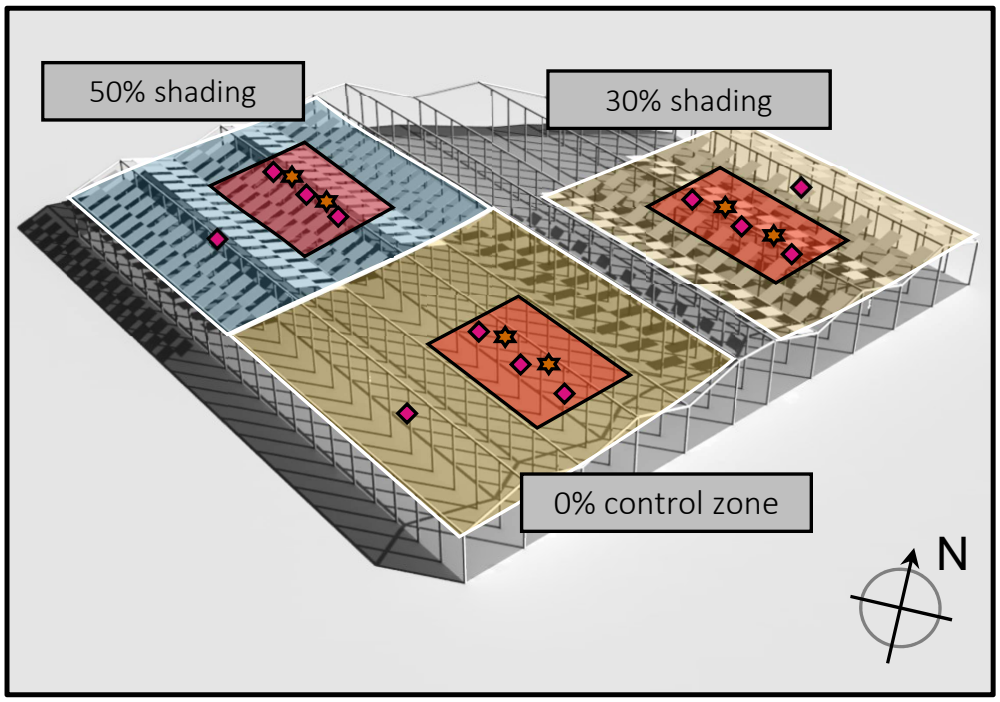


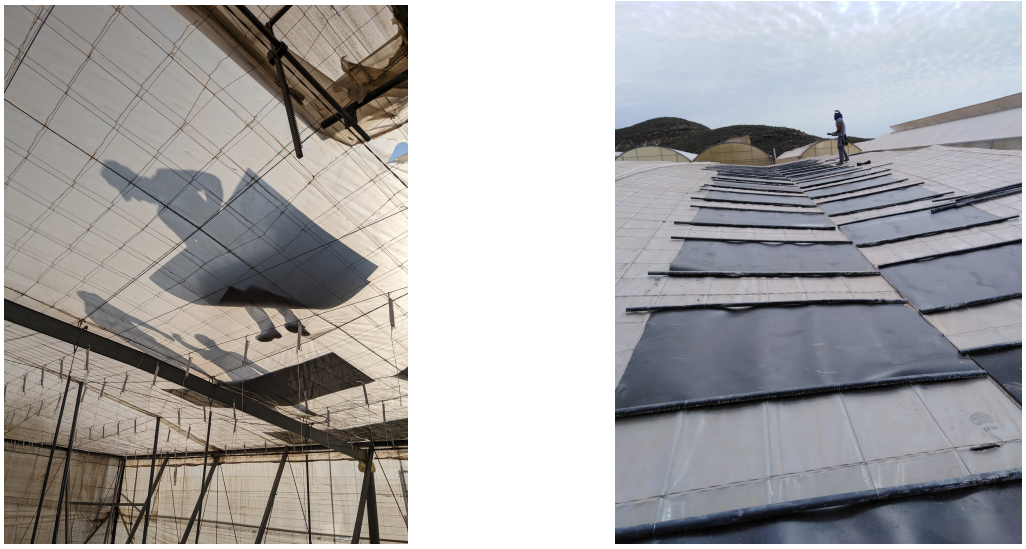
Figure 4.4: Rendering of the experimental GH based on the APV simulation framework presented in Chapter 3. Pink squares: pyranometers. Orange stars: temperature and RH sensors. Red area: measurements of physiological and crop yield parameters.

Based on the 3D GH representation in the irradiance model presented in Chapter 3, the panels were arranged in a checkerboard pattern to improve light homogeneity and to avoid boundary effects and shade overlapping issues throughout the year. In the 50% shading zone, 140 panels were installed (14 per row with 0.56 m gaps between modules), whereas the 30% zone contained 90 panels (9 per row with 1.44 m gaps). Figure 4.5 shows the PV pattern from the inside of the GH, while Figure 4.6 shows two pictures from the mounting of the PV modules.



a) **b)** **c)**

Figure 4.5: Pictures from inside the GH. **a)** Control zone. **b)** 30% shading zone. **c)** 50% shading zone. Image credit: Anna Kujawa (DLR).



a) **b)**

Figure 4.6: The mounting of the opaque polyethylene sheets, mimicking the PV modules, took place on 11 September 2023. **a)** View from inside the GH. **b)** Two lines of modules in the 50% shading zone. Image credit: Anna Kujawa (DLR).

4.1.2 MICROCLIMATE MONITORING SYSTEM

Throughout the experiment, the microclimate parameters GHI, RH and temperature were measured with a temporal resolution of one minute. The location of the different sensors inside the GH is included in Figure 4.4.

In each test zone, three pyranometers were installed at the center of the zones and one pyranometer was placed near the edge of the zones to monitor boundary effects caused by radiation entering from the side walls. Temperature and RH were recorded at two distinct locations in the center of each zone. All microclimate measurement sensors, i.e., four pyranometers, and two temperature and RH sensors per zone, were mounted at a height of 2.8 m above ground, corresponding to the maximum canopy height of the tomato plants during cultivation. The two shading zones and the control zone were not physically separated from one another, which allowed air exchange and partial mixing of their microclimates. Table 4.1 summarizes all microclimate measurement devices. Figure 4.7 presents pictures of the sensors mounted in the GH during different stages of the growing cycle.

Table 4.1: Microclimate measurement devices used in the GH.

Parameter	Unit	Device	Manufacturer
GHI (center)	$W\,m^{-2}$	CMP10	Kipp & Zonen, OTT HydroMet B.V., Delft, Netherlands
GHI (center)	$W\,m^{-2}$	SP110	Apogee Instruments, Logan, United States of America
GHI (boundary)	$W\,m^{-2}$	SPlite2	Kipp & Zonen, OTT HydroMet B.V., Delft, Netherlands
Temperature	°C	RC-51H	Elitech, Greenwich, United Kingdom
Relative Humidity	%	RC-51H	Elitech, Greenwich, United Kingdom



a) b) c)

Figure 4.7: a) Kipp and Zonen CMP10 pyranometer and Elitech RC-51H temperature and RH sensor. **b)** Kipp and Zonen SPlite2 pyranometer. **c)** Apogee Instruments SP110 pyranometer. Image credit: Anna Kujawa (DLR).

4.1.3 PLANT PHYSIOLOGY AND FRUIT QUALITY PARAMETERS

Two categories of measurements were conducted on the plants during the experiment: plant physiological and fruit quality measurements. For each treatment zone, 20 plants were selected within a central, representative area of each GH zone, as indicated in Figure 4.4. Physiological measurements were taken weekly between 16 October 2023 and 9 January 2024, when the plants were pruned. Table 4.2 summarizes all measured plant physiological parameters.

Table 4.2: Measured plant physiological parameters.

Parameter	Unit	Device/Method
Height of stem 1	cm	Measuring tape
Height of stem 2	cm	Measuring tape
Number of branches	–	Visual count
Number of leaves for stem 1	–	Visual count
Number of leaves for stem 2	–	Visual count
Trunk diameter of stem 1	mm	Digital caliper
Trunk diameter of stem 2	mm	Digital caliper
Distance between leaves in apical part	cm	Measuring tape
Distance between developed clusters in apical part	cm	Measuring tape
Number of fruits	–	Visual count

In addition, fruit quality measurements were performed at each harvest date, beginning on 18 January 2024 (125 days after transplantation) and ending on 4 March 2024 (171 days after transplantation). The harvest dates were 18 January, 30 January, 7 February, 20 February, 26 February and 4 March 2024.

Immediately after harvesting, fruits from each repetition were washed and examined. Fruit firmness was measured using a digital fruit penetrometer. Then, fruits were cut in half and total width and length and flesh wall thickness were determined. The solid matter content, expressed as °Brix, was determined by squeezing out some drops of liquid from the halves and adding them to a refractometer according to the AOAC method no. 932.12 [197]. In addition, for six selected plants per treatment zone, fresh and dry weight of the harvested fruits were determined. For dry weight, the cut-in-halves tomatoes were dried in a drying oven at 70 °C for five days. If the samples still contained liquid after five days, they were kept an additional day in the oven. Table 4.3 summarizes the measured parameters.

Table 4.3: Measured fruit quality parameters.

Parameter	Unit	Device	Manufacturer
Fruit width and length	mm	Digital caliper	–
Flesh wall thickness	mm	Digital caliper	–
Fruit firmness	kg/cm^3	Digital fruit penetrometer (model 4105)	STEP Systems, Nürnberg, Germany
Soluble Solids Content	°Brix	Pocket Refractometer PAL-1	ATAGO, Saitama, Japan
Fresh weight	g	NewClassic ML scale	Mettler Toledo, Gießen, Germany
Dry weight	g	Universal drying oven	Memmert, Schwabach, Germany

4.2 EXPERIMENTAL RESULTS OF THE AGRIVOLTAIC GREENHOUSE

This section presents the microclimate, plant physiological and fruit quality measurements for the experiment performed in 2023/2024.

4.2.1 SHADING EFFECT ON MICROCLIMATE

4.2.1.1 IRRADIANCE

The pyranometers in the GH monitored GHI throughout the study period. In this section, the data from the CMP10 pyranometers are presented as a representative example for all irradiance measurements. Figure 4.8 shows the daily mean PPFD, estimated from GHI according to the method presented in Section 3.2.1, as well as the relative fraction of the 30 and 50% zones with respect to the control zone.

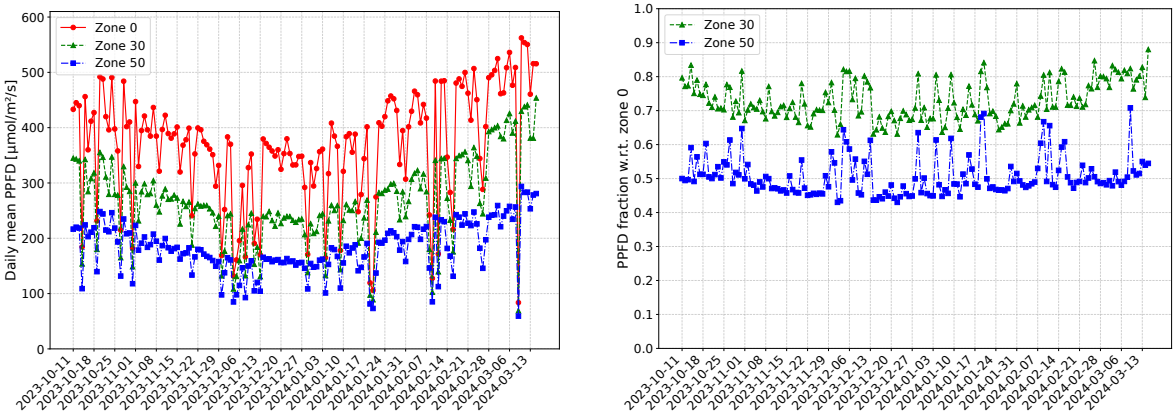


Figure 4.8: a) PPFD values in the three zones. The daily mean of the CMP10 pyranometer of each zone is presented. **b)** PPFD fraction in the 30% and 50% shading zones with respect to the 0% control zone.

The daily average PPFD measurements show that irradiance decreased in the winter months and increased again towards the end of the crop cycle in March 2024 in all three zones. The lowest consecutive irradiance values were monitored during December 2023 with values below 150 $\mu mol\,m^{-2}\,s^{-1}$ for the control zone, below 110 $\mu mol\,m^{-2}\,s^{-1}$ for the 30% shading zone and below 90 $\mu mol\,m^{-2}\,s^{-1}$ for the 50% shading zone. The highest PPFD values were reached in March 2024 with values of up to 600 $\mu mol\,m^{-2}\,s^{-1}$ for the control zone, 490 $\mu mol\,m^{-2}\,s^{-1}$ for the 30% shading zone and 300 $\mu mol\,m^{-2}\,s^{-1}$ for the 50% shading zone. Low PPFD values in all three zones on the same day could be identified throughout the entire crop cycle and were mostly caused by cloudy and rainy conditions at the test site.

The daily light integral (DLI) can be calculated by integrating the PPFD over 24 hours according to Equation 2.1 [64]. Tomatoes are classified as high-light demanding crops, requiring DLI levels between 30 mol m^{-2} d^{-1} and 15 mol m^{-2} d^{-1} for sufficient crop growth according to [161]. Figure 4.9 shows the DLI in the three zones from 11 October 2023 to 15 March 2024.

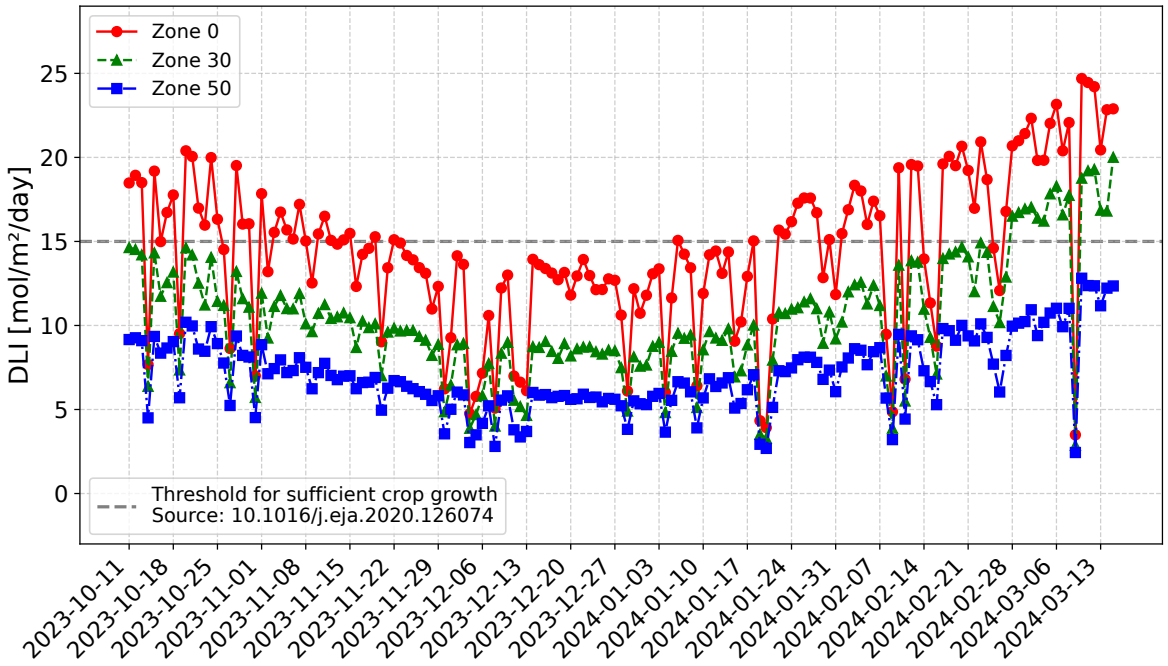


Figure 4.9: DLI values calculated from the PPFD of the CMP10 pyranometers in each zone. The dashed line refers to the threshold for sufficient crop growth taken from [161].

The overall trend of decreasing DLI towards the winter months and increasing DLI towards the ripening stage of the fruits in March is visible in all zones. The 0% control zone exceeded 15 mol m^{-2} d^{-1} on clear sky days until November 2023. After December 2023, the 0% zone shows an increasing trend. In the months January to March 2024, a few days fell below the threshold again due to cloudy weather and therefore reduced radiation levels at the test site. The DLI values of the 30% zone already fell below 15 mol m^{-2} d^{-1} from October 2023. Starting from the end of February 2024, the overall trend in the DLI values of the 30% zone is above the threshold. The values of the 50% zone remained constantly below the threshold for the entire study period.

Throughout the study period, radiation levels were reduced on average by 48% in the 50% zone and 25% in the 30% zone. This slight decrease with respect to the theoretical shading reduction of the 30% zone was caused by the orientation of the GH and the positioning of the zones. For comparison, the study of [126] indicated that the annual global radiation decreases by 0.8% for each additional 1.0% of PV panels located in a roof-top PV GH. As we only compare two shading zones against the control zone, we do not present a general linear regression for the radiation reduction. In the presented study, each 1% of additional shadowed area caused a 0.83% (30% zone) or 0.96% (50% zone) decrease in PAR according to the measurements, which aligns well with the observations of [126].

4.2.1.2 TEMPERATURE AND RELATIVE HUMIDITY

In the following subsection, the experimentally measured temperature and RH are analyzed. Optimal growing conditions for tomatoes are sunny weather with constant temperatures between 20 °C and 25 °C [198]. Fruit quality is strongly influenced by temperature. High temperatures together with high RH promote diseases [198]. Increased temperatures due to projected climate change might therefore affect crop yield due to a reduced fruit set and changes in fruit quality [199]. Hence, APV systems with reduced temperatures below the PV panels might be beneficial for GH temperature control in future scenarios. Figure 4.10 shows the diurnal mean temperature and RH, calculated between sunrise and sunset of each day, and the temperature and RH difference with respect to the control zone. The mean of the two sensors per zone is presented.

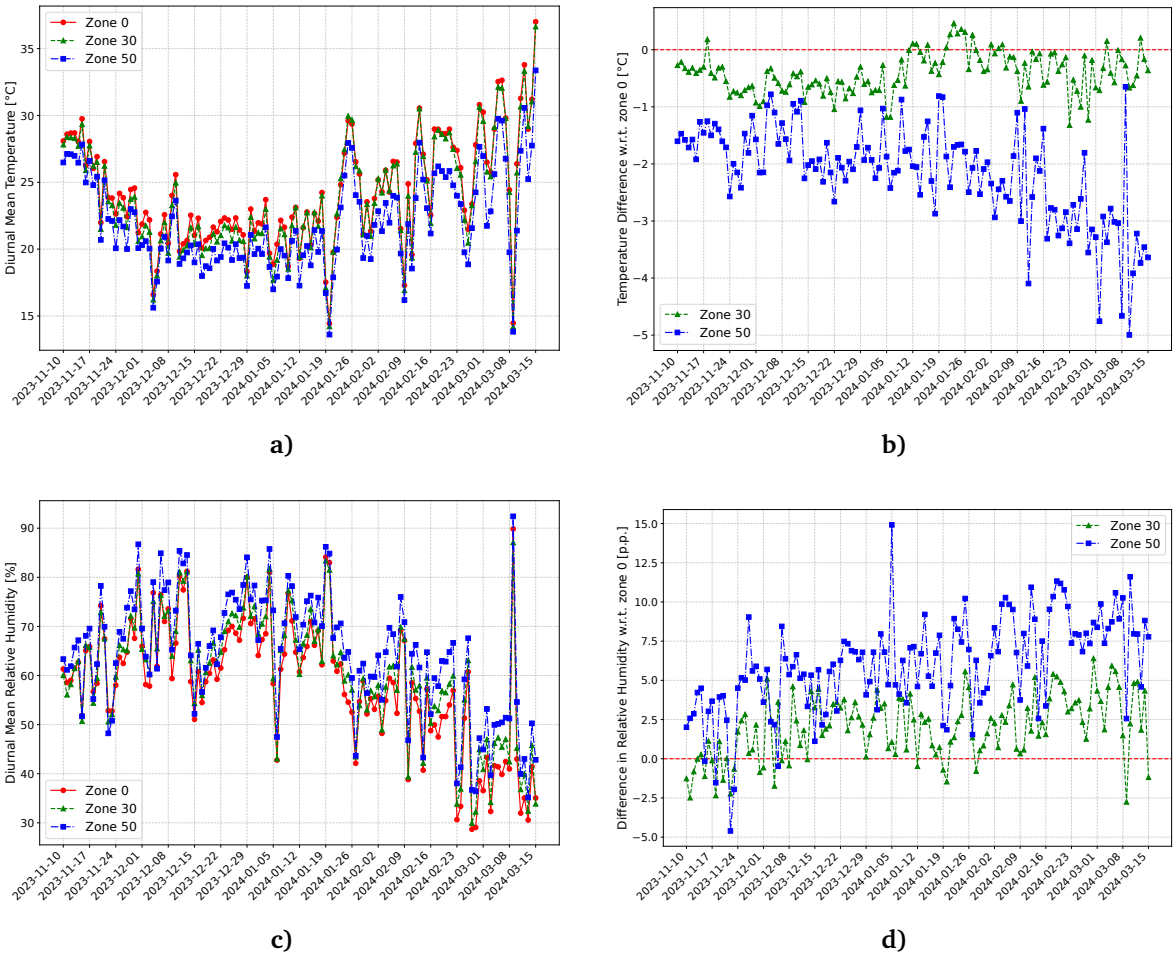


Figure 4.10: **a)** Diurnal mean temperature in the three zones calculated between sunrise and sunset of each day. **b)** Temperature difference with respect to the 0% control zone. **c)** Diurnal mean RH in the three zones. **d)** RH difference with respect to the 0% control zone.

The evolution of temperature in the GH shows a decreasing trend among all zones from the start of the study period towards the winter months followed by a temperature increase towards the end of the study period. At the beginning of the study period, the temperature values exceeded 25 °C in all three zones. The lowest temperature measurements were

recorded at the end of December 2023, with values below 12 °C in the 50% shading zone. Starting from January 2024 the mean diurnal temperature values increased again in all zones and the highest measured values were obtained at the beginning of March 2024 with values above 35° in both the 0% and 30% zone. On average for the entire study period, the mean temperature values were 24.2 °C for the control zone, 23.8 °C for 30% shading and 23.0 °C for 50% shading.

The differences in temperature with respect to the control zone show that temperature values in the 50% zone were consistently lower than in the unshaded control zone with an increasing trend towards the end of the study period. On average, the diurnal mean temperature in the 50% zone was 2.2 °C lower than in the control zone throughout the study period. The temperature measured in the 30% shading zone behaves similarly to the measurements in the control zone. On average, the diurnal mean temperature in the 30% zone was 0.4 °C lower than in the control zone.

RH generally increased during the colder months and declined as temperatures rose towards spring. On average for the entire study period, 58.5% RH was measured in the control zone, 60.5% in the 30% shading zone and 64.5% in the 50% shading zone. Looking at the difference in RH with respect to the control zone, the data shows that in both shading zones an increase in diurnal mean RH values was observed except from few days at the beginning of the study period. The measured RH in the 30% zone was on average 2.0 percentage points (p.p.) higher than in the control zone. For the 50% zone, the measured RH was on average 6.0 p.p. higher than in the control zone.

Figure 4.11 shows the tomato plants in the GH during different stages of the growing cycle.

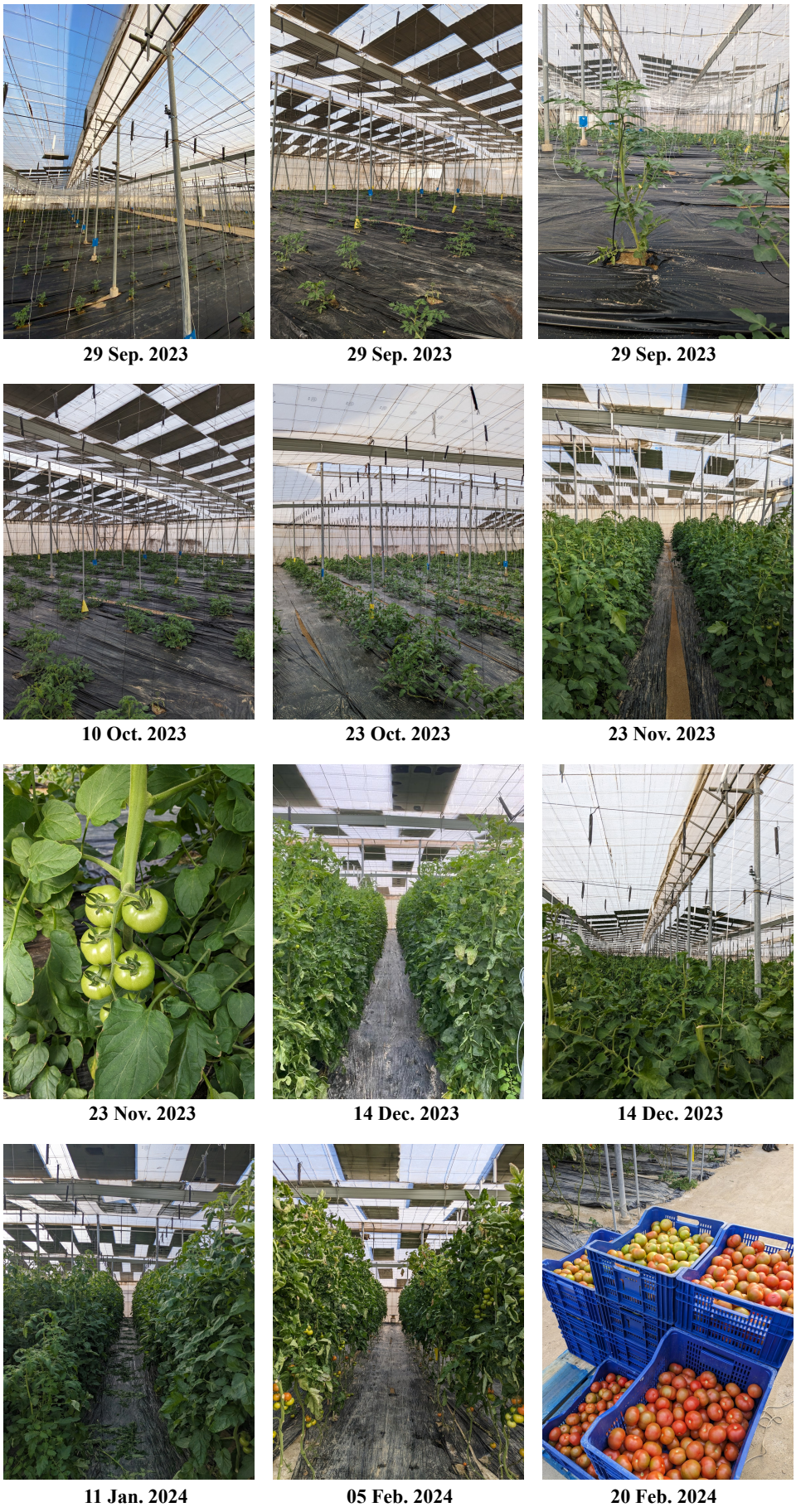


Figure 4.11: Pictures from the APV GH during different stages of the tomato growing cycle. Image credit: Anna Kujawa (DLR).

4.2.2 CROP YIELD

This section presents the fresh and dry weight measurements of the investigated fruits. Fresh weight and dry weight are mathematically related through the moisture content of the tomato samples, but both quantities serve distinct purposes. Fresh yield represents the marketable yield, which will be critical to evaluate the economic viability of the APV GH. Dry weight represents total biomass without variability due to water content. Dry weight of the fruits can be linked to photosynthetic efficiency, nutrient uptake, environmental conditions and overall plant growth. Additionally, dry weight data was required for parameterization and validation of the reduced TOMGRO model used presented in Chapter 6.

The tomato plants were distributed with a density of 2 plants per m^2 in the GH; hence, absolute weight measurements of the single fruits were normalized to $g\,m^{-2}$. Figure 4.12 presents the accumulated fresh weight measurements and the measurements for the different days of the harvest as well as the relative and the absolute deviation from the control zone.

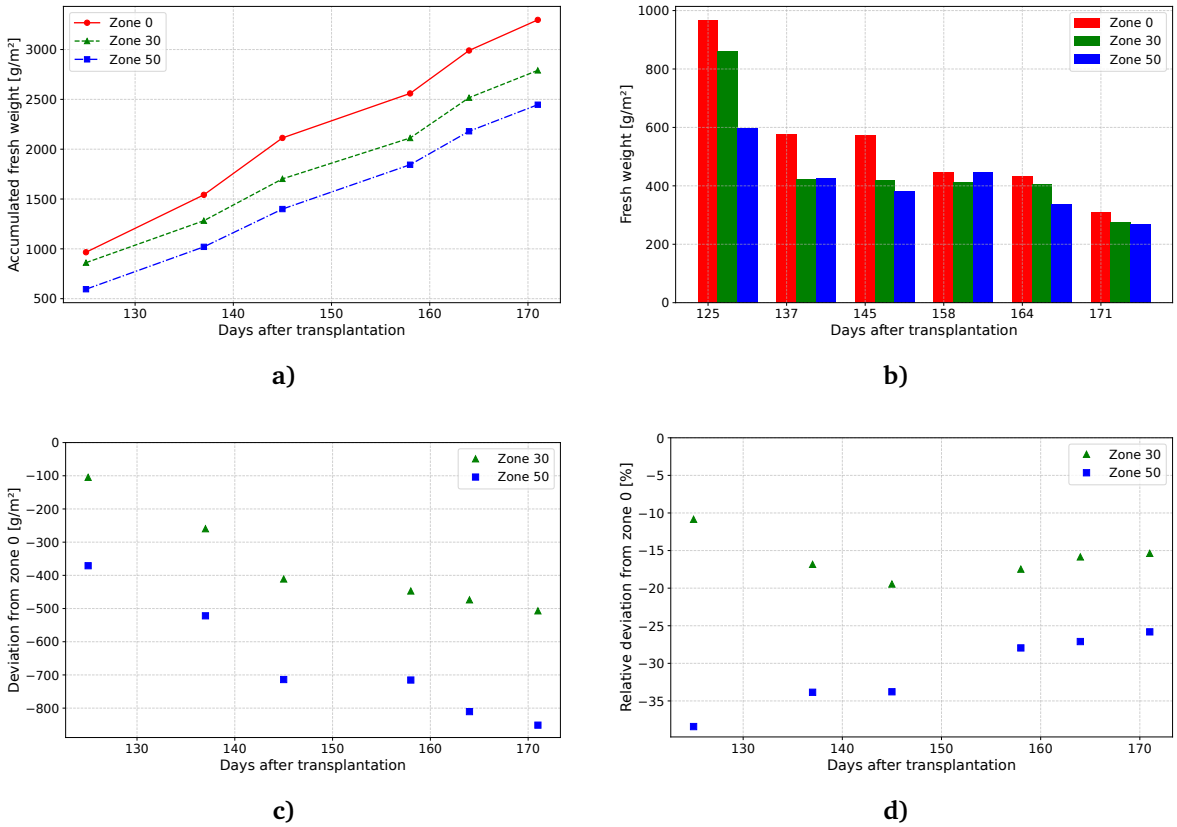


Figure 4.12: a) Accumulated fresh weight of collected tomato fruits for the three zones as a function of the time after transplantation. **b)** Fresh weight measurements on the specific days for the three zones. **c)** Absolute deviation in accumulated fresh weight of the two shading zones with respect to the control zone. **d)** Relative deviation in accumulated fresh weight of the two shading zones with respect to the control zone.

The highest accumulated fresh weight of mature tomato fruit was measured in the control zone throughout the harvesting period. The relative difference in fresh weight between the control zone and both shaded zones progressively decreased, thus indicating a potential

delay in ripening due to shading. By the end of the harvest, the control zone accumulated the highest fresh weight at 3298 g m^{-2}, followed by the 30% shading zone with 2791 g m^{-2} and 2446 g m^{-2} measured in the 50% shading zone. Compared to the control zone, a 15% yield reduction was measured in the 30% shading zone with a difference of 507 g m^{-2}. For the 50% shading zone, a 26% yield reduction (851 g m^{-2}) was recorded with respect to the control zone on the final day of harvest. The highest relative deviation between fresh weight in the shaded zones and fresh weight in the control zone was already measured on the first day of harvest in January 2024. Overall there is a decreasing trend in relative deviation for the 50% zone. The numbers align with the study of [88], who investigated the effect of aluminised shading screens on tomato production in a commercial "raspa y amagado" GH in Almería. By applying different shading ratios above 30%, they demonstrated a proportional decrease in total yield with increasing shading intensity. The study of [200] analyzed the effect of reductions in PAR on tomato yield and quality due to artificial shading. They also observed lower values of tomato yield under lower PAR levels compared to full natural sunlight. They found that a 30% and 50% reduction in incoming PAR led to a 14.3% and 38.1% reduction in tomato yield, respectively.

In addition to fresh weight of the mature fruits, the dry weight was also monitored to trace back the shading effect on the quality of the fruits. Figure 4.13 presents the dry weight of mature tomato fruit across the three different shading zones.

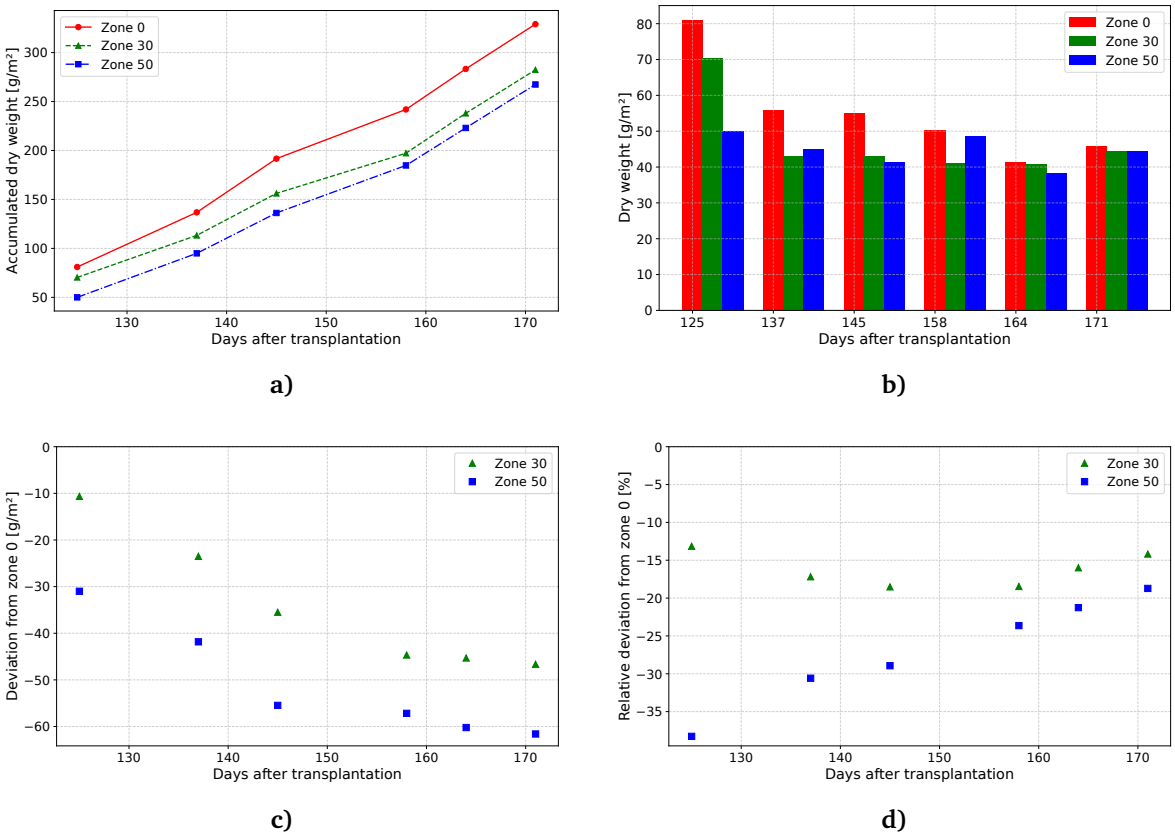


Figure 4.13: a) Accumulated dry weight for the three zones as a function of the time after transplantation. **b)** Dry weight measurements on the specific days for the three zones. **c)** Absolute deviation in accumulated dry weight of the two shading zones with respect to the control zone. **d)** Relative deviation in accumulated dry weight of the two shading zones compared to the control zone.

At the end of the growing season, the highest dry weight was measured in the control zone with an accumulated total value of 330 $g\,m^{-2}$. In the 30% shading zone 282 $g\,m^{-2}$ were measured and in the 50% shading zone 267 $g\,m^{-2}$ were measured. The 30% zone had therefore an overall yield reduction in dry weight of 46 $g\,m^{-2}$ with respect to the control zone, which is equivalent to a 14% reduction. For the 50% shading zone, the overall reduction in dry weight with respect to the control zone was determined to be 61 $g\,m^{-2}$ at the end of the crop cycle, which is approximately 19% less yield. Similar to the observations in the fresh weight measurements in Figure 4.12, the largest relative deviation in dry yield was already observed at the first day of harvest. On the first harvest day, the control zone exhibited the highest yield with 81 $g\,m^{-2}$ in dry weight. On that day, 12% less dry weight was measured in the 30% zone and 38% less in the 50% zone compared to the control zone. Towards the end of the study period, this relative difference decreases in both shading zones.

4.2.3 Plant physiology and fruit quality

In the presented experiment, differences in the development of the tomato plants were visible early in the growing stage. This aligns with the findings of [165] who showed that plant growth and productivity are directly correlated with the light intensity and environment temperature in the GH. The figures of the plant physiological measurements listed in Table 4.2 are collectively summarized in Appendix B. On average for the entire growing period, the plants in the 50% shading zone were 38 cm higher with a 0.6 mm smaller diameter of the trunk (see Figures B.1–B.4). The plants had on average 5.1 more leaves than the plants in the control zone (Figures B.7 and B.8). For 30% shading, the plants were on average 9 cm higher with a 0.2 mm smaller trunk diameter and had 5.0 more leaves for the whole growing period (see Figures B.1–B.4, B.7 and B.8).

In addition to plant physiology, fruit quality was determined by measuring fruit width and length, flesh wall thickness, fruit firmness and SSC [°Brix] (as described in Table 4.3) of the single harvested fruits for each date of measurement during the harvest period. Since the SSC is a particularly interesting variable to assess the quality of tomatoes, it will be investigated in more detail in what follows. The mean SSC values alongside the sample standard deviations are depicted in Figure 4.14 for all harvested fruits among the zones. The figures of the other fruit quality parameters are collectively summarized in Appendix B.2.

In general, all zones show an increase in SSC towards the end of the harvest period, as later-harvested fruits grow higher on the plant and receive more irradiance throughout the growing period. The fruits taken from the 50% shading zone show on average an absolute reduction of 0.6 °Brix compared to the fruits of the control zone throughout the entire harvest period, which corresponds to an average reduction of 11%. On the last measurement day, the fruits of the 50% zone show an absolute reduction of 1.0 °Brix compared to the control zone. The fruits of the 30% shading zone follow a similar trend as the 50% zone; however, an increase in SSC towards the end of the harvest period is notable. On average, a reduction of 3% in SSC was observed throughout the harvest period. On the last day of harvest, the fruits of the 30% zone had a reduction of 0.4 °Brix compared to the control zone. These observations align well with the study of [40], who

found that shading levels over 30% decreased the SSC in the investigated tomato crop in comparison with the control treatment for a "Venlo" GH in Almería. In the study of [88], the measured SSC of tomato crops was decreased for shading ratios above 40%. Furthermore, other studies showed that the SSC of tomatoes can increase slightly with increasing temperature, which might have a positive influence on the flavor of the crops [165, 172].

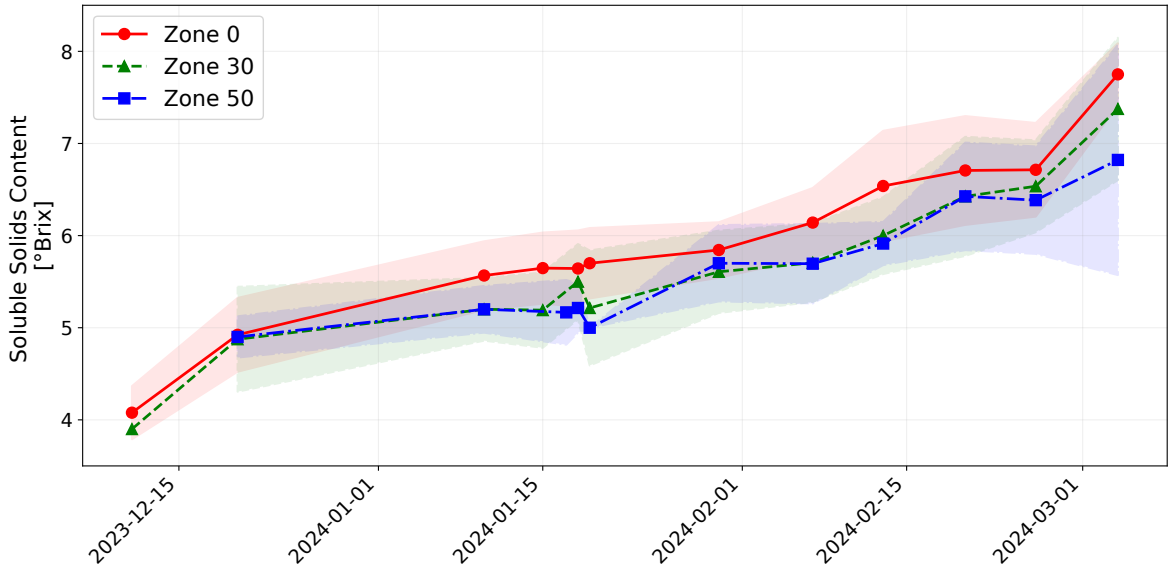


Figure 4.14: Soluble Solids Content of the measured tomato fruits. The average values of the measured fruits per zone are presented as lines while the respective standard deviations are shown as shaded regions.

Similar to the observed trend of an increase in SSC for the fruits of the 30% shading zone, the fruits also showed an increase in firmness towards the end of the harvest period and a similar behavior compared to the fruits of the control zone could be observed (see Figure B.13). These observations are also in agreement with the previous study of [88] who showed that shading over 40% increases the firmness of the fruits. In the study of [40], it was also observed that with shading levels over 30% an increase in firmness compared to the control treatment can be expected. In addition, different studies observed a decrease in the proportion of larger fruits and an increase in the proportion of smaller fruits at 50% shading [200, 162].

Since both the plant physiology as well as the fruit quality parameters were measured from a set of representative plants in each zone, a statistical compatibility analysis was performed to complement the above comparison of the mean parameter values in the different zones. The measurement samples in the different zones were compared on the last day of measurements with a Welch's t-test (allowing for unequal variances of the two compared populations) with a standard significance threshold value of $\alpha = 0.05$.

Table 4.4 summarizes the means and standard deviations for all plant physiology and fruit quality parameters on the last day of measurement as well as the *p*-values for the compatibility of 30% shading to the reference zone and 50% shading to the reference zone. The 50% shading zone shows significant deviations from the reference zone for almost all parameters, except for the distance between branches, the number of fruits and the fruit firmness. The only significant deviations in the 30% shading zone are determined to be the height of stem 2, the number of leaves in stem 2 and the fruit firmness.

Table 4.4: Overview of mean and standard deviation values of the measured plant physiological and fruit quality parameters on the last date of measurement. The last two columns represent the *p*-values for the null hypothesis that the measured values in the 30 and 50% zones are compatible with the measurements in the control zone ($\alpha = 0.05$).

		0% Shading	30% Shading	50% Shading	*p*-Value 30	*p*-Value 50
Plant physiology						
Height stem 1	(cm)	270.8(144)	281.1(172)	296.1(124)	0.052	1.1×10^{-6}
Height stem 2	(cm)	251.2(222)	284.4(260)	269.3(306)	1.5×10^{-4}	0.045
Trunk diameter stem 1	(mm)	15.4(13)	15.2(13)	13.7(13)	0.62	3.1×10^{-4}
Trunk diameter stem 2	(mm)	15.4(11)	15.0(8)	14.0(11)	0.22	4.7×10^{-4}
Number of branches		21.8(16)	21.6(19)	18.5(14)	0.73	5.1×10^{-8}
Distance branches	(cm)	15.6(50)	15.8(39)	14.8(28)	0.93	0.59
Number of leaves stem 1		36.1(33)	37.5(31)	38.6(26)	0.17	0.01
Number of leaves stem 2		32.3(47)	38.3(31)	36.4(33)	4.8×10^{-5}	0.003
Distance leaves	(cm)	5.8(17)	6.8(18)	8.5(17)	0.12	5.9×10^{-5}
Number of fruits		34.8(45)	36.1(31)	32.9(43)	0.30	0.20
Fruit quality						
Fruit diameter	(mm)	52.6(25)	51.8(36)	48.1(50)	0.58	0.01
Flesh wall thickness	(mm)	5.8(5)	5.5(7)	5.0(7)	0.29	0.004
Fruit firmness	($kg\,cm^{-3}$)	3.4(4)	3.9(5)	3.3(7)	0.02	0.54
Soluble Solids Content	(°Brix)	7.8(3)	7.4(7)	6.8(12)	0.14	0.02

4.3 Discussion of the agrivoltaic greenhouse experiment

The artificial shading in the presented experiment not only caused a radiation reduction but directly impacted the microclimate in the GH. Therefore, the development of the cultivated tomato plants was affected early on from the beginning of the crop cycle. Over the entire study period, there was an average reduction of 48% in radiation in the 50% shading zone, and a 25% reduction in the 30% shading zone in comparison to the control zone. These findings align well with the radiation reductions determined by [126], who indicated a radiation reduction of 0.8% for each additional 1.0% of PV shading.

The provided shading in the experiment resulted in 15% yield reduction for the 30% shading zone and 26% yield reduction for the 50% shading zone in measured fresh weight at the end of the crop cycle. These numbers align well with the findings of [88] and [200], who both reported a similar decrease in yield with an increase in shading ratio. Several other experimental studies also confirm that high shading levels lead to reduced tomato yield in GHs due to radiation reduction [162, 201, 39, 202, 203, 40].

Nevertheless, it is important to point out that tomato yield is not an isolated characteristic and depends on the growth of the whole plant [165]. If the tomato plant does not grow well then it will never give a high yield. Therefore yield is determined by the interaction between plant morphology, physiology and growth conditions.

In the presented experiment, the two shading zones and the control zone were not physically separated from one another. Hence, there was an exchange in air flow between the zones and no separation of temperature or RH within the different areas in the GH. Nevertheless, changes in temperature and RH were measured at the sensor locations at the center of the zones. The combination of changes in temperature and RH and reduction in irradiance directly affected the tomato plants at each stage of their development. In the presented experiment, differences in the development of the tomato plants were visible early in the growing stage, as the plant physiological measurements confirmed. These observations align well with the findings of [165], who showed that plant growth and productivity are directly correlated with the light intensity and environment temperature in the GH, which affect two important physiological processes: photosynthesis and respiration. Photosynthesis depends on both light intensity and temperature, while respiration only depends on temperature. Therefore, final yield and sugar content depend on the trend of these two physiological processes [203].

It was observed that plants from both shading zones developed on average 20% less fruits than the plants in the control zone throughout the entire crop cycle. Furthermore, a delay in ripening of the fruits was determined for both shading treatments, i.e., 6 days for 30% shading and 9 days for 50% shading after the first harvest in the control zone. Previous studies also showed that shading in GHs caused by PV panels reduces the number of produced fruits and causes a delay in ripening [162, 204, 205]. A delay in ripening and a delayed tomato harvest can actually have strategic market advantages, especially if it shifts production into a period of lower supply and higher prices. The study of [206] analyzed price trends in GH tomatoes across several Spanish regions and found that the highest seasonal price indices occurred in March and April. By strategically timing the delay in yield in an APV GH to coincide with periods of reduced supply and higher selling prices, growers could potentially compensate yield reductions resulting from the shading.

Apart from their influence on plant physiological development and yield, the effect of shading treatments on tomato quality, fruit size and dry matter content was also determined. At the end of the crop cycle a reduction in dry weight of 14% and 19% was observed for the 30% and 50% shading zones, respectively. In addition, for the fruits of the 50% shading zone, a reduction of 0.9 °Brix was measured at the end of the crop cycle. For the fruits of the 30% shading zone, a reduction of 0.2 °Brix was observed. SSC is an important quality parameter considering that the amount of sugar and acid and their interactions are related to flavor quality in tomatoes [207]. According to [79], SSC is highly affected by the GH microclimate and environment including solar radiation, temperature, day-length, water availability, soil mineral content, irrigation and fertilization.

4.4 Economic assessment

The installation of PV modules on GHs has several economic advantages. The key benefit of APV systems is the dual-land-use, i.e. agricultural activity and producing energy at the same time. Firstly, the electricity generated by the PV system can be used to cover the energy demand of the GH. Secondly, surplus energy can be sold to the grid. This way, APV systems stabilize the income of growers and reduce dependence on fluctuating crop and energy market prices.

4.4.1 Electricity self-consumption and grid feed-in during the winter tomato growing cycle

This section provides an estimation of the potential economic benefits from self-consumption and energy sales that can be expected for a winter crop cycle from September to March, similar to the tomato crop cycle conducted in the experiment of Chapter 4. The estimations are based on simplified assumptions and are not intended as a detailed economic analysis. Rather, they offer an initial indication of how APV systems can overcompensate crop yield reductions, which were experienced during the tomato growing cycle in the experiment. The here presented numbers were previously published in [43].

For the economic evaluation, we assume the same 1765 m^2 GH as in the experiment, as this a typical commercial-scale GH of the Almería region, and consider three hypothetical scenarios: (1) no PV modules installed, (2) 30% of the roof covered with PV modules, and (3) 50% of the roof covered with PV modules. Crop and PV yield values are scaled to per square meter GH area for each of the three scenarios.

Based on the crop yield measurements of the 0% shading zone, the tomato yield of the 1765 m^2 GH without PV installation is 5820 kg. The experiment was conducted during the winter months, from September to March, when natural light levels were already low for the reference zone without PV. Consequently, light availability in the two shaded zones was even lower, leading to a reduction in crop yield toward the end of the growing cycle. According to the measurements of the two shading zones, the applied shading treatments resulted in a 15% crop yield reduction for the 30% shading zone and 26% reduction for the 50% shading zone. This corresponds to approximately 895 kg less tomatoes for the 30% APV GH and 1504 kg less tomatoes for the 50% shading scenario. At a market price for tomatoes of 0.58€ kg^{-1} for the 2023–2024 campaign [208], the traditional GH without PV would have led to an income of 1.91€ m^{-2} by solely selling the tomatoes after the seven months of the growing cycle. The reduction in crop yield in the two APV scenarios would have resulted in 1.62€ m^{-2} and 1.42€ m^{-2} for 30% and 50% shading respectively.

To estimate the PV yield of the two APV systems (30% and 50% roof coverage of the entire GH roof), the PVGIS SARAH radiation database was used [61]. The breakdown of the monthly PV yield, as well as monthly prices for electricity are given in Table 4.5. For the winter period from September to March, the estimated energy production was 32.44 kWh m^{-2} for the 30% shading scenario and 54.07 kWh m^{-2} for the 50% shading scenario, assuming standard silicon modules and default system losses according to the PVGIS default parameters. The energy consumption of the GH during the seven months of the tomato cycle was approximately 1.17 kWh m^{-2} according to internal information provided by Fundacíon UAL-Anecoop.

For the economic analysis, we assume the same energy consumption for all three scenarios. Based on average Spanish electricity prices from September 2023 to March 2024 [209, 210], self-consumption of PV electricity to cover the GH's energy demand during the tomato cycle could therefore save around 9.3 ct m^{-2}, which means approximately 165 € in both APV scenarios.

To account for installation-related costs when evaluating revenues from excess PV electricity, the levelized cost of electricity (LCOE) was subtracted from the applicable feed-in electricity price. The LCOE for the PV systems was estimated as 5.2 ct kWh^{-1}, based on the findings for rooftop PV from [211] for the irradiation level of the site of this study. This resulted in a levelized net selling price, which was used in the economic assessment of surplus PV energy exported to the grid. For electricity self-consumption, the LCOE was not subtracted from the electricity price as the energy demand of the GH only corresponds to 3% and 6% of the total PV yield for 30% and 50% shading respectively.

Table 4.5: Monthly prices for electricity consumption, electricity feed-in tariffs and the levelized prices corrected with the levelized costs of electricity. The PV yields for the 30% shading scenario and the 50% shading scenario are given as well as the consumption of the GH. The savings due to self-consumption and the revenues from the two PV systems are calculated.

	Days	Electricity Price [209, 210] [ct/kWh]	Feed-In Price [212, 213] [ct/kWh]	Levelized Price [211] [ct/kWh]	PV Yield 30% [60] [kWh/m²]	PV Yield 50% [60] [kWh/m²]	Consumption [kWh/m²]	Saving Self-Cons. [ct/m²]	Revenue 30% PV [ct/m²]	Revenue 50% PV [ct/m²]
09/2023	14	11.2	10.3	5.1	3.44	5.74	0.09	1.02	17.22	29.00
10/2023	31	10.4	9.0	3.8	6.19	10.32	0.20	2.10	22.82	38.58
11/2023	30	8.0	6.3	1.1	4.75	7.91	0.19	1.53	5.21	8.84
12/2023	31	8.5	7.2	2.0	4.45	7.42	0.20	2.10	8.55	14.56
01/2024	31	8.6	7.4	2.2	4.79	7.99	0.20	2.10	10.14	17.22
02/2024	29	5.0	4.0	−1.2	5.35	8.92	0.19	0.96	−6.17	−10.48
03/2024	15	3.4	2.0	−3.1	3.46	5.77	0.10	0.34	−10.65	−18.02
Sum	181	–	–	–	32.43	54.07	1.17	9.15	47.12	79.70

To calculate potential revenues from selling excess electricity, average feed-in tariffs during the study period [213, 212] were considered. For the 30% shading scenario, the overall energy sales would therefore yield approximately 0.47 € m^{-2}, while for the 50% shading scenario, the selling of the excess PV energy would yield about 0.80 € m^{-2}. Table 4.6 summarizes the comparison of the calculated PV and crop yield revenues per square meter and estimates the overall profit increase for the two APV scenarios.

Table 4.6: Overview for the economic analysis.

		0% PV	30% PV	50% PV
Crop yield	kg/m^2	3.30	2.79	2.45
Crop revenue	$€/m^2$	1.91	1.62	1.42
PV yield	kWh/m^2	0.00	32.43	54.07
GH energy consumption	kWh/m^2	1.17	1.17	1.17
Costs energy consumption	$€/m^2$	−0.09	0.00	0.00
Feed-In revenue	$€/m^2$	0.00	0.47	0.80
Total sum	$€/m^2$	1.82	2.09	2.22
Profit increase in comparison to 0% PV			+0.27 $€/m^2$ +14.8%	+0.40 $€/m^2$ +21.8%

In APV GH systems, the revenue generated from the PV installation can serve as a supplementary income and help offset operational costs of the GH such as electricity for climate control, irrigation or lighting. Over time, the APV GH dual-use approach can improve the economic viability and resilience of horticulture to varying crop market prices, particularly in regions with high solar irradiance [30, 214]. Figure 4.15 summarizes the results of the presented economic assessment.

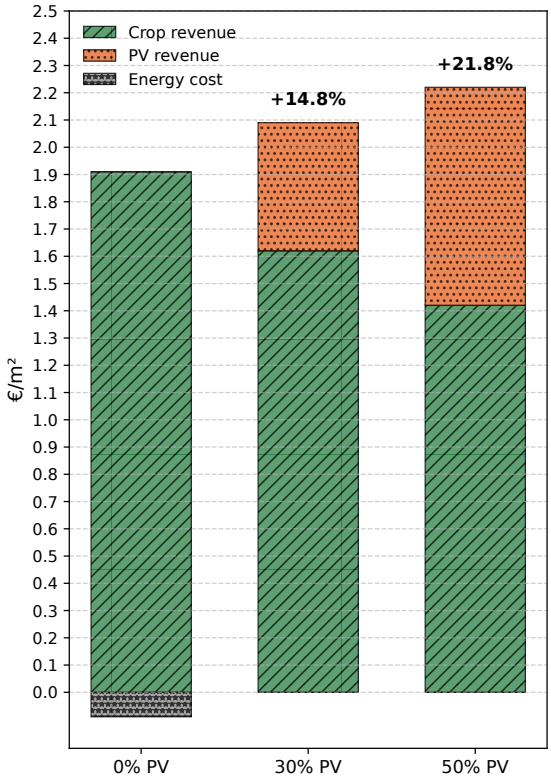


Figure 4.15: Comparison of economic performance per square meter for the GH with different PV cover ratios (0%, 30%, and 50%) during one crop cycle (September–March). Bars represent the contribution of crop revenue, PV revenue, and energy costs to the total profit per square meter.

In our two theoretical APV GH scenarios, both systems would overcompensate the reduction in crop yield and lead to a net profit increase by the end of the crop cycle. For the 30% shading scenario, the additional income can be estimated at 0.27€ m^{-2}, corresponding to a profit increase of +14.8% compared to the conventional greenhouse without PV. The 50% cover ratio APV GH would have resulted in an additional 0.40€ m^{-2}, corresponding to a profit increase of +21.8%.

These results already demonstrate the economic potential of APV GH systems. Even during the winter months of the study period, when irradiance and PV output are naturally lower, a positive net income could be observed. During summer, PV yields are higher and radiation levels can even be harmful to crops. It can therefore be expected that the benefits of APV systems considering the full year are even greater, leading to a higher overall annual advantage.

4.4.2 Electricity self-consumption and grid feed-in during the full year

Shading of PV modules gets particularly helpful in the summer months when photosynthetic saturation can occur and the naturally higher irradiation levels might become harmful for the crops in the GHs. In order to provide a qualitative outlook on the potential benefits of APV greenhouse systems during summer months with high solar availability, the previously presented economic assessment of the winter months with low light conditions is extended to the full year. Therefore, the same assumptions as previously described are applied and it is assumed that no further agricultural activity was carried out in the GH after the end of the tomato cycle in March. Table 4.7 summarizes the annual PV yield, electricity prices, savings from self-consumption during the tomato cycle, and feed-in revenues from selling excess electricity to the grid.

Table 4.7: Monthly prices for electricity consumption, electricity feed-in tariffs and the levelized prices corrected with the LCOE. The PV yields for the 30% and 50% shading scenarios are given as well as the consumption of the GH. The savings due to self-consumption and the feed-in revenues from the two PV systems are calculated.

	Days	Electricity Price [209, 210] [ct/kWh]	Feed-In Price [212, 213] [ct/kWh]	Levelized Price [211] [ct/kWh]	PV Yield 30% [60] [kWh/m²]	PV Yield 50% [60] [kWh/m²]	Consumption [kWh/m²]	Saving Self-Cons. [ct/m²]	Revenue 30% PV [ct/m²]	Revenue 50% PV [ct/m²]
09/2023	30	11.2	10.3	5.1	7.38	12.30	0.09	1.02	37.18	62.27
10/2023	31	10.4	9.0	3.8	6.19	10.32	0.20	2.10	22.82	38.58
11/2023	30	8.0	6.3	1.1	4.75	7.91	0.19	1.53	5.21	8.84
12/2023	31	8.5	7.2	2.0	4.45	7.42	0.20	2.10	8.55	14.56
01/2024	31	8.6	7.4	2.2	4.79	7.99	0.20	2.10	10.14	17.22
02/2024	29	5.0	4.0	−1.2	5.35	8.92	0.19	0.96	−6.17	−10.48
03/2024	31	3.4	2.0	−3.1	7.15	11.92	0.10	0.34	−21.86	−36.64
04/2024	30	3.1	1.3	−3.8	8.18	13.64	–	–	−31.01	−51.83
05/2024	31	4.4	3.0	−2.1	9.32	15.52	–	–	−19.57	−32.59
06/2024	30	6.8	5.6	0.4	9.61	16.01	–	–	3.84	6.40
07/2024	31	8.1	7.2	2.0	9.66	16.10	–	–	19.32	32.20
08/2024	31	10.0	9.1	3.9	8.96	14.93	–	–	34.94	58.23
Sum	366	–	–	–	40.07	66.78	1.17	9.15	63.36	106.76

For the calculation of self-consumption, the months of September and March are each counted as half months, in accordance with the values reported in Table 4.6. For the calculation of the feed-in revenues, the whole year is taken into account. According to the PVGIS SARAH radiation database [61], the expected PV yield in July is more than twice as high than in December for both cases of PV coverage of the GH. At the same time, electricity prices and feed-in prices increased towards the summer months of 2024 [210, 213]. Under the simplified assumption of no further agricultural activity in the GH, the savings due to energy self-consumption during the winter months of the tomato cycle would remain at 0.09€ m^{-2}. The 30% PV system would therefore lead to a feed-in revenue of 0.63€ m^{-2} by selling the excess energy to the grid. The feed-in revenue of the 50% PV system is estimated at 1.06€ m^{-2}. The total revenues of selling crops and energy are therefore estimated to be 2.25€ m^{-2} for the 30% shading system for the full year, i.e. a net profit increase of +23.6%. For the GH with 50% roof coverage, the total revenue is estimated to be 2.48€ m^{-2}, i.e. a net profit increase of +36.3%.

In order to take into account the continuous agricultural activity of the GH, the seasonal structure of a typical crop year in Almería should be considered. Common horticultural practice consists of an 8–9 month crop cycle, e.g. with tomato, pepper, or cucumber, followed by a shorter 2–3 month cycle with crops such as watermelons [22]. An alternative, also widely practiced, is the cultivation of two consecutive tomato cycles [22]. The experimentally measured DLI values inside the GH during the study period (Figure 4.9) consistently exceeded the minimum threshold of 15 mol m^{-2} d^{-1} from the beginning of March onward. This indicates that a subsequent crop cycle from March to August would not suffer from yield reductions, even under 30% shading caused by a PV system. This assumption aligns with the findings of [32] and [215], who evaluated monthly DLI levels for Spain. They reported that high-light demanding crops are photosynthetically saturated and shading is needed to avoid light-level related stress and damages. According to their calculations, even a 50% PV roof coverage would not lead to yield reductions during the summer months. Consequently, the economic assessment assumes full crop yield for the second growing cycle, resulting in additional crop revenue of 1.91€ m^{-2} for the annual calculation. By expanding the energy demand of the GH to the full year, energy savings due to self-consumption would increase to 0.17€ m^{-2}. For the 30% shading scenario, the combined revenue of two crop cycles and the PV system would be at 4.16€ m^{-2} for the full year. For a GH with 50% roof coverage, the total income can be estimated to be 4.39€ m^{-2}. Compared with a conventional GH without PV installation (3.64€ m^{-2} for two crop cycles), the net annual profit increase is +14.3% for 30% PV coverage and +20.6% for 50% PV coverage.

4.4.3 Potential application of agrivoltaic-generated electricity for desalination plants

The generated electricity of the PV system could be used to power desalination plants for water production, which could subsequently be used for GH irrigation [216]. Such estimations become particularly important in years with low tomato market prices or under extreme climatic conditions. The desalination plant of Carboneras in the Almería region, for example, has an energy requirement of 4.25 kW h per 1 m^3 produced freshwater [217].

It should be noted that this value refers to one specific, exemplary plant and more modern and energy-efficient desalination technologies may require less energy. The PV yield of the 50% cover ratio system could lead to a production of 22,455 m^3 of desalinated water during the tomato cycle. The presented 30% cover ratio GH could supply up to 13,473 m^3 of freshwater during the same period.

The experimental GH required 271 m^3 of water during the tomato cultivation period according to internal information provided by Fundacíon UAL-Anecoop. The PV yield from the 50%-cover-ratio APV system could hence supply the experimental GH 82 times with freshwater. For the 30%-cover-ratio APV system, the water consumption would be covered 49 times. As mentioned in the previous subsection, PV yields are even higher in summer. The overall annual advantage can therefore be even higher considering the full year.

5

Validation irradiance model

"The way to learn mathematics is to do mathematics."

—Mary Cartwright

In this chapter, the validation of the irradiance model, described in chapter 3, is presented with the help of two case studies. The validation is divided into two parts: a short-term validation with a calibration of the GH cover material using data from a previously published study (case study 1), and a long-term validation with the assessment of model accuracy using data from the experiment described in chapter 4 (case study 2).

For the short-term validation, we used the experimental results from López-Díaz et al., who conducted an APV GH study in 2015 on tomato crops in a "Venlo"-type GH [40]. This allowed for a detailed validation on a single clear-sky day, as well as an assessment of overall irradiance reduction across an entire crop cycle. The results of this validation were published in [42] and are detailed in Section 5.1. The second part of the validation, presented in Section 5.2, consists of a comprehensive long-term comparison using data from the APV GH experiment, which included a 8 month tomato cycle followed by a 3 months watermelon cycle.

5.1 Case study 1: "Venlo" greenhouse

The experiment presented by López-Díaz et al. [40] was performed from from 17 September 2014 to 14 May 2015 in a "Venlo"-type GH covering an area of 2145 m^2 (57.5 m long in north–south-direction, and 42.0 m width in east–west-direction) at the Tecnova experimental center in the province of Almería, southern Spain (36°53′ N, 2°22′ W, 185 m above sea level) [40]. The experimental design consisted of three shaded zones (15%, 30%, and 50% roof area covered) and a 0% control zone without any shading. Based on the information given by López-Díaz et al [40], a virtual copy of the experimental test GH was implemented in the simulation framework. Each zone was equipped with two radiation sensors, which are used for the validation of the irradiance model. Figure 5.1 presents the virtual copy of the GH and the estimated sensor positions.

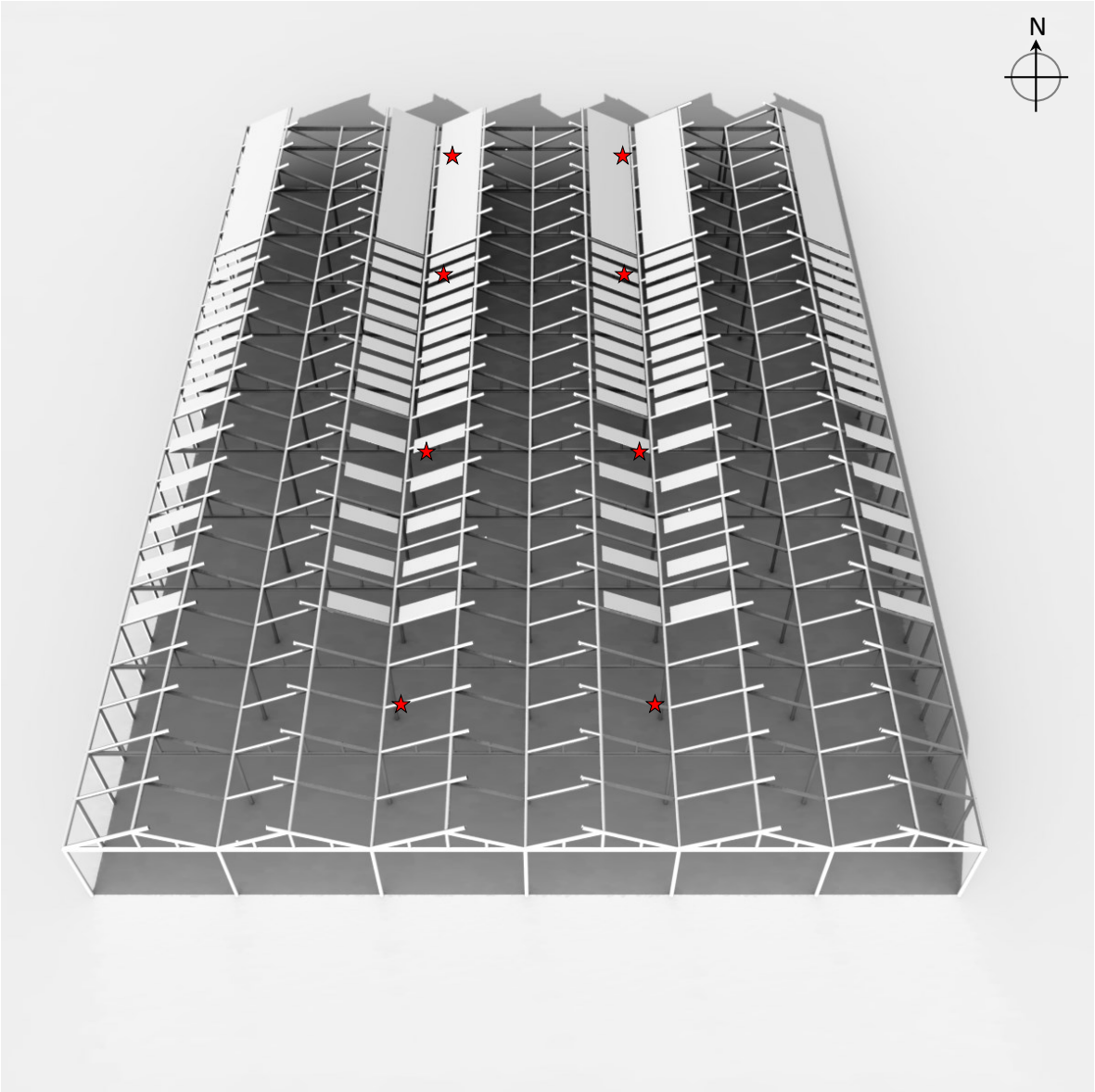


Figure 5.1: Rendering of the experimental "Venlo" GH implemented in the simulation framework. The estimated position of radiation sensors are indicated by stars.

The experimental shading zones are positioned along the long side of the GH in a north–south-direction. Thirty-six PV modules as well as additional opaque polyethylene sheets, each measuring 1.65 m in length and 1.00 m in width, were installed on the rooftop of the GH. In the simulation, ground albedo of the GH is set constant to 0.2, representing albedo of tomato plants of the study [22, 40]. For simplicity, albedo is kept constant in this study, but the developed model could also handle spatial and temporal dependent albedo.

5.1.1 DEFINITION GREENHOUSE PLASTIC

The plastic cover of the experimental GH in López-Díaz et al. had a thickness of 200 µm and a transmission of 84% [40]. Based on the sensitivity analysis presented in Section 3.1.3, the parameter range for suitable T_{diff} and T_{spec} combinations was determined to match the overall target transmission of 84%. Testing different parameter combinations yielded $T_{diff} = 0.892$ and $T_{spec} = 0.796$. According to Section 3.1.3, this parameter combination represents a haze of $\Phi = 42\%$.

The final material definition for the simulations is given in Table 5.1.

Table 5.1: Parameter definition of the `trans` material to match the description of the GH plastic used by López-Díaz et al. [40].

Red	*Green*	*Blue*	*Specularity*	*Roughness*	T_{diff}	T_{spec}
0.938	0.938	0.938	0.010	0.000	0.892	0.796

In the simulation, plastic cover materials are modeled as uniform surfaces with constant material properties and uniform transmission properties. The time-dependent changes in material properties and transmission values are not accounted for but can be the subject of future studies. In `Radiance`, the `trans` material is designed to model transmissive surfaces with diffuse transmission [135]. `trans` materials do not inherently account for complex, angle-dependent transmission properties. While more advanced material definitions, such as *transdata* material, can incorporate angular-dependent transmittance [135], their implementation would require detailed experimental measurements of the incident-angle-dependent transmission profile of the GH cover materials, which are often not available.

In the simulation framework, the virtual GHs consist of a large number of surface points, each with a different angle of incidence. Each of these incident points contributes to the diffuse light profile inside the GH. Furthermore, Figure 3.5 shows that in order to achieve a realistic overall transmittance of the material, high values of T_{diff}, which causes the diffusing effect, are needed. Hence, the approach of using two parameters (T_{diff} and T_{spec}) to describe light transmission in the simulation is considered sufficient. Nevertheless, the simplification can still pose limitations to the application of the presented model. If diffuse light transmission is not 100% correctly modeled and the direct contribution of the incident rays is overly pronounced, these could lead to a geometrical mismatch in the irradiation maps. However, such an effect was not observed in the presented application of the model.

5.1.2 DEFINITION SENSOR POSITION

For the validation of the model with the APV GH of López-Díaz et al., the positions of the radiation sensors in the experiment had to be estimated for the simulation. First, the x- and y-coordinates of all eight radiation sensors in the experiment were estimated based on the description in [40]. We assumed that there might be a geometrical mismatch between the estimated coordinates and the respective coordinates in the simulation, since

the virtual GH was designed based on the general description given in [40]. To account for this uncertainty, a search window of 2 m × 2 m with a resolution of $\Delta x = \Delta y = 0.05$ m was applied around the primary estimated coordinates of each sensor. For each search window, containing $41^2 = 1681$ coordinate sets, ray-tracing simulations, according to Section 3.1.5, were performed with a 15-min temporal resolution on 23 January 2015, selected as reference day because corresponding raw radiation sensor data were provided by the authors of [40].

For each radiation sensor and each of the 1681 simulated coordinate sets, the nRMSE between simulated and experimentally measured GHI was calculated, according to Equation 2.3, where the experimental GHI was derived as 15-min means from the minutely raw data. By minimizing the nRMSE, the best fitting sensor coordinates were identified. Figure 5.2 presents the distribution of the nRMSE values for the west sensor in the 0% control zone.

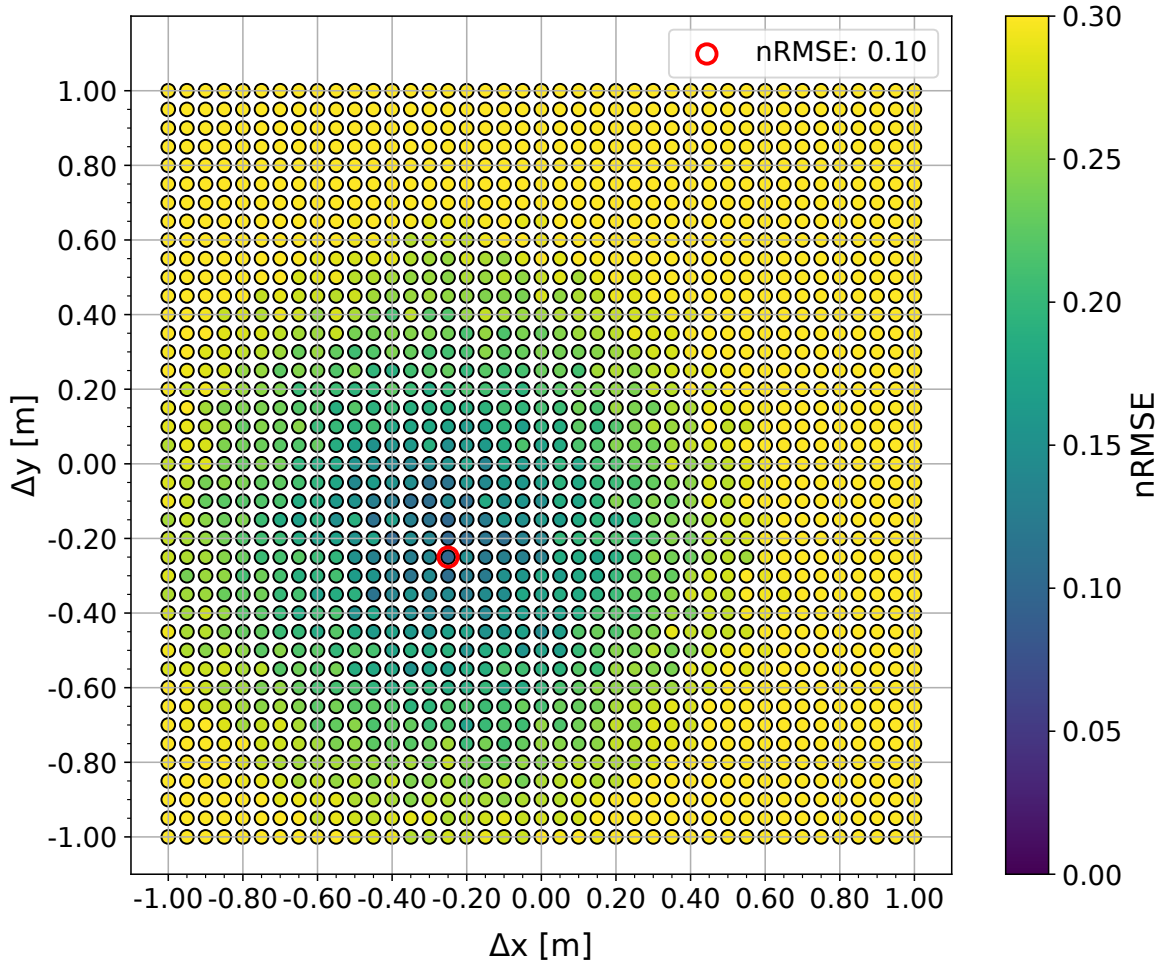


Figure 5.2: Minimization of nRMSE values to find the coordinates of the radiation sensors in the simulation. The nRMSE values for the west sensor in the 0% control zone are presented. For that sensor, the pair of x- and y-coordinates with the lowest nRMSE of 0.10 is located at $\Delta x = -0.25$ m and $\Delta y = -0.20$ m with respect to the primary guess of the position in the center of the plot.

The minimization of the nRMSE resulted in a reduction from 0.22 (initial coordinate guess in the center of the plot) to 0.1. The nRMSE distribution of the presented sensor shows that values can range between 0.1 and 0.5 within a distance of less than 1.00 m. Using this approach, the coordinates for all eight virtual sensors were optimized and applied to simulate the entire crop cycle of the experiment, i.e. from 17 September 2014 to 14 May 2015.

5.1.3 VALIDATION BASED ON SINGLE-DAY IRRADIANCE MEASUREMENTS

The presented simulations were performed with a 15-min resolution. The input CAMS irradiance data represent the mean values for the respective 15-min. For each 15-min interval, the sun's position was modeled at the middle of this interval. For example, for the period from 12:00:00 to 12:15:00, the sun's position was modeled at 12:07:30. For 23 January 2015, experimental raw data were available and a comparison of the experimentally measured irradiance data and the irradiance simulation was performed. To quantify the deviation between the simulation and experimentally measured data, the nRMSE and the irradiation error were calculated according to Equations 2.3 and 2.9. Figure 5.3 shows the simulated GHI in comparison to the experimentally measured data on that day for all eight sensors.

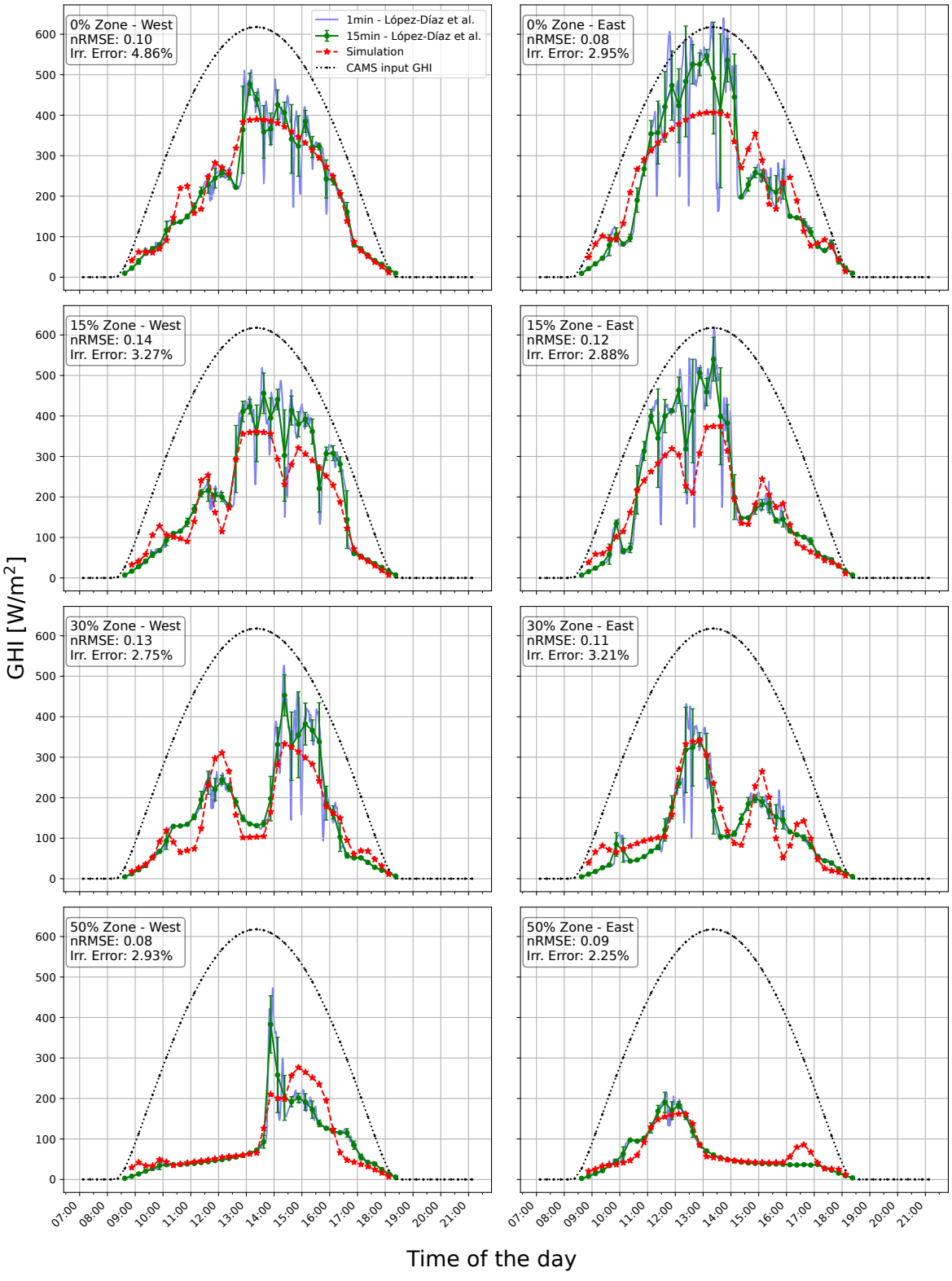


Figure 5.3: Comparison between simulated and experimentally measured GHI of López-Díaz et al. [40] for 23 January 2015. The plots on the left refer to the sensors placed on the west of the GH; the plots on the right refer to the sensors placed on the east. The zones are presented in ascending order, with the 0% zone in the first row and 50% in the last row. Red stars: simulation; blue line: GHI measured by López-Díaz et al. [40]; green points: 15-min means of experimentally measured data with $\pm 1\sigma$ standard deviation; black curve: outside GHI from CAMS used as model's input.

The simulated irradiance curves align with the experimentally measured values, showing that the model is capable of simulating the measured irradiance conditions inside the GH on the presented day. Focusing on the two sensors in the 0% shading zone, the experimentally measured values display fluctuations even though there is no artificial shading from PV modules in this area. This suggests that the differences in irradiance measurements are influenced by localized shading from the structural elements of the GH that obstruct the sensors' field of view.

Furthermore, the experimentally measured data show short-term fluctuations at a minute level for all sensors despite clear-sky conditions outside, as indicated by the GHI curve. The possible explanations for these fluctuations are that the roof is not homogeneously soiled, and thus changes in the irradiation measurement at the same location in the GH are possible due to slightly different sun positions. Other potential factors are sensor soiling due to the GH environment and general inhomogeneities of the plastic cover, e.g., small holes in the plastic or localized abrasion of the plastic cover due to the influences of wind, sun, rain, and other external factors.

The simulation generally aligns well with the overall shape of the curves of the experimentally measured data for all sensors on the presented day. Additionally, the model can simulate changes in the irradiance distribution throughout the day at a sub-hourly temporal resolution. This confirms an accurate representation of the GH structure based on the general description in [40] and justifies the optimization of the sensor coordinates. For the presented day, the nRMSE values range from 0.08 to 0.13, and the irradiation error remains below 5% for all sensors. However, for other days, the bias and nRMSE values might be higher, as the sensor positions were fine-tuned based on the same day's data.

Notably, the simulations of the two sensors in the 50% shading zone show the highest agreement with the experimental measurements and the lowest irradiation error values, despite the overall low absolute irradiance levels. On the west side of the 50% shading zone, irradiance values remain below $100\,\mathrm{W\,m^{-2}}$ during the first half of the day. In contrast, for the sensor on the east side, this occurs during the second half of the day. The model replicates these patterns, highlighting the advantage of high-resolution irradiance simulations.

5.1.4 RADIATION REDUCTION FOR ONE CROP CYCLE

The radiation reduction was evaluated based on the simulations of the whole crop cycle, i.e. from 17 September 2014 to 14 May 2015, at the previously chosen grid points (averaged for the two sensors per zone). Figure 5.4 shows the overall reduction in radiation for the three shading zones with respect to the control zone.

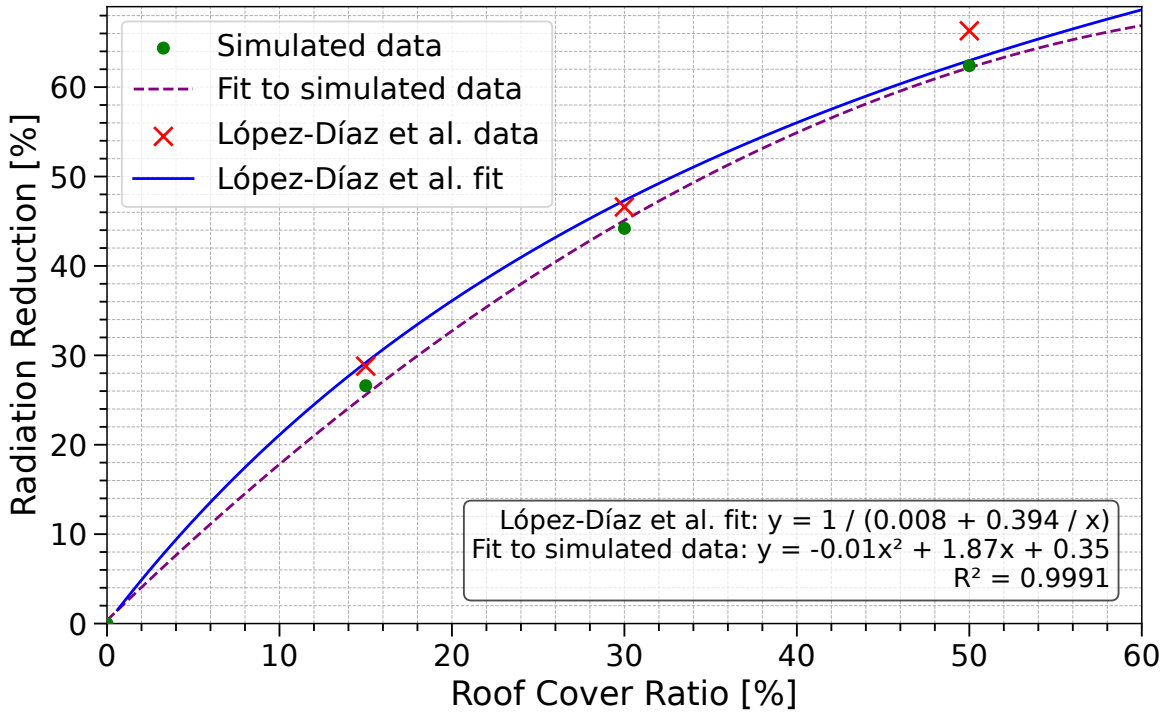


Figure 5.4: Overallradiation reduction with respect to the control zone as a function of shading treatments of 15%, 30% and 50% for the simulation and experimental values of López-Díaz et al. [40]. A 2nd-degree polynomial function is fitted to the simulated data ($R^2 > 0.99$).

The simulation produces radiation reduction values consistent with the experimentally measured data. This means that the model is capable of taking into account changing outside climatic conditions and solar zenith over a prolonged timeframe of several months. For both the simulation and experimentally measured data, the presented radiation reduction values are generally higher than the roof cover ratio. López-Díaz et al. reported a radiation reduction of 28.8% for 15% shading, 46.6% for 30% shading, and 66.3% for 50% shading. In comparison, the presented simulation leads to values of 26.6%, 44.2%, and 62.4% for the respective shading zones, which is on average 2.88 p.p. lower than the experimentally measured data.

In Figure 5.3, the east radiation sensor of the 0% shading zone recorded higher irradiance values compared to the west sensor in the same zone. Additionally, the experimentally measured irradiance exceeds the outside GHI taken from the CAMS database on the presented day several times. Hence, if there were systematically higher irradiance readings from one of the sensors in the control zone in the experiment, this could have resulted in overall lower values in the analysis of the simulations.

Furthermore, deviations can also be caused by geometric mismatches, such as discrepancies in the overall GH structure and small misalignments in sensor positioning relative to the GH structure. Additionally, in the real world, the material properties of a GH cover can change over time due to progressive degradation, which causes a change in their visible appearance, as well as in their chemical structure, and consequently affects their physical and mechanical properties [218]. Degradation is mostly caused by exposure to UV radiation [219, 220]. Other factors that also intervene, albeit to a lesser extent, are air temperature and humidity, possible mechanical stress (especially caused by wind), contact with agrochemicals, and possible internal stress related to the installation phase [218, 221]. As the degradation of the material is an important aspect, it should be considered in future research and applications of the model. In addition, the model uses a simplified approach to model the light transmission through the GH cover, and the angular dependence of the incident light might lead to deviations in the long-term analysis. Furthermore, the radiation sensors in the experiment might have been soiled or affected by the local environmental conditions inside the GH or even shading by the crops, which could have also caused deviations in the presented comparison.

5.1.5 DISCUSSION OF CASE STUDY 1: "VENLO" GREENHOUSE

In the presented validation of the irradiance model with the APV GH of López et al. [40], the simulated irradiance was on average 2.88 p.p. lower than the experimentally measured data over the extended timeframe of one crop cycle. The reasons for the deviations in the comparison between the presented localized simulations and the experimental measurements include geometric mismatches, such as discrepancies in the overall GH structure and small misalignments in sensor positioning relative to the GH structure, which are still possible even after the optimization of sensor coordinates. Additionally, the properties of the GH materials can change over time, e.g., plastic coverings may degrade over time, leading to a different transmittance than at the start of their use. The constant exposure to solar radiation and chemical products during cultivation can cause the degradation of GH plastic films [86]. In the Mediterranean region, GH coverings are usually changed every three years due to a decline in their performance and eventual loss of utility. [22]. The study of [222] showed that the transmission of LDPE materials exposed to arid conditions for one year decreased by roughly 32%. In the simulation, plastic cover materials are modeled as uniform surfaces with constant material properties, and such an aging effect is neglected. For the application of the model to the GH experiment in López-Díaz et al., the material definition of the plastic covering was optimized based on the available dataset of one exemplary day and with the information given in [40] to match the experimental results of one crop cycle. In order to improve model accuracy for long-term predictions, given the extended timeframe of GH operations, a temporal evolution of material properties could improve model accuracy. This could be realized in the simulation by gradually adjusting material properties or, as a simplified approach, applying a continuous degradation factor on the assumed plastic transmittance value. However, detailed knowledge of the degradation processes and additional experimental data would be needed to implement such a method.

Furthermore, spontaneous changes in light diffraction can also occur due to the movement of the plastic covering caused by wind or even small holes in the roof, which would further contribute to measurement fluctuations in an experiment but are not included in the simulation. Other potential factors include inhomogeneous soiling of the plastic roof, which can cause variations in irradiance measurements at the same location depending on the sun's position, as well as sensor soiling due to the GH's microclimate.

It might be of interest to compare the presented model to the findings of Torrente et al. [127], who also simulated the GH studied by López-Díaz et al., and of Cossu et al. [126], who conducted more general simulations of various north–south-oriented APV GHs. Both modeling approaches were also presented in Chapter 2. Such a comparison is not directly possible with the presented application of our model due to the differences in the GH types studied, the timeframes of the simulations, and the methodologies used, particularly the averaging of larger areas rather than point-like simulations as in the presented model.

Torrente et al. [127] proposed a method incorporating the transmission of GH plastic dependent on the solar incidence angle. The resulting radiation reduction was calculated by averaging the radiation distribution across the entire GH for each individual shading zone of the experimental setup. Their calculations of the irradiance maps for the experimental GH in López-Díaz et al. were based on representative days for each month taken from a typical meteorological year (TMY). By integrating these values over time, Torrente et al. estimated both monthly and annual radiation levels for different points inside the GH and provided averaged irradiation maps for the GH. Their findings showed radiation reductions of 11%, 24%, and 32% for 15%, 30%, and 50% shading, respectively. Furthermore, their model predicted lower absolute irradiance values in the 0% shading zone.

Cossu et al. [126] simulated the irradiance distribution for various GH types with different roof cover ratios and estimated the yearly radiation reductions based on the entire GH area. They estimated the annual average values of global solar radiation within GHs equipped with PV modules and evaluated the impact of different PV cover ratios, orientations, and structural parameters on light uniformity and availability over the course of a year. The simulations in their study did not use actual input irradiance data but instead estimated yearly trends based on representative climate data. Their findings reported yearly averaged radiation reductions of 9%, 18%, and 30% for 15%, 30%, and 50% shading, respectively, for north–south-oriented GHs at a height of 1.5 m.

Both studies focused on estimating spatially averaged irradiance values rather than modeling local light distribution. Their methods can account for the irradiance entering through the GH's side walls, but they do not resolve the detailed shading patterns created by structural elements and PV modules at specific positions inside the GH. Additionally, their use of annual average irradiance or TMY files means that local variations in environmental conditions are not considered.

Both studies reported radiation reduction values that are generally lower than the theoretical roof cover ratios of the investigated GHs. Possible explanations for this deviation from the here-presented findings include the north–south orientation of the GH, which causes the shadow of the PV modules to fall outside the GH at various times during the crop cycle. Additionally, a considerable fraction of irradiance enters through the side

walls. By averaging the irradiance over the entire zone area, the models of [127] and [126] account for this additional amount of irradiance. Furthermore, differences in input irradiance data, GH types, and the investigated timeframes prevent a direct comparison between the studies. The presented model incorporates a more detailed representation of the GH structure and cover materials. Actual satellite-derived irradiance data from the time period of the experiment in López-Diaz et al. rather than annual averages or TMY files are used to model the input irradiance conditions. Hence, the climatic conditions of the time period are illustrated more precisely. This presented model makes it possible to highlight the influence of the local environmental conditions, different sun positions, and the shading caused by the GH structure itself.

In principle, the presented model can also be used to generate an averaged overview of different zones. However, the strength and novelty of the model is its ability to perform localized simulations and to visualize the shading effects caused by the PV modules. The model can also simulate the impact of finer structures, such as components of the GH frame and the light transmission through the GH covering plastic, which contribute to a non-uniform irradiance distribution. Furthermore, the simulations can be performed at any point in the virtual scene, such as at a different height or close to the side walls.

5.2 CASE STUDY 2: "RASPA Y AMAGADO" GREENHOUSE

The long-term performance of the irradiance model was evaluated using continuous measurements of GHI collected in two successive GH crop cycles in the experimental APV GH presented in Chapter 4. The 185-day cycle with tomatoes ran from 14 September 2023 to 15 March 2024. The 80-day watermelon cycle took place in the experimental APV GH from 22 March to 10 June 2024. To match the lower canopy of the watermelon plants, the pyranometers in the GH were lowered from a height of 2.8 m to 0.5 m during that cycle. This combination of crop cycles reflects a typical growing campaign in the Almería region [22].

Figure 5.5 shows a rendered view of the experimental GH, including the position of the pyranometers across the three shading zones. In each zone, four pyranometers were installed, as described in Chapter 4. The following sections present a detailed comparison between the model's simulated GHI and the corresponding experimental measurements. The results from the comparison with the CMP10 pyranometers, marked in green in Figure 5.5, are presented as a representative example for all pyranometers.

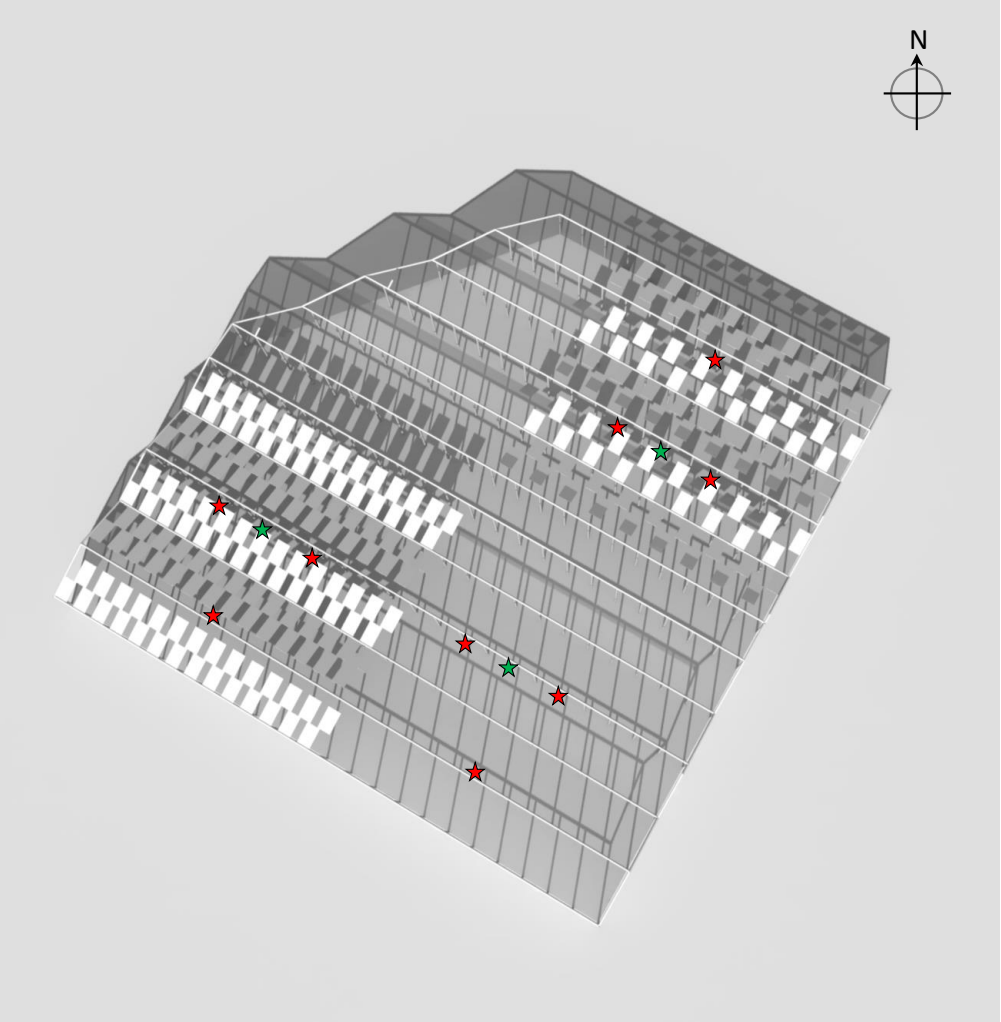


Figure 5.5: Top view rendering of the experimental APV GH implemented in the simulation framework. The estimated position of the twelve pyranometers are indicated by the stars. Green stars: CMP10 pyranometers.

5.2.1 DEFINITION SENSOR POSITION

For the application of the model to the experimental APV GH, the same approach as previously described in Section 5.1.2 was followed. First, the coordinates of each of the twelve pyranometers were mapped from the physical setup into the simulation by measuring their x–y-coordinates inside the experiemntal GH. As the positioning of the sensors was more precise than those for case 1 of [40], the geometrical mismatch was assumed to be minimal. Consequently, a tighter search window of 0.80 m × 0.80 m was defined around each sensor's initial estimate, with a spatial resolution of $\Delta x = \Delta y = 0.05$ m. Within each search window (17^2 grid points, yielding 289 candidates per pyranometer), ray-tracing simulations were executed at 15-minute intervals for a set of clear-sky days during the experimental period to simulate GHI at each timestamp. The simulated sensor grid was rotated to match the overall orientation of the GH. For every sensor and each of its 289 simulated coordinates, the nRMSE between simulated and measured GHI was computed. The coordinate yielding the minimum nRMSE was defined as the pyranometer's optimal position in the model. Figure 5.6 shows the nRMSE distributions for the CMP10 pyranomters in the three zones of the GH.

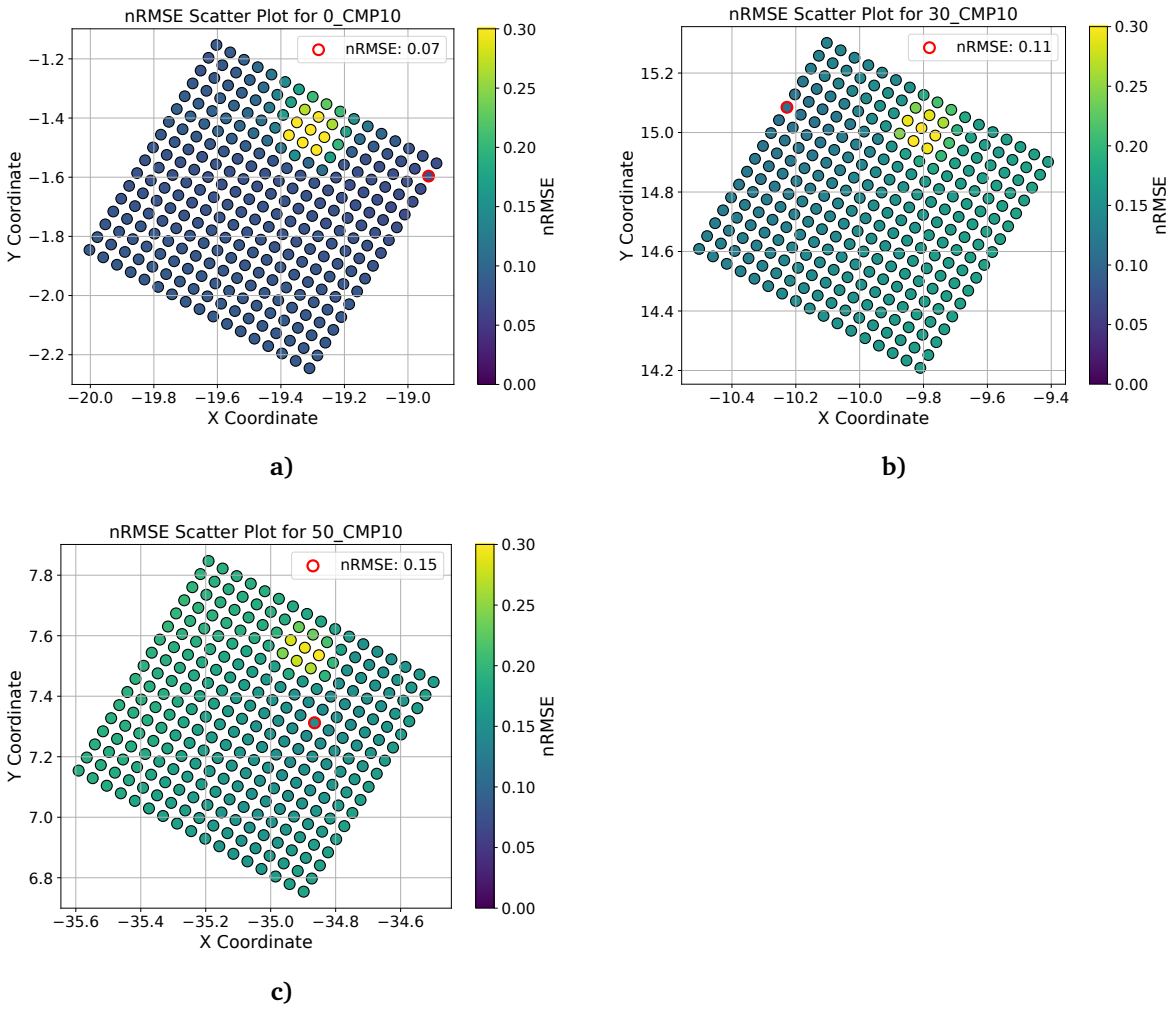


Figure 5.6: Minimization of nRMSE values to find the coordinates of the CMP10 pyranometers in the simulation. The coordinate set with the lowest nRMSE is marked with a red circle. **a)** 0% zone. **b)** 30% zone. **c)** 50% zone.

For the 0% control zone the nRMSE minimization yields 0.07 for the CMP10 sensor. For the 30% shading zone, the nRMSE values generally increased due to the shading pattern of the PV modules. Within the search window, the coordinate set with the lowest nRMSE value was 0.11 for the CMP10 pyranometer. For the 50% shading zone, the nRMSE values generally increased again due to the increase in density of the PV modules. Within the search window, the coordinate set with the lowest nRMSE value was 0.15 for the CMP10. Notably, for the 0% and 30% zone, the sensor position with the lowest nRMSE are located at the edge of the search window in 0.4 m distance to the initial estimate.

5.2.2 VALIDATION BASED ON SINGLE-DAY IRRADIANCE MEASUREMENTS

This section compares simulated and experimentally measured GHI for the clear-sky day of 11 April 2024 as an example day because clear conditions facilitate a better understanding of both the ray-tracing capabilities and the limitations. Figures 5.7, 5.8, and 5.9 show the GHI curves for this example day.

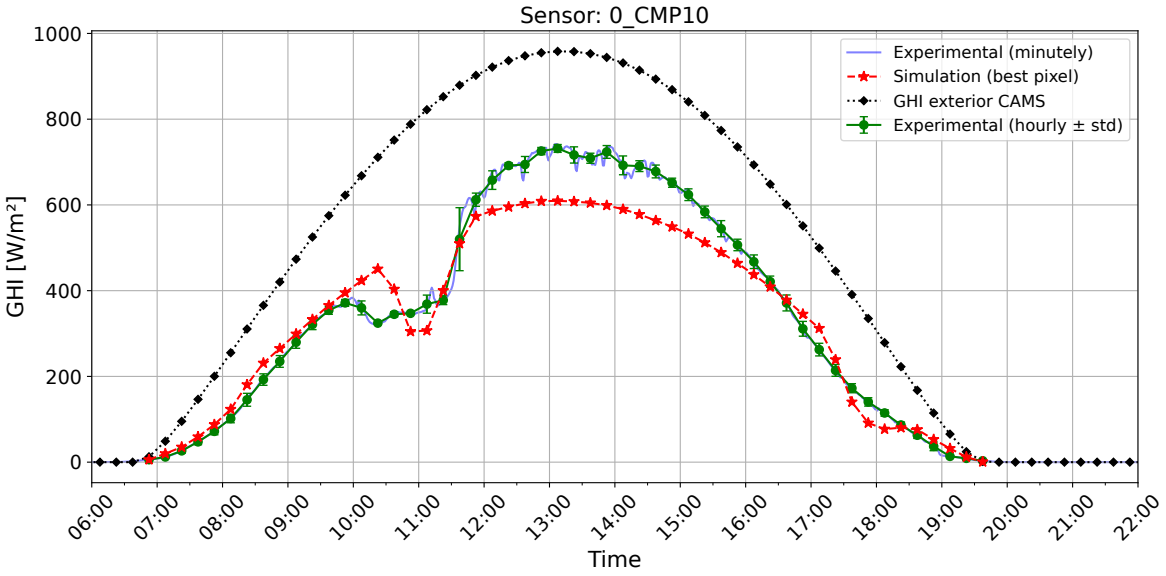


Figure 5.7: Comparison of outside, experimentally measured, and simulated GHI at the CMP10 pyranometer location in the 0% shading zone. GHI input from CAMS (black dashed), minutely GH measurements (blue), 15-min means of experimental data $\pm 1\sigma$ standard deviation (green), and 15-minute interval simulated GHI (red).

In Figure 5.7 it can be seen that the experimentally measured data follows the shape of the input GHI curve but is attenuated by 15–20% which aligns with the overall transmittance of the GH plastic cover described in Chapter 4. In addition, a decrease in GHI between 10:00 and 11:00 is measured, which is caused by the shading of structural elements of the GH itself.

The simulation captures the overall diurnal trend of the experimentally measured data and also reproduces the decrease in GHI caused by structural elements, which means that the overall GH 3D representation aligns well with the experimental GH. Nevertheless, the

simulations underestimated the measured 15-minute mean GHI values by approximately 10%, particularly around solar noon. This underestimation can be attributed to the way `Radiance` models solar radiation. Radiance uses three broadband RGB channels that represent the visible range of the spectrum (approximately 380 nm to 780 nm). When using the `rtrace` sky generators (`gendaylit`, `gensky`), as described in Section 3.1.5, `Radiance` internally assumes the solar spectrum is fixed without any spectral variations with air mass and that the scaling of the three RGB channels follows an approximate daylight chromaticity [135]. Hence, the three RGB channels in the `rtrace` output are weighted broadband integrals over the visible range and do not track how the solar spectrum shifts with changing solar zenith. Energy-wise, the NIR portion of the solar spectrum is implicitly included in the broadband DNI input and therefore not neglected in the simulation, however, it is distributed according to the fixed visible spectral shape assumed by `Radiance` [135]. As a result, when comparing the mean of the three RGB values to the broadband GHI measured by the pyranometers, which measure the full spectrum, the NIR contribution is only weakly represented due to this spectral weighting. Consequently, the simulated GHI underestimates the experimentally measured GHI inside the GH especially during central hours, when the NIR fraction of the solar spectrum is naturally higher.

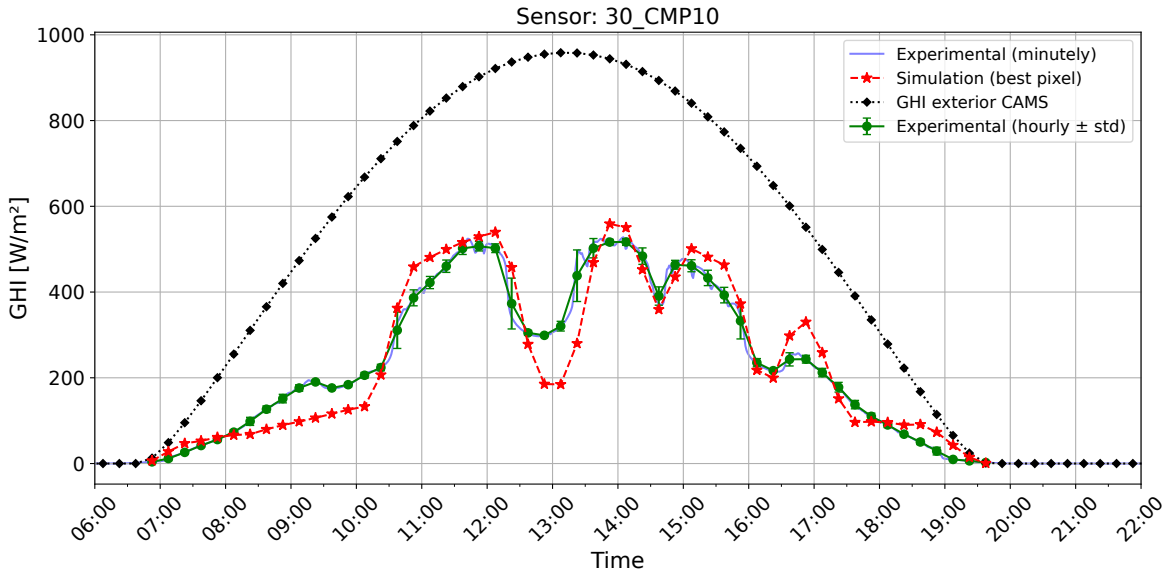


Figure 5.8: Comparison of outside, experimentally measured, and simulated GHI at the CMP10 pyranometer location in the 30% shading zone. GHI input from CAMS (black dashed), minutely GH measurements (blue), 15-min means of experimental data $\pm 1\sigma$ standard deviation (green), and 15-minute interval simulated GHI (red).

In Figure 5.8 for the 30% shading zone, the shading pattern caused by the PV modules is clearly visible in the experimentally measured data and is reproduced by the simulation. However, the experimentally measured GHI rises more steeply during the early morning hours, reflecting the model's general tendency to underestimate irradiance due to the spectral weighting and lower contribution of NIR irradiance by `Radiance`.

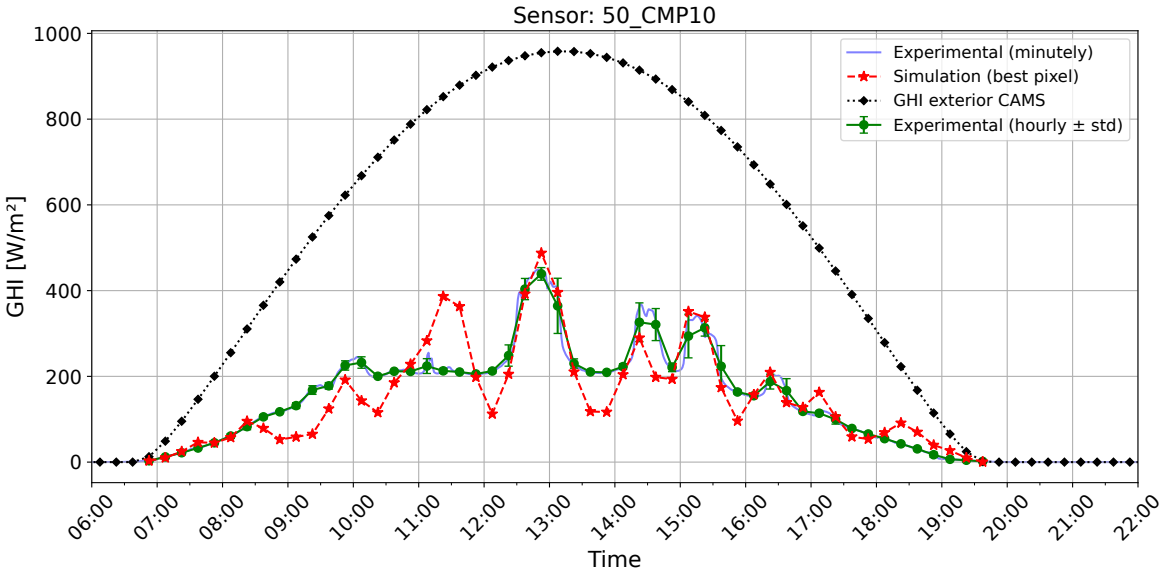


Figure 5.9: Comparison of outside, experimentally measured, and simulated GHI at the CMP10 pyranometer location in the 50% shading zone. GHI input from CAMS (black dashed), minutely GH measurements (blue), 15-min means of experimental data $\pm 1\sigma$ standard deviation (green), and 15-minute interval simulated GHI (red).

In Figure 5.9 for the 50% shading zone, the measurements of the pyranometer display distinct shading patterns, corresponding to the movement of shadows cast by the PV modules. The simulated GHI curve successfully reproduces both the number and approximate timing of these shading events. In general, the shading pattern is reproduced by the simulation, in particular after 12:00. One mismatch is apparent between 11:00 and 12:00 when the simulation rises but the experimental measurements suggest a shaded time interval. This indicates a slight misalignment in the PV layout geometry or model configuration. Such minor discrepancies are to be expected, as the GH model used in the simulation is ideally symmetrical, while the real GH has a slightly inclined roof, which likely causes a shift in the shading pattern.

5.2.3 VALIDATION BASED ON IRRADIANCE MEASUREMENTS OF TWO COMPLETE CROP CYCLES

For each day of the experiment, simulations with 15-minute temporal resolution were performed at the previously defined sensor positions to obtain GHI inside the GH within the three shading zones. Figure 5.10 presents the comparison of the experimentally measured GHI by the three CMP10 pyranometers with the simulated GHI at the specified coordinate sets.

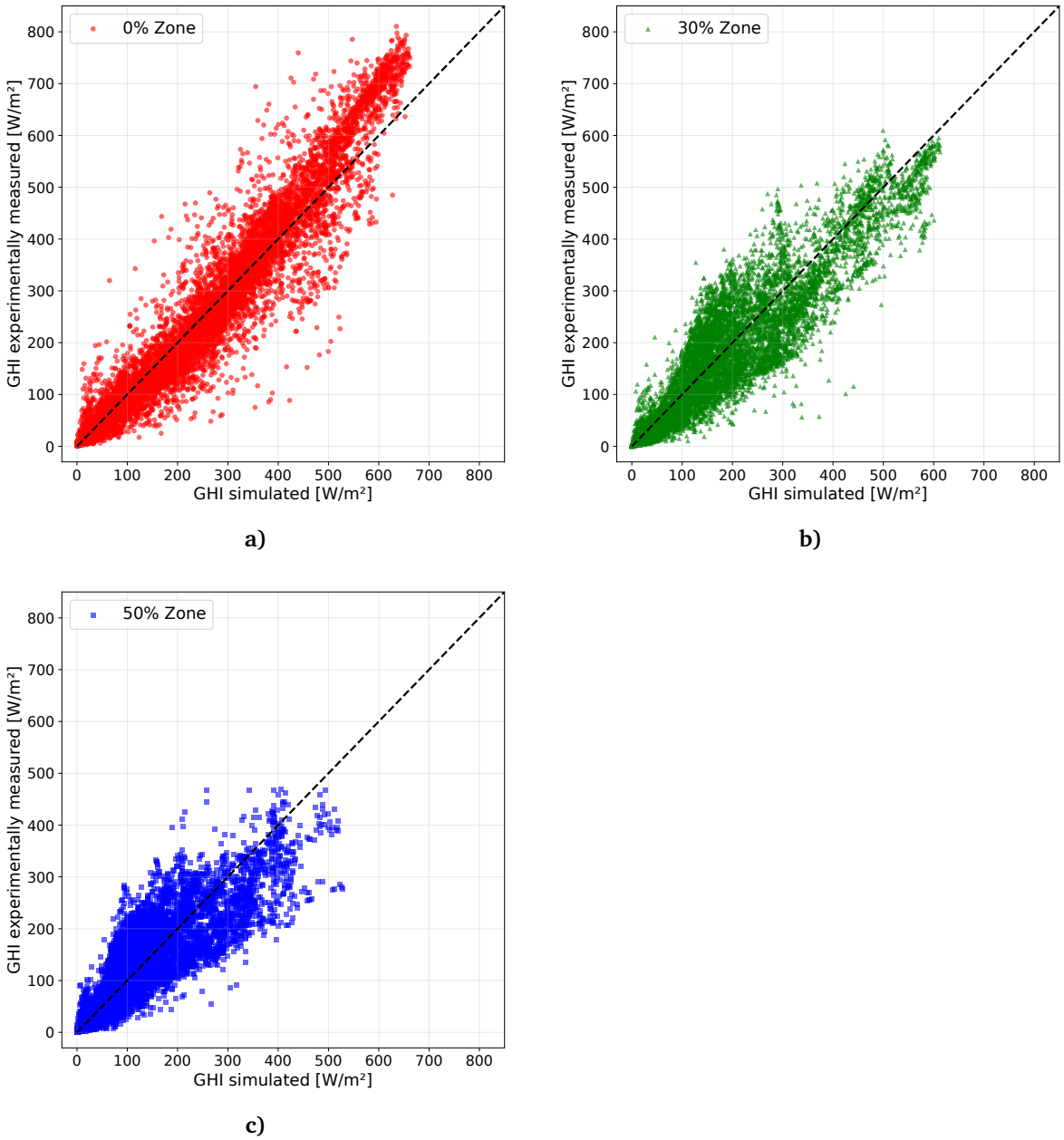


Figure 5.10: Comparison between experimentally measured GHI by the three CMP10 pyranometers and simulated GHI at the previously defined coordinate points. Dashed line: line of equality where $GHI_{sim} = GHI_{exp}$. (**a**) 0% shading. (**b**) 30% shading. (**c**) 50% shading.

The comparison between simulated and experimentally measured GHI shows a general agreement for all three shading zones. In all three scatter plots, the GHI data points are distributed homogeneously around the agreement line, which indicates that the model does not show a consistent trend of either overestimating or underestimating the experimentally measured values.

For the 0% shading zone, the model tends to slightly underestimate the measurements for higher irradiance levels (above 500 $W\,m^{-2}$), which is consistent with the discussion in the previous section. In the 30% shading zone, on the other hand, a slight tendency of the model to overestimate the measured values can be observed for irradiance values above 300 $W\,m^{-2}$. For the 50% shading zone, both measured and simulated values show

the expected decrease in irradiance magnitude due to the stronger shading by the PV modules. Again, for GHI values above 300 W m^{-2}, the model tends to overestimate the experimentally measured values.

Most importantly, the simulation reproduces well the magnitude of irradiance across the three zones, reflecting the gradual decrease in light availability with increasing shading due to the PV modules. This indicates that the model successfully represents the general lighting conditions inside the GH, including the contribution of diffuse light transmitted through and around the shading structures.

In order to evaluate the model accuracy for the extended time frame of the experiment, the nRMSE, as defined in Equation 2.3, was calculated for each day of the crop cycle between experimentally measured GHI of the CMP10 pyranometers and simulated GHI. Figure 5.11 shows the nRMSE values for the three shading zones of the APV GH for each day of the experiment.

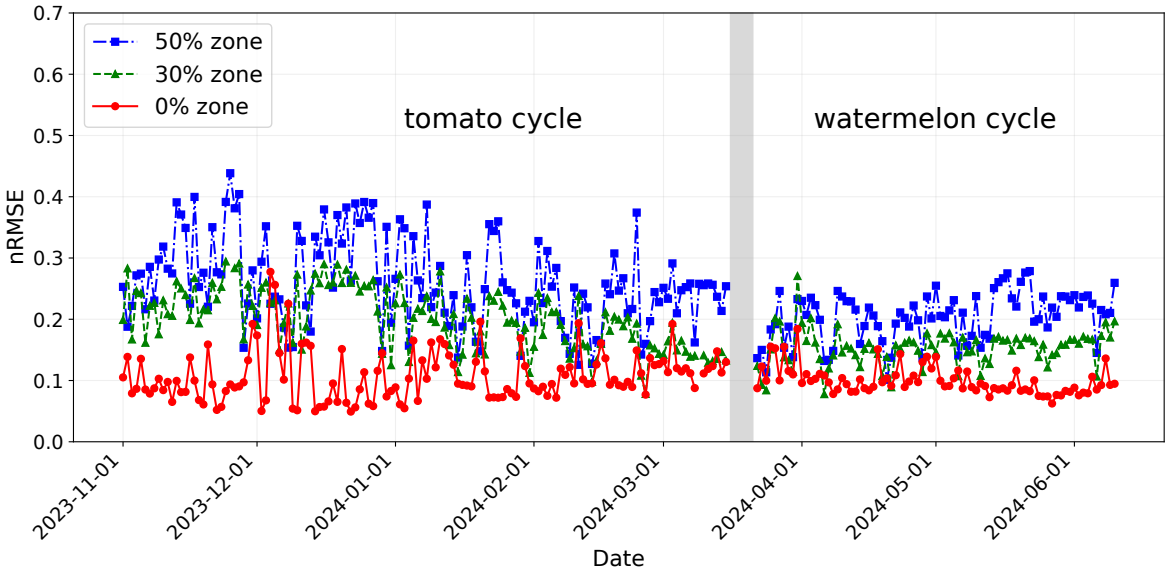


Figure 5.11: Long term validation (nRMSE values) of the irradiance model with experimentally measured GHI of the CMP10 pyranometers in the three shading zones. Red circles, solid curve: 0% control zone. Green triangles, dashed curve: 30% shading zone. Blue squares, dashed-dotted curve: 50% shading zone.

The day-wise comparison shows that within each zone, the nRMSE values behave consistently without larger differences. For the 0% control zone, the nRMSE values accumulate around 0.1, with some higher values above 0.2 at the beginning of December 2023. As the shading ratio increases, the nRMSE values per zone also increase due to the increased shading pattern of the PV modules. For the 30% shading zone, the nRMSE values generally stay below 0.3 with the majority below 0.2. The 50% shading zones shows the highest deviation between simulation and experiment with values around 0.3 for the tomato cycle and values below 0.3 for the watermelon cycle. This is mostly caused by the model's sensitivity to the sun position so that misalignments in the geometric positioning of the PV modules in the simulation compared to the real-world APV GH can lead to deviations.

Additionally, a slight decrease in nRMSE values and greater uniformity among the shading zones is observed when transitioning from the tomato cycle to the watermelon cycle (indicated by the grey area). Here, the nRMSE values of the 50% shading zone decrease from below 0.4 during December 2023 to consistently below 0.3 after 15 March 2024. For the 30% shading zone, the nRMSE values consistently decrease below 0.2 after March 2024. Intriguingly, the 0% control zone is not affected by the changes, which means that the effect is related to the PV modules. During the watermelon cycle, the pyranometers in the GH were lowered from a height of 2.8 m to 0.5 m, increasing the distance between the sensors and the diffusing GH plastic cover. In the simulation, this increased distance means that more diffused rays reach the sensor positions and the dominant contribution of the direct sun rays is reduced compared to measurements and simulations taken at 2.8 m.

In order to assess the accuracy of the irradiance simulations for the presented case study, the error metrics nRMSE, nMAE, nMBE, RMSE, MAE and MBE are calculated for the entire timeframe of the experiment and summerized in Table 5.2.

Table 5.2: Error metrics for the comparison between simulated and experimentally measured GHI for the three zones in the APV GH.

Zone	nRMSE	nMAE	nMBE [%]	RMSE [$W\,m^{-2}$]	MAE [$W\,m^{-2}$]	MBE [$W\,m^{-2}$]
0% Shading	0.09	0.13	−2.40	52.1	36.2	−6.4
30% Shading	0.18	0.19	0.41	51.0	37.9	0.8
50% Shading	0.27	0.19	−6.16	31.0	21.8	−6.7

For the unshaded control zone, the irradiance model shows the lowest relative errors (nRMSE = 0.09, nMAE = 0.13), which indicates a very good agreement between simulated and experimentally measured GHI. The small negative bias (MBE = -6.4 $W\,m^{-2}$, nMBE = -2.4%) confirms the underestimation of GHI by the irradiance model, but the deviation remains small over the two crop cycles. In the 30% shading zone, the nRMSE increases to 0.18, which was discusses previously due to the greater geometric and material complexity caused by the PV system. Here, the bias is almost zero (MBE = +0.8 $W\,m^{-2}$, nMBE = +0.4%), which demonstrates that the model reproduces the experimentally measured GHI very well on average. Under 50% shading, the nRMSE further increases to 0.27, which reflects again the higher uncertainty associated with the more dense PV system and more complex light interactions such as reflections and side-wall contributions. Notably, the absolute RMSE remains small (31 $W\,m^{-2}$) because irradiance levels in this zone are generally lower, which was also observed in Figure 5.10. The MBE (MBE = -6.7 $W\,m^{-2}$, nMBE = -6.2%) indicates a slight underestimation by the model. This deviation is within the range typically considered acceptable for radiative transfer or daylight modeling studies, where MBE values within ±10% are generally regarded as satisfactory [144, 223].

5.2.4 UNCERTAINTY ANALYSIS BASED ON IRRADIANCE MEASUREMENTS OF TWO COMPLETE CROP CYCLES

This section evaluates the uncertainties and error sources of the irradiance model based on the data from case study 2. Subsection 5.2.4.1 examines the angular dependence of light transmittance through the GH cover material and its implementation in the irradiance model. Section 5.2.4.2 investigates the correlation of CAMS GHI from the experimentally measured GHI inside the GH.

5.2.4.1 ANGULAR DEPENDENCE OF TRANSMITTANCE

In the horticulture sector, especially in the Mediterranean region, LDPE films are widely used as GH covering materials [86]. As already introduced in Chapter 2, these plastic films are often multi-layered with a UV-protection film toward the outside and agrochemical-resistant films toward the inside of the GH [40]. The materials have been developed to maximize the fraction of diffuse light inside GHs, which has been proven to have positive effects on crop growth and yield in GHs [84, 87]. The transmittance of LDPE materials is known to depend on the angle of light incidence, as experimentally measured by [224] and [225] for different types of GH cladding materials.

For the development of the irradiance model, special focus was therefore placed on the accurate representation of the GH plastics, with focus on diffuse light transmission. Angular-dependent light transmission, inhomogeneous soiling of the GH and material degradation due to internal and external forces and stressors are not considered, and therefore represent a limitation of the model.

In order to assess the effect of angular-dependent light transmission, the transmittance was calculated as the ratio between the GHI inside the control zone and the corresponding outside GHI provided by CAMS, using 15-minute mean values over the entire experimental period. Figure 5.12 shows the transmittance dependent on the sun elevation angle for both simulated and experimentally measured values from the CMP10 pyranometer in the control zone of the GH.

In the simulation plot in Figure 5.12, most values cluster around three horizontal bands centered at approximately 0.25, 0.45 and 0.60–0.65 transmittance. The spread in transmittance narrows at elevation angles between 50° and 70°, while a broader distribution is observed at lower elevations ($< 20°$), including some values above 0.8. This wider spread is likely due to side-wall light contributions during early morning and late afternoon hours.

The experimentally measured transmittance distribution in Figure 5.12 is more scattered and shows an increased variability due to material characteristics of the plastic and changing environmental conditions such as moving cloud cover, uneven soiling, damage to the plastic covering, and surface reflections. A trend of increasing transmittance with rising solar elevation can be observed, which indicates a dependence of transmittance on the angle of incidence.

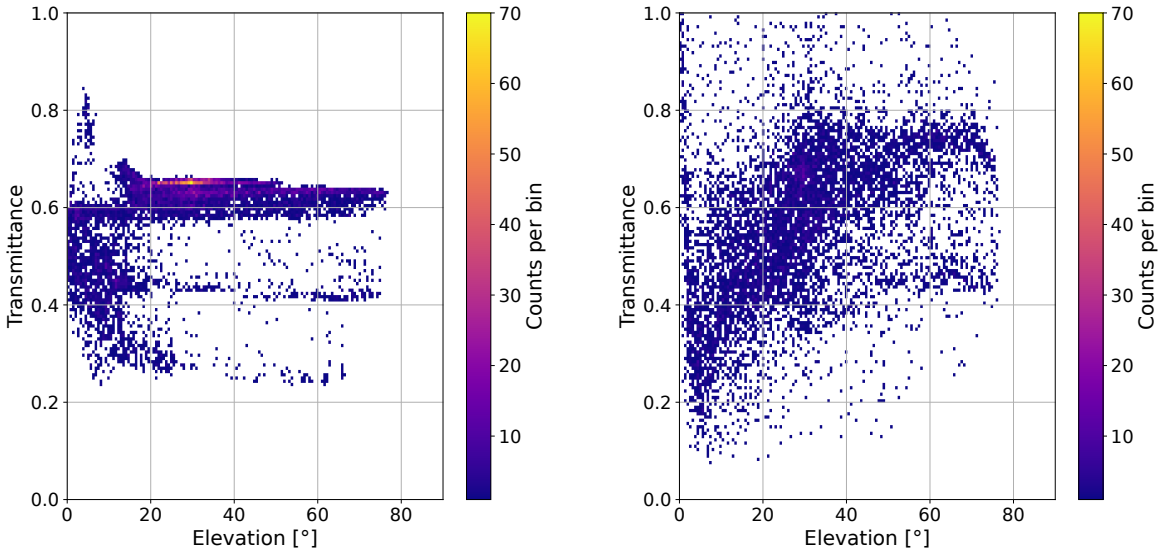


Figure 5.12: Long-term transmittance as a function of solar elevation angle for the control zone (0% shading), based on simulated GHI (left column) and experimentally measured GHI (right column) throughout the experiment. The density plot illustrates the frequency of measured transmittance values at each elevation angle. **a)** CMP10 simulation. **b)** CMP10 experimental.

In both plots in Figure 5.12, a cluster of values around a transmittance of approximately 0.45 can be observed, which corresponds to the decrease in GHI between 10:00 and 11:30 shown in Figure 5.7. This drop in irradiance is most likely caused by an internal structural element which reduced the GHI to a similar level. The presence of this pattern in both the measured and simulated data further supports that the overall GH geometry was accurately represented in the model.

The methodology presented here is a simplified approach to simulate light transmission through GH cover materials using `Radiance`. In this approach, angular dependence of the material properties was not explicitly implemented. In general, objects in `Radiance` are surface materials, meaning surfaces have no thickness, and all light–material interactions are calculated at the surface. When a ray intersects a surface, `Radiance` computes the interaction only at that specific point, with no path length through the medium. Diffuse reflection, specular reflection, transmission, and absorption are all resolved at this boundary. In `Radiance`, the `trans` material is designed to model diffusely transmitting surfaces [135]. To simulate transmittance, `Radiance` applies a bidirectional-scattering distribution function (BSDF) at the surface and generates new rays accordingly. However, `trans` materials do not inherently account for complex, angle-dependent transmission behavior. All transmitted rays are either diffusely scattered into a hemisphere around the forward direction or passed straight through specularly, as described in Chapter 3.

More advanced material definitions, such as `transdata`, can incorporate angle-dependent transmission [135], but their use requires detailed experimental data on the angular transmission characteristics of GH cover materials, which are often unavailable. Alternatively, the BSDF of a specific GH plastic could be measured at various angles and wavelengths in a lab setting and then used in `Radiance`. However, this would require a separate measurement campaign for each material of interest.

Graefe et al. [224] developed and validated a radiation transfer prediction model for single and double layers of plastic covering over kohlrabi canopies in GHs. Their model used laboratory-measured angular-resolved transmittances, which were then upscaled to non-planar cover geometries in the field. Additional measured and upscaled parameters included absorptance and haze at multiple angles. Effects of plastic aging and surface wetting were incorporated using simple empirical methods. They emphasize the importance of scaling lab-measured optical properties to field conditions, particularly to account for the varying sun incidence angle over non-flat surfaces. They also noted that the wetness of the inner plastic surface changes throughout the day. Pollet et al. [225] also studied the influence of wetness on LDPE transmission. They found that condensation droplets significantly reduced transmittance and compared to dry LDPE, transmittance of normally incident radiation dropped to 65%. Furthermore, wet LDPE exhibited nearly constant transmission values for incident angles between 0° and 60°.

These studies show that the transferability of lab-measured BSDFs to real-world GH conditions is not straightforward and will remain a challenging task in future model enhancements. In principle, the implementation of angle-dependent light transmission is feasible, however, the experimental effort required to obtain accurate data is substantial. Moreover, the transferability of lab-measured BSDFs to GH conditions is not straightforward and will mean further investigation for future model extensions.

5.2.4.2 DISCREPANCY BETWEEN OUTSIDE GHI AND MEASURED GHI INSIDE THE GREENHOUSE

The presented results are based on simulations that use CAMS satellite-derived irradiance data as input conditions to define the sky and sun in `Radiance`. The use of satellite-derived data makes the model flexible and independent of ground-based measurements, which are often unavailable. However, as discussed in Chapter 3, CAMS data may be less accurate for locations distant from validation sites. In the simulations presented here, instances were observed where the experimentally measured GHI from the pyranometers inside the GH exceeded the corresponding CAMS input values. To evaluate this effect over the entire experimental period, Figure 5.13 compares the measured GHI from the three CMP10 pyranometers in the different zones of the GH with the CAMS-derived input GHI. The comparison includes all 15-minute mean values of CAMS GHI and CMP10 GHI for sun elevation angles greater than 0°.

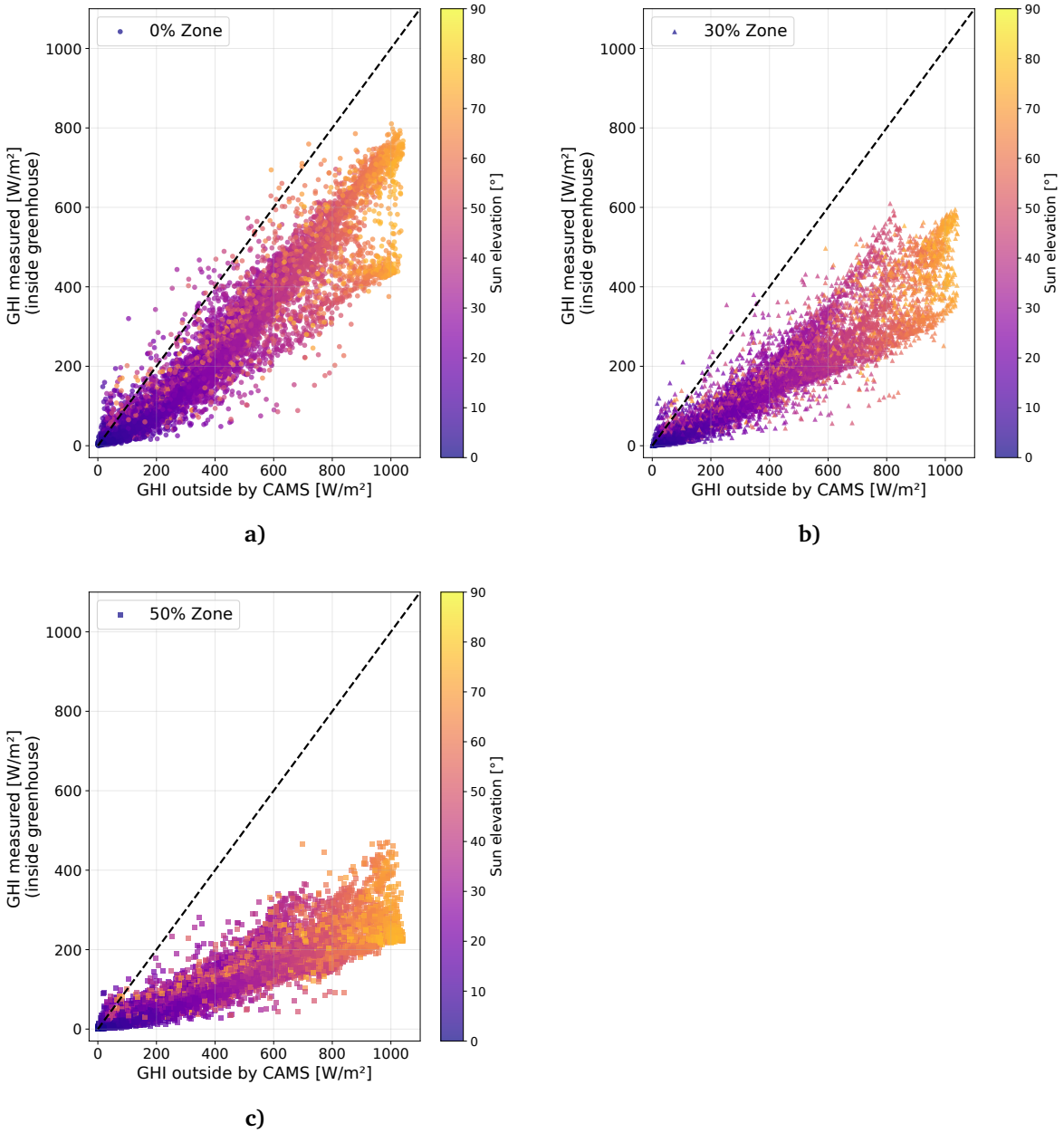


Figure 5.13: Comparison between experimentally measured GHI by the three CMP10 pyranometers and outside GHI provided by CAMS. Dashed line: line of equality where $GHI_{CAMS} = GHI_{exp}$. **a)** 0% shading. **b)** 30% shading. **c)** 50% shading.

In Figure 5.13 it can be seen that with increasing shading ratio, the amount of data points, where the outside GHI by CAMS is smaller than the experimentally measured GHI inside the GH, decreases. Furthermore, no systematic correlation to the sun elevation angle can be observed. However, it mainly occurs under overcast conditions, when the simulation cannot capture local fluctuations in irradiance due to a fast-moving cloud cover. Out of 9860 investigated data points in Figure 5.13, the input GHI was smaller for 4.26% in the control zone, 2.31% for the 30% shading zone and 1.38% for the 50% shading zone. Hence, this effect can be considered negligible over the entire experimental period. Nevertheless, for short-term comparisons between measured and simulated values it might influence simulation results, in particular on overcast days.

5.3 DISCUSSION OF THE IRRADIANCE MODEL

In this chapter, we validated the presented irradiance model with two case studies. For case study 1, we recreated the APV GH experiment of López-Díaz et al. [40], who conducted their study in 2015 on tomato crops in a "Venlo"-type GH in Almería. This allowed for a detailed validation on a single clear-sky day, as well as an assessment of overall irradiance reduction across an entire crop cycle. Case study 2 consisted of a comprehensive long-term comparison, using data from the APV GH experiment presented in Chapter 4, which included a 8 month tomato cycle followed by a 3 months watermelon cycle in a "raspa y amagado" GH in Almería. For both case studies, we presented simulations with a temporal resolution of 15-minutes, which allowed us to recreate irradiance and shading patterns similar to the data recorded by the radiation sensors in the experiments.

In case study 1, the sensor position in the simulation was fine-tuned with the help of one day of raw data from the original experiment. For the presented day, the nRMSE values ranged from 0.08 to 0.13, and the irradiation error remained below 5% for all sensors. However, for other days, the bias and nRMSE values might be higher, as the sensor positions were fine-tuned based on the same day's data. Case study 1 was then also used to perform simulations over the entire time frame of the experiment and compare the overall reduction in radiation in the APV zones of the experiment to the results published by [40]. On average, the reduction in radiation based on the simulated GHI was 2.88 p.p. lower than the experimentally measured data.

The application of the irradiance model to the "raspa y amagado" GH of Chapter 4 imposed a more challenging task than the replication of the "Venlo" GH in case study 1. The "raspa y amagado" GH of the our study was rotated away from a perfect south-facing position and not as symmetrical as the "Venlo" GH of [40]. In addition, the distance between GH roof and pyranometer position in the experiment was only about 0.5 m during the tomato cycle, which increased the dominant contribution of the direct sun rays in the `Radiance` simulations and decreased the contributions of the diffuse sky. Overall, the irradiance model shows very good performance for the long-term validation across all zones, with the lowest errors in the unshaded area (nRMSE = 0.09, nMBE = –2.4%). For 30% shading (nRMSE = 0.18, nMBE = +0.4%) and 50% shading (nRMSE = 0.27, nMBE = –6.2%) the error metrics indicated a decrease in accuracy of the model, however, the shading patterns measured in both zones were successfully reproduced by the simulations. In addition, the results showed that the irradiance model is capable to simulate the correct magnitude of irradiance inside the GH within the shaded zone and that diffuse light contribution is also modeled correctly.

As discussed before for both case studies, deviations between experimentally measured and simulated irradiance values are inevitable due to the complexity of both the GH environment and the simulation framework. Part of this complexity comes from geometrical details of the GH and its surroundings, which are difficult to reproduce with complete accuracy. In addition, the plastic cover exhibits a non-uniform transmission profile, and its transmission properties are subject to change over time through soiling and aging. Uncertainties of the input irradiance data from CAMS also propagate into the model, as discussed before.

Future improvements can include the direct coupling with crop models to provide crop-specific yield predictions. Previous studies demonstrated that hourly time steps are sufficient for both crop modeling and energy yield modeling. The study of [226] confirmed that hourly data provide realistic energy yield predictions in various climatic conditions, while the study of [227] demonstrated that hourly mean values are suitable for modeling solar irradiance in agricultural setups and assessing APV performance. Most crop models operate effectively on a daily or an hourly time scale and could be coupled directly to the presented model. The studies of [228] and [229] highlighted that many crop models, such as DSSAT, effectively utilize daily time steps to simulate crop growth by integrating weather inputs, including irradiance. The TOMGRO model of Jones et al. [129] works with hourly time steps to simulate tomato crop development in GHs, making it possible to display the reaction to finer-scale variations in irradiance, which will be presented in detail in Chapter 6. However, when using hourly averaged irradiance data, information on short-term fluctuations in irradiance, as presented here, can be lost. Beyond the coupling to specific crop models, the model could also be integrated into a comprehensive framework including an economic yield estimation, e.g., similar to the evaluations of [230] on a regional scale for the Canary islands [230] or [231] on the national scale for the United States.

The simulation results of case study 1 showed that the line placement of PV modules along the roof of a north–south-oriented GH leads to significant shading periods, as was already proven by the experimentally measured values in the study of López-Diaz et al. [40]. The results of case study 2 showed that light homogeneity improved with the placement of the PV modules in a checkerboard pattern and changes between shaded and unshaded periods were less pronounced. The results from the presented application of the model in both case studies indicate that the irradiance distribution inside the GH is not only influenced by the PV shading, but, depending on the position in the GH, the structure itself leads to an inhomogeneous irradiance distribution. For each GH configuration and dependent on the site, different PV configurations might be more beneficial and there is no general, optimal solution for PV placement. This agrees with the experimental studies and pilot sites across Europe, which showed that the design of APV solutions always has to be adapted to location-specific climatic conditions [41]. For GHs, different studies indicate that checkerboard patterns and semi-transparent PV modules improve light uniformity [39, 131]. Furthermore, small and fast-moving shade patterns can be more beneficial to plant growth [232]. Nevertheless, the final decision on an APV installation does not consider only the PV array but also the grower's perspective and the specific characteristics of each GH when assessing whether the reduction in crop yield is adequately compensated by energy savings and other factors [131].

Finally, we compared the model with state-of-the-art modeling approaches for irradiance modeling for APV GH. The presented model is the first ray-tracing-based irradiance model for APV GHs in the Mediterranean region that has been validated with experimental data from two complete crop cycles. The model is capable to simulate the complex interaction between sunlight and GH cover materials and has a high spatial and temporal resolution of the simulations. Comparable models, such as the methods of [126] or [127], were not tested over such an extended time frame. Both methods rely on simplified, spatially averaged irradiance estimates derived from TMY or annual climate data, which neglect

short-term and local variations in weather and sunlight conditions. The approaches do not resolve local light distributions or the fine shading patterns created by PV modules and GH structures. Additionally, both models approximate the GH transmission and side-wall effects but lack a detailed geometric representation of the structure and materials, which reduces their accuracy for complex configurations or time-specific analyses. In contrast, the presented ray-tracing-based irradiance model provides an explicit and detailed representation of the GH geometry, the optical properties of the cover materials, and the layout of the PV modules. This level of detail enables the simulation of localized irradiance conditions rather than spatially averaged values. Moreover, the model performs time-resolved calculations, which makes it possible to capture complex light interactions such as reflections, shading, and transmission effects throughout the day and crop cycle. By using actual satellite-derived irradiance data from the experimental period, the model also reflects the real climatic conditions more accurately than approaches based on TMYs or annual averages.

5.3.1 Analysis of computational resources

The presented simulations for both case study 1 and 2 were run on a high-performance computer running Ubuntu 18.04 LTS, equipped with dual 64-bit CPUs clocked at 2.6 GHz and 512 GB of DDR4 memory operating at 3200 MT/s. This section has been published as part of [42] and discusses the computational resources based on the simulations and findings of case study 1.

Balancing computational efficiency and the desired accuracy of simulations is crucial for ensuring both the reliability and practical applicability of the presented ray-tracing-based model. In general for APV simulations, accuracy is referred to as the spatial resolution in the x- and y-directions, relating to the number of sensor points/pixels chosen for the ray-tracing scan.

Figure 5.14 relates the number of pixels and spatial accuracy to the computation time for the presented application of the model in case study 1.

Using a theoretical resolution of $\Delta x = \Delta y = 0.05\,\text{m}$ for the virtual GH requires approximately 10^6 virtual sensors. Under these conditions, simulating 23 January 2015 at 12:00 would take 4 h 35 min 18 s. Reducing the resolution to $\Delta x = \Delta y = 0.20\,\text{m}$ lowers the computation time to 1 h 10 min 2 s. When simulating only the eight specified sensor positions, the runtime is 7 min 4 s. With the same configuration, the simulation of one single pixel takes 1 min and 8 s.

In Figure 5.3, each sensor has 37 simulated data points (from 8:15 to 17:30 in 15-min intervals), resulting in a total of 296 simulations for that day. By running 30 timestamps in parallel, the entire day's simulations for all sensors are completed in approximately one hour, assuming each timestamp requires the same computation time. Extending this approach to cover the full crop cycle from 17 September 2014 to 14 May 2015 at a 15-min resolution requires under two days of total runtime.

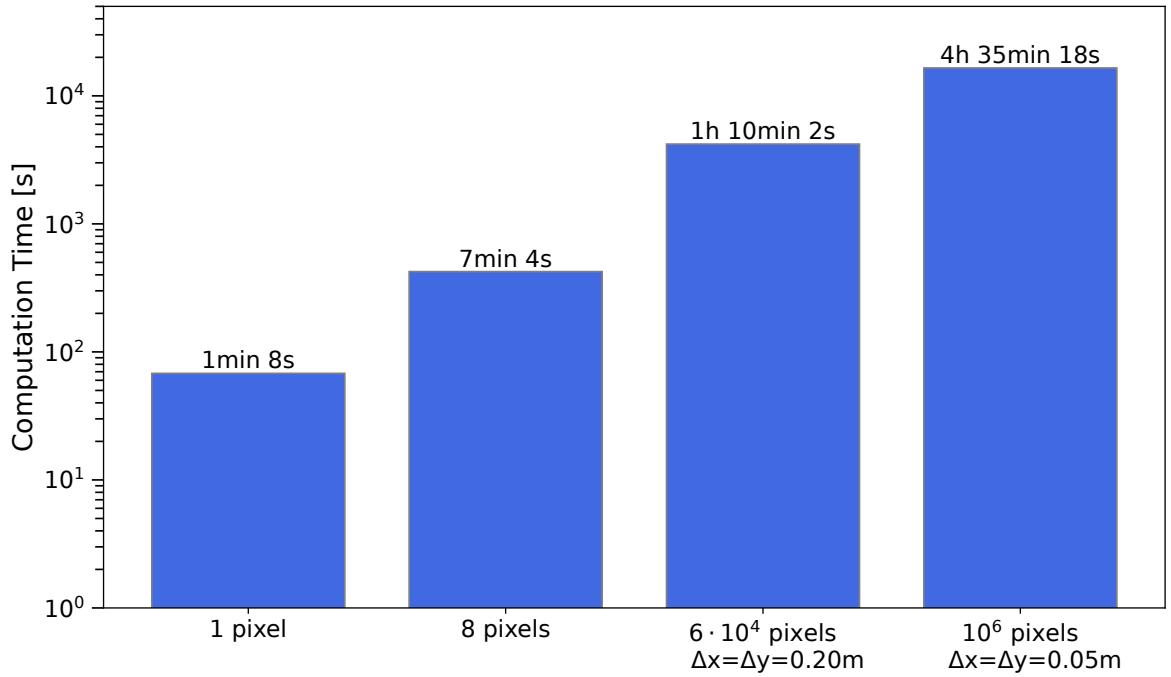


Figure 5.14: Computation times for timestamp 23.01.2015 at 12:00:00 for varying numbers of pixels.

Not every simulated timestamp requires the same amount of computation time. In addition to spatial resolution, other factors, such as the optical properties of the GH cover materials and outside climatic conditions, affect how long each simulation runs. Higher irradiance levels (e.g., summer vs. winter) and diffuse light conditions (e.g., overcast days or strongly diffusing cover materials) tend to increase computation time per timestamp. The dimensions of the modeled system and the complexity of the materials also impact the simulation duration. As the experimental GH in López-Díaz et al. was relatively large (57.5 m × 42.0 m × 10.0 m) and had a highly diffusing cover material, the simulation times per timestamp were relatively long. In comparison, the simulations of case study 2 took less time per simulated timestamp due to the smaller size of the GH itself (44 m × 43.0 m × 4.0 m). In general, simulation time and computational efficiency are dependent and can be adjusted with the choice of internal `Radiance` ambient parameters, such as the number of primary rays or ambient bounces. The correct setting of these parameters can be difficult, as an incorrect value can potentially lead to increases in noise or decreases in overall accuracy. Information on how to choose these values for each specific simulation can be found in the `Radiance` documentation and the literature [135, 137]. For the application of the model up until now, ambient bounces were set to 2, and number of primary rays was set to 2048.

In general, it is difficult to give overall statements about total simulation time, as it can vary significantly with timestamp and use case. Examining previous studies, the trade-off between computational efficiency and accuracy in the deployment of ray-tracing algorithms is an important topic. Bruno et al. developed a PV tracking optimization model based on `Radiance` for open-field APV installations and pointed out that computational cost is already one of the main limitations of the developed optimization [233]. They mentioned a runtime of 10 h per simulated day in the optimization process and encouraged the usage

of typical days to represent a full year [233]. Sánchez et al. evaluated the relationship between computation time and spatial resolution for an open-field APV system, modeled with `Radiance`, and mentioned a run time of 430 s for a spatial resolution of 100 × 100 pixels using a regular laptop computer (1.8 GHz processor, 16 GB RAM, 8 GB GPU) [234]. Ovaitt et al. compared ray-tracing-based simulations for open-field APV systems with `Radiance` against view factor models and noted that their simulations were run on an HPC cluster [235].

Ray-tracing simulations for APV systems can be fast and accurate if set up in an efficient way. In general, it is not possible to establish proper computational benchmarks due to the complexity of the information (hardware, scene, input data) and the differences in modeling approaches as well as a lack of detailed information on the temporal and spatial resolution used in different studies. Ray-tracing offers precise modeling of light distribution in APV systems and the GHs included as well as provides more customization options for complicated setups in comparison to other modeling approaches, e.g., Torrente at el. [127] or Cossu et al. [126]. A mindful choice of the spatial and temporal resolution is always beneficial. The user should be aware of the goal of their simulations. For a long-term analysis or evaluation of light homogeneity inside a GH, a different modeling approach, e.g., view-factor models or the models of Torrente et al. [127] or Cossu et al. [126], might be more suitable and effective than applying ray-tracing algorithms. However, for a high level of detail in the spatial and temporal distribution of the irradiance inside a GH, as well as a connection to actual input irradiance data, ray-tracing and the presented model are more suitable. Strategies to reduce the computation time of ray-tracing simulations include simplifying the geometry, lowering the number of ambient bounces, or identifying representative days via clustering similar meteorological conditions, thus minimizing the number of detailed simulations without losing information.

6

Validation crop model

"In life, we must keep our curiosity alive."

—Rita Levi-Montalcini

In this chapter, the validation of the two approaches to obtain crop yield is performed. The first approach is based on radiation by DLI values. The validation of the DLI approach is presented in Section 6.1. The second presented approach, called TOMGRO, uses a FSPM to apply a biophysical modeling approach to simulate tomato yield grown under APV conditions. The validation of the FSPM can be found in Section 6.2. These results were obtained within the Master thesis of J. Kornas [160], which was supervised within the scope of this PhD thesis. Part of these results were published in [43]. Section 6.3 compares the approaches and discusses uncertainties and limitations of each approach.

6.1 Daily light integral-based models

The goal of the DLI-based crop modeling approach is to estimate total accumulated yield over time, i.e. how much yield would be harvested at the end of the crop cycle, depending on the DLI values of each day. In this section, two methods are presented. The first application uses solely the DLI values and is compared to tomato yield data from the APV GH experiment described in Chapter 4. The second approach extends the DLI-based method and takes into account additionally daily RH and temperature values measured in the experimental APV GH.

6.1.1 YIELD ESTIMATION BASED ON DAILY LIGHT INTEGRAL

Figure 6.1, left hand side, depicts the DLI values for the tomato crop cycle from November 2023 until March 2024 for the three shading zones for both experimentally measured values within the GH described in Chapter 4 and DLI values derived from the simulated GHI according to Section 3.2.1. On the right hand side of Figure 6.1 the daily yield with respect to no shading is depicted, with modeled curves according to the yield estimation described in Section 3.2.2.1 (Equation 3.26) with $\mathrm{DLI}_{\mathrm{min}} = 15\,\mathrm{mol\,m^{-2}\,d^{-1}}$. Parameter k_{DLI} in Equation 3.26 was fitted to the experimentally measured yield reductions from the 50% zone, resulting in $k_{\mathrm{DLI}} = 0.379$. The fitted parameter was then applied for the 0% and 30% shading treatments.

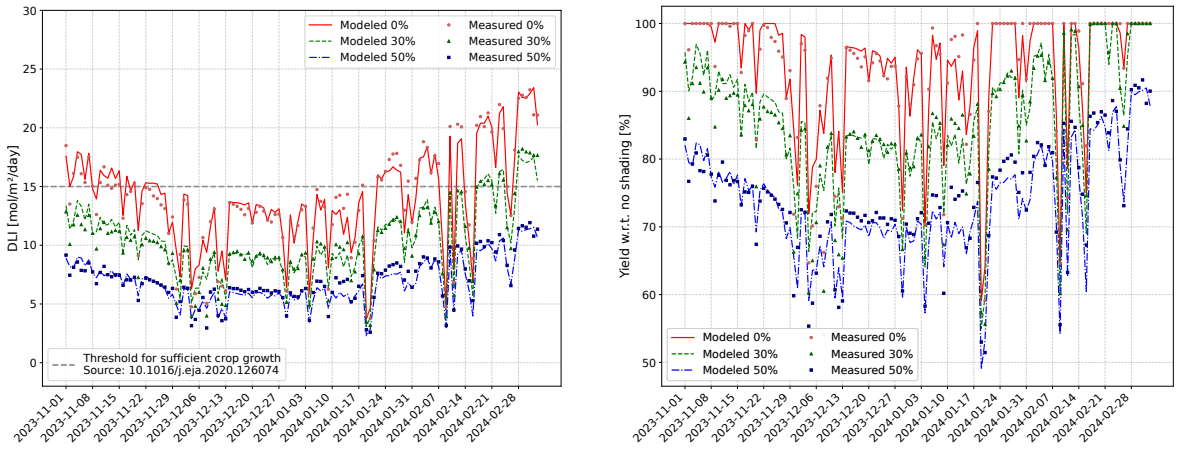


Figure 6.1: DLI and corresponding modeled daily yield over the crop cycle for three shading levels: 0% (red solid line), 30% (green dashed line), and 50% (blue dash-dotted line). **a)** DLI values based on simulation results and experimentally measured values for each shading treatment. **b)** Relative daily yield based on simulated DLI values (lines) and experimentally measured DLI values (markers) calculated from the nonlinear DLI-yield model (Equation 3.26) using the calibrated exponent $k_{\mathrm{DLI}} = 0.379$.

In order to obtain the total accumulated yield at the end of the crop cycle for the 30% and 50% shading zone, the daily yield values are summed and normalized to the unshaded control zone. Figure 6.2 depicts the accumulated yield $Y_{\mathrm{cum}}(t)$ for the three shading zones based on the simulations of the irradiance model. The experimentally measured fresh weight, normalized to the control zone without shading, is included for comparison.

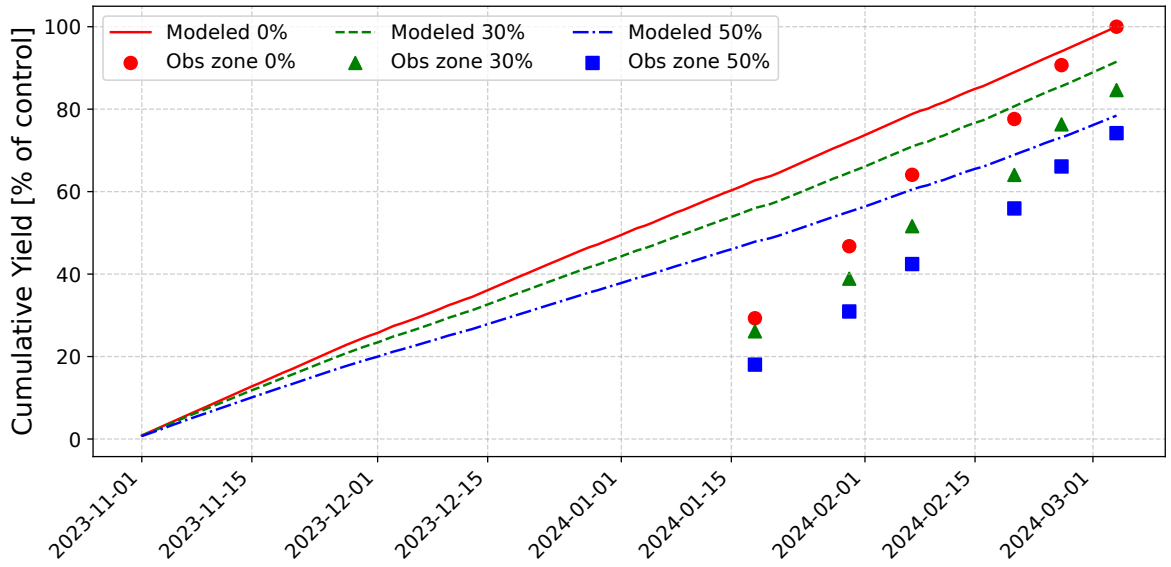


Figure 6.2: Cumulative relative yield with respect to no shading over time for three shading treatments: 0% (red), 30% (green), and 50% (blue). Solid, dashed, and dash-dotted lines show the modeled cumulative yield normalized to the control zone (0%) based on the nonlinear DLI-yield relationship with calibrated parameter $k_{\mathrm{DLI}} = 0.379$. Markers represent the experimentally measured cumulative fresh weight expressed as percentage of total yield in the unshaded control zone.

The plot shows that according to the model, harvestable yield is theoretically accumulated right from the start of the crop cycle, whereas the experimental measurements show that yield accumulation is only observed during the late stages of the crop cycle. Furthermore, final accumulated yield is overestimated by the simulation in comparison to the experimentally measured values. In the experiment, a reduction in fresh weight in comparison to the control zone of the harvested fruits of 15% for 30% shading and 26% for 50% shading was determined. Using the DLI-based crop modeling approach, the final yield decreased by 8% under 30% shading and by 20% under 50% shading compared to the control zone at the end of the crop cycle.

This overestimation of yield originates from the simplicity of the modeling approach, using only radiation as input data. Similarly, the model is unable to generate a natural shape for the yield accumulation curve. DLI is not the only factor influencing crop growth and yield in GHs. In a GH system other microclimate variables, such as temperature, RH, CO_2 content, etc., do also influence plant development and final yield. Furthermore, differences in airflow, irrigation or source-sink dynamics may also affect crop development, which is not depicted in the simulation.

Nevertheless, the modeling approach can be used in the design process for APV GHs with certain limitations. First, the model yields relative values with respect to an unshaded, conventional GH scenario. In order to obtain final crop yield quantities in $\mathrm{kg\,m^{-2}}$, the expected crop yield for the traditional GH case without APV installation has to be known. So far, only relative changes are calculated, as it is also the case in similar approaches as proposed by [126]. Additionally, the model was fed with localized simulations based on pyranometer positions within the investigated APV GH of Chapter 4, coupled with the results of the irradiance model. If the user requires a more generalized overview of

the irradiance conditions in the APV GH, the irradiance model would need to include a grid covering the entire GH area, with possible subdivisions into zones or multiple points of interest. Furthermore, in order to use the model as a stand-alone model, the user has to be aware of the uncertainties of the approach. In the presented results, we experienced an overestimation of 7 p.p. for 30% shading and 6 p.p. for 50% shading. This discrepancy originates from the simplicity of the approach, neglecting other microclimate and environmental conditions influencing the development process of the plants. In terms of final yield, such a discrepancy in yield may lead to unexpected economical losses.

6.1.2 YIELD ESTIMATION BASED ON DAILY LIGHT INTEGRAL, TEMPERATURE AND RELATIVE HUMIDITY

This section introduces the second DLI-based crop yield modeling method. In contrast to the previous approach, which relied solely on DLI values, this method also incorporates temperature and RH data to account for the influence of the greenhouse microclimate on crop yield and to generate a more realistic yield accumulation curve. In the presented approach, according to Section 3.2.2.2 Equation 3.27, we assume the following optimal conditions:

$$\mathrm{DLI}_{\mathrm{min}} = 15\,\mathrm{mol\,m^{-2}\,d^{-1}}, \quad T_{\mathrm{opt}} = 22\,^{\circ}\mathrm{C}, \quad RH_{\mathrm{opt}} = 70\,\%.$$

First, the cumulative DLI threshold before yield onset (D_0) was determined by fitting a linear model to the experimentally measured fresh yield data of the control zone. D_0 corresponds to the sum of all DLI values up to the point where the fitted line intersects the x-axis. This procedure resulted in $D_0 = 778\,\mathrm{mol\,m^{-2}\,d^{-1}}$, which was reached on 29 December 2023.

The remaining parameters ($\alpha, \gamma_{\mathrm{T}}, \varepsilon_{\mathrm{RH}}$, and k_{DLI}) were then estimated by applying a non-linear least-squares fit to the control zone data (simulated DLI together with measured temperature and RH). These parameters were subsequently used to simulate yield in the 30% and 50% shading zones. Figure 6.3 shows the cumulative yield with respect to the final experimentally measured yield of the 0% shading zone.

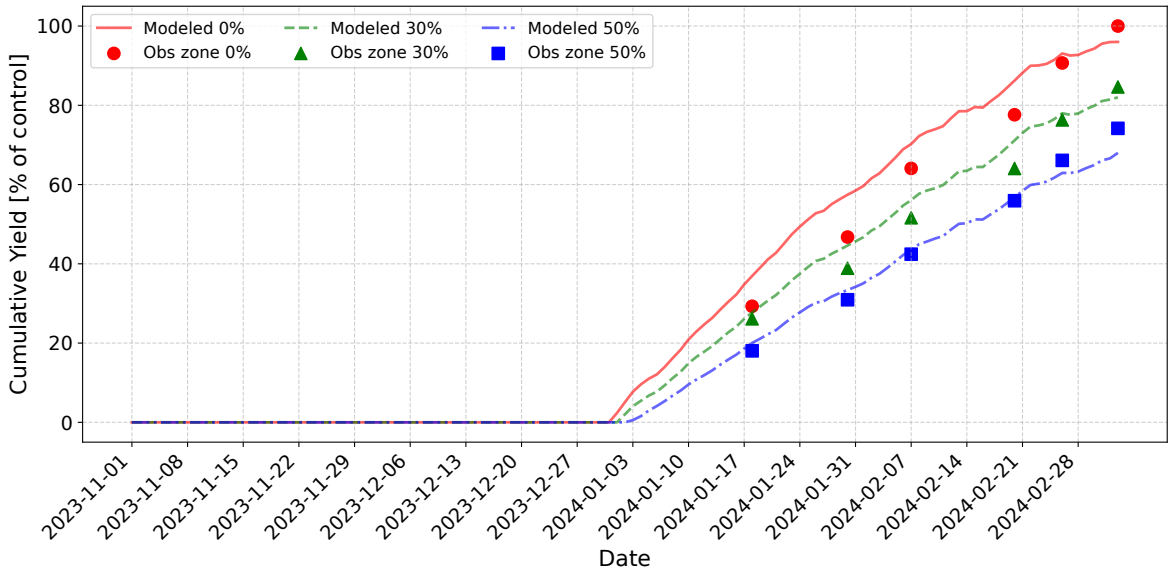


Figure 6.3: Cumulative tomato yield over time under three shading levels (0%, 30%, 50%), fitted using a Mitscherlich-type model. Points indicate experimentally measured cumulative fresh weight relative to the control zone, while lines represent simulations. Red, solid line: control zone. Green, dashed line: 30% shading. Blue, dash-dotted line: 50% shading.

The plot shows a sudden yield onset in all three zones, with delays of 2 days under 30% shading and 4 days under 50% shading. Overall, the simulated curves tend to overestimate measured data during most of the crop cycle, but converge towards the experimentally observed accumulated yield by the end. At the final harvest date, the model slightly underestimated total yield in all three zones. For the control zone, yield was underestimated by 4 p.p.. Under 30% shading, the underestimation was 3 p.p., corresponding to an 18% reduction relative to the final yield of the control zone. Under 50% shading, the underestimation reached 6 p.p., equivalent to a 32% reduction in final yield relative to the control zone.

The deviation between the simulated fresh weight curves and the experimentally measured fresh weight is evaluated based on the RMSE, nRMSE, MAE, nMAE and R^2 values. Table 6.1 summarizes the error metrics for the three shading zones.

Table 6.1: Error metrics by shading zone

Zone	RMSE	nRMSE	MAE	nMAE	R^2
0% Shading	0.07	0.10	0.07	0.09	0.91
30% Shading	0.04	0.07	0.04	0.07	0.95
50% Shading	0.03	0.06	0.03	0.05	0.97

In general, the factorization approach captured the yield behavior of the APV tomatoes with respect to the experimentally measured fresh weight data and presents a more natural curve for yield accumulation than the previously presented DLI approach in Figure 6.2. All error metrics (RMSE, nRMSE, MAE, nMAE) decreased, and R^2 increased with higher shading ratios. Interestingly, this indicates that the model simulates yield more accurately under 30% and 50% shading than in the control zone.

As shown in Figure 6.3, the simulated curves for the control zone and 30% shading tend to lie above most of the experimentally measured data points. In all three zones, the measured data show a steep increase in yield throughout the harvest period without entering a saturation phase toward the end of the crop cycle. This pattern results from the horticultural intervention of fruit pruning, which causes the tomato plants to stop growing and producing new fruits. Since no new fruits develop after pruning, the experimentally measured yield does not reflect a natural yield curve and appears nearly linear, which is difficult to simulate with the presented modeling approach.

Nevertheless, the approach demonstrates that using three input variables results in a more accurate reproduction of the natural shape of the yield accumulation curves compared to using only DLI as presented in Figure 6.2. To use the simulations as a stand-alone model fully independent from experimentally measured data a GH microclimate model is required to simulate RH and temperature based on the APV shading ratio. The current modeling approach is fitted to data from a single crop cycle of the APV GH experiment and cannot yet operate without these measured inputs. Developing such a microclimate model and integrating it into the current simulation workflow is beyond the scope of this thesis and could be addressed in future work.

6.1.3 Discussion of daily light integral-based crop modeling and comparison to state of the art

The modeling results presented in the previous section showed deviations from the experimentally measured fruit fresh weight at the the end of the harvest. The simulation results showed that yield response in APV scenarios can be approximated using DLI and microclimate, however, certain limitations have to be taken into account. This section aims to discuss the uncertainty sources and limitations of the general modeling approach using DLI thresholds and microclimate data of the greenhouse.

Firstly, deviations were generally expected as the presented yield modeling approaches are simplifications. The approach using accumulated DLI values assumes an accumulation of yield starting from the first day of the crop cycle. In reality, yield accumulation, as observed in the tomato crops during the experiment, only starts to accumulate after certain plant physiological stages have been passed.

Secondly, it has to be taken into account that in each development stage different DLI thresholds might be required. So far, DLI requirements are assumed to be constant throughout the crop cycle to simplify the model.

In addition, yield was treated as a smooth nonlinear function of DLI in the first approach. In reality, plant responses are more buffered, and non-linearities are not uniform across all stages of development. The presented modeling approach does not capture plant acclimation, phenology, or source-sink dynamics.

In order to take into account microclimatic changes in the APV scenarios, experimentally measured temperature and RH values were added to the modeling approach in the second presented method. The results showed that the addition of two further parameters to the model increased the ability of the model to reproduce the experimentally measured

data. Nevertheless, one has to take into account that the addition of experimentally measured data acts as a calibration to local conditions in the GH. Biological variability and measurement uncertainties always play a role in experiments, which might influence modeling results.

Nevertheless, the approach of DLI thresholds to estimate yield in APV scenarios is a common tool, frequently discussed and presented in the APV field due to its simplicity. For example, [236] used a modified GECROS model based on DLI values to simulate soybean under various shading levels and observed underestimations of yield with up to 16.5% RMSE at 27% shading. They noted that the parameterization of reproductive sink strength under reduced radiation remains a key source of error. [31] employed the STICS model based on radiation data to simulate wheat and lettuce under PV shading and found that their model consistently overestimated wheat yield under severe shading. They showed limitations in representing stomatal conductance adjustments and respiratory costs during fluctuating light levels as the major error source. Moreover, broad-scale models based on radiation, such as EPIC, tend to overestimate root and tuber crops in APV scenarios [45].

A different, commonly used approach for crop modeling based on experimentally measured crop yield data is presented in the empirical meta-analysis of [132]. The publication summarized the susceptibility of different crop types to shading based on literature data. The authors used the experimental yield results of open-field agrivoltaic studies and studies using shading nets to extract yield response curves for different groups of crops. Interestingly, their results suggested that berries, fruits, and fruity vegetables like tomatoes may show initial benefits up to 40% shade [132]. In particular, fruity vegetables may even experience increases in harvestable yield until about 20% reduction of solar radiation [132]. However, it is important to point out that the sub-category of fruity vegetables contained only the experimental results from three studies. Two of them were conducted on bell pepper during the summer months of the respective study periods in sub-tropical climate regions, where light levels are typically too high for the crops and were therefore reduced purposely with the shading cloths [237, 238]. The authors clarified that crop types with low availability of data points resulted in higher uncertainty, i.e. for fruity vegetables under 20% solar reduction the 95% confidence interval spans around the mean of +8% yield change roughly from –18% to +35% yield change compared to the unshaded control zone. At 40% reduction of solar radiation their results spans around +2% yield change with approximately –33% to +56%. Even though the authors excluded any type of GH study for their meta-analysis as the system difference to open-field APV was considered too large [132], there are similar studies conducted in "raspa y amagado" GHs in the Almería region which delivered comparable results. The study of [88] investigated the impact of aluminised shading screens with 40%, 50% and 60% shading in comparison to an unshaded control treatment on tomato yield during two consecutive years: For one of the investigated years they found no reduction in crop yield and marketable production throughout all shading treatments. In addition, the APV study of [36] was conducted during two growing seasons in a commercial GH for tomato production in Almería with approximately 10% shading provided by flexible PV panels mounted on the GH roofs. Their results showed that the reduction in radiation caused by the PV panels on the roof did not affect the total and marketable yield during both growing seasons. The results of [132] provide a set of initial indicators that may be used in assessing the suitability of crop

types for shade systems, and thus for APV or other dual land-use systems. Detailed yield response curves, as provided by their study, are valuable tools in optimizing the output of annual crop components in these systems. The results of our study complemented by the study results of [36] and [88] indicate that a similar classification of crop response for APV GH tomatoes to shading into shade-benefiting, -tolerating and -susceptible is possible. However, each study has to be clearly investigated for crop type, soil type, climate and provided shading in order to find homogeneous groups. This is also confirmed by [132] who pointed out that their meta-analysis cannot directly capture interactions of shading with other factors, such as water availability, where shading may reduce evapotranspiration and thus water stress. Therefore, dynamic crop growth models as presented in Section 6.1.2 may help to further optimize APV systems. The study of [132] also claims that further field experiments are needed especially for different APV designs (e.g., top-mounted PV panels with or without tracking or vertically mounted panels) to provide the input to calibrate these data driven models. Based on the shortcomings of their study they also formulated general recommendations for future APV research and e.g. mentioned that different levels of shading should be included at the same sites so that yield response curves can be created to optimize the level of shade, as done in our study. Furthermore, they recommended that crop types need to be studied based on the same type of measurement, e.g. dry matter-based yield should be preferred to assure that increased yields in fruits are not just the result of higher water contents. This approach was also already followed by our study as tomato dry weight directly correlates with their flavor and overall quality.

In summary, DLI-based approaches offer a practical framework for simulating yield in APV systems. However, the results point out that DLI-driven yield models must be calibrated to crops, and that microclimate interactions, e.g., changes in temperature and RH further influence model accuracy. This is in alignment with the results of empirical crop modeling analysis, as presented by [132]. One has to be aware of uncertainties arising from the simplicity of the different approaches, such as that yield is accumulated linearly and local microclimate effect might not be taken into account properly.

6.2 TOMGRO

This section evaluates the application of the reduced TOMGRO model to simulate tomato dry weight under APV conditions. As introduced in Section 3.2.3, the inputs of the reduced TOMGRO model are PPFD and temperature in hourly time resolution. The plant development is simulated based on these hourly time steps. The yield of the plant, described by the five output variables, is then calculated on a daily time scale.

To validate the reduced TOMGRO model with the presented APV GH experiment, the experimentally measured microclimate data was used. For each shading zone of the GH, the hourly PPFD, calculated based on GHI according to the method presented in Section 3.2.1, and the hourly averaged temperature, measured by the two temperature sensors in the central area, were used as input data. In the experiment, mature fruit dry weight was the only output variable of the reduced TOMGRO model that was measured.

Therefore, the TOMGRO model has been calibrated and validated on the basis of this variable. Figure 6.4 shows the workflow of the reduced TOMGRO model.

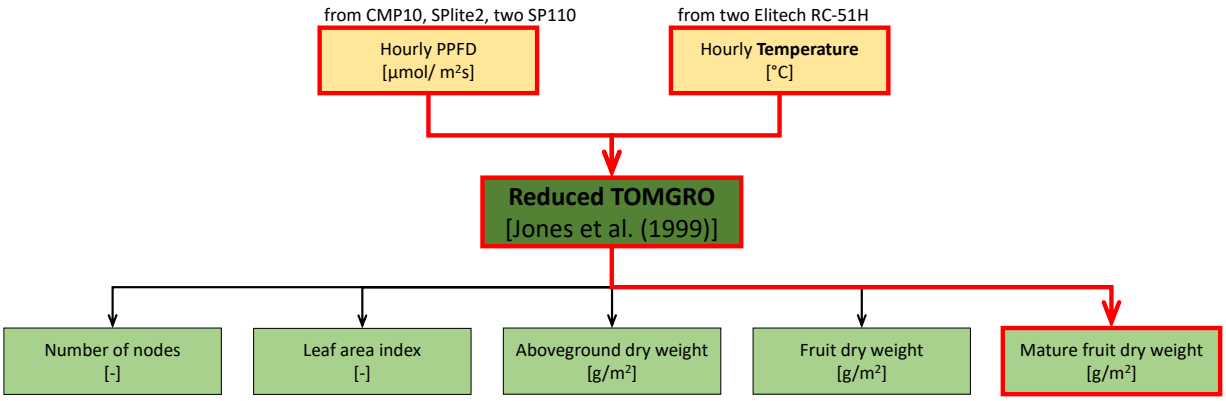


Figure 6.4: Scheme of the reduced TOMGRO model according to Jones et al. [190]. The mature fruit dry weight (marked in red) was simulated using the experimentally measured input data.

6.2.1 Calibration TOMGRO

To apply the model to local conditions of the experimental GH, a calibration of the model parameters was necessary. First, all model parameters and their value ranges were summarized from the literature. Table 3.4 in Section 3.2 summarizes all model parameters, their initial values and the corresponding variation range.

In [160], an eFAST sensitivity analysis was performed, which quantifies the influence of each parameter on the model output by computing both first-order and total effect sensitivity indices [194]. This analysis, implemented using the open source Python package SALib [239, 240], using Python version 3.9.13, identified those parameters as sensitive that contribute more than 10% to the total effect. In total, six parameters were found to be sensitive and transferred to the calibration process, i.e., Nm, D, Qe, T_{CRIT}, α_{F}, and $fF_$.

The PSO algorithm, a stochastic population-based optimization method, was employed for the calibration process [195]. The PSO algorithm iteratively refines candidate solutions based on both local and global best positions. For the implementation, the Python library Pyswarms was used [241].

To achieve an independent validation from the calibration process with data for only one crop cycle available, the model was calibrated using measurements from the 50% shading zone. Following the sensitivity analysis, the PSO algorithm [195] was then employed to find the set of calibrated model parameters by minimizing the RMSE between simulated and observed mature fruit dry weights. The resulting set of parameters was then tested against data from the 30% shading and control zones. In order to quantify the deviation between the simulated dry weight curves and the experimentally measured dry weight for the two remaining zones, the RMSE, MAE and R^2 were calculated.

Seven model parameters were selected for calibration based on the eFAST sensitivity analysis. The PSO algorithm was applied to minimize the RMSE between simulated and experimentally measured dry weight data. Table 6.2 summarizes the seven parameters and their calibrated values. The whole parameter set and the initial values are summarized in Table 3.4. The minimum RMSE value found in the calibration process was 8.54 $g\,m^{-2}$ for the 50% shading zone.

Table 6.2: Calibrated model parameters.

	Description	Calibrated Value
`Nm`	Node appearance rate per day	0.38 d^{-1}
`D`	Maximum leaf conductance to water vapor	2.33 $g\,m^{-2}\,h^{-1}$
`Qe`	Quantum efficiency of photosynthesis	0.44 mol(CO_2) / mol(photons)
`T_CRIT`	Critical temperature for photosynthesis decline	19.76 °C
α_F	Assimilate fraction allocated to fruit growth per day	0.86 d^{-1}
`fF_`	Fraction of dry matter allocated to fruits	0.90

6.2.2 Validation TOMGRO with experimental data

The calibrated TOMGRO model was then tested against the experimentally measured data of the 0% and 30% shading zone of the experiment. Figure 6.5 presents the simulated and observed dry weight data for all three shading zones.

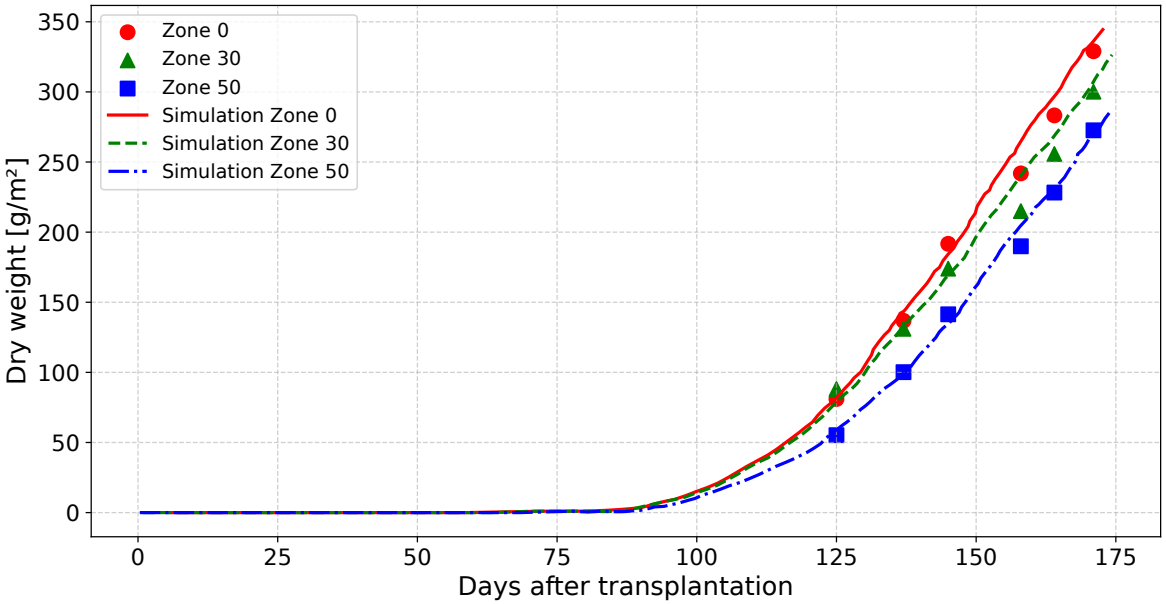


Figure 6.5: With TOMGRO simulated and experimentally measured dry weight data for all three shading treatments using the calibrated parameters based on the 50% shading zone. Red circles: experimentally measured dry weight control zone. Green triangles: experimentally measured dry weight 30% shading zone. Blue squares: experimentally measured dry weight 50% shading zone. Red, solid curve: simulation control zone. Green, dashed curve: simulation 30% shading zone. Blue, dashed-dotted curve: simulation 50% shading zone.

The deviation between the simulated dry weight curves and the experimentally measured dry weight for the two remaining shading zones is evaluated based on the RMSE, MAE and R^2 and summarized in Table 6.3 for the control zone and the 30% and 50% shading zones.

Table 6.3: Error metrics for the control zone and the 30% shading zone for the validation of the calibrated reduced TOMGRO model. The values of the 50% shading zone were obtained in the calibration process and are given for comparison.

Zone	RMSE [$g\,m^{-2}$]	nRMSE	MAE [$g\,m^{-2}$]	nMAE	R^2
0% Shading	7.76	0.04	4.14	0.02	0.99
30% Shading	11.56	0.07	7.11	0.04	0.98
50% Shading	8.54	0.05	4.34	0.03	0.99

In general, both datasets of the experimentally measured values are described realistically by the simulation with an RMSE below 12 $g\,m^{-2}$. The lower RMSE and MAE values of the 0% zone indicate better agreement of the simulation with the experimentally measured values than for the 30% zone. The MAE remains at 7.11 $g\,m^{-2}$ for the 30% shading zone

and 4.14 g m^{-2} for the control zone. At the end of the crop cycle, the deviation of the model from the experimentally measured values of the 30% shading zone was 4 p.p.. For the control zone, the simulations resulted in a deviation of 3 p.p. from the experimentally measured values at the end of the crop cycle.

The results point out the importance of a careful parameter calibration and also the need for independent validation datasets. The results presented here would potentially look different if the calibration had been performed with the dataset from a different zone than the 50% zone. Furthermore, the results highlight the importance of using real experimentally measured input data that correctly maps the microclimate in the APV GH. A common approach in recent studies using TOMGRO for yield estimation in APV GHs is yield simulation without real experimental input data under the assumption of constant and optimal temperature conditions [131, 242]. The presented study showed that for shading levels and PV patterns similar to the presented experiment, a change in microclimate should be expected, which can lead to non-optimal temperature conditions. Hence, adapted development of the tomatoes to the shading conditions should be observed subsequently. These changes can only be modeled accurately if the input data is adapted and a calibration of the model parameters to the site's conditions is performed. The main objective of the simulation was the application of a biophysical modeling approach to estimate crop yield under real APV GH conditions. The results of the simulation show that the reduced TOMGRO model can be adapted in general to simulate crop yield under reduced irradiance and temperature conditions. For future studies, the work can be extended to test the parameter calibration for additional crop cycles and crop types. An extension of the model to different GH types or climatic scenarios can also be studied in the future. The goal for the future and a possible application of the model would be one in which growers who are potentially interested in an APV setup for their GH could estimate the evolution of crop yield for their specific use case. Thus, an optimization of the APV setup related to ripening delays and market entry could be possible.

6.2.3 Discussion of simulation with the TOMGRO model

The modeling results presented in the previous chapter show a reasonable agreement with the experimentally measured dry weight data. In comparison to other studies that also used the reduced TOMGRO model or its adaptions to simulate APV scenarios, the presented results point out the advantages of a detailed calibration and validation. The study of [130] integrated the reduced TOMGRO model into their APV GH; however, they validated their simulations against the experimental measurements of [243] and the simulation values from the work of [244]. The modeling results of [130] underestimated both the experimental and the simulated values, with deviations of approximately 14% at the end of the crop cycle. Other studies on tomato yield in APV GHs neglect the calibration to site-dependent conditions and do not validate their application of the reduced TOMGRO model against experimental measurements [131, 242]. Furthermore, these models assume optimal and stable temperature conditions and do not take into account the potential effect of shading on temperature inside the GH. The presented experiment showed that shading may alter the microclimate inside the GH such that the cultivated plants adapt to these conditions.

Nevertheless, it is important to mention possible limitations of the presented modeling approach and discuss potential improvements for future studies. First, the presented experiment covered the time period of one growing cycle. To utilize the data from one growing cycle to test the TOMGRO model, the data from the 50% shading zone was used for model calibration. Subsequently, the model was applied to the 30% and 0% shading zones. In order to perform an independent validation, the experimentally measured data of a second crop cycle would be necessary. In future studies, the model could also be tested against measurements from different GH types or sites.

In the presented study, the model was calibrated and tested using experimentally measured mature fruit dry weight data. The reduced TOMGRO model also simulates four other state variables, i.e., number of nodes, leaf area index, aboveground dry weight and fruit dry weight. These datasets were not recorded in the presented study as the main goal was to monitor experimentally the changes in microclimate and successively changes in plant physiology and yield of the tomato crops. In order to perform a comprehensive model calibration and validation, additional datasets of these four parameters would be beneficial and could be monitored during a second growing cycle.

In addition to the available data, there are several other factors influencing the growth process of the tomato plants, which were not considered in the current modeling approach. These include information about soil, irrigation and diseases that are not directly included in the reduced TOMGRO model, as well as the assumption of a constant CO_2 content in the GH. In general, soil properties, irrigation and fluctuations in CO_2 concentration in the GH can play a non-negligible role in how plants develop and might not be mapped fully correctly in the presented modeling approach. Consequently, performing simulations with a new independent dataset could lead to diverging results as certain stress factors or growth conditions may not be correctly considered. In future studies, a comprehensive measurement campaign could focus on monitoring such additional GH environment and tomato growth variables.

6.3 COMPARISON AND EVALUATION OF CROP MODELS

To conclude, two approaches for crop yield modeling were presented and validated in the previous sections: DLI-based models and FSPMs. The DLI-based modeling approach is divided into two methods; one relying only on radiation data and the other one is an extension that additionally takes into account temperature and RH in the GH. For the FSPM, the application of the reduced TOMGRO model was presented.

6.3.1 GENERAL COMPARISON OF THE THREE METHODS

Depending on the simulation goals, each approach has its advantages and disadvantages. The two DLI-based methods do not simulate detailed plant phenology or growth. Instead, yield is aggregated over time and expressed as a relative fraction compared to the conventional, no-APV scenario. In contrast, the FSPM approach simulates yield in absolute terms.

The DLI-based method using solely radiation data can be coupled directly to the presented irradiance model and offers a flexible tool that can be easily adapted for different crops. For this method, simulated yield was compared against experimentally measured tomato yield data from the APV GH experiment. The comparison showed that with this method harvestable yield is produced from the beginning of the crop cycle and a natural shape of yield accumulation is not reproduced. However, at the end of the crop cycle the simulated yield for the 30% shading overestimated the experimentally measured data by only 7 p.p.. For 50% shading, the simulation overestimated the experimentally measured yield by 6 p.p..

The DLI-based method extended with temperature and RH data is an approach to additionally take into account GH microclimate and its effect on crop growth and yield. This approach does only work if these three parameter sets (radiation, temperature and RH) are available. To solely work simulation-based, an additional GH microclimate model would be needed. In this thesis, the method was tested using a hybrid approach: simulated radiation data from the irradiance model combined with experimentally measured microclimate data from the APV GH experiment. The simulated yield was then compared to the experimentally measured yield from the same experiment. Overall, the simulation underestimated the final yield across all three zones of the experiment. Specifically, the simulation underestimated yield by 4 p.p. in the control zone, 3 p.p. under 30% shading, and 6 p.p. under 50% shading.

The coupling of FSPMs to the irradiance model is more complex than the DLI-based methods. For the application of the reduced TOMGRO model, a detailed calibration to site-specific conditions was necessary. The calibrated model can be used as a stand-alone model coupled to the irradiance model using radiation and temperature as input data (needing a microclimate model for temperature data). A key advantage of TOMGRO is the detailed simulation it offers, providing insights into tomato plant development at the organ level. This allows for easy identification of stress factors and their impacts on crop yield. Additionally, TOMGRO directly simulates the weight of harvested fruits rather than a relative yield. However, TOMGRO is specific to tomatoes and the presented calibrated model only valid under the climate conditions of the test site. In this thesis, the reduced TOMGRO model was applied using experimentally measured irradiance and temperature data from the APV GH experiment. The simulated dry weight of the tomatoes was then compared to experimentally measured dry weight. The simulation produced a natural shape of yield accumulation and aligned well with the experimentally measured yield data, as confirmed by the evaluation of RMSE, MAE and R^2.

6.3.2 Error sources of the three methods

While the presented crop yield modeling approaches reproduced the observed yield reductions, both the experimental measurements and the simulations of the presented study have additional sources of uncertainty that should be taken into account in the interpretation of the data.

First, uncertainties in our microclimate inputs may propagate through the yield simulations as experimental measurements always carry certain uncertainties. Sensor soiling,

environmental influences or technical limitations might affect the accuracy of the input data of the model and thus influence the outputs of the simulations. The sensors deployed in the experiment were calibrated in advance and constantly cleaned during the measurement period in order to minimize uncertainties due to soiling or tilting. Furthermore, daily quality control was performed with the measured microclimate data. Nevertheless, residual errors may remain.

In addition, the use of the linear regression model to convert GHI to PAR by [159] introduces its own uncertainty. Although deviations are minimal for validation locations, it should be kept in mind that the method may introduce additional uncertainties to the model, as the relationship between GHI and PAR is not always linear and can be influenced by local environmental conditions. Furthermore, the method of Vindel et al. [159] has been developed for outside conditions. The irradiance spectrum within the GH can be different from the one outside due to the transmission through the GH plastic, which introduces another source of uncertainty in the presented study. In a future measurement campaign, specifically chosen PAR radiation sensors, only monitoring the PAR spectrum, could be deployed in the GH to avoid the additional conversion step in the data evaluation.

In the presented experimental study all three zones were located within the same GH without any physical separation. Hence, a constant exchange of air flow between the zones was not actively prevented. In addition, all plants were irrigated equally and a potential change in water needs of the plants due to shading was not observed. Ideally, a separate GH would be needed for each shading treatment to ensure that the specific conditions of each zone are studied without interference from neighboring zones. Nevertheless, clear differences in the microclimate were observed with the presented experimental setup. These deviations were then also mapped realistically in the crop yield simulations of the three different zones.

In general, the presented crop modeling approaches showed that calibration to local climatic conditions is necessary to understand crop response to APV conditions. In APV systems, understanding the interaction between crops and partial shading by PV panels is crucial. The validation of crop models like TOMGRO plays a significant role in enhancing the prediction of crop growth and yield under APV conditions. In this thesis, the validation of the crop models was limited to the data set of one crop cycle which was divided into the three shading zones. In order to achieve an independent validation and use the model to forecast yield, further datasets of following crop cycles would be necessary. Future research could focus on further independent validation of the model with additional crop cycle data.

The coupling of the presented crop modeling framework with a techno-economic model could also be explored in future work, as the true benefit of APV systems lies in the synergy between electricity generation and crop production. This was already highlighted in the economic assessment of the APV GH experiment presented in Section 4.4. One potential approach is the development of a comprehensive framework that includes economic yield estimation, similar to the regional-scale evaluations conducted by [230] for the Canary Islands or the national-scale assessment by [231] for the United States.

7

Conclusion and outlook

"Long story short, I survived."

—Taylor Swift

7.1 Conclusion

Agrivoltaic (APV) systems are a promising tool to decrease potential conflicts over land between the agricultural and energy sector [30]. Furthermore, they promote sustainable land use through reduced irrigation needs [20, 27, 28] and a higher economic profitability for farmers [26]. APV systems are particularly suited for semi-arid and arid regions [20, 21], where light intensity might be higher than the crops' needs, and additional shading can have a positive impact on crop growth [30, 31]. Even in temperate climates, APV systems can protect crops from increasingly frequent extreme weather events, such as hail and heavy rainfall [245, 246]. Research in APV is steadily increasing [46, 247, 248, 249, 250]. Nevertheless, the application of APV concepts to Mediterranean greenhouses (GHs) in the Almería region has so far been addressed in only a few studies, leaving several scientific and practical questions unanswered [35, 36, 37, 38, 39, 40]. This thesis expands the available experimental datasets and presents a simulation tool for irradiance distribution and crop yield estimation in APV GHs.

Four research questions were defined at the beginning of this thesis. The first question examined how irradiance distribution inside APV GHs can be modeled for different GH designs and PV module configurations. The second question addressed how crop yield can be estimated based on the irradiance levels obtained from these simulations. The third research question focused on how the additional shading introduced by PV modules influences the microclimate inside the GH. Finally, the fourth question explored whether the integration of PV modules on GH roofs can provide economic benefits to farmers.

In Chapter 3, the methodology of the simulation framework is presented. The modeling chain is split into the irradiance and the crop yield modeling part. The software framework of the irradiance model is based on the ray-tracing software `Radiance`. With the model, detailed 3D-replicates of APV GHs can be generated. A workflow to implement complex GH cover materials consisting of multi-layered LDPE has been developed and tested. The

transmitted global horizontal irradiance (GHI) inside the GH is then simulated based on the transmission properties of the GH cover materials and the arrangement of the PV modules. The crop model presents two different approaches. The first approach is based on the daily light integral (DLI) requirements of various crops and is divided into two methods. The first method compares the DLI calculated from the simulated GHI with the crop-specific DLI requirements on a daily basis. The second method extends this comparison by including additional thresholds for temperature and relative humidity inside the APV GH to account for microclimatic effects on crop growth. The second approach focuses specifically on tomatoes and applies the reduced TOMGRO model to estimate yield under different shading scenarios.

In Chapter 4, the APV GH experiment performed from September 2023 to March 2024 is presented. The experiment was conducted in a commercial scale "raspa y amagado" GH in Almería, and two roof cover ratios of 30% and 50% shading were compared against an unshaded control zone. During the experiment, data on the GH microclimate, plant physiology, and crop yield and quality were collected. The irradiance measurements showed that throughout the study period, radiation levels were reduced on average by 48% in the 50% zone and by 25% in the 30% zone. This slight decrease with respect to the theoretical shading reduction of the 30% zone was caused by the orientation of the GH and the positioning of the zones. The high shading levels of the APV GH experiment altered the GH microclimate, which in turn affected yield, fruit quality, and harvest timing. The 30% and 50% shading zones led to yield reductions of 15% and 26%, respectively, in fresh weight at the end of the crop cycle compared with the control zone. The 30% shading zone had a smaller impact on fruit quality than the 50% shading zone, showing an increasing trend in soluble solids content toward the end of the experiment. In contrast, 50% shading caused significant reductions in both yield and fruit quality. The experiment was conducted with relatively high shading ratios compared with previous studies, which reported no yield decline for shading ratios of around 10% [35, 36]. In the presented APV GH experiment, high shading levels have been selected in order to add data points to the experimental data available in literature for "raspa y amagado" GHs. An expanded dataset will help the scientific community move closer to identifying the shading threshold that still allows for optimal crop growth.

To address the research question of whether integrating PV modules on GH roofs provides an economic benefit, an economic assessment was conducted for the winter study period. The crop revenue from a GH without PV installation was estimated at 1.82€ m^{-2} for the tomato cycle during winter months with low light availability. When including the electricity revenue from the PV modules, the energy demand of the GH was covered by the electricity generated by the PV system and crop yield losses were overcompensated by feeding excess energy into the grid. The results showed that 50% roof coverage with PV could achieve a profit increase of up to +22%, while a 30% coverage could already result in a +15% increase in profit for the winter months of the tomato cycle with low light availability. Shading of PV modules gets particularly helpful in the summer months when photosynthetic saturation can occur and the naturally higher irradiation levels might become harmful for the crops in the GHs. Therefore, the economic assessment was extended for the full year under the assumption of a hypothetical, consecutive tomato growing cycle. This second growing cycle increased the total crop revenue to 3.64€ m^{-2} for

the full year for a GH without PV installation. For the 30% shading scenario, the combined revenue of two crop cycles and the PV system would be at 4.16€ m^{-2} for the full year. For a GH with 50% roof coverage, the total income can be estimated at 4.39€ m^{-2}. Compared with a conventional greenhouse without PV installation, this corresponds to a net annual profit increase of 14.3% and 20.6% for 30% and 50% PV coverage, respectively. These findings highlight the economic potential of APV GH systems and point out the advantages of APV systems: APV GHs can generate an additional income source for growers, enhance self-sufficiency, and reduce dependence on fluctuating crop and energy market prices.

In Chapter 5, the irradiance model is validated using both literature data and experimentally measured data from the APV GH experiment. For the literature-based validation, a “Venlo”-type APV GH experiment conducted in 2014–2015 was reproduced. The positions of the radiation sensors in the experimental GH were estimated by minimizing the nRMSE for one day of irradiance raw data. Subsequently, the GHI inside the GH was simulated for the entire crop cycle in 15-min intervals, resulting in a deviation of 2.88 percentage points in the simulated reduction in radiation over the full crop cycle. For the validation with the experimental data from the "raspa y amagado" APV GH experiment, the same procedure was applied. The radiation sensors position were transferred to the simulation and defined by minimizing the nRMSE for a set of clear-sky days during the time frame of the experiment. Simulations were then performed for the defined sensor coordinates to simulate GHI inside the GH for the entire time period of the experiment. The nRMSE of the GHI of the irradiance model was determined to be 0.09 for the control zone, 0.18 for 30% shading and 0.27 for 50% shading using the irradiance data from the experiment. The model is capable to clearly reproduce the shading patterns caused by the PV modules and also simulate shading related to the GH structure itself. Overall, these validations have shown that the irradiance model can augment the scope of irradiance modeling for APV GHs over the state-of-the-art: The spatial and temporal resolution of the simulations, the adaptability to different sites, time periods and GH types and the accuracy of the ray-tracing-based irradiance simulations were all increased notably.

In Chapter 6, the validation of the different approaches for crop modeling are presented. All approaches were validated exclusively with data from the 2023–2024 APV GH experiment. The solely DLI-based method overestimated crop yield by 7 percentage points for 30% shading and by 6 percentage points for 50% shading. The extension of the solely DLI-based method with data for GH temperature and RH helped achieve a more natural curve for yield accumulation of the tomatoes in the GH. The nRMSE of the fresh weight for the crop cycle was 0.07 for the unshaded control zone, 0.04 for 30% shading and 0.03 for 50% shading. The validation of the reduced TOMGRO model yielded an nRMSE of dry weight of 0.04 for the unshaded control zone and 0.07 for the 30% shading zone, while the data from the 50% shading zone was used to calibrate the model. The results of the reduced TOMGRO validation point out the importance of a careful parameter calibration and also the need for independent validation datasets. Nevertheless, the results highlight the importance of using real experimentally measured input data that correctly maps the microclimate in the APV GH. The validation of the reduced TOMGRO model in the presented application augmented the scope of yield modeling for APV systems over the state-of-the art by using real experimental input data instead of the assumption of constant and optimal temperature conditions inside the GH.

In conclusion, the presented simulation framework, validated under real GH conditions, demonstrates a high spatial and temporal resolution. It offers a reliable framework for designing and optimizing APV GH systems. Its application can support the development of efficient and sustainable APV GH designs in future research and practice.

7.2 OUTLOOK

This thesis presents one of the first holistic research works on yield modeling for APV GHs combined with the results from a real-scale APV GH experiment. In the thesis further enhancements and possible approaches were already identified that are not implemented and investigated yet. This section summarizes the main enhancements and gives an outlook for future studies.

Firstly, regarding the irradiance model, so far incident-angle dependent light transmission is not accounted for in the current implementation of the GH cover materials. In order to extend the model by including the new material category `transdata`, laboratory measurements of BSDFs of specific GH plastics would be needed. Adding angle-sensitive light transmission could be an interesting step to be able to compare different films and GH cover materials, e.g. clear, diffuse, anti-reflective coatings and their performance could be studied across seasons and latitudes. This would allow for an even more detailed optimization of the cover materials for APV applications.

Secondly, the crop yield estimations, particularly the calibration and validation of the reduced TOMGRO model were performed with the data from one crop cycle. Here, the dataset of one shading zone was used to calibrate the model, while the validation was done with the data of the other two remaining shading zones. In order to perform an independent validation, the experimentally measured data of a second crop cycle would be necessary. In future studies, the model could also be tested against measurements from different GH types or sites. In addition to that, the reduced TOMGRO model was calibrated and tested using experimentally measured mature fruit dry weight data. The reduced TOMGRO model also simulates four other state variables, i.e., number of nodes, leaf area index, aboveground dry weight and fruit dry weight. In order to perform a comprehensive model calibration and validation, additional datasets of these four parameters would be beneficial and could be monitored during a second growing cycle. This could be an interesting step toward application and validation of the presented model in a broader context.

Several other APV studies already pointed out that water use efficiency is improved underneath PV panels in APV systems by lowering crops' evaporation rates and their overall water needs [20, 27, 28]. In the presented experiment, irrigation was not monitored as it was not part of the scope of the thesis, hence, no conclusion on improved water-use efficiency was drawn from the experiment. In future studies, a comprehensive measurement campaign could focus on monitoring evapotranspiration and irrigation of the GH crops, which can be an interesting topic in future climate scenarios with limited water resources.

Lastly, this thesis included a preliminary economic assessment, which we used to demonstrate a potential profit increase for the presented APV GH experiment. This economic assessment was based on simplified assumptions and could be enhanced in future studies. Particularly, questions about installation, maintenance, exchange of GH cover materials without PV replacement, whitewashing practice and also system costs have only been briefly answered in this thesis. A detailed feasibility study on APV concepts for "raspa y amagado" GHs could support social acceptance and motivate growers to invest in APV systems for their GHs.

The presented work improved the understanding of how PV modules installed on GH roofs influence GH microclimate, crop development and yield under APV conditions. The developed model can be used in the future to optimize PV module layouts to maintain light homogeneity inside the GH and minimize yield losses due to shading. In the next step, the model can be applied to develop dynamic shading strategies for APV GHs with tracked PV modules. This approach is particularly promising, as in conventional GHs the roof transmittance is typically adjusted according to crops' needs and market demands.

What remains to be finally addressed is the broader picture. APV as a research topic combines multiple scientific fields. Within this thesis alone, topics from physics-based light modeling and biophysical crop modeling to plant physiological measurements and crop yield and quality assessments were investigated. Yet, APV as a practical approach to mitigating climate change, especially when implemented at large scales, is more than only a scientific question. Its development and success are also influenced by socio-cultural, regulatory, and political-institutional contexts that determine how the technology is funded, sited, deployed, managed, and maintained.

In the region of Almería, for instance, GHs form an essential part of the local landscape, economy, and cultural identity. However, this thesis did not address aspects of social acceptance, stakeholder perception, or the current legal and policy frameworks governing APV systems in Spain. These dimensions are crucial for ensuring the long-term feasibility and acceptance of APV technologies. Future studies should therefore also integrate perspectives from farm owners, local communities, policymakers, and technical experts to better understand how APV is perceived and can be adopted in real-world contexts. Combining such insights with scientific work, such as the technical and agronomic results presented in this thesis, will be important to successfully upscale and integrate APV GH systems into regional and national sustainability strategies.

Bibliography

[1] Umweltbundesamt Deutschland. *Indikator: Globale Lufttemperatur*. 2025. URL: https://www.umweltbundesamt.de/daten/umweltindikatoren/indikator-globale-lufttemperatur#die-wichtigsten-fakten. Accessed: 2025-09-12. (Cit. on p. 1).

[2] NASA's Goddard Institute for Space Studies (GISS). *Global Temperature*. 2025. URL: https://climate.nasa.gov/vital-signs/global-temperature/?intent=121. Accessed: 2025-09-12. (Cit. on p. 1).

[3] K. Myers et al. "Consensus revisited: quantifying scientific agreement on climate change and climate expertise among Earth scientists 10 years later". In: *Environmental Research Letters* 16.10 (Oct. 2021), p. 104030. DOI: 10.1088/1748-9326/ac2774 (cit. on p. 1).

[4] M. Lynas et al. "Greater than 99% consensus on human caused climate change in the peer-reviewed scientific literature". In: *Environmental Research Letters* 16.11 (Oct. 2021), p. 114005. DOI: 10.1088/1748-9326/ac2966 (cit. on p. 1).

[5] J. Cook et al. "Consensus on consensus: a synthesis of consensus estimates on human-caused global warming". In: *Environmental Research Letters* 11.4 (Apr. 2016), p. 048002. DOI: 10.1088/1748-9326/11/4/048002 (cit. on p. 1).

[6] J. Cook et al. "Quantifying the consensus on anthropogenic global warming in the scientific literature". In: *Environmental Research Letters* 8.2 (May 2013), p. 024024. DOI: 10.1088/1748-9326/8/2/024024 (cit. on p. 1).

[7] W. R. L. Anderegg. "Expert Credibility in Climate Change". In: *Proceedings of the National Academy of Sciences* 107.27 (June 2010), pp. 12107–12109. DOI: 10.1073/pnas.1003187107 (cit. on p. 1).

[8] P. T. Doran and M. K. Zimmerman. "Examining the Scientific Consensus on Climate Change". In: *Eos Transactions American Geophysical Union* 90.3 (2009), p. 22. DOI: 10.1029/2009EO030002 (cit. on p. 1).

[9] N. Oreskes. "Beyond the Ivory Tower: The Scientific Consensus on Climate Change". In: *Science* 306.5702 (Dec. 2004), p. 1686. DOI: 10.1126/science.1103618 (cit. on p. 1).

[10] Intergovernmental Panel on Climate Change (IPCC). *Climate Change 2021 – The Physical Science Basis: Working Group I Contribution to the Sixth Assessment Report of the Intergovernmental Panel on Climate Change*. Cambridge University Press, 2023 (cit. on p. 1).

[11] UNFCCC. *The Paris Agreement*. Publication. Published in conjunction with the Paris Climate Change Conference (COP 21), November 2015. Nov. 2018. URL: https://unfccc.int/process-and-meetings/the-paris-agreement/the-paris-agreement (cit. on p. 1).

[12] European Commission. *The European Green Deal*. 2024. URL: https://commission.europa.eu/. Accessed: 2024-05-14. (Cit. on p. 1).

[13] European Union. *Directive (EU) 2023/2413 of the European Parliament and of the Council of 18 October 2023 amending Directive (EU) 2018/2001 on the promotion of the use of energy from renewable sources*. Accessed: 2025-10-03. URL: http://data.europa.eu/eli/dir/2023/2413/oj (cit. on p. 1).

[14] United Nations, Department of Economic and Social Affairs, Population Division. *World Population Prospects 2022: Summary of Results*. Tech. rep. UN DESA/POP/2022/TR/NO. 3. New York: United Nations, 2022. URL: https://www.un.org/development/desa/pd/sites/www.un.org.development.desa.pd/files/wpp2022_summary_of_results.pdf (cit. on p. 1).

[15] Food and Agriculture Organization of the United Nations. *How to Feed the World in 2050*. Briefing Paper. Accessed: 2025-10-03. Rome: High-Level Expert Forum, 2009. URL: https://www.fao.org/fileadmin/templates/wsfs/docs/expert_paper/How_to_Feed_the_World_in_2050.pdf (cit. on p. 1).

[16] Food and Agriculture Organization of the United Nations. *Biofuels and Food Security. A report by the High Level Panel of Experts on Food Security and Nutrition*. June 2013. URL: https://www.osti.gov/biblio/22110315 (cit. on p. 1).

[17] D. Ketzer. "Land Use Conflicts between Agriculture and Energy Production: Systems Approaches to Allocate Potentials for Bioenergy and Agrophotovoltaics". PhD dissertation. Stockholm University, Department of Physical Geography, 2020. URL: https://urn.kb.se/resolve?urn=urn:nbn:se:su:diva-177399 (cit. on p. 2).

[18] A. Chatzipanagi, N. Taylor, and A. Jaeger-Waldau. *Overview of the potential and challenges for Agri-Photovoltaics in the European Union*. Scientific analysis or review, Policy assessment KJ-NA-31-482-EN-N (online). Luxembourg (Luxembourg), 2023. DOI: 10.2760/208702(online) (cit. on p. 2).

[19] European Environmental Bureau. *Land for Renewable Energy Sources: A Sustainable Approach to Land Use Planning*. Retrieved from European Environmental Bureau. 2024. URL: https://eeb.org/wp-content/uploads/2024/07/Land_for_RES_Report.pdf (cit. on p. 2).

[20] H. Marrou, L. Dufour, and J. Wery. "How does a shelter of solar panels influence water flows in a soil–crop system?" In: *European Journal of Agronomy* 50 (2013), pp. 38–51. ISSN: 1161-0301. DOI: 10.1016/j.eja.2013.05.004 (cit. on pp. 2, 129, 132).

[21] S. Ravi et al. "Colocation opportunities for large solar infrastructures and agriculture in drylands". In: *Applied Energy* 165 (2016), pp. 383–392. ISSN: 0306-2619. DOI: 10.1016/j.apenergy.2015.12.078 (cit. on pp. 2, 129).

[22] D. Valera, L. Belmonte, F. Molina-Aiz, and A. López. *Greenhouse Agriculture in Almeria. A comprehensive techno-economic analysis*. Mar. 2016, p. 504. ISBN: 978-84-95531-75-9 (cit. on pp. 2, 8, 12–17, 37, 51, 59, 82, 86, 93, 96).

[23] A. Marucci, A. Gusman, B. Pagniello, and A. Cappuccini. "Limits and prospects of photovoltaic covers in Mediterranean greenhouses". In: *Journal of Agricultural Engineering* 44 (2013), e1. DOI: 10.4081/jae.2013.e1 (cit. on p. 2).

[24] M. Carlini, T. Honorati, and S. Castellucci. "Photovoltaic Greenhouses: Comparison of Optical and Thermal Behaviour for Energy Savings". In: *Mathematical Problems in Engineering* 2012 (2012), pp. 743–764. DOI: 10.1155/2012/743764 (cit. on p. 2).

[25] A. Baille, C. Kittas, and N. Katsoulas. "Influence of whitening on greenhouse microclimate and crop energy partitioning". In: *Agricultural and Forest Meteorology* 107 (2001), pp. 293–306. DOI: 10.1016/S0168-1923(01)00216-7 (cit. on pp. 2, 16).

[26] A. Kujawa, N. Hanrieder, S. Wilbert, F. Wolfertstetter, J. Carballo, N. Osterthun, J. Polo, C. Alonso, and R. Pitz-Paal. "Economic study of agrivoltaic greenhouses in Spain and the Netherlands." In: *AgriVoltaics2022*. 2022. URL: https://elib.dlr.de/189270/ (cit. on pp. 2, 129).

[27] E. Hassanpour Adeh, J. Selker, and C. Higgins. “Remarkable agrivoltaic influence on soil moisture, micrometeorology and water-use efficiency”. In: *PLOS ONE* 13.11 (Nov. 2018), pp. 1–15. DOI: 10.1371/journal.pone.0203256 (cit. on pp. 2, 129, 132).

[28] Y. Elamri, B. Cheviron, J.-M. Lopez, C. Dejean, and G. Belaud. “Water budget and crop modelling for agrivoltaic systems: Application to irrigated lettuces”. In: *Agricultural Water Management* 208 (2018), pp. 440–453. ISSN: 0378-3774. DOI: 10.1016/j.agwat.2018.07.001 (cit. on pp. 2, 129, 132).

[29] L. Hannah et al. “Climate change, wine, and conservation”. In: *Proceedings of the National Academy of Sciences* 110.17 (2013), pp. 6907–6912. DOI: 10.1073/pnas.1210127110 (cit. on p. 2).

[30] G. A. Barron-Gafford, M. A. Pavao-Zuckerman, R. L. Minor, L. F. Sutter, I. Barnett-Moreno, D. T. Blackett, M. Thompson, K. Dimond, A. K. Gerlak, G. P. Nabhan, and J. Macknick. “Agrivoltaics provide mutual benefits across the food–energy–water nexus in drylands”. In: *Nature Sustainability* 2 (2019), pp. 848–855. DOI: 10.1038/s41893-019-0364-5 (cit. on pp. 2, 80, 129).

[31] H. Dinesh and J. M. Pearce. “The potential of agrivoltaic systems”. In: *Renewable & Sustainable Energy Reviews* 54 (2016), pp. 299–308. DOI: 10.1016/j.rser.2015.10.024 (cit. on pp. 2, 6, 119, 129).

[32] N. Hanrieder, A. Kujawa, A. B. Seychelles, M. Blanco, J. Carballo, and S. Wilbert. “Estimation of maximum photovoltaic cover ratios in greenhouses based on global irradiance data”. In: *Applied Energy* 365 (2024), p. 123232. DOI: 10.1016/j.apenergy.2024.123232 (cit. on pp. 2, 82).

[33] A. Götzberger and A. Zastrow. “On the Coexistence of Solar-Energy Conversion and Plant Cultivation”. In: *International Journal of Solar Energy* 1.1 (1982), pp. 55–69. DOI: 10.1080/01425918208909875 (cit. on pp. 2, 5).

[34] C. Dupraz, H. Marrou, G. Talbot, L. Dufour, A. Nogier, and Y. Ferard. “Combining solar photovoltaic panels and food crops for optimising land use: Towards new agrivoltaic schemes”. In: *Renewable Energy* 36 (2011), pp. 2725–2732. DOI: 10.1016/j.renene.2011.03.005 (cit. on pp. 2, 6).

[35] R. Urena-Sanchez, A. J. Callejon-Ferre, J. Perez-Alonso, and A. Carreño-Ortega. “Greenhouse tomato production with electricity generation by roof-mounted flexible solar panels”. In: *Scientia Agricola* 69 (2011), pp. 233–239. DOI: 10.1590/S0103-90162012000400001 (cit. on pp. 3, 18, 20, 129, 130).

[36] R. Aroca-Delgado, J. Perez-Alonso, A. J. Callejon-Ferre, and M. Diaz-Perez. “Morphology, yield and quality of greenhouse tomato cultivation with flexible photovoltaic rooftop panels (Almería-Spain)”. In: *Scientia Horticulturae* 257 (2019), p. 108768. DOI: 10.1016/j.scienta.2019.108768 (cit. on pp. 3, 20, 119, 120, 129, 130).

[37] K. Ezzaeri, H. Fatnassi, R. Bouharroud, L. Gourdo, A. Bazgaou, A. Wifaya, H. Demrati, A. Bekkaoui, A. Aharoune, C. Poncet, et al. “The effect of photovoltaic panels on the microclimate and on the tomato production under photovoltaic Canarian greenhouses”. In: *Solar Energy* 173 (2018), pp. 1126–1134. DOI: 10.1016/j.solener.2018.08.043 (cit. on pp. 3, 21, 129).

[38] K. Ezzaeri, H. Fatnassi, A. Wifaya, A. Bazgaou, A. Aharoune, C. Poncet, A. Bekkaoui, and L. Bouirden. “Performance of photovoltaic canarian greenhouse: A comparison study between summer and winter seasons”. In: *Solar Energy* 198 (2020), pp. 275–282. ISSN: 0038-092X. DOI: 10.1016/j.solener.2020.01.057 (cit. on pp. 3, 21, 129).

[39] M. Cossu, L. Murgia, L. Ledda, P. Deligios, A. Sirigu, F. Chessa, and A. Pazzona. “Solar radiation distribution inside a greenhouse with south-oriented photovoltaic roofs and effects on crop productivity”. In: *Applied Energy* 133 (2014), pp. 89–100. DOI: 10.1016/j.apenergy.2014.07.070 (cit. on pp. 3, 18, 21, 22, 76, 109, 129).

[40] G. Lopez-Diaz, A. Carreno-Ortega, H. Fatnassi, C. Poncet, and M. Diaz-Perez. “The Effect of Different Levels of Shading in a Photovoltaic Greenhouse with a North–South Orientation”. In: *Applied Sciences* 10 (2020), p. 882. DOI: 10.3390/app10030882 (cit. on pp. 3, 15, 16, 23, 74–76, 85–88, 90–93, 97, 104, 108, 109, 129).

[41] B. Willockx et al. “Geospatial assessment of elevated agrivoltaics on arable land in Europe to highlight the implications on design, land use and economic level”. In: *Energy Reports* 8 (July 2022), pp. 8736–8751. DOI: 10.1016/j.egyr.2022.06.076 (cit. on pp. 3, 109).

[42] A. Kujawa, N. Hanrieder, S. Wilbert, A. Fernandez Solas, S. Gonzalez Rodriguez, M.d.C. Alonso-Garcia, J. Polo, J.A. Carballo, G. Lopez-Diaz, C. Cornaro, and R. Pitz-Paal. “A Ray-Tracing-Based Irradiance Model for Agrivoltaic Greenhouses: Development and Application”. In: *Agronomy* 15 (2025), p. 665. DOI: 10.3390/agronomy15030665 (cit. on pp. 5, 85, 110).

[43] A. Kujawa, J. Kornas, N. Hanrieder, S. González Rodríguez, L. Hristov, Á. Fernández Solas, S. Wilbert, M. J. Blanco, L. Berzosa Álvarez, A. Martínez Gallardo, A. Amate González, M. Casas Fernandez, F. J. Palmero Luque, M. López Godoy, M. d. C. Alonso-García, J. A. Carballo, L. F. Zarzalejo Tirado, C. Cornaro, and R. Pitz-Paal. “Tomato Yield Under Different Shading Levels in an Agrivoltaic Greenhouse in Southern Spain”. In: *AgriEngineering* 7.6 (2025). ISSN: 2624-7402. DOI: 10.3390/agriengineering7060178 (cit. on pp. 5, 59, 78, 113).

[44] J. Movellan. *Japan Next-Generation Farmers Cultivate Crops and Solar Energy*. Accessed: 11.09.2025. 2013. URL: https://www.renewableenergyworld.com/solar/japan-next-generation-farmers-cultivate-agriculture-and-solar-energy/ (cit. on p. 6).

[45] IEA PVPS Task 13. *Dual Land Use for Agriculture and Solar Power Production: Overview and Performance of Agrivoltaic Systems*. Tech. rep. T13-29. International Energy Agency, Photovoltaic Power Systems Programme, 2025. DOI: 978-3-907281-70-3 (cit. on pp. 6, 119).

[46] M. Mamun et al. “A review of research on agrivoltaic systems”. In: *Renewable and Sustainable Energy Reviews* 161 (2022), p. 112351. ISSN: 1364-0321. DOI: 10.1016/j.rser.2022.112351 (cit. on pp. 6, 7, 129).

[47] R. Mead and R. W. Willey. “The Concept of a ‘Land Equivalent Ratio’ and Advantages in Yields from Intercropping”. In: *Experimental Agriculture* 16.3 (1980), 217–228. DOI: 10.1017/S0014479700010978 (cit. on p. 6).

[48] S. Amaducci, X. Yin, and M. Colauzzi. “Agrivoltaic systems to optimise land use for electric energy production”. In: *Applied Energy* 220 (2018), pp. 545–561. ISSN: 0306-2619. DOI: 10.1016/j.apenergy.2018.03.081 (cit. on p. 6).

[49] M. Trommsdorff et al. *Agrivoltaics: Opportunities for Agriculture and the Energy Transition. A Guideline for Germany*. Tech. rep. Freiburg, Germany: Fraunhofer Institute for Solar Energy Systems ISE, Feb. 2024. URL: https://www.ise.fraunhofer.de/content/dam/ise/en/documents/publications/studies/APV-Guideline.pdf (cit. on p. 7).

[50] A. Weselek, A. Ehmann, S. Zikeli, et al. “Agrophotovoltaic systems: applications, challenges, and opportunities. A review”. In: *Agronomy for Sustainable Development* 39.35 (2019). DOI: 10.1007/s13593-019-0581-3 (cit. on p. 7).

[51] S. Gorjian et al. “Progress and challenges of crop production and electricity generation in agrivoltaic systems using semi-transparent photovoltaic technology”. In: *Renewable and Sustainable Energy Reviews* 158 (2022), p. 112126. ISSN: 1364-0321. DOI: 10.1016/j.rser.2022.112126 (cit. on p. 7).

[52] L. J. Walston, T. Barley, I. Bhandari, B. Campbell, J. McCall, H. M. Hartmann, and A. G. Dolezal. “Opportunities for agrivoltaic systems to achieve synergistic food-energy-environmental needs and address sustainability goals”. In: *Frontiers in Sustainable Food Systems* Volume 6 - 2022 (2022). ISSN: 2571-581X. DOI: 10.3389/fsufs.2022.932018 (cit. on p. 7).

[53] A. Ghosh. “Nexus between agriculture and photovoltaics (agrivoltaics, agriphotovoltaics) for sustainable development goal: A review”. In: *Solar Energy* 266 (2023), p. 112146. ISSN: 0038-092X. DOI: 10.1016/j.solener.2023.112146 (cit. on p. 7).

[54] J. Widmer, B. Christ, J. Grenz, and L. Norgrove. “Agrivoltaics, a promising new tool for electricity and food production: A systematic review”. In: *Renewable and Sustainable Energy Reviews* 192 (2024), p. 114277. ISSN: 1364-0321. DOI: 10.1016/j.rser.2023.114277 (cit. on p. 7).

[55] S. Asa’a, T. Reher, J. Rongé, J. Diels, J. Poortmans, H.S. Radhakrishnan, A. van der Heide, B. Van de Poel, and M. Daenen. “A multidisciplinary view on agrivoltaics: Future of energy and agriculture”. In: *Renewable and Sustainable Energy Reviews* 200 (2024), p. 114515. ISSN: 1364-0321. DOI: 10.1016/j.rser.2024.114515 (cit. on p. 7).

[56] R. K. Chopdar, N. Sengar, N. C. Giri, and D. Halliday. “Comprehensive review on agrivoltaics with technical, environmental and societal insights”. In: *Renewable and Sustainable Energy Reviews* 197 (2024), p. 114416. ISSN: 1364-0321. DOI: 10.1016/j.rser.2024.114416 (cit. on p. 7).

[57] S. Zainali et al. “Modelling, simulation, and optimisation of agrivoltaic systems: a comprehensive review”. In: *Applied Energy* 386 (2025), p. 125558. ISSN: 0306-2619. DOI: 10.1016/j.apenergy.2025.125558 (cit. on pp. 7, 25).

[58] SolarPower Europe. *Agrisolar Policy Map*. Published October 21, 2025. SolarPower Europe, 2025. URL: https://api.solarpowereurope.org/uploads/Agrisolar_Policy_Map_Final_34d0583fc4.pdf?updated_at=2025-10-21T08:23:58.227Z (cit. on p. 7).

[59] Diario de Almería. *Los invernaderos de Almería no son los mayores del mundo, aquí están los más grandes*. Accessed: 2025-11-24. URL: https://www.diariodealmeria.es/almeria/invernaderos-almeria-no-son-mayores_0_2005162763.html (cit. on p. 8).

[60] T. Huld, R. Müller, and A. Gambardella. “A new solar radiation database for estimating PV performance in Europe and Africa”. In: *Solar Energy* 86 (2012), pp. 1803–1815. DOI: 10.1016/j.solener.2012.03.006 (cit. on pp. 8, 79, 81).

[61] European Commission. *Photovoltaic Geographical Information System (PVGIS)*. Accessed:2025-03-20. 2025. URL: https://re.jrc.ec.europa.eu/pvg_tools/en/tools.html (cit. on pp. 8, 79, 82).

[62] European Union, Copernicus Sentinel-2 imagery. *The sea of greenhouses - Almería*. Accessed: 2026-01-27. 2020. URL: https://www.copernicus.eu/en/media/image-day-gallery/sea-greenhouses-almeria (cit. on p. 8).

[63] https://www.juntadeandalucia.es/organismos/agriculturapescaaguaydesarrollorural/servicios/actualidad/noticias/detalle/599713.html. Accessed: 2025-09-24. (cit. on p. 8).

[64] K. J. McCree. “The action spectrum, absorptance and quantum yield of photosynthesis in crop plants”. In: *Agricultural Meteorology* 9 (1971), pp. 191–216. DOI: 10.1016/0002-1571(71)90022-7 (cit. on pp. 9, 10, 50, 53, 68).

[65] M. Mõttus, M. Sulev, F. Baret, R. Lopez-Lozano, and A. Reinart. “Photosynthetically active radiation: measurement and modeling”. In: *Encyclopedia of Sustainability Science and Technology*. Ed. by Robert A. Meyers. New York, NY: Springer New York, 2012, pp. 7902–7932. ISBN: 978-1-4419-0851-3. DOI: 10.1007/978-1-4419-0851-3_451 (cit. on p. 9).

[66] ASTM International. *ASTM G173-03: Standard Tables for Reference Solar Spectral Irradiances: Direct Normal and Hemispherical on 37° Tilted Surface*. Tech. rep. Data retrieved from the National Renewable Energy Laboratory (NREL). West Conshohocken, PA: ASTM International, 2008. URL: https://www.nrel.gov/grid/solar-resource/spectra-am1.5 (cit. on pp. 9, 10).

[67] K. Mishra, C. Stanghellini, and S. Hemming. “Technology and Materials for Passive Manipulation of the Solar Spectrum in Greenhouses”. In: *Advanced Sustainable Systems* 7.5 (2023), p. 2200503. DOI: 10.1002/adsu.202200503 (cit. on pp. 10, 11, 17).

[68] Z. S. Ilic and E. Fallik. “Light quality manipulation improves vegetable quality at harvest and postharvest: A review”. In: *ENVIRONMENTAL AND EXPERIMENTAL BOTANY* 139 (2017), pp. 79–90. ISSN: 0098-8472. DOI: 10.1016/j.envexpbot.2017.04.006 (cit. on p. 10).

[69] X. He, C. Maier, S. G. Chavan, C. Zhao, Y. Alagoz, C. Cazzonelli, O. Ghannoum, D. T. Tissue, and Z. Chen. “Light-altering cover materials and sustainable greenhouse production of vegetables: a review”. In: *PLANT GROWTH REGULATION* 95.1 (2021), pp. 1–17. ISSN: 0167-6903. DOI: 10.1007/s10725-021-00723-7 (cit. on p. 10).

[70] L. Huche-Thelier, L. Crespel, J. Le Gourrierec, P. Morel, S. Sakr, and N. Leduc. “Light signaling and plant responses to blue and UV radiations-Perspectives for applications in horticulture”. In: *ENVIRONMENTAL AND EXPERIMENTAL BOTANY* 121.SI (2016), pp. 22–38. ISSN: 0098-8472. DOI: 10.1016/j.envexpbot.2015.06.009 (cit. on p. 10).

[71] C. Stanghellini, J. Dai, and F. Kempkes. “Effect of near-infrared-radiation reflective screen materials on ventilation requirement, crop transpiration and water use efficiency of a greenhouse rose crop”. In: *BIOSYSTEMS ENGINEERING* 110.3 (2011), pp. 261–271. ISSN: 1537-5110. DOI: 10.1016/j.biosystemseng.2011.08.002 (cit. on p. 10).

[72] H. L. Smith, L. McAusland, and E. H. Murchie. “Don’t ignore the green light: exploring diverse roles in plant processes”. In: *JOURNAL OF EXPERIMENTAL BOTANY* 68.9 (2017), pp. 2099–2110. ISSN: 0022-0957. DOI: 10.1093/jxb/erx098 (cit. on p. 11).

[73] T. Li and Q. Yang. “Advantages of diffuse light for horticultural production and perspectives for further research”. In: *Frontiers in Plant Science* 6 (2015), p. 704. DOI: 10.3389/fpls.2015.00704 (cit. on p. 11).

[74] L. Gu, D. Baldocchi, S. B. Verma, T. A. Black, T. Vesala, E. M. Falge, and P. R. Dowty. “Advantages of diffuse radiation for terrestrial ecosystem productivity”. In: *Journal of Geophysical Research: Atmospheres* 107 (2002), ACL 2–1–ACL 2–23. DOI: 10.1029/2001JD001242 (cit. on p. 11).

[75] L. M. Mercado, N. Bellouin, S. A. Sitch, O. Boucher, C. Huntingford, M. Wild, and P. M. Cox. “Impact of changes in diffuse radiation on the global land carbon sink”. In: *Nature* 458 (2009), pp. 1014–1017. DOI: 10.1038/nature07949 (cit. on p. 11).

[76] T. Li, E. Heuvelink, T. A. Dueck, J. Janse, G. Gort, and L. F. M. Marcelis. “Enhancement of crop photosynthesis by diffuse light: quantifying the contributing factors”. In: *Annals of Botany* 114.1 (Apr. 2014), pp. 145–156. ISSN: 0305-7364. DOI: 10.1093/aob/mcu071 (cit. on p. 11).

[77] B. Marshall and P. V. Biscoe. “A Model for C 3 Leaves Describing the Dependence of Net Photosynthesis on Irradiance: I. DERIVATION”. In: *Journal of Experimental Botany* 31.120 (1980), pp. 29–39. ISSN: 00220957, 14602431. URL: http://www.jstor.org/stable/23689820 (cit. on p. 11).

[78] S. Ma Lu, S. Zainali, B. Stridh, A. Avelin, S. Amaducci, M. Colauzzi, and P. E. Campana. “Photosynthetically active radiation decomposition models for agrivoltaic systems applications”. In: *Solar Energy* 244 (2022), pp. 536–549. ISSN: 0038-092X. DOI: 10.1016/j.solener.2022.05.046 (cit. on pp. 11, 12).

[79] M. Dorais, D. Ehret, and A. Papadopoulos. “Tomato (Solanum lycopersicum) health components: From the seed to the consumer”. In: *Phytochemistry Reviews* 7 (2008), pp. 231–250. DOI: 10.1007/s11101-007-9085-x (cit. on pp. 12, 51, 77).

[80] Y. Dumas, M. Dadomo, G. Di Lucca, and P. Grolier. “Effects of environmental factors and agricultural techniques on antioxidant content of tomatoes”. In: *Journal of the Science of Food and Agriculture* 83 (2003), pp. 369–382. DOI: 10.1002/jsfa.1370 (cit. on pp. 12, 53, 54).

[81] H. Gautier, V. Diakou-Verdin, C. Bénard, M. Reich, M. Buret, F. Bourgaud, J. L. Poëssel, C. Caris-Veyrat, and M. Génard. “How Does Tomato Quality (Sugar, Acid, and Nutritional Quality) Vary with Ripening Stage, Temperature, and Irradiance?” In: *Journal of Agricultural and Food Chemistry* 56 (2008), pp. 1241–1250. DOI: 10.1021/jf072196t (cit. on pp. 12, 53, 54).

[82] Growspan Greenhouse Structures. *Typical glass Venlo greenhouse*. Accessed: 2025-11-24. URL: http://www.growspan.com/wp-content/uploads/2019/04/Venlo-picture-10.jpg (cit. on p. 15).

[83] G. López-Díaz. “Evaluación del potencial de los invernaderos hortícolas en el área de Almería para la compatibilización de la producción agrícola con la producción de energía fotovoltaica”. PhD thesis. Almería, España: Universidad de Almería, 2021. URL: https://repositorio.ual.es/bitstream/handle/10835/10364/01.%20Tesis.pdf.pdf?sequence=1 (cit. on p. 15).

[84] L. Zheng et al. “Effects of Diffuse Light on Microclimate of Solar Greenhouse, and Photosynthesis and Yield of Greenhouse-grown Tomatoes”. In: *HortScience horts* 55.10 (2020), pp. 1605 –1613. DOI: 10.21273/HORTSCI15241-20 (cit. on pp. 16, 104).

[85] Ginegar. *Cubierts invernaderos*. Accessed: 2024-05-06. URL: https://ginegar.es/ (cit. on p. 16).

[86] M. Rujnić Havstad, I. Tucman, Z. Katančić, and A. Pilipović. “Influence of Ageing on Optical, Mechanical, and Thermal Properties of Agricultural Films”. In: *Polymers* 15.17 (2023). DOI: 10.3390/polym15173638 (cit. on pp. 16, 93, 104).

[87] S. Hemming, V. Mohammadkhani, and J. van Ruijven. “Material Technology of Diffuse Greenhouse Covering Materials - Influence on Light Transmission, Light Scattering and Light Spectrum”. In: *Acta Horticulturae* 1037 (2014), pp. 883–895. DOI: 10.17660/ActaHortic.2014.1037.118 (cit. on pp. 16, 104).

[88] A. Callejon-Ferre, F. Manzano-Agugliaro, M. Diaz-Perez, A. Carreno-Ortega, and J. Perez-Alonso. “Effect of shading with aluminised screens on fruit production and quality in tomato (Solanum lycopersicum L.) under greenhouse conditions”. In: *Spanish Journal of Agricultural Research* 7 (2009), pp. 41–49. DOI: 10.5424/sjar/2009071-396 (cit. on pp. 16, 73, 75, 76, 119, 120).

[89] P. Lorenzo, R. Reyes, E. Medrano, R. Granados, S. Bonachela, J. Hernández, J. C. López, J. J. Magán, F. M. del Amor, and M. C. Sánchez-Guerrero. “Hybrid passive cooling and heating system for Mediterranean greenhouses. Microclimate and sweet pepper crop response”. In: *Agricultural Water Management* 301 (2024), p. 108937. DOI: 10.1016/j.agwat.2024.108937 (cit. on p. 16).

[90] E. Schettini and G. Vox. “Greenhouse plastic films capable of modifying the spectral distribution of solar radiation”. In: *Journal of Agricultural Engineering* 41 (2010), p. 19. DOI: 10.4081/jae.2010.1.19 (cit. on p. 16).

[91] N. Alwadai and S. El-Bashir. “Infrared Efficiency and Ultraviolet Management of Red-Pigmented Polymethylmethacrylate Photoselective Greenhouse Films”. In: *Polymers* 14 (2022), p. 531. DOI: 10.3390/polym14030531 (cit. on p. 16).

[92] X. Tong, X. Zhang, R. Fensholt, et al. “Global area boom for greenhouse cultivation revealed by satellite mapping”. In: *Nature Food* 5 (2024), pp. 513–523. DOI: 10.1038/s43016-024-00985-0 (cit. on p. 17).

[93] E. K. Liu, W. Q. He, and C. Yan. “‘White revolution’ to ’white pollution’ - Agricultural plastic film mulch in China”. In: *Environmental Research Letters* 9 (Sept. 2014), p. 091001. DOI: 10.1088/1748-9326/9/9/091001 (cit. on p. 17).

[94] M. MacLeod, H. Arp, M. Tekman, and A. Jahnke. “The global threat from plastic pollution”. In: *Science* 373.6550 (2021), pp. 61–65. DOI: 10.1126/science.abg5433 (cit. on p. 17).

[95] D. Zhang, E. L. Ng, W. Hu, H. Wang, P. Galaviz, H. Yang, W. Sun, C. Li, X. Ma, B. Fu, P. Zhao, F. Zhang, S. Jin, M. Zhou, L. Du, C. Peng, X. Zhang, Z. Xu, B. Xi, X. Liu, et al. “Plastic pollution in croplands threatens long-term food security”. In: *Global Change Biology* 26.6 (2020), pp. 3356–3367. DOI: 10.1111/gcb.15043 (cit. on p. 17).

[96] E. F. Fernández, A. Villar-Fernández, J. Montes-Romero, L. Ruiz-Torres, P. M. Rodrigo, A. J. Manzaneda, and F. Almonacid. “Global energy assessment of the potential of photovoltaics for greenhouse farming”. In: *Applied Energy* 309 (2022), p. 118474. ISSN: 0306-2619. DOI: 10.1016/j.apenergy.2021.118474 (cit. on p. 17).

[97] M. Kashif et al. “Food-energy-water nexus with agrivoltaics integration in greenhouses for sustainable food production: A review”. In: *Energy Nexus* 19 (2025), p. 100469. ISSN: 2772-4271. DOI: 10.1016/j.nexus.2025.100469 (cit. on pp. 17, 18).

[98] H. Yao, J. Liang, Y. Wang, M. Li, F. Fan, X. Ma, and X. Xiao. “The influence of photovoltaic modules on the greenhouse micro-environment - A review”. In: *Renewable and Sustainable Energy Reviews* 210 (2025), p. 115214. ISSN: 1364-0321. DOI: 10.1016/j.rser.2024.115214 (cit. on p. 17).

[99] A. A. Zahrawi and A. M. Aly. “A Review of Agrivoltaic Systems: Addressing Challenges and Enhancing Sustainability”. In: *Sustainability* 16.18 (2024). ISSN: 2071-1050. DOI: 10.3390/su16188271 (cit. on pp. 17, 18).

[100] R. Aroca-Delgado, J. Pérez-Alonso, A. J. Callejón-Ferre, and B. Velázquez-Martí. “Compatibility between Crops and Solar Panels: An Overview from Shading Systems”. In: *Sustainability* 10.3 (2018). ISSN: 2071-1050. DOI: 10.3390/su10030743 (cit. on p. 17).

[101] S. Seme, E. Simonič, and K. Sredenšek. “Agrivoltaic - A Photovoltaic System on a Greenhouse”. In: Oct. 2024, pp. 121–124. DOI: 10.1109/SST61991.2024.10755502 (cit. on p. 18).

[102] A. Abdel-Ghany and I. Al-Helal. “Solar energy utilization by a greenhouse: General relations”. In: *Renewable Energy* 36 (2011), pp. 189–196. DOI: 10.1016/j.renene.2010.06.020 (cit. on p. 18).

[103] E. Medrano, P. Lorenzo, M. Sánchez-Guerrero, and J. Montero. “Evaluation and modelling of greenhouse cucumber-crop transpiration under high and low radiation conditions”. In: *Scientia Horticulturae* 105 (2005), pp. 163–175. DOI: 10.1016/j.scienta.2005.01.024 (cit. on p. 18).

[104] M. Kadowaki, A. Yano, F. Ishizu, T. Tanaka, and S. Noda. “Effects of greenhouse photovoltaic array shading on Welsh onion growth”. In: *Biosystems Engineering* 111 (2012), pp. 290–297. DOI: 10.1016/j.biosystemseng.2011.12.006 (cit. on p. 18).

[105] S. Moretti and A. Marucci. “A Photovoltaic Greenhouse with Variable Shading for the Optimization of Agricultural and Energy Production”. In: *Energies* 12.13 (2019). ISSN: 1996-1073. DOI: 10.3390/en12132589 (cit. on p. 18).

[106] Trisolar. *Trisolar solar panels integrated into a REGACE greenhouse*. Accessed: 2025-11-26. URL: https://www.pv-magazine-australia.com/2023/02/14/new-agrivoltaic-project-to-test-crop-responsive-pv-trackers-for-greenhouses/ (cit. on p. 18).

[107] E. Magadley, M. Teitel, M. F. Peretz, M. Kacira, and I. Yehia. “Outdoor behaviour of organic photovoltaics on a greenhouse roof”. In: *Sustainable Energy Technologies and Assessments* 37 (2020), p. 100641. ISSN: 2213-1388. DOI: 10.1016/j.seta.2020.100641 (cit. on pp. 18, 19).

[108] M. E. Loik, S. A. Carter, G. Alers, C. E. Wade, D. Shugar, C. Corrado, D. Jokerst, and C. Kitayama. “Wavelength-Selective Solar Photovoltaic Systems: Powering Greenhouses for Plant Growth at the Food-Energy-Water Nexus”. In: *Earth’s Future* 5.10 (2017), pp. 1044–1053. DOI: 10.1002/2016EF000531 (cit. on pp. 18–20).

[109] Voltiris. *Voltiris spectral reflectors integrated into a glass GH*. Accessed: 2025-11-26. URL: https://www.startupticker.ch/en/news/voltiris-raises-chf-1-4m-to-help-greenhouses-produce-energy (cit. on p. 18).

[110] A. Al-Ibrahim, N. Al-Abbadi, and I. Al-Helal. “PV greenhouse system - System description, performance and lesson learned”. In: *Acta Horticulturae* 710 (June 2006), pp. 251–264. DOI: 10.17660/ActaHortic.2006.710.26 (cit. on p. 18).

[111] C. A. Campiotti, C. Bibbiani, F. Dondi, M. Scoccianti, and C. Viola. “Energy efficiency and photovoltaic solar for greenhouse agriculture”. In: 2011. URL: https://api.semanticscholar.org/CorpusID:55950294 (cit. on p. 18).

[112] A. Yano, A. Furue, M. Kadowaki, T. Tanaka, E. Hiraki, M. Miyamoto, F. Ishizu, and S. Noda. “Electrical energy generated by photovoltaic modules mounted inside the roof of a north–south oriented greenhouse”. In: *Biosystems Engineering* 103.2 (2009), pp. 228–238. ISSN: 1537-5110. DOI: 10.1016/j.biosystemseng.2009.02.020 (cit. on p. 18).

[113] A. Yano, M. Onoe, and J. Nakata. “Prototype semi-transparent photovoltaic modules for greenhouse roof applications”. In: *Biosystems Engineering* 122 (2014), pp. 62–73. ISSN: 1537-5110. DOI: 10.1016/j.biosystemseng.2014.04.003 (cit. on p. 18).

[114] R. Hassanien and L. Ming. “Influences of greenhouse-integrated semi-transparent photovoltaics on microclimate and lettuce growth”. In: *International Journal of Agricultural and Biological Engineering* 10 (Nov. 2017), pp. 11–22. DOI: 10.25165/j.ijabe.20171006.3407 (cit. on p. 18).

[115] R. Hassanien, M. Li, and F. Yin. “The integration of semi-transparent photovoltaics on greenhouse roof for energy and plant production”. In: *Renewable Energy* 121 (2018), pp. 377–388. ISSN: 0960-1481. DOI: 10.1016/j.renene.2018.01.044 (cit. on p. 18).

[116] A. Tani, S. Shiina, K. Nakashima, and M. Hayashi. “Improvement in lettuce growth by light diffusion under solar panels”. In: *Journal of Agricultural Meteorology* 70 (Sept. 2014), pp. 139–149. DOI: 10.2480/agrmet.D-14-00005 (cit. on p. 19).

[117] G. Trypanagnostopoulos, A. Kavga, M. Souliotis, and Y. Tripanagnostopoulos. “Greenhouse performance results for roof installed photovoltaics”. In: *Renewable Energy* 111 (2017), pp. 724–731. ISSN: 0960-1481. DOI: 10.1016/j.renene.2017.04.066 (cit. on p. 19).

[118] Ö. E. Özdemir, T. Bretzel, L. Gfüllner, S. Gorjian, Y. Katircioglu, B. Dur, and M. Trommsdorff. “Design, simulation, and experimental evaluation of an agrivoltaic greenhouse in Turkey”. In: *Results in Engineering* 26 (2025), p. 105278. ISSN: 2590-1230. DOI: 10.1016/j.rineng.2025.105278 (cit. on p. 19).

[119] E. Seri, M. Petitta, C. Papaioannou, N. Katsoulas, and C. Cornaro. “Sustainable greenhouse microclimate modeling: A comparative analysis of recurrent and Graph Neural Networks”. In: *Building and Environment* 284 (2025), p. 113473. ISSN: 0360-1323. DOI: 10.1016/j.buildenv.2025.113473 (cit. on p. 19).

[120] G. Bovesecchi, M. Petitta, M. Pierro, A. Agresti, S. Pescetelli, E. Leonardi, A. Di Carlo, and C. Cornaro. “Outdoor Performance Monitoring Method for Degradation Studies of Perovskite Modules”. In: *Progress in Photovoltaics: Research and Applications* 33.3 (2025), pp. 445–461. DOI: 10.1002/pip.3860 (cit. on p. 19).

[121] A. Sohani, M. Pierro, D. Moser, and C. Cornaro. “Comparison of physical models for bifacial PV power estimation”. In: *Energy Conversion and Management* 327 (2025), p. 119515. ISSN: 0196-8904. DOI: 10.1016/j.enconman.2025.119515 (cit. on p. 19).

[122] C. Corrado, S. W. Leow, M. Osborn, I. Carbone, K. Hellier, M. Short, G. Alers, and S. A. Carter. “Power generation study of luminescent solar concentrator greenhouse”. In: *Journal of Renewable and Sustainable Energy* 8.4 (July 2016), p. 043502. ISSN: 1941-7012. DOI: 10.1063/1.4958735 (cit. on p. 19).

[123] C. Corrado, S. W. Leow, M. Osborn, E. Chan, B. Balaban, and S. A. Carter. “Optimization of gain and energy conversion efficiency using front-facing photovoltaic cell luminescent solar concentratordesign”. In: *Solar Energy Materials and Solar Cells* 111 (2013), pp. 74–81. ISSN: 0927-0248. DOI: 10.1016/j.solmat.2012.12.030 (cit. on p. 19).

[124] P.-V. Broccard, J. Roch, D. Tran, C. Camps, and J. Löffler. “Photovoltaic Energy Production in Greenhouses With Spectral Splitting Solar Trackers: Analysis of the Novel Voltiris System”. In: *AgriVoltaics World Conference 2023 Proceedings, Vol. 2*. Reports agronomic and energetic results from Agroscope’s 8-month trial of the Voltiris system. 2024. DOI: 10.52825/agripv.v2i.1017 (cit. on p. 20).

[125] A. Marucci, I. Zambon, A. Colantoni, and D. Monarca. “A combination of agricultural and energy purposes: Evaluation of a prototype of photovoltaic greenhouse tunnel”. In: *Renewable and Sustainable Energy Reviews* 82 (2018), pp. 1178–1186. ISSN: 1364-0321. DOI: 10.1016/j.rser.2017.09.029 (cit. on p. 22).

[126] M. Cossu, A. Cossu, P. A. Deligios, L. Ledda, Z. Li, H. Fatnassi, C. Poncet, and A. Yano. "Assessment and comparison of the solar radiation distribution inside the main commercial photovoltaic greenhouse types in Europe". In: *Renewable and Sustainable Energy Reviews* 94 (2018), pp. 822–834. DOI: 10.1016/j.rser.2018.06.001 (cit. on pp. 23, 24, 68, 76, 94, 95, 109, 112, 115).

[127] C. J. Torrente, J. Reca, R. López-Luque, J. Martínez, and F. J. Casares. "Simulation model to analyze the spatial distribution of solar radiation in agrivoltaic Mediterranean greenhouses and its effect on crop water needs". In: *Applied Energy* 353 (2024), p. 122050. DOI: 10.1016/j.apenergy.2023.122050 (cit. on pp. 24, 25, 94, 95, 109, 112).

[128] J. S. Pulido-Mancebo, R. López-Luque, L. M. Fernández-Ahumada, J. C. Ramírez-Faz, F. J. Gómez-Uceda, and M. Varo-Martínez. "Spatial Distribution Model of Solar Radiation for Agrivoltaic Land Use in Fixed PV Plants". In: *Agronomy* 12.11 (2022). ISSN: 2073-4395. DOI: 10.3390/agronomy12112799 (cit. on p. 24).

[129] J. Jones, E. Dayan, L. Allen, H. Keulen, and H. Challa. "A dynamic tomato growth and yield model (TOMGRO)". In: *Transactions of the ASAE* 34 (1991), pp. 663–672. DOI: 10.13031/2013.31715 (cit. on pp. 25, 54–56, 109).

[130] Z. Ghaffarpour, M. Fakhroleslam, and M. Amidpour. "Calculation of energy consumption, tomato yield, and electricity generation in a PV-integrated greenhouse with different solar panels configuration". In: *Renewable Energy* 229 (2024), p. 120723. DOI: 10.1016/j.renene.2024.120723 (cit. on pp. 25, 124).

[131] A. Moreno, D. Chemisana, and E. Fernández. "Energy performance and crop yield production of a semitransparent photovoltaic greenhouse". In: *Applied Energy* 382 (2025), p. 125285. DOI: 10.1016/j.apenergy.2025.125285 (cit. on pp. 25, 109, 124).

[132] M. Laub, L. Pataczek, A. Feuerbacher, S. Zikeli, and P. Högy. "Contrasting yield responses at varying levels of shade suggest different suitability of crops for dual land-use systems: a meta-analysis". In: *Agronomy for Sustainable Development* 42.3 (2022), p. 51. DOI: 10.1007/s13593-022-00783-7 (cit. on pp. 25–27, 119, 120).

[133] D. A. Way and R. W. Pearcy. "Sunflecks in trees and forests: from photosynthetic physiology to global change biology". In: *Tree Physiology* 32.9 (Aug. 2012), pp. 1066–1081. ISSN: 0829-318X. DOI: 10.1093/treephys/tps064 (cit. on p. 26).

[134] C. Dupraz. "Assessment of the ground coverage ratio of agrivoltaic systems as a proxy for potential crop productivity". In: *Agroforestry Systems* 98 (2024), pp. 2679–2696. DOI: 10.1007/s10457-023-00906-3 (cit. on pp. 26, 27).

[135] G. Ward and R. Shakespeare. *Rendering with radiance: the art and science of lighting visualization*. San Francisco, CA, USA: Morgan Kaufmann Publishers Inc., 1998. ISBN: 1558604995. URL: https://radsite.lbl.gov/radiance/book/ (cit. on pp. 31, 32, 35–37, 40, 45, 47, 87, 99, 105, 106, 111).

[136] Lawrence Berkeley National Laboratory, Building Technologies Department. *The Radiance 6.0 Synthetic Imaging System*. Radiance v6.0 Documentation. Regents of the University of California. Berkeley, CA, USA, 2025. URL: https://radsite.lbl.gov/radiance/refer/refman.pdf (cit. on p. 32).

[137] C. Andres, C. Ruben, G. David, B. Pavel, M. Patrizio, Z. Miro, and I. Olindo. "Time-varying, ray tracing irradiance simulation approach for photovoltaic systems in complex scenarios with decoupled geometry, optical properties and illumination conditions". In: *Progress in Photovoltaics: Research and Applications* 31.2 (2023), pp. 134–148. DOI: 10.1002/pip.3614 (cit. on pp. 32, 111).

[138] S. A. Pelaez and C. Deline. “bifacial_radiance: a python package for modeling bifacial solar photovoltaic systems”. In: *Journal of Open Source Software* 5.50 (2020), p. 1865. DOI: 10.21105/joss.01865 (cit. on pp. 32, 36).

[139] I. T. Horvath, P. Manganiello, H. Goverde, D. Anagnostos, B. Aldalali, E. Voroshazi, F. Catthoor, and J. Poortmans. “Towards efficient and accurate energy yield modelling of bifacial PV systems”. In: *Poster at EUPVSEC 2018*. Nov. 2018 (cit. on p. 32).

[140] S. A. Pelaez, C. Deline, P. Greenberg, J. S Stein, and R. K. Kostuk. “Model and Validation of Single-Axis Tracking With Bifacial PV”. In: *IEEE Journal of Photovoltaics* PP (Feb. 2019), pp. 1–7. DOI: 10.1109/JPHOTOV.2019.2892872 (cit. on p. 32).

[141] S. A. Pelaez, C. Deline, S. M. MacAlpine, B. Marion, J. S. Stein, and R. K. Kostuk. “Comparison of Bifacial Solar Irradiance Model Predictions With Field Validation”. In: *IEEE JOURNAL OF PHOTOVOLTAICS* 9.1 (2019), pp. 82–88. ISSN: 2156-3381. DOI: 10.1109/JPHOTOV.2018.2877000 (cit. on p. 32).

[142] G. J. Ward. “The RADIANCE lighting simulation and rendering system”. In: *Proceedings of the 21st annual conference on Computer graphics and interactive techniques*. 1994, pp. 459–472. URL: https://radsite.lbl.gov/radiance/papers/sg94.1/abstract.html (cit. on pp. 33–36).

[143] J. T. Kajiya. “The rendering equation”. In: *SIGGRAPH Comput. Graph.* 20.4 (Aug. 1986), 143–150. ISSN: 0097-8930. DOI: 10.1145/15886.15902 (cit. on pp. 33, 35, 36).

[144] R. Perez, P. Ineichen, R. Seals, J. Michalsky, and R. Stewart. “Modeling daylight availability and irradiance components from direct and global irradiance”. In: *Solar Energy* 44.5 (1990), pp. 271–289. DOI: 10.1016/0038-092X(90)90055-H (cit. on pp. 34, 35, 46, 103).

[145] J. A. Duffie and W. A. Beckman. “Frontmatter”. In: *Solar Engineering of Thermal Processes*. Wiley Online Library, 2013, pp. i–xxvi. ISBN: 9781118671603. DOI: 10.1002/9781118671603.fmatter (cit. on p. 35).

[146] F. Kasten and A. T. Young. “Revised optical air mass tables and approximation formula”. In: *Appl. Opt.* 28.22 (1989), pp. 4735–4738. DOI: 10.1364/AO.28.004735 (cit. on p. 35).

[147] Fred E. Nicodemus, Joseph C. Richmond, Jack J. Hsia, Irving W. Ginsberg, T. Limperis, Sidney Harman, and Jordan J Baruch. “Geometrical considerations and nomenclature for reflectance”. In: 1977. URL: https://api.semanticscholar.org/CorpusID:18645782 (cit. on p. 36).

[148] *RTRACE - Radiance Manual*. https://radsite.lbl.gov/radiance/man_html/rtrace.1.html. Accessed: 2026-01-14. (cit. on pp. 36, 39).

[149] *Spectral (RGB) irradiance values from `rtrace -I`*. https://www.radiance-online.org/community/workshops/2003-berkeley/presentations/Mardaljevic/rwr_ch6.pdf. Accessed: 2026-01-14. 2003 (cit. on p. 36).

[150] Konica Minolta, Inc. *2.4 COLORIMETRY — Language of Light*. https://www.konicaminolta.com/instruments/knowledge/light/concepts/07.html. Accessed: 2026-01-23. 2011 (cit. on p. 36).

[151] T. Laue. “Using ray tracing to model agri-PV greenhouse energy production and PAR levels”. MA thesis. University of Oslo, 2022 (cit. on p. 37).

[152] G. J. Ward. *Behavior of Materials in RADIANCE*. https://radsite.lbl.gov/radiance/refer/materials.pdf. Radiance technical reference note on material models. 2022 (cit. on p. 41).

[153] *Copernicus Atmosphere Monitoring Service (CAMS) Radiation Service: Product User Manual*. Accessed: 2024-08-01. 2023. URL: https://atmosphere.copernicus.eu/site/default/files/2023-03/CAMS_Solar_V4-1_0.pdf (cit. on p. 46).

[154] A. Forstinger et al. *Worldwide benchmark of modelled solar irradiance data annex*. 2023. DOI: 10.5281/ZENODO.7867003 (cit. on p. 46).

[155] Copernicus Atmosphere Monitoring Service. *CAMS Solar Radiation Documentation*. Accessed: 2024-02-29. URL: https://atmosphere.copernicus.eu/solar-radiation-supplementary-products (cit. on p. 46).

[156] M. Schroedter-Homscheidt, F. Azam, J. Lezaca, . Lefèvre, Y.-M. Saint-Drenan, L. Saboret, and J. Betcke. "Method Development and Variability Class-Dependent Validation of the New CAMS Radiation Service V4.5". In: *EU PVSEC 2023 (41st European Photovoltaic Solar Energy Conference)*. Lisboa, Portugal, Sept. 2023. URL: https://minesparis-psl.hal.science/hal-04379232 (cit. on p. 46).

[157] W. Holmgren et al. "pvlib python: a python package for modeling solar energy systems". In: *Journal of Open Source Software* 3.29 (2018), p. 884. DOI: 10.21105/joss.00884 (cit. on p. 46).

[158] W. Holmgren et al. *pvlib/pvlib-python: v0.9.4*. Version v0.9.4. 2022. DOI: 10.5281/zenodo.7465822 (cit. on p. 46).

[159] J. M. Vindel, R. X. Valenzuela, A. A. Navarro, L. F. Zarzalejo, A. Paz-Gallardo, J. A. Souto, R. Méndez-Gómez, D. Cartelle, and J. J. Casares. "Modeling Photosynthetically Active Radiation from Satellite-Derived Estimations over Mainland Spain". In: *Remote Sensing* 10 (2018), p. 849. DOI: 10.3390/rs10060849 (cit. on pp. 49, 50, 127).

[160] J. Kornas. "Tomato yield under different shading levels in an agrivoltaic greenhouse in southern Spain - Analysis and calibration of the reduced state-variable Tomato Growth Model (TOMGRO)." MA thesis. Ludwig-Maximilians-Universität München, 2024. URL: https://elib.dlr.de/207502/ (cit. on pp. 49, 54, 113, 121).

[161] M. Cossu, A. Yano, S. Solinas, P. Deligios, M. Tiloca, A. Cossu, and L. Ledda. "Agricultural sustainability estimation of the European photovoltaic greenhouses". In: *European Journal of Agronomy* 118 (2020), p. 126074. DOI: 10.1016/j.eja.2020.126074 (cit. on pp. 50, 68).

[162] K. E. Cockshull and C. R. J. Cave. "The influence of shading on yield of glasshouse tomatoes". In: *Journal of Horticultural Science* 67 (1992), pp. 11–24. DOI: 10.1080/00221589.1992.11516215 (cit. on pp. 51, 75–77).

[163] M. Dorais. "Canadian Greenhouse Conference". In: *The Use of Supplemental Lighting for Vegetable Crop Production: Light Intensity, Crop Response, Nutrition, Crop Management, Cultural Practices* (2003). URL: https://www.agrireseau.net/legumesdeserre/documents/69919 (cit. on p. 51).

[164] P. R. Fisher and E. S. Runkle. *Lighting up profits: understanding greenhouse lighting*. Meister Media Worldwide, 2004. ISBN: 189282910X (cit. on p. 51).

[165] A. van der Ploeg and E. Heuvelink. "Influence of sub-optimal temperature on tomato growth and yield: A review". In: *Journal of Horticultural Science and Biotechnology* 80 (2005), pp. 652–659. DOI: 10.1080/14620316.2005.11511994 (cit. on pp. 51, 74, 75, 77).

[166] L. F. M. Marcelis, A. G. M. Broekhuijsen, E. Meinen, E. M. F. M. Nijs, and M. G. M. Raaphorst. "Quantification of the growth response to light quantity of greenhouse grown crops". In: *V International Symposium on Artificial Lighting in Horticulture 711*. 2005, pp. 97–104 (cit. on p. 51).

[167] J. J. Spaargaren. "Supplemental lighting for greenhouse crops". In: *Hortilux Schreder* (2001), p. 178. URL: https://agris.fao.org/search/en/providers/122575/records/6472376d53aa8c8963029130 (cit. on p. 51).

[168] L. F. M. Marcelis. "Fruit growth and biomass allocation to the fruits in cucumber. 1. Effect of fruit load and temperature". In: *Scientia Horticulturae* 54.2 (1993), pp. 107–121. ISSN: 0304-4238. DOI: 10.1016/0304-4238(93)90059-Y (cit. on p. 51).

[169] C. Kang, Y. Zhang, R. Cheng, E. Kaiser, Q. Yang, and T. Li. "Acclimating Cucumber Plants to Blue Supplemental Light Promotes Growth in Full Sunlight". In: *Frontiers in Plant Science* Volume 12 - 2021 (2021). ISSN: 1664-462X. DOI: 10.3389/fpls.2021.782465 (cit. on p. 51).

[170] H. J. M. Nilwik. "Growth Analysis of Sweet Pepper (Capsicum annuum L.): 2. Interacting Effects of Irradiance, Temperature and Plant Age in Controlled Conditions*". In: *Annals of Botany* 48.2 (Aug. 1981), pp. 137–146. ISSN: 0305-7364. DOI: 10.1093/oxfordjournals.aob.a086107 (cit. on p. 51).

[171] T. K. Jeong, S. R. Kim, F. A. Mohammad, M. C. S. C. Emparang, J. G. Lee, and J. S. Kang. "Impact of Supplemental LED Lighting Regimes on Sweet Pepper Growth under Winter Light Deficit". In: *Journal of Bio-Environment Control* 34.4 (2025), pp. 647–660. DOI: 10.12791/KSBEC.2025.34.4.647 (cit. on p. 51).

[172] A. N. M. de Koning. "Development and dry matter distribution in glasshouse tomato: A quantitative approach". PhD thesis. Wageningen, Netherlands: Landbouwuniversiteit Wageningen, 1994. DOI: 10.18174/205947 (cit. on pp. 51, 75).

[173] A. R. De Pinheiro Henriques and L. F. M. Marcelis. "Regulation of Growth at Steady-state Nitrogen Nutrition in Lettuce (Lactuca sativa L.): Interactive Effects of Nitrogen and Irradiance". In: *Annals of Botany* 86.6 (2000), pp. 1073–1080. ISSN: 0305-7364. DOI: 10.1006/anbo.2000.1268 (cit. on p. 51).

[174] E. P. Glenn, P. Cardran, and T. L. Thompson. "Seasonal effects of shading on growth of greenhouse lettuce and spinach". In: *Scientia Horticulturae* 24.3 (1984), pp. 231–239. ISSN: 0304-4238. DOI: 10.1016/0304-4238(84)90106-7 (cit. on p. 51).

[175] R. Bhuiyan and M. W. van Iersel. "Only Extreme Fluctuations in Light Levels Reduce Lettuce Growth Under Sole Source Lighting". In: *Frontiers in Plant Science* Volume 12 - 2021 (2021). ISSN: 1664-462X. DOI: 10.3389/fpls.2021.619973 (cit. on p. 51).

[176] J. E. Faust. *Light management in greenhouses. Daily Light integral: a useful tool for the US floriculture industry.* Tech. rep. Accessed: 2026-01-27. 2002. URL: https://de.scribd.com/document/295331613/A051 (cit. on p. 51).

[177] J. H. Lee, J. Goudriaan, and H. Challa. "Using the Expolinear Growth Equation for Modelling Crop Growth in Year-round Cut Chrysanthemum". In: *Annals of Botany* 92.5 (Nov. 2003), pp. 697–708. ISSN: 0305-7364. DOI: 10.1093/aob/mcg195 (cit. on p. 51).

[178] N. Zieslin and Y. Mor. "Light on roses. A review". In: *Scientia Horticulturae* 43.1 (1990), pp. 1–14. ISSN: 0304-4238. DOI: 10.1016/0304-4238(90)90031-9 (cit. on p. 51).

[179] X. Xu and R. Hernández. “The Effect of Light Intensity on Vegetative Propagation Efficacy, Growth, and Morphology of “Albion” Strawberry Plants in a Precision Indoor Propagation System”. In: *Applied Sciences* 10.3 (2020). ISSN: 2076-3417. DOI: 10.3390/app10031044 (cit. on p. 51).

[180] H. Dou, G. Niu, M. Gu, and J. Masabni. “Responses of Sweet Basil to Different Daily Light Integrals in Photosynthesis, Morphology, Yield, and Nutritional Quality”. In: *HortScience* 53 (Apr. 2018), pp. 496–503. DOI: 10.21273/HORTSCI12785-17 (cit. on p. 51).

[181] D. H. Larsen, E. J. Woltering, C. C. S. Nicole, and L. F. M. Marcelis. “Response of Basil Growth and Morphology to Light Intensity and Spectrum in a Vertical Farm”. In: *Frontiers in Plant Science* 11 (2020), p. 597906. DOI: 10.3389/fpls.2020.597906 (cit. on p. 51).

[182] T. Zou, C. Huang, P. Wu, L. Ge, and Y. Xu. “Optimization of Artificial Light for Spinach Growth in Plant Factory Based on Orthogonal Test”. In: *Plants* 9.4 (2020), p. 490. DOI: 10.3390/plants9040490 (cit. on p. 51).

[183] W. John S. Downton and E Torokfalvy. “Photosynthesis in Developing Asparagus Plants”. In: *Functional Plant Biology* 2 (1975), pp. 367–375. URL: https://api.semanticscholar.org/CorpusID:87957964 (cit. on p. 51).

[184] L. M. Mortensen and S. O. Grimstad. “The effect of lighting period and photon flux density on growth of six foliage plants”. In: *Scientia Horticulturae* 41.4 (1990), pp. 337–342. ISSN: 0304-4238. DOI: 10.1016/0304-4238(90)90114-T (cit. on p. 51).

[185] RaboResearch Food & Agribusiness. *Global Greenhouse Update 2025*. Tech. rep. Accessed: 2025-09-02. Rabobank, 2025. URL: https://topsectortu.nl/wp-content/uploads/2025/03/RaboResearch_Global-greenhouse-update_2025.pdf (cit. on pp. 51, 52).

[186] Ceres Greenhouse Solutions. *Quality versus Quantity: Which is More Important for Greenhouse Lighting Optimization?* Accessed: 2025-09-02. 2020. URL: https://ceresgs.com/quality-versus-quantity-which-is-more-important-for-greenhouse-lighting-optimization-2/ (cit. on p. 51).

[187] University of California Statewide IPM Program. *Greenhouse Tomato Production Timeline*. Tech. rep. Accessed: 2025-09-02. UC Agriculture and Natural Resources, 2009. URL: https://ipmdata.ipmcenters.org/documents/timelines/USgreenhousetomato.PDF (cit. on p. 53).

[188] E. A. Mitscherlich. *Bodenkunde für Land- und Forstwirte*. 2nd ed. Original from University of California; Digitized 5 October 2007. P. Parey, 1913, p. 317 (cit. on p. 53).

[189] J. Vos, J. B. Evers, G. H. Buck-Sorlin, B. Andrieu, M. Chelle, and P. H. B. de Visser. “Functional–structural plant modelling: a new versatile tool in crop science”. In: *Journal of Experimental Botany* 61.8 (Dec. 2009), pp. 2101–2115. ISSN: 0022-0957. DOI: 10.1093/jxb/erp345 (cit. on p. 54).

[190] J. Jones, A. Kenig, and C. E. Vallejos. “Reduced state-variable tomato growth model”. In: *Transactions of the ASAE* 42 (1999), pp. 255–265. DOI: 10.13031/2013.13203 (cit. on pp. 54, 56, 121).

[191] A. Arias, F. Rodriguez, M. Berenguel, and E. Heuvelink. “Calibration and validation of complex and simplified tomato growth models for control purposes in the Southeast of Spain”. In: *Acta Horticulturae* 654 (2004), pp. 147–154. DOI: 10.17660/ActaHortic.2004.654.15 (cit. on p. 56).

[192] M. Vazquez-Cruz, R. Guzman-Cruz, I. Lopez-Cruz, O. Cornejo-Perez, I. Torres-Pacheco, and R. Guevara-Gonzalez. “Global sensitivity analysis by means of EFAST and Sobol’ methods and calibration of reduced state-variable TOMGRO model using genetic algorithms”. In: *Computers and Electronics in Agriculture* 100 (2014), pp. 1–12. DOI: 10.1016/j.compag.2013.10.006 (cit. on p. 56).

[193] F. Hernández-Hernández, I. Lopez-Cruz, R. Guevara-Gonzalez, E. Rico-García, R. Ocampo-Velaszquez, G. Herrera-Ruiz, M. Chavira, and I. Pacheco. “Growth and development simulation of pepper (Capsicum annumm L.) under greenhouse conditions”. In: *Revista Mexicana de Ciencias Agrícolas* 2 (2011), pp. 385–397. URL: https://scielo.org.mx/pdf/remexca/v2n3/v2n3a7.pdf (cit. on p. 56).

[194] A. Saltelli, S. Tarantola, and K. Chan. “A Quantitative Model-Independent Method for Global Sensitivity Analysis of Model Output”. In: *Technometrics* 41 (2012), pp. 39–56. DOI: 10.1080/00401706.1999.10485594 (cit. on pp. 56, 121).

[195] J. Kennedy and R. Eberhart. “Particle swarm optimization”. In: *Proceedings of ICNN’95 - International Conference on Neural Networks*. 27 November–1 December 1995. Perth, WA, Australia, Nov. 1995 (cit. on pp. 56, 121).

[196] El Agro Autentico. *El Proyecto Lygalan o la Busqueda del Sabor en Tomate*. Accessed: 2025-01-14. 2022. URL: https://agroautentico.com/2022/03/el-proyecto-lygalan-o-la-busqueda-del-sabor-en-tomate/ (cit. on p. 61).

[197] W. Horwitz. “Official methods of analysis of the Association of Official Analytical Chemists, 13th ed.” In: *Journal of Pharmaceutical Sciences* 70.4 (1981), pp. 468–468. DOI: 10.1002/jps.2600700437 (cit. on p. 66).

[198] P. Greidanus and M. Verhoeven. *Product Data of Tomatoes*. Accessed: 2025-03-20. 1986. URL: https://edepot.wur.nl/444068 (cit. on p. 69).

[199] N. Garg and D. S. Cheema. “Assessment of fruit quality attributes of tomato hybrids involving ripening mutants under high temperature conditions”. In: *Scientia Horticulturae* 131 (2011), pp. 29–38. DOI: 10.1016/j.scienta.2011.09.024 (cit. on p. 69).

[200] P. Riga, M. Anza, and C. Garbisu. “Tomato quality is more dependent on temperature than on photosynthetically active radiation”. In: *Journal of the Science of Food and Agriculture* 88 (2008), pp. 158–166. DOI: 10.1002/jsfa.3065 (cit. on pp. 73, 75, 76).

[201] H. Challa and M. Bakker. “Potential production within the greenhouse environment”. In: *Ecosystems of the World, Vol. 20: Greenhouse Ecosystems*. Ed. by G. Stanhill and Z.H. Enoch. Elsevier, 1999, pp. 333–348 (cit. on p. 76).

[202] R. Bulgari, G. Cola, A. Ferrante, G. Franzoni, L. Mariani, and L. Martinetti. “Micrometeorological environment in traditional and photovoltaic greenhouses and effects on growth and quality of tomato (Solanum lycopersicum L.)” In: *Italian Journal of Agrometeorology* 20 (2015), pp. 27–38. DOI: 10.19199/2015.2.2038-5625.027 (cit. on p. 76).

[203] H. P. Kläring and A. Krumbein. “The Effect of Constraining the Intensity of Solar Radiation on the Photosynthesis, Growth, Yield and Product Quality of Tomato”. In: *Journal of Agronomy and Crop Science* 199 (2013), pp. 351–359. DOI: 10.1111/jac.12018 (cit. on pp. 76, 77).

[204] M. Gent. “Effect of Shade on Quality of Greenhouse Tomato”. In: *Acta Horticulturae* 39 (2007), pp. 107–112. DOI: 10.17660/ActaHortic.2007.747.10 (cit. on p. 77).

[205] C. Bénard, S. Bernillon, B. Biais, S. Osorio, M. Maucourt, P. Ballias, C. Deborde, S. Colombie, C. Cabasson, D. Jacob, et al. “Metabolomic profiling in tomato reveals diel compositional changes in fruit affected by source-sink relationships”. In: *Journal of Experimental Botany* 66 (2015), pp. 3391–3404. DOI: 10.1093/jxb/erv151 (cit. on p. 77).

[206] M. García-Martínez, P. Caballero, and M. Zamudio. “Price trends in greenhouse tomato and pepper and choice of adoptable technology”. In: *Spanish Journal of Agricultural Research* 6 (2008), pp. 320–332. DOI: 10.5424/sjar/2008063-325 (cit. on p. 77).

[207] M. Stevens, A. Kader, and M. Albright. “Potential for Increasing Tomato Flavor via Increased Sugar and Acid Content”. In: *Journal of the American Society for Horticultural Science* 104 (1979), pp. 40–42. DOI: 10.21273/JASHS.104.1.40 (cit. on p. 77).

[208] Junta De Andalucia. *Hortícolas Protegidos—Tomate*. Accessed: 2025-04-08. 2024. URL: https://ws142.juntadeandalucia.es/agriculturaypesca/observatorio/servlet/FrontController?ec=default&action=Static&url=openData.jsp&page=1 (cit. on p. 78).

[209] OMIE—Operador del Mercado Ibérico de Energía. *OMIE Electricity Prices—Monthly Averages 2023*. Accessed: 2025-04-08. 2023. URL: https://www.omie.es/en/market-results/annual/average-final-prices/spanish-demand?scope=annual&year=2023 (cit. on pp. 79, 81).

[210] OMIE—Operador del Mercado Ibérico de Energía. *OMIE Electricity Prices—Monthly Averages 2024*. Accessed: 2025-04-08. 2024. URL: https://www.omie.es/en/market-results/annual/average-final-prices/spanish-demand?scope=annual&year=2024 (cit. on pp. 79, 81, 82).

[211] C. Kost, P. Mueller, J. S. Schweiger, V. Fluri, and J. Thomsen. *Levelized Cost of Electricity Renewable Energy Technologies*. Tech. rep. Accessed: 2025-04-25. Freiburg, Germany: Fraunhofer, 2024. URL: https://www.ise.fraunhofer.de/content/dam/ise/en/documents/publications/studies/EN2024_ISE_Study_Levelized_Cost_of_Electricity_Renewable_Energy_Technologies.pdf (cit. on pp. 79, 81).

[212] OMIE—Operador del Mercado Ibérico de Energía. *OMIE Electricity Feed-In Prices—Monthly Averages 2023*. Accessed: 2025-03-24. 2024. URL: https://www.omie.es/en/market-results/annual/daily-market/daily-prices?scope=annual&year=2023&system=1 (cit. on pp. 79, 81).

[213] OMIE—Operador del Mercado Ibérico de Energía. *OMIE Electricity Feed-In Prices—Monthly Averages 2024*. Accessed: 2025-03-24. 2024. URL: https://www.omie.es/en/market-results/annual/daily-market/daily-prices?scope=annual&year=2024&system=1 (cit. on pp. 79, 81, 82).

[214] M. Cossu, A. Yano, Z. Li, M. Onoe, H. Nakamura, T. Matsumoto, and J. Nakata. “Advances on the semi-transparent modules based on micro solar cells: First integration in a greenhouse system”. In: *Applied Energy* 162 (2016), pp. 1042–1051. DOI: 10.1016/j.apenergy.2015.11.002 (cit. on p. 80).

[215] A. Jung, D. Szabó, Z. Varga, A. Lausch, M. Vohland, and L. Sipos. “Daily light integral maps for agriculture lighting design in Spain”. In: *Smart Agricultural Technology* 9 (2024), p. 100681. ISSN: 2772-3755. DOI: 10.1016/j.atech.2024.100681 (cit. on p. 82).

[216] M. A. Martinez-Medina, M. A. Perez-Martin, and T. Estrela. “Desalination in Spain and the Role of Solar Photovoltaic Energy”. In: *Journal of Marine Science and Engineering* 12 (2024), p. 859. DOI: 10.3390/jmse12060859 (cit. on p. 82).

[217] acuaMed. *Planta Desaladora de Carboneras*. Accessed: 2025-04-14. 2024. URL: https://www.acuamed.es/sites/default/files/actuaciones/739carboneras-corta-def.pdf (cit. on p. 82).

[218] P. Picuno, Z. Godosi, and C. Picuno. "Agrochemical Contamination and Ageing Effects on Greenhouse Plastic Film for Recycling". In: *Applied Sciences* 12.19 (2022). ISSN: 2076-3417. DOI: 10.3390/app121910149 (cit. on p. 93).

[219] J. V. Gulmine, P. R. Janissek, H. M. Heise, and L. Akcelrud. "Degradation profile of polyethylene after artificial accelerated weathering". In: *Polymer Degradation and Stability* 79.3 (2003), pp. 385–397. ISSN: 0141-3910. DOI: 10.1016/S0141-3910(02)00338-5 (cit. on p. 93).

[220] P. Picuno. "Innovative Material and Improved Technical Design for a Sustainable Exploitation of Agricultural Plastic Film". In: *Polymer-Plastics Technology and Engineering* 53.10 (2014), pp. 1000–1011. DOI: 10.1080/03602559.2014.886056 (cit. on p. 93).

[221] E. Espí, A. Salmerón, A. Fontecha, Y. García, and A. I. Real. "Plastic Films for Agricultural Applications". In: *Journal of Plastic Film & Sheeting* 22.2 (2006), pp. 85–102. DOI: 10.1177/8756087906064220 (cit. on p. 93).

[222] A. M. Abdel-Ghany, I. M. Al-Helal, A. Kumar, et al. "Effect of Aging on the Spectral Radiative Properties of Plastic Film-Covered Greenhouse under Arid Conditions". In: *International Journal of Thermophysics* 39 (2018), p. 115. DOI: 10.1007/s10765-018-2434-8 (cit. on p. 93).

[223] C. F. Reinhart and O. Walkenhorst. "Validation of dynamic RADIANCE-based daylight simulations for a test office with external blinds". In: *Energy and Buildings* 33.7 (2001), pp. 683–697. DOI: 10.1016/S0378-7788(01)00058-5 (cit. on p. 103).

[224] J. Graefe and M. Sandmann. "Shortwave radiation transfer through a plant canopy covered by single and double layers of plastic". In: *Agricultural and Forest Meteorology* 201 (2015), pp. 196–208. ISSN: 0168-1923. DOI: 10.1016/j.agrformet.2014.10.011 (cit. on pp. 104, 106).

[225] I. V. Pollet and J. G. Pieters. "SE—Structures and Environment: Condensation and Radiation Transmittance of Greenhouse Cladding Materials, Part 3: Results for Glass Plates and Plastic Films". In: *Journal of Agricultural Engineering Research* 77.4 (2000), pp. 419–428. ISSN: 0021-8634. DOI: 10.1006/jaer.2000.0628 (cit. on pp. 104, 106).

[226] A. Perna. "Modeling Irradiance Distributions in Agrivoltaic Systems". In: (Jan. 2021). DOI: 10.25394/PGS.9971399.v1. URL: https://hammer.purdue.edu/articles/thesis/Modeling_Irradiance_Distributions_in_Agrivoltaic_Systems/9971399 (cit. on p. 109).

[227] C. Toledo and A. Scognamiglio. "Agrivoltaic Systems Design and Assessment: A Critical Review, and a Descriptive Model towards a Sustainable Landscape Vision (Three-Dimensional Agrivoltaic Patterns)". In: *Sustainability* 13 (June 2021), p. 6871. DOI: 10.3390/su13126871 (cit. on p. 109).

[228] K. J. Boote, J. W. Jones, and N. B. Pickering. "Potential uses and limitations of crop models". In: *Agronomy Journal* 88.5 (1996), pp. 704–716. DOI: 10.2134/agronj1996.00021962003600030016x (cit. on p. 109).

[229] J. W. Jones, G. Hoogenboom, C. H. Porter, K. J. Boote, W. D. Batchelor, L. A. Hunt, P. W. Wilkens, U. Singh, A. J. Gijsman, and J. T. Ritchie. "The DSSAT cropping system model". In: *European Journal of Agronomy* 18.3-4 (2003), pp. 235–265. DOI: 10.1016/S1161-0301(02)00107-7 (cit. on p. 109).

[230] J. Schallenberg-Rodriguez, J.-J. Rodrigo-Bello, and B. Del Río-Gamero. “Agrivoltaic: How much electricity could photovoltaic greenhouses supply?” In: *Energy Reports* 9 (2023), pp. 5420–5431. ISSN: 2352-4847. DOI: 10.1016/j.egyr.2023.04.374 (cit. on pp. 109, 127).

[231] K. Q. Loh, K. Harbick, N. J. Eylands, U. R. Kortshagen, and V. E. Ferry. “Design Guidelines for Luminescent Solar Concentrator Greenhouses in the United States”. In: *Advanced Sustainable Systems* n/a.n/a (), p. 2400749. DOI: 10.1002/adsu.202400749 (cit. on pp. 109, 127).

[232] G. Minuto, F. Tinivella, E. Dani, F. Gimelli, and A. Minuto. “Serre fotovoltaiche a duplice attitudine”. In: *Colture Protette* 39.9 (2010), pp. 70–77 (cit. on p. 109).

[233] M. Bruno. “Tracking Optimization in Agrivoltaic Systems: A Comparative Study for Apple Orchards”. https://urn.kb.se/resolve?urn=urn:nbn:se:kth:diva-333634. MA thesis. KTH Royal Institute of Technology, 2023 (cit. on pp. 111, 112).

[234] H. Sánchez, R. Bruhwyler, S. Dittmann, N. Cook, F. Lebeau, C. Meza, and R. Gottschalg. “A Computational Comparison and Validation Between Ray Tracing Techniques Under Special Light-Sharing Trade off Scenarios in Photovoltaics”. In: Sept. 2024. DOI: 10.4229/EUPVSEC2024/4DO.3.3 (cit. on p. 112).

[235] S. Ovaitt. *NREL/bifacial_radiance: v0.4.1*. 2022. DOI: 10.5281/zenodo.6342434 (cit. on p. 112).

[236] E. Potenza, M. Croci, M. Colauzzi, and S. Amaducci. “Agrivoltaic System and Modelling Simulation: A Case Study of Soybean (*Glycine max* L.) in Italy”. In: *Horticulturae* 8.12 (2022), pp. 1160–1180. DOI: 10.3390/horticulturae8121160 (cit. on p. 119).

[237] I. Rylski and M. Spigelman. “Effect of shading on plant development, yield and fruit quality of sweet pepper grown under conditions of high temperature and radlation”. In: *Scientia Horticulturae* 29.1 (1986), pp. 31–35. ISSN: 0304-4238. DOI: 10.1016/0304-4238(86)90028-2 (cit. on p. 119).

[238] J. C. Díaz-Pérez. “Bell Pepper (Capsicum annum L.) Crop as Affected by Shade Level: Fruit Yield, Quality, and Postharvest Attributes, and Incidence of Phytophthora Blight (caused by Phytophthora capsici Leon.)” In: *HortScience* 49.7 (2014), pp. 891–900. ISSN: 0018-5345. DOI: 10.21273/HORTSCI.49.7.891 (cit. on p. 119).

[239] J. Herman and W. Usher. “SALib: An open-source Python library for Sensitivity Analysis”. In: *Journal of Open Source Software* 2 (2017), p. 97. DOI: 10.21105/joss.00097 (cit. on p. 121).

[240] T. Iwanaga, W. Usher, and J. Herman. “Toward SALib 2.0: Advancing the accessibility and interpretability of global sensitivity analyses”. In: *Socio-Environmental Systems Modelling* 4 (2022), p. 18155. DOI: 10.18174/sesmo.18155 (cit. on p. 121).

[241] L. J. V. Miranda. “PySwarms, a research-toolkit for Particle Swarm Optimization in Python”. In: *Journal of Open Source Software* 3 (2018), p. 433. DOI: 10.21105/joss.00433 (cit. on p. 121).

[242] S. Dipta, J. Schoenlaub, M. H. Rahaman, and A. Uddin. “Estimating the potential for semitransparent organic solar cells in agrophotovoltaic greenhouses”. In: *Applied Energy* 328 (2022), p. 120208. DOI: 10.1016/j.apenergy.2022.120208 (cit. on p. 124).

[243] S. Hemming, F. d. Zwart, A. Elings, A. Petropoulou, and I. Righini. “Cherry Tomato Production in Intelligent Greenhouses—Sensors and AI for Control of Climate, Irrigation, Crop Yield, and Quality”. In: *Sensors* 20 (2020), p. 6430. DOI: 10.3390/s20226430 (cit. on p. 124).

[244] L. Gong, M. Yu, S. Jiang, V. Cutsuridis, S. Kollias, and S. Pearson. “Studies of evolutionary algorithms for the reduced Tomgro model calibration for modelling tomato yields”. In: *Smart Agricultural Technology* 1 (2021), p. 100011. DOI: 10.1016/j.atech.2021.100011 (cit. on p. 124).

[245] J. Böhm. “Key advantages of agrivoltaic systems in Germany – A comparison of the electricity yield of different systems”. In: *AgriVoltaics Conference Proceedings 2/2023*. Thünen-Institut, Germany. 2024. DOI: 10.52825/agripv.v2i.986 (cit. on p. 129).

[246] T. Reher, B. Willockx, A. Schenk, J. Bisschop, Y. Huyghe, B. M. Nicolaï, J. A. Martens, J. Diels, J. Cappelle, and B. Van de Poel. “Agrivoltaic cultivation of pears under semi-transparent panels reduces yield consistently and maintains fruit quality in Belgium”. In: *Agronomy for Sustainable Development* 45 (25 2025). DOI: 10.1007/s13593-025-01019-0 (cit. on p. 129).

[247] A. Chalgynbayeva, Z. Gabnai, P. Lengyel, A. Pestisha, and A. Bai. “Worldwide Research Trends in Agrivoltaic Systems—A Bibliometric Review”. In: *Energies* 16.2 (2023), p. 611. DOI: 10.3390/en16020611 (cit. on p. 129).

[248] E. B. Agyekum. “A comprehensive review of two decades of research on agrivoltaics, a promising new method for electricity and food production”. In: *Sustainable Energy Technologies and Assessments* 72 (2024), p. 104055. DOI: 10.1016/j.seta.2024.104055 (cit. on p. 129).

[249] A. G. A. Omer et al. “Understanding Trends, Influences, Intellectual Structures, and Future Directions in Agrivoltaic Systems Research: A Bibliometric and Thematic Analysis”. In: *World* 6.1 (2025), p. 2. DOI: 10.3390/world6010002 (cit. on p. 129).

[250] G. Pandey, S. Lyden, E. Franklin, B. Millar, and M. T. Harrison. “A systematic review of agrivoltaics: productivity, profitability, and environmental co-benefits”. In: *Sustainable Production and Consumption* 56 (2025), p. 13. DOI: 10.1016/j.spc.2025.03.006 (cit. on p. 129).

Appendix

A Fertilizer and phytosanitary treatments

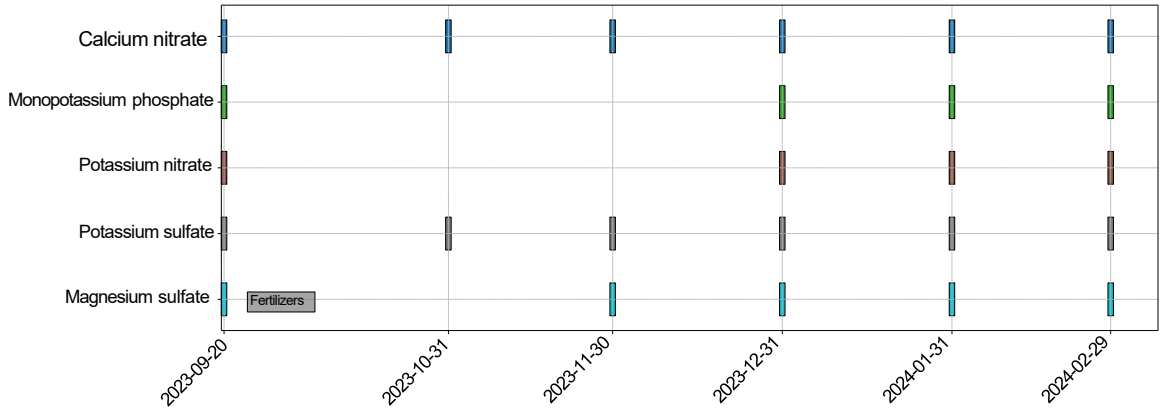


Figure A.1: Use of fertilizers during the study period.



Figure A.2: Use of phytosanitary treatments during the study period.

B Plant physiological and fruit quality measurements

B.1 Additional figures plant physiology

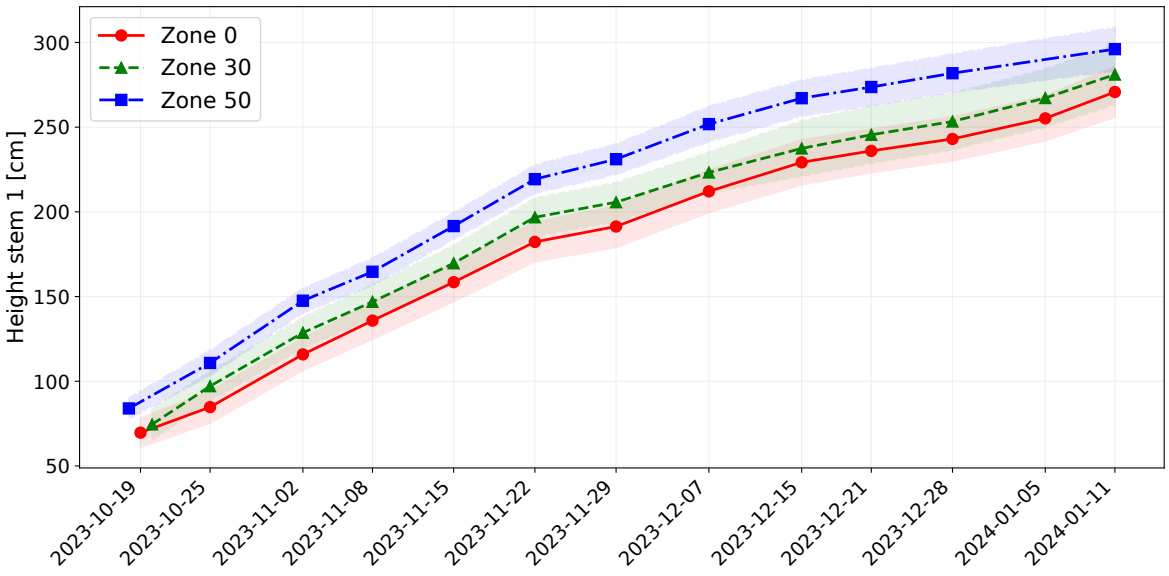


Figure B.1: Height of the tomato plants in the three shading zones for stem 1. The mean of the 20 representative plants per zone is depicted as a line while the respective standard deviation is indicated by the shaded region.

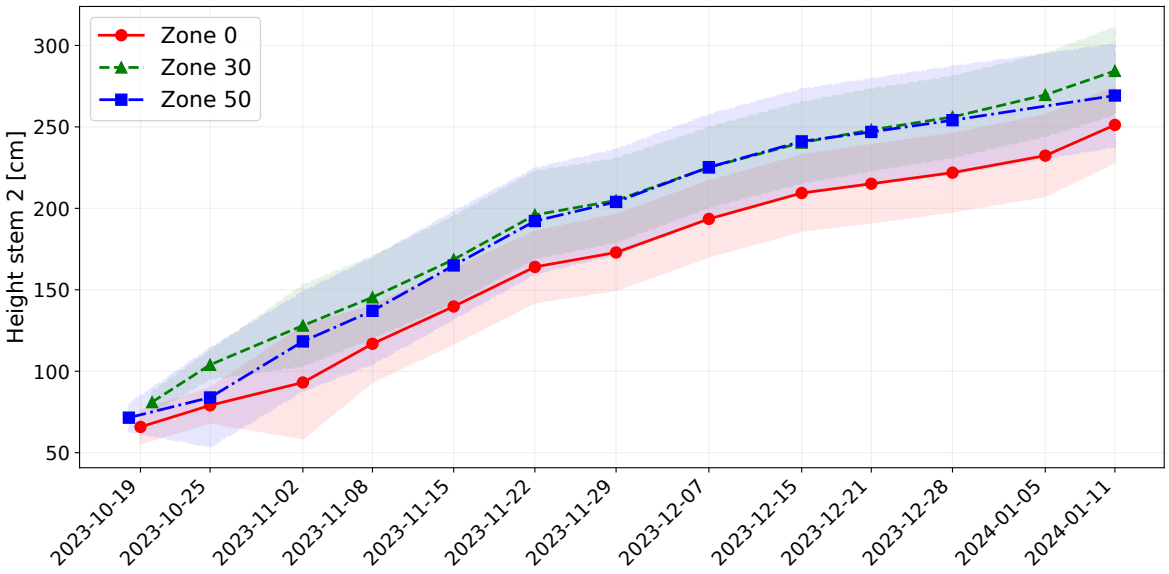


Figure B.2: Height of the tomato plants in the three shading zones for stem 2. The mean of the 20 representative plants per zone is depicted as a line while the respective standard deviation is indicated by the shaded region.

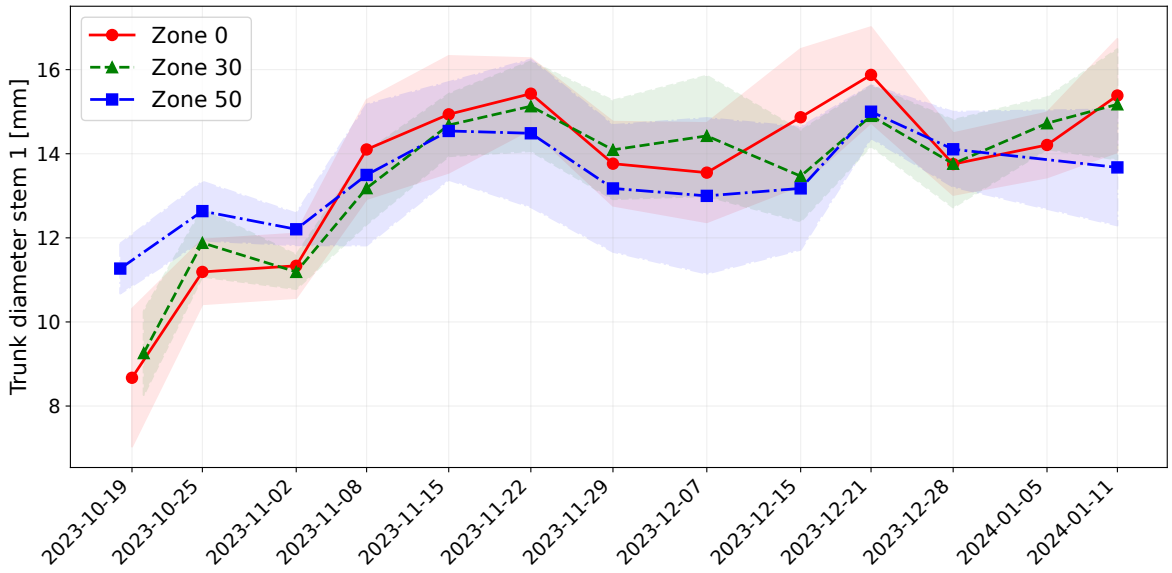


Figure B.3: Diameter of the trunk of the tomato plants in the three shading zones for stem 1. The mean of the 20 representative plants per zone is depicted as a line while the respective standard deviation is indicated by the shaded region.

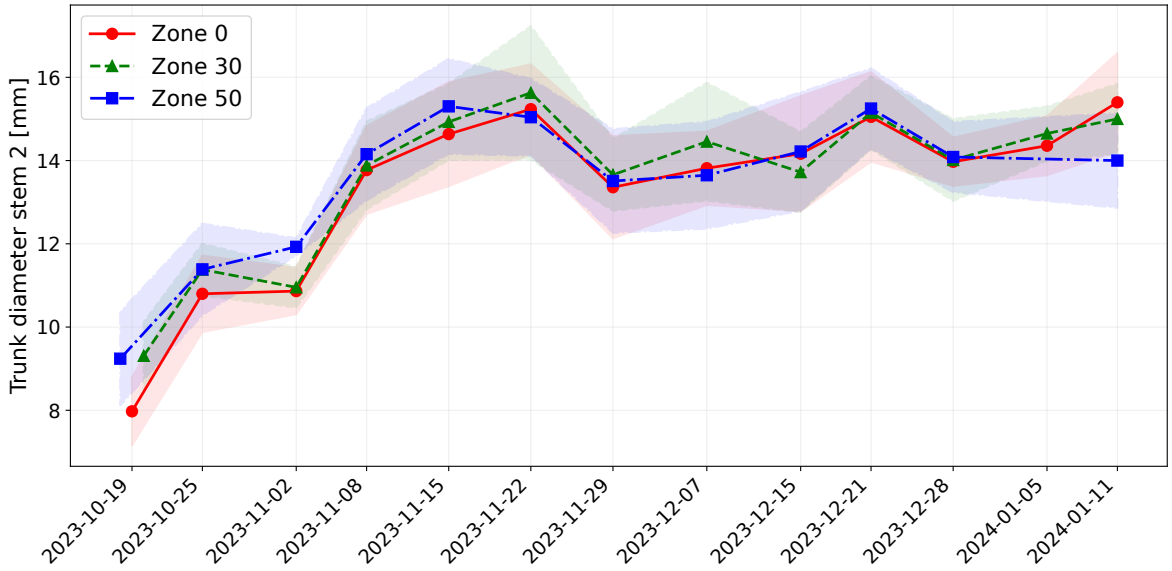


Figure B.4: Diameter of the trunk of the tomato plants in the three shading zones for stem 2. The mean of the 20 representative plants per zone is depicted as a line while the respective standard deviation is indicated by the shaded region.

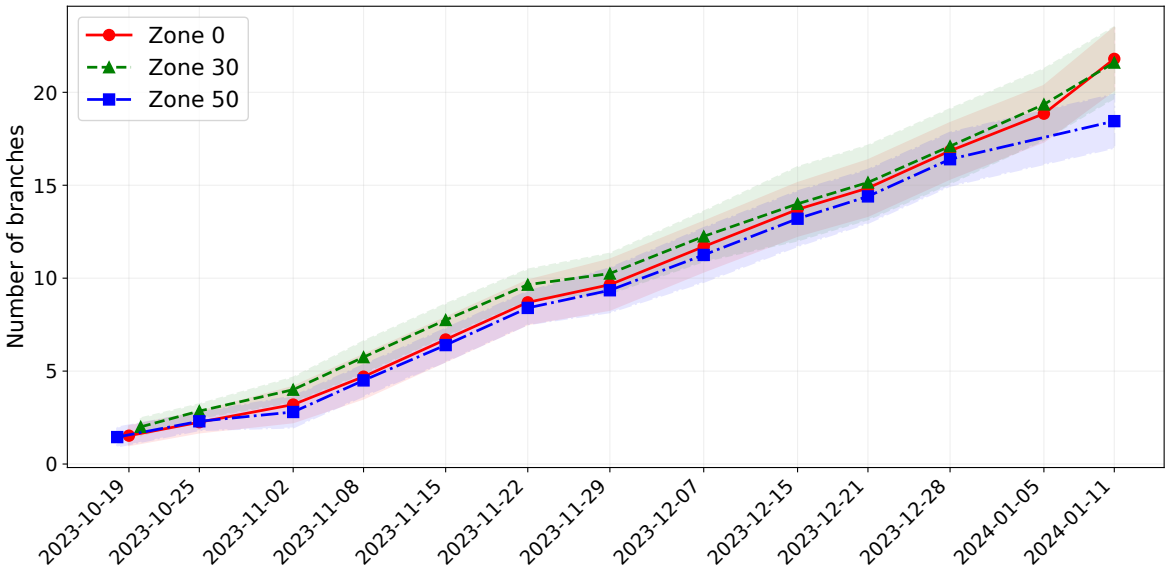


Figure B.5: Number of branches of the tomato plants in the three shading zones. The mean of the 20 representative plants per zone and 2 main stems per plant is depicted as a line while the respective standard deviation is indicated by the shaded region.

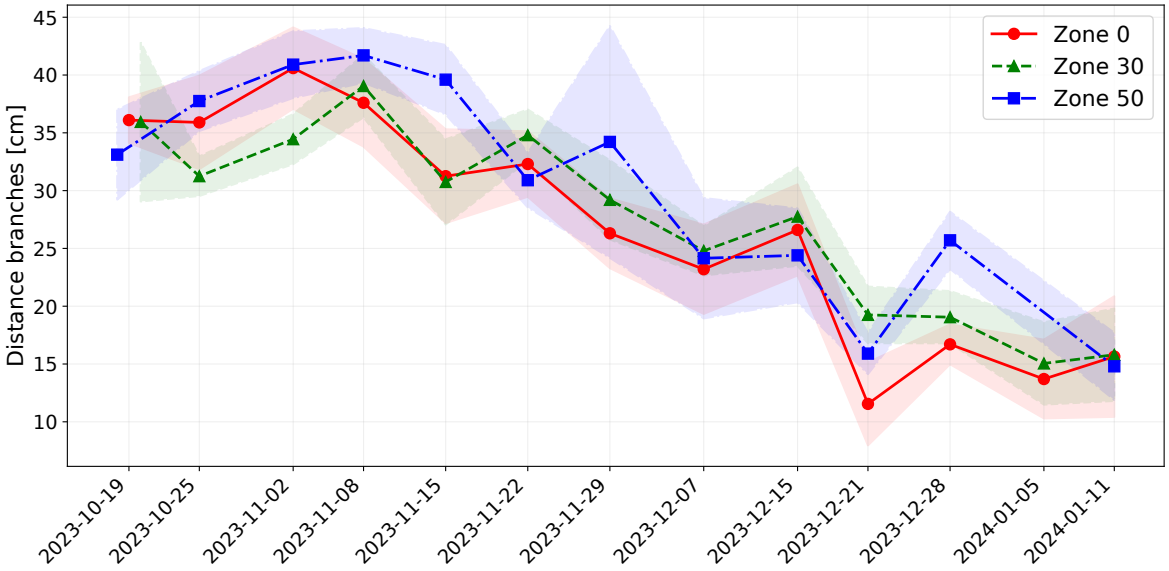


Figure B.6: Distance between the branches of the tomato plants in the three shading zones. The mean of the 20 representative plants per zone and 2 main stems per plant is depicted as a line while the respective standard deviation is indicated by the shaded region.

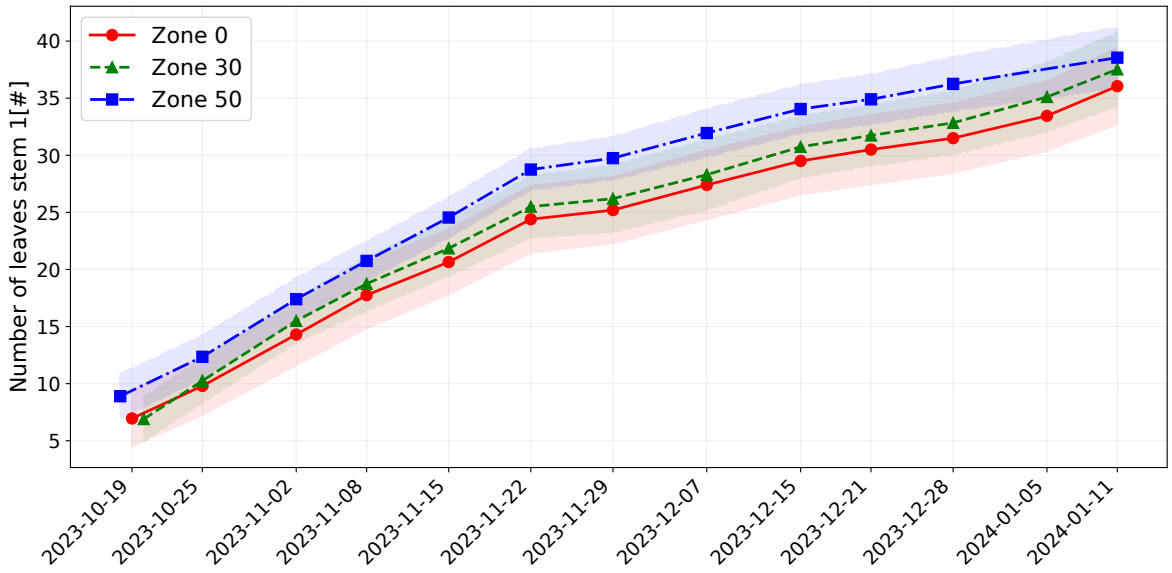


Figure B.7: Number of leaves per branch of the tomato plants in the three shading zones for stem 1. The mean of the 20 representative plants per zone e is depicted as a line while the respective standard deviation is indicated by the shaded region.

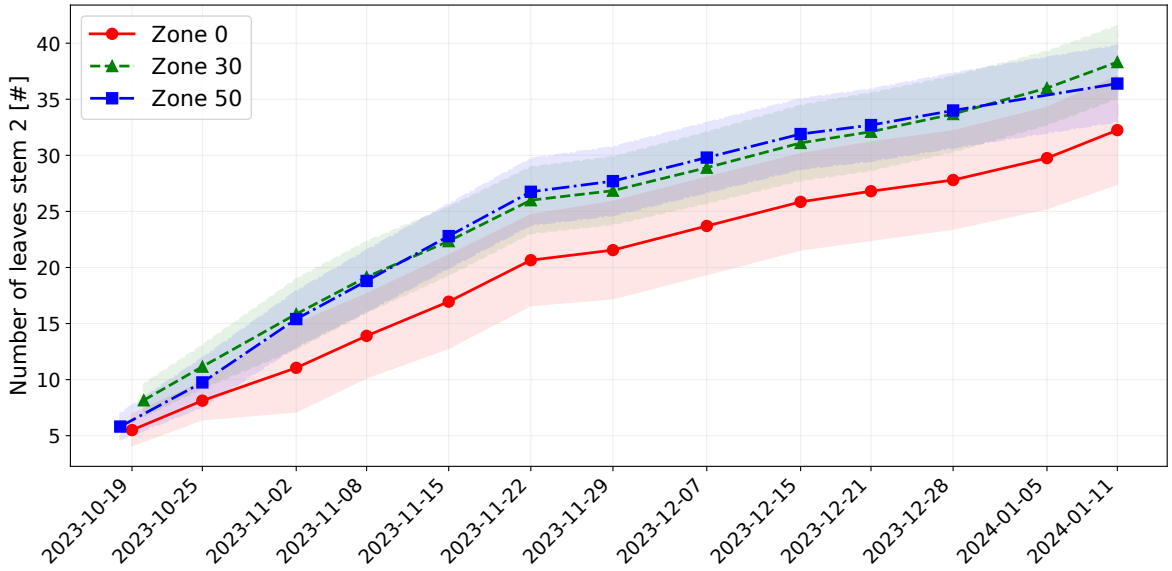


Figure B.8: Number of leaves per branch of the tomato plants in the three shading zones for stem 2. The mean of the 20 representative plants per zone is depicted as a line while the respective standard deviation is indicated by the shaded region.

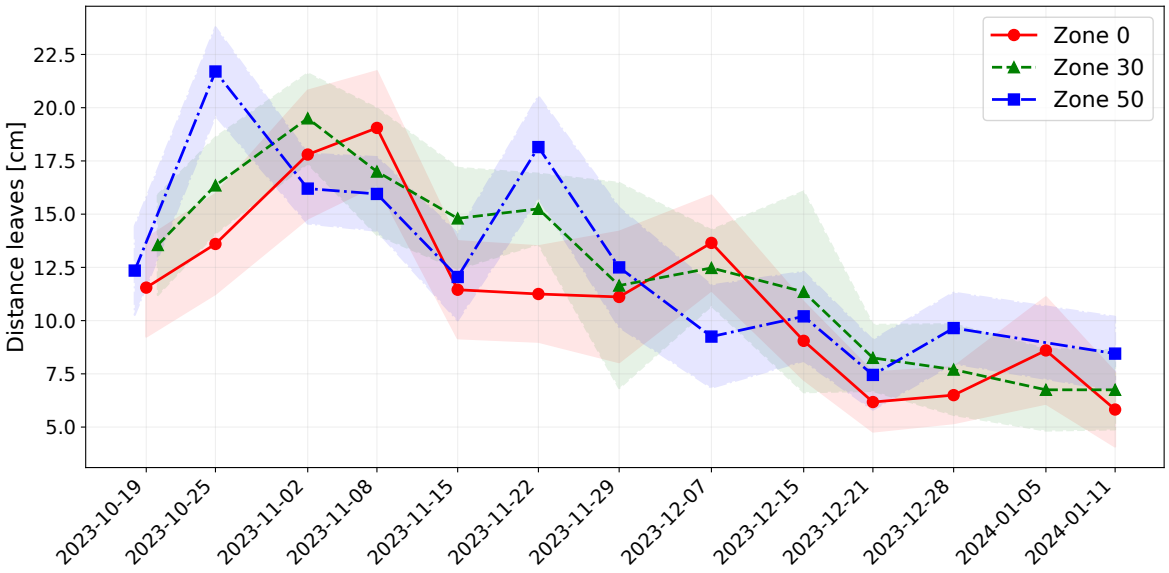


Figure B.9: Distance between leaves per branch of the tomato plants in the three shading zones. The mean of the 20 representative plants per zone and 2 main stems per plant is depicted as a line while the respective standard deviation is indicated by the shaded region.

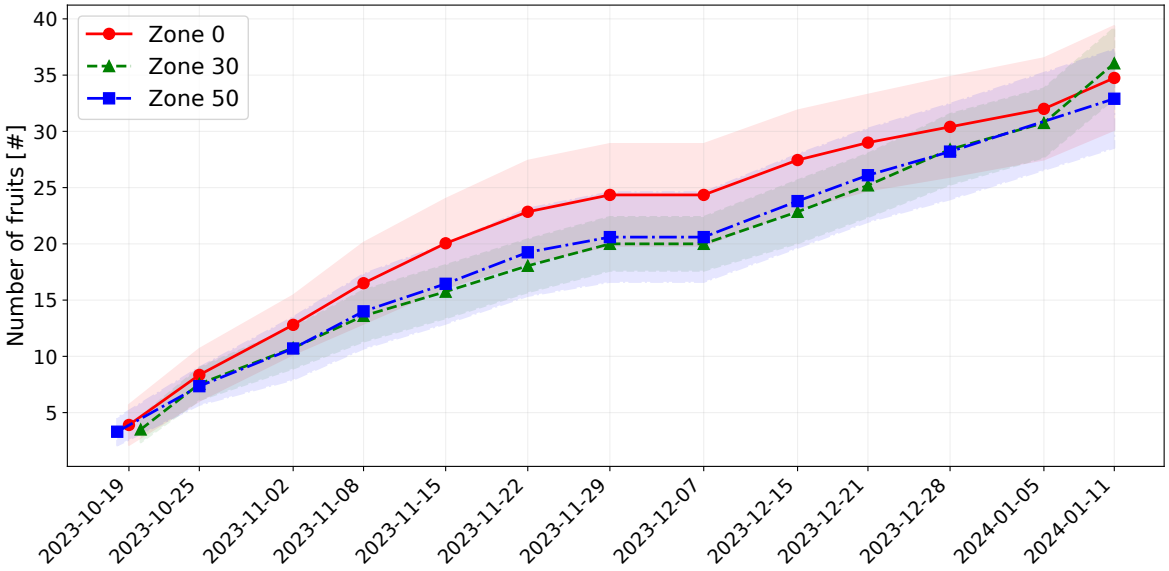


Figure B.10: Number of fruits of the tomato plants in the three shading zones. The mean of the 20 representative plants per zone and 2 main stems per plant is depicted as a line while the respective standard deviation is indicated by the shaded region.

B.2 ADDITIONAL FIGURES FRUIT QUALITY

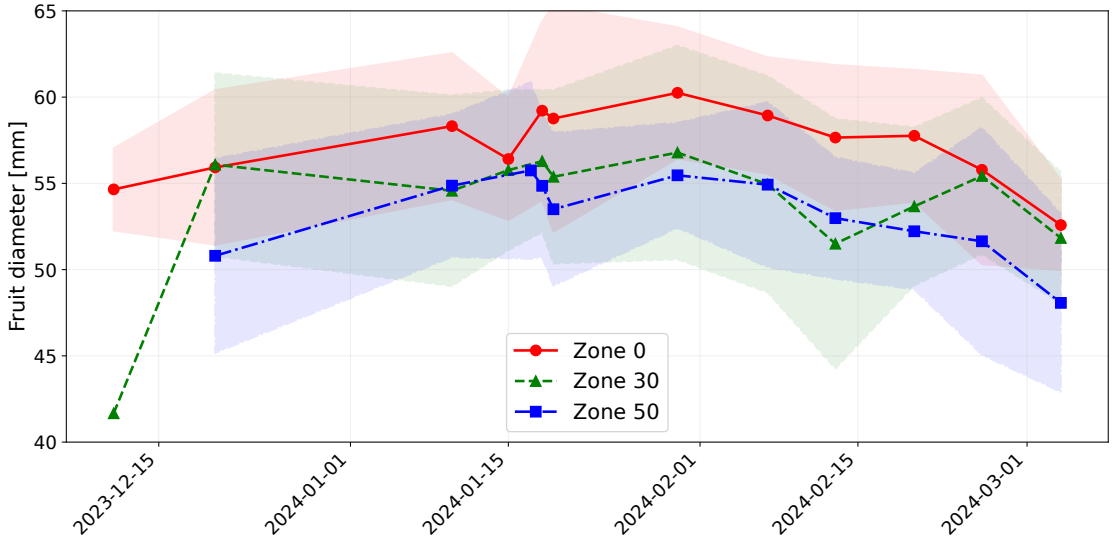


Figure B.11: Mean fruit diameter of the measured tomato fruits. The average values of the measured fruits per zone are presented as lines while the respective standard deviations are shown as shaded regions.

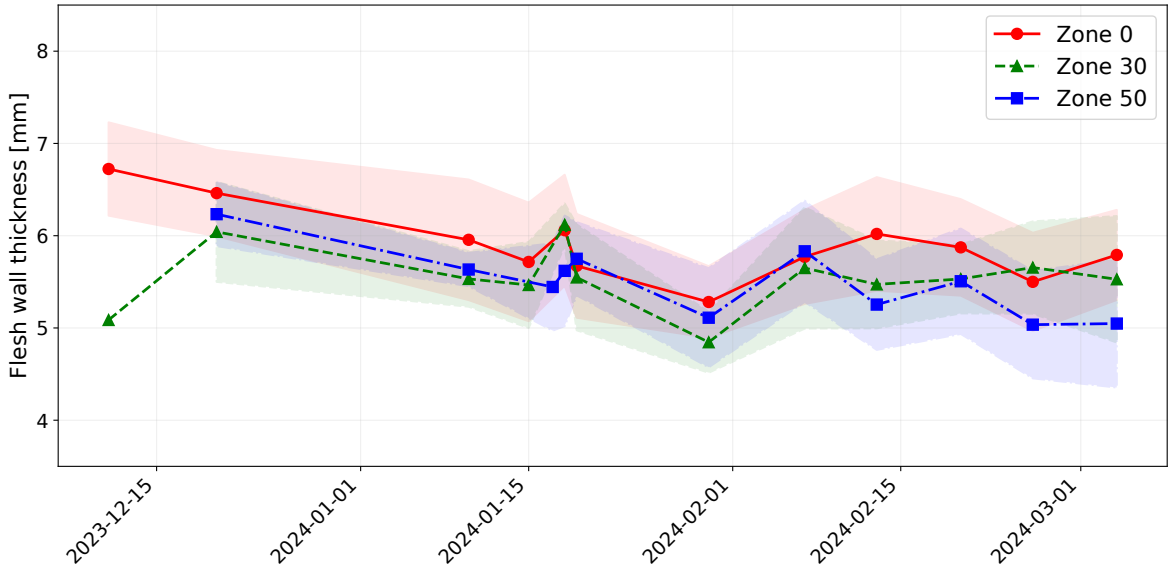


Figure B.12: Mean flesh wall thickness of the measured tomato fruits. The average values of the measured fruits per zone are presented as lines while the respective standard deviations are shown as shaded regions.

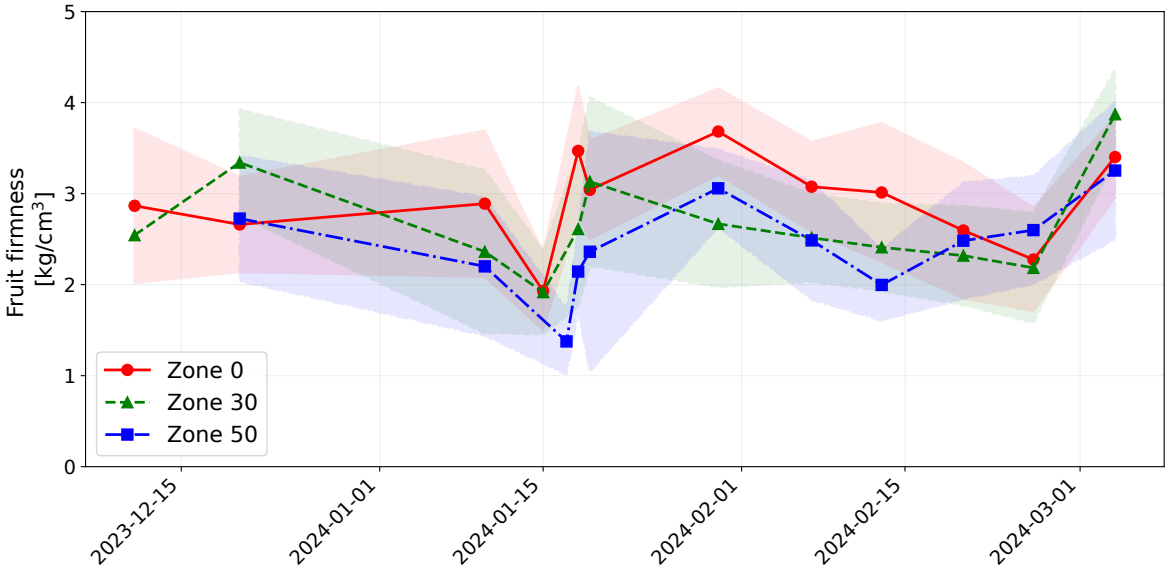


Figure B.13: Mean firmness of the measured tomato fruits. The average values of the measured fruits per zone are presented as lines while the respective standard deviations are shown as shaded regions.

Acknowledgements

This chapter is dedicated to all the people, without whom this thesis would have never been possible. While I tried my best to include everyone, I am very sorry if I forgot someone and already apologize in advance.

First of all, I would like to thank my advisor, Prof. Dr. Robert Pitz-Paal, who gave me the opportunity to work on the interesting topic of agrivoltaics and develop this thesis in the first place. I highly respect his wise mentoring and appreciate his trust in my research. I am thankful for all the positive feedback and important thought-provoking impulses I received during our progress talks, which guided me in the right direction. I am thankful for his faith in my capabilities and the freedom to explore my own ideas. Furthermore, I am glad for the opportunities to present the progress of my work at various conferences all around the world, which broadened my knowledge of the topic and put everything into perspective.

Secondly, I would like to thank Prof. Dr. Cristina Cornaro for her willingness to co-supervise this thesis as the second reviewer – thanks a lot for that. I am grateful for all our scientific discussions, both online and on-site, during my three-month research stay, which I was able to spend with her working group in Rome, Italy. I am very grateful for her openness in welcoming me in her group and making my stay as perfect as it was. Furthermore, I appreciate all her help and support along the way, and I am thankful for always believing in me.

I am grateful for the constant and strong engagement of my supervisor, Natalie Hanrieder. The discussions with her were crucial for the planning, development, and successful realization of this thesis. I appreciate her support throughout the entire thesis process, whether it was organizing project tasks and budget, speaking Spanish (or Andaluz) with our project partners, sending me to conferences or even acting as my landlord during my first months in Almería. Her work has been invaluable to me and to this thesis.

Special thanks go to the heads of the Qualification Department, Peter Heller and Stefan Wilbert, for their support and in particular for their dedication to growing the topic of agrivoltaics within DLR, which made this work possible.

I am grateful for my students Ana Bendejacq Seychelles, Lyubomir Hristov and Julian Kornas, whom I was able to supervise during their stay in Almería. Ana, you were there right at the beginning of my PhD and, with your work, you made it so easy for me to get familiar with the topic of agrivoltaics, making it possible for me to dive right into it. Lyubomir, you took care of the monitoring system for our greenhouse experiment and, without your dedication, I would never have managed to set everything up as quickly and reliable as we did. Julian, you did an outstanding job on your master thesis, the very first master's thesis on agrivoltaics within DLR, and your support with the experiment, data cleaning and analysis was invaluable. Without the support and hard work of all three of you, this thesis would not have been possible in its current form.

A big thank you goes to Sergio González Rodríguez and David Muruve Tejada for their amazing work on mounting structures, cable systems, data logger programming, and all other hardware-related aspects of the greenhouse experiment. Your quick, logical thinking and problem-solving skills saved me countless times from having to find solutions on my own. Thank you for all your efforts in and around the greenhouse, even when it meant waking up at 5 a.m. to escape the intense Almería heat in August. I will never forget our car rides with Lyubomir to and from the greenhouse back to PSA, which were always filled with laughter and an hour of Spanish practice. Sergio, thank you especially for encouraging me to speak and practice Spanish with you, which helped me become fluent in no time.

I would like to thank the entire Almería team for a warm and productive work environment. In particular, my female colleagues – Fernanda, Anja, Tamy, Maria, Elena, Natalie, Anne, and Sonja – made this place truly special for me. I deeply appreciate our mutual support for each other. A special thanks goes to Tamy for our Monday and Wednesday lunch breaks, which were always a highlight of my week. I am also very grateful to Anja for always picking me up, listening to my worries, and sharing valuable insights into systematic structures. Your explanations eased my nerves and helped me understand things much better. Of course, I am equally thankful for all my other colleagues. I am glad to have met Yann, Rafal, Alex, Jakob, Michael, Lukas, Niels, Lothar, Rone, Eduardo, Bijan, Niklas and Álvaro. I will never forget our time together, both inside and outside of work, from our New Year's parties and beach gatherings to padel classes, casual 10Ks, and even half marathons.

Similarly, I would like to thank the Italian ESTER lab working group – Cristina, Gianluigi, Federico, Ali, Luca, Emiliano, Marco, Francesco, and Marcello – for warmly welcoming me into their team. I always felt comfortable and included. I truly appreciated our wide-ranging and insightful discussions, whether about PV systems or Italian cuisine. During my stay with you, I significantly improved my `Radiance` simulations and gained a much deeper understanding of the software. Beyond the technical learning, you taught me many cultural lessons: no cappuccino after 11, Gianluigi's wife makes the best food and gnocchi only on Thursdays.

In this context, I would like to express my gratitude towards my mentor, Maria Isabel Roldan Serrano, who was there for me during difficult times and always guided me calmly and thoughtfully. I truly appreciate the time she took to listen to me and help me develop a clear game plan. From every conversation, I gained valuable lessons which helped me find my own path and set healthy boundaries.

I was fortunate to be part of the Role Model Team of the DLR "Women+ in Science and Technology" network and have worked with Larissa Dietz, Caroline Lange, Larissa Queda, Phyo Myat Kyaw and Chiara Amato. Organizing and hosting the role model talks for our network was always a welcome task besides my usual daily PhD business.

I would also like to thank Daniel Schmitt, Michael Nieslony, and Robert Kujawa for volunteering to proofread my thesis and spending a significant amount of time with this document. Thank you for providing me with many thoughtful comments and your valuable input – I appreciate it a lot!

This thesis would also not have been possible without the support of my friends over the years – a particular thank you to Vanessa, Alice, Christina, Daria, Ina, Kathrin and Annika, who are the best friends I could wish for. I am truly thankful for our unconditional bond even after many years after finishing school together. I am also thankful for Rosa and Maike for our numerous video calls and all the care packages you sent me from Germany. I am grateful for my friend Julia, who didn't hesitate to visit me right after I moved to Almería and who has endless patience when it comes to calling me. Similarly, I am thanking Daniel and Willy, who both know what it takes to do a PhD and who both gave me nothing but understanding.

Thank you so much to my family, who always made sure I felt included even though I moved far away. Thank you also to the wonderful family of my partner, who warmly welcomed me into their lives and offered me nothing but love and support. Finally, I am blessed with my supportive and loving partner, Michael, who was always there for me and supported me through all the ups and downs. You did more than I could ever put into words here, and I could not wish for a better partner in life. Thank you for always being there for me and believing in me, this thesis would not have been possible without you!